

Structural Health Monitoring through Computational and Experimental Methods as a Generic Approach to the Damage Detection Problem



Panagiotis Seventekidis

Supervisor: Assoc. Prof. Dimitrios Giagopoulos

Department of Mechanical Engineering

University of Western Macedonia

A thesis submitted in partial fulfilment of the requirements
for the award of Doctor of Philosophy

July 2022

Three member Scientific Advisory Committee:

- Assoc. Prof. Dimitrios Giagopoulos, Aristotle University of Thessaloniki
- Prof. Sotirios Natsiavas, Aristotle University of Thessaloniki
- Prof. Costas Papadimitriou, University of Thessaly

Seven member Selection Committee:

- Prof. Spilios Fasois, University of Patras
- Prof. Ioannis Antoniadis, National Technical University of Athens
- Prof. Panagiotis Seferlis, Aristotle University of Thessaloniki
- Asst. Prof. Ioannis Sakellariou, University of Patra

Declaration

I hereby declare that except where specific reference is made to the work of others, the contents of this dissertation are original and have not been submitted in whole or in part for consideration for any other degree or qualification in this, or any other university. This dissertation is my own work and contains no material which is the outcome of work done in collaboration with others, except as specified in the text and Acknowledgements.

Panagiotis Seventekidis

July 2022

Acknowledgements

I take the opportunity to express my gratitude to my supervisor Assoc. Professor Dimitrios Giagopoulos for his help, support, guidance and collaboration throughout the presented research and writing of my thesis. I would also like to thank all the members of the committee Profs. Sotirios Natsiavas, Costas Papadimitriou, Spilios Fasois, Ioannis Antoniadis, Panagiotis Seferlis and Ioannis Sakellariou for their participation. Finally, I thank my parents for all their support in the past years.

Abstract

Detecting damage or changes in structures by monitoring their response has emerged as a field in engineering known as Structural Health Monitoring (SHM). A majority of applications in SHM involve vibration measurements and processing of signals to detect changes in the dynamics related to damage or degradation. The primary points of attention are found, first in the data processing and decision system and second in the data availability for building reliable health prediction models. In the proposed thesis, both problems are tackled in an innovative framework by combining Machine Learning (ML) damage detection and Finite Element (FE) simulations for the necessary training data of ML models. Focus is given on the increasingly popular Artificial Neural Networks (ANN) applied in Deep Learning (DL) form. DL models are able to process and classify signals with little to no pre-processing making them ideal for vibration based SHM tasks. FE models on the other hand can provide arbitrary amounts of simulated vibration responses and generate labelled training data. This is especially useful in cases where access to data of damaged states is not available but may be simulated with an accurate numerical model updated on the experimental intact state. The proposed methodology of FE data generation, DL training on the simulated responses and final validation on corresponding experimental health statuses is tested on three different structures of increasing complexity. The goal of the framework can be summarized in studying the phenomenon of generalizing damage information or patterns in FE simulated signals to the real structures. For the tested cases, detailed studies are presented on how DL model architecture, damage identification problem formulation and FE model error affect the final experimental generalization capability of the proposed SHM framework.

Keywords: Structural Dynamics, Machine Learning, Deep Learning, Finite Element Modeling, Structural Health Monitoring, Damage Detection, Damage Identification, Vibration Measurements, Finite Element Model Updating

Περίληψη

Η ανίχνευση βλαβών ή ανωμαλιών σε κατασκευές μέσω παρακολούθησης της απόκρισής τους είναι ένας αναπτυσσόμενος κλάδος της μηχανικής γνωστός ως Structural Health Monitoring (SHM) ή αλλιώς Παρακολούθηση της Δομικής Ακεραιότητας. Η πλειονότητα των εφαρμογών SHM αφορά τη μέτρηση της απόκρισης μέσω ταλαντωτικών σημάτων και την επεξεργασία των δεδομένων για την ανίχνευση δομικών σφαλμάτων. Τα σημεία ενδιαφέροντος εντοπίζονται, πρώτον στη μέθοδο επεξεργασίας σημάτων και στο σύστημα αποφάσεων και δεύτερον στη διαθεσιμότητα των απαραίτητων δεδομένων. Στην προτεινόμενη διατριβή τα προβλήματα αυτά αντιμετωπίζονται με μια καινοτόμα μεθοδολογία που συνδυάζει ανίχνευση βλαβών μέσω μηχανικής μάθησης (Machine Learning-ML) και μοντέλα πεπερασμένων στοιχείων (Finite Element-FE) για την παραγωγή δεδομένων. Στο κομμάτι του ML χρησιμοποιούνται τεχνητά νευρωνικά δίκτυα (Artificial Neural Networks-ANN) σε μορφή βαθιάς μάθησης (Deep Learning-DL). Τα μοντέλα DL μπορούν να επεξεργαστούν και να κατηγοριοποιήσουν σήματα με μικρή ή και καθόλου προ επεξεργασία, κάτι το οποίο τα καθιστά ιδανικά για εφαρμογές SHM. Τα μοντέλα FE επίσης, μπορούν να παράγουν πλήθος ταλαντωτικών δεδομένων χωρίς περιορισμούς και να δημιουργήσουν επαρκή δεδομένα για την εκπαίδευση των DL. Αυτό μπορεί να αποδειχθεί ιδιαίτερα χρήσιμο για περιπτώσεις όπου η πειραματική μέτρηση αποκρίσεων με βλάβες είναι αδύνατη, αλλά μπορεί να προσομοιωθεί με αριθμητικά μοντέλα που έχουν βελτιστοποιηθεί στην υγιή κατάσταση. Η προτεινόμενη μεθοδολογία της παραγωγής αριθμητικών δεδομένων με FE, εκπαίδευση μοντέλων DL στις προσομοιωμένες αποκρίσεις και τελική επιβεβαίωση με αναγνώριση αντίστοιχων πειραματικών βλαβών, εξετάζεται σε τρεις κατασκευές διαφορετικής πολυπλοκότητας. Στόχος είναι η μελέτη του φαινομένου γενίκευσης πληροφορίας και μοτίβων από την προσομοιωμένη ταλαντωτική απόκριση στην πραγματική κατασκευή. Για τις εξεταζόμενες κατασκευές και την προτεινόμενη μεθοδολογία SHM, μελετάται, η επίδραση της αρχιτεκτονικής των μοντέλων DL, τα ζητούμενα του προβλήματος ανίχνευσης βλαβών και το σφάλμα των μοντέλων FE στην τελική γενίκευση στην πραγματική κατασκευή.

Λέξεις κλειδιά: Δυναμική Κατασκευών, Μηχανική Μάθηση, Βαθιά Μάθηση, Μοντέλα Πεπερασμένων Στοιχείων, Παρακολούθηση Δομικής Ακεραιότητας, Ανίχνευση Βλαβών, Αναγνώριση Βλαβών, Ταλαντωτικές Μετρήσεις, Ενημέρωση Μοντέλων Πεπερασμένων Στοιχείων

Εκτεταμένη Περίληψη

Αντικείμενο της προτεινόμενης διδακτορικής διατριβής είναι η ανάπτυξη μεθοδολογίας διάγνωσης και αναγνώρισης βλαβών, σε ένα πλαίσιο παρακολούθησης της δομικής ακεραιότητας κατασκευών μέσω ταλαντωτικών σημάτων. Για την κατηγοριοποίηση της κατάστασης βλάβης που εμπεριέχεται στα ταλαντωτικά σήματα χρησιμοποιούνται μοντέλα μηχανικής μάθησης που έχουν εκπαιδευτεί από αριθμητικά δεδομένα. Σκοπός είναι η αποτελεσματική χρήση μοντέλων πεπερασμένων στοιχείων για την παραγωγή δεδομένων που προσομοιώνουν τις βλάβες και χρήση αυτών για εκπαίδευση μοντέλων βαθιάς μάθησης. Η μεθοδολογία επαληθεύεται πειραματικά για διαφορετικές εργαστηριακές κατασκευές και πλήθος βλαβών, ώστε να επιβεβαιωθεί η γενίκευση των μοτίβων δυναμικής απόκρισης από την προσομοίωση στην πραγματική κατασκευή. Μελετήθηκε η επίδραση βασικών παραμέτρων που επηρεάζουν την γενίκευση στις αντίστοιχες πραγματικές βλάβες. Η ιδιαίτερη χρησιμότητα της μεθοδολογίας μπορεί να εντοπιστεί σε περιπτώσεις όπου δεν υπάρχει πρόσβαση σε πειραματικά δεδομένα βλαβών, αλλά η αριθμητική μοντελοποίηση μπορεί να πραγματοποιηθεί με επαρκή ακρίβεια. Με τον τρόπο αυτό υπάρχει η δυνατότητα για συστήματα αναγνώρισης βλάβης σε κατασκευές χωρίς να χρειάζονται καταστροφικές δοκιμές, αλλά ακριβή μοντέλα πεπερασμένων στοιχείων τα οποία ενημερώνονται στην υγιή κατασκευή. Η παραγωγή αριθμητικών δεδομένων εντός του προτεινόμενου πλαισίου εργασιών πραγματοποιήθηκε με το εμπορικό λογισμικό πεπερασμένων στοιχείων MSC NASTRAN μέσω ρουτίνας MATLAB. Τα μοντέλα βαθιάς μάθησης αναπτύχθηκαν στο keras, μια ανοικτού κώδικα βιβλιοθήκη της rython. Οι ταλαντωτικές μετρήσεις καθώς και η διέγερση των κατασκευών πραγματοποιήθηκε με εξοπλισμού του εργαστηρίου Ταλαντώσεων και Δυναμικής Μηχανών του Πανεπιστημίου Δυτικής Μακεδονίας.

Η έρευνα που έχει εκπονηθεί επικεντρώνεται:

- Στην εφαρμογή πειραματικών μεθόδων συλλογής ταλαντωτικών σημάτων κατασκευών για διαφορετικές περιπτώσεις βλαβών μέσω δικτύου αισθητήρων (επιταχυνσιόμετρα).
- Στην αξιοποίηση πειραματικών μετρήσεων της υγιούς κατάστασης της κατασκευής για την κατάστρωση βελτιστοποιημένου μοντέλου πεπερασμένων στοιχείων, το οποίο χρησιμοποιείται για δημιουργία αριθμητικών δεδομένων (dataset) σε διαφορετικές καταστάσεις βλαβών.
- Στην κατάστρωση μεθοδολογίας συστήματος παρακολούθησης δομικής ακεραιότητας και αναγνώρισης βλαβών μέσω μοντέλων βαθιάς μάθησης που επεξεργάζονται ταλαντωτικά σήματα. Χρήση των μοντέλων βαθιάς μάθησης ως σύστημα διάγνωσης κατάστασης με προηγούμενη επιβλεπόμενη εκπαίδευση (supervised learning) στο dataset των προσομοιωμένων καταστάσεων.

- Στην αναγνώριση και μελέτη των παραμέτρων που επηρεάζουν την αξιοπιστία και σωστή γενίκευση των αριθμητικώς εκπαιδευμένων μοντέλων βαθιάς μάθησης στις αντίστοιχες πραγματικές αντίστοιχες καταστάσεις.
- Μελέτη της επίδρασης στην τελική πειραματική γενίκευση και αξιοπιστία σύμφωνα με: την αρχιτεκτονική βαθιάς μάθησης, την ιεραρχική δομή του προβλήματος αναγνώρισης βλάβης, την προσομοίωση των αβεβαιοτήτων, τον τύπο και την ποιότητα των δεδομένων και το σφάλμα μοντέλου που περιέχονται στα αριθμητικά dataset εκπαίδευσης.

Τα παραπάνω ερευνητικά αποτελέσματα παρουσιάζονται στα επιμέρους κεφάλαια της προτεινόμενης διδακτορικής διατριβής, οργανωμένα ως εξής:

- Στο Κεφάλαιο 1 παρουσιάζονται τα κίνητρα και οι καινοτομίες κατά την εκπόνηση της διατριβής και περιγράφεται η προτεινόμενη ροή εργασιών της μεθοδολογίας.
- Στο Κεφάλαιο 2 παρουσιάζεται το θεωρητικό υπόβαθρο.
- Στο Κεφάλαιο 3 παρουσιάζεται η πρώτη εφαρμογή της προτεινόμενης μεθοδολογίας που αποτελείται από μια κατασκευή μεταλλικής δοκού. Μελετάται η επίδραση της αρχιτεκτονικής βαθιάς μάθησης και η ακρίβεια του μοντέλου στην πειραματική γενίκευση για αναγνώριση καταστάσεων βλαβών.
- Στο Κεφάλαιο 4 παρουσιάζεται η δεύτερη εφαρμογή της προτεινόμενης μεθοδολογίας που αποτελείται από ένα δικτύωμα σύνθετου υλικού. Μελετάται η επίδραση της ιεραρχίας του προβλήματος αναγνώρισης βλαβών στην πειραματική γενίκευση .
- Στο Κεφάλαιο 5 παρουσιάζεται η τρίτη εφαρμογή της προτεινόμενης μεθοδολογίας στο δικτύωμα σύνθετου υλικού. Μελετάται η επίδραση της προσομοίωσης αβεβαιοτήτων στα αριθμητικά δεδομένα και της βελτίωσης της ποιότητας αυτών, στην τελική πειραματική αξιοπιστία.
- Στο Κεφάλαιο 6 παρουσιάζεται η τέταρτη εφαρμογή της προτεινόμενης μεθοδολογίας σε κατασκευή δικτύωματος μεταλλικής γέφυρας εργαστηριακής κλίμακας. Μελετάται η επίδραση του σφάλματος μοντέλου που εμπεριέχεται στα προσομοιωμένα δεδομένα για εκπαίδευση βαθιάς μάθησης, στην πειραματική γενίκευση και αξιοπιστία.
- Στο Κεφάλαιο 7 παρουσιάζονται τα γενικά συμπεράσματα και η μελλοντική προτεινόμενη έρευνα.

Οι κύριες συνεισφορές της προτεινόμενης διατριβής εστιάζονται στην:

- Ανάπτυξη ενός συνδυασμένου πειραματικού και υπολογιστικού πλαισίου για παραγωγή δεδομένων εκπαίδευσης μοντέλων βαθιάς μάθησης μέσω πεπερασμένων στοιχείων και χρήση των εκπαιδευμένων μοντέλων για την παρακολούθηση της δομικής ακεραιότητας και της αναγνώρισης βλαβών κατασκευών
- Ανάπτυξη και παρουσίαση μεθοδολογίας δημιουργίας ενός συνόλου δεδομένων (data set) λαμβάνοντας υπόψη τις αβεβαιότητες κατά την μοντελοποίηση με πεπερασμένα στοιχεία.

- Ανάπτυξη και παρουσίαση μεθοδολογίας ιεραρχικής οργάνωσης των προβλημάτων ανίχνευσης και αναγνώρισης βλαβών.
- Ανάπτυξη και παρουσίαση μεθοδολογίας εκτίμησης της επίδρασης του σφάλματος των μοντέλων πεπερασμένων στοιχείων στην πειραματική γενίκευση των εκπαιδευμένων μοντέλων βαθιάς μάθησης.

List of Tables

Table 3.1: Optimal FE model structural parameters after model updating	59
Table 3.2: Computed eigenfrequencies of healthy and damaged states using optimal FE model along with the difference compared to the healthy state.....	60
Table 3.3: FE generated data for SHM classifiers learning	62
Table 3.4: 1D-CNN Grid-Search hyperparameter ranges for the multi-head CNNs	65
Table 3.5: 1D-CNN Grid-Search hyperparameter ranges for the single-head CNNs	65
Table 3.6: Learning results for the multi-head and single-head 1D CNN architectures on the binary DI problem	66
Table 3.7: Learning results for the 1D-CNN for the multi and single head architectures on the multiclass DI problem.....	69
Table 4.1: Updated FE model material parameters.....	81
Table 4.2: Comparison between identified, nominal and updated FE predicted modal frequencies	81
Table 4.3: Comparison between identified F6 damage case and FE calculated frequencies for different simulated connection stiffnesses	85
Table 4.4: Data sets and classification labels according to hierarchical SHM stage classifiers ..	89
Table 4.5: <i>Multihead</i> CNN filters, neuron numbers, activations and loss function for the for the hierarchical classifiers.....	90
Table 4.6: Learning scores on different SHM classification stages.....	91
Table 4.7: Learning score of the multiclass classifier.....	91
Table 5.1: Material parameter values used in the FE model which were updated on the healthy state	114
Table 5.2: Organization of learning data.....	118
Table 5.3: Scores on experimental states predictions by trained classifier ensembles for a total of 100 inputs for each case.....	122
Table 5.4: Scores on FE simulated states by trained classifier ensembles for a total of 100 inputs for each case.....	125
Table 5.5: Scores on experimental states predictions by trained classifier ensembles with single damage approximation constants r for a total of 100 inputs for each case	129
Table 5.6: Scores on FE simulated states by trained classifier ensembles for a total of 100 inputs for each case with single damage approximation constants r for a total of 100 inputs for each case	129
Table 5.7: Scores on experimental states predictions by the trained classifier ensemble with 3% material uncertainty simulation for a total of 100 inputs for each case	130
Table 5.8: Scores on FE simulated states by the trained classifier ensemble with 3% material uncertainty simulation for a total of 100 inputs for each case	131

Table 5.9: Generalization from numerical to experimental data in terms of mismatch between correct classification scores for numerical and experimental inputs	132
Table 6.1: Identified modal values for the experimental intact or Healthy case of the bridge ..	142
Table 6.2: FE Model Parameters Updating	145
Table 6.3: Updated FE model natural frequencies comparison with the experimentally identified	146
Table 6.4: Identified modal values for the experimental D1 and D3 cases of the bridge	152
Table 6.5: Training cases per class in each Damage Identification Problem.....	154
Table 6.6: CNN architecture used	155
Table 6.7: FE material stiffness in training data sets	163

List of Figures

Figure 2.1: Flow chart of the proposed monitoring and damage identification by simulated damage responses.....	38
Figure 2.2: Example of Damage scenarios on FE model of truss and the corresponding entries in the label vector \mathbf{Y}	43
Figure 2.3: Simple linear spring system with 2 DOFs and damage simulated as 10% increased mass on the right edge.....	44
Figure 2.4: Eigenfrequency data generated with FE model and measurement uncertainties for the healthy and the damaged state of the 2 DOF linear system. Graphs A and B depict results for 1% uncertainty in stiffness, while C and D represent 2 and 3% respectively	46
Figure 2.5: Example of Forward Propagation in a network with a Convolutional and Classification (fully connected perceptron) part.....	47
Figure 2.6: Example of a linear separation boundary with a single perceptron neuron	49
Figure 3.1: Experimental set-up with accelerometer and excitation equipment (up). Damage case 1 (down left) simulated as mounted mass on the beam. Damaged case 2 (down right) with a cut on the beam	56
Figure 3.2: Sketch of the experimental setup (left) and the optimal FE model (right) including also modeling of the base support	57
Figure 3.3: FE model parameters to be updated for the FE optimal model construction	58
Figure 3.4: Comparison of acceleration time responses for the optimal and nominal FE models against the experimental measurement for accelerometer locations A1 (up) and A2 (down).....	60
Figure 3.5: CNN head architecture (left) and 4-headed CNN (right)	64
Figure 3.6: Class predictions on experimental Healthy (up) and Damaged (below) inputs. Results on single (left) and multi (right) filter architectures from optimal FE training data.....	66
Figure 3.7: Class predictions on experimental Healthy (up) and Damaged (below) inputs. Results on single (left) and multi (right) filter architectures from nominal FE training data.....	67
Figure 3.8: Confusion matrices of the network class predictions on the experimental measurements for the binary DI problem according to FE model learning data and network architecture.....	68
Figure 3.9: Class predictions on experimental Healthy (up), Damaged 1(middle) and Damaged 2 (below) inputs. Results on single (left) and multi (right) filter architectures from optimal FE training data	70
Figure 3.10: Class predictions on experimental Healthy (up), Damaged 1(middle) and Damaged 2 (below) inputs. Results on single (left) and multi (right) filter architectures from nominal FE training data	71
Figure 3.11: Confusion matrices of the network class predictions on the experimental measurements for the multiclass DI problem according to FE model learning data and network architecture.....	72

Figure 3.12: Receiver Operating Characteristic (ROC) curves of classifiers on experimental state recognition	73
Figure 4.1: Flow chart of the proposed damage detection and identification by simulated damage responses	76
Figure 4.2: Truss structure set-up along with the measuring and excitation equipment	77
Figure 4.3: Recorded consecutive impact forces on the truss.....	78
Figure 4.4: Frequency response functions of the healthy truss structure.....	79
Figure 4.5: FE model of the truss.....	79
Figure 4.6: Parametrized FE model in different parts according to color and design variables..	80
Figure 4.7: MAC Matrix between optimal FE model and nominal FE model mode shapes.....	82
Figure 4.8: Time response comparison between experimental and updated FE time histories for the same impact excitation.....	82
Figure 4.9: Damage scenarios and location description on the truss structure	83
Figure 4.10: SHM hierarchical problem formulation	84
Figure 4.11: First four modes of the truss for healthy state and F6 damage with $k=1000$ N/mm	86
Figure 4.12: Comparison between (numerical and experimental) healthy and F6 damage for different simulated connection stiffnesses and experimental o-ring preload gaps	87
Figure 4.13: Signal training window sampled during the free structure response.....	89
Figure 4.14: <i>Multihead</i> CNN architecture of the hierarchical classifiers. Convolutional Head layers (left) and perceptron classifiers (right).....	90
Figure 4.15: Accuracy (grey lines) and loss (gold lines) curves for randomly initialized backpropagations for Stage I, II and III networks	92
Figure 4.16: Accuracy (grey lines) and loss (gold lines) curves for randomly initialized backpropagations for Stage IV networks.....	92
Figure 4.17: Accuracy (grey lines) and loss (gold lines) curves for randomly initialized backpropagations for the multiclass classifier	93
Figure 4.18: Stage I Predictions on the experimental, (a) Healthy and (b)-(e) Damaged state inputs	94
Figure 4.19: Stage II Predictions on the experimental, Single and Multi Damage inputs.....	94
Figure 4.20: Stage III Predictions on the (a) D1, (b), D2, (c) D3 and (e) D4 cases.....	95
Figure 4.21: Stage IV Predictions on the (a) D1, (b), D2, (c) D3 and (e) D4 cases	95
Figure 4.22: Stage III Predictions on the (a) D5, (b), D6, (c) D7 and (e) D8 cases.....	96
Figure 4.23: Stage IV Predictions on the (a) D5, (b), D6, (c) D7 and (e) D8 cases	97
Figure 4.24: Multiclass predictions on the, (a) Healthy and (b)-(e) D1, D2, D3, D4 cases	97
Figure 4.25: Confusion matrices for the Stage I and II experimental inputs	98
Figure 4.26: Confusion matrices for the Stage III and IV experimental inputs of Single Damage cases	98
Figure 4.27: Confusion matrices for the Stage III and IV experimental inputs of Multi Damage cases	98

Figure 4.28: Confusion matrix for the multiclass predictions on the experimental measurements	99
Figure 4.29: ROC curves of the class prediction performance on the experimental states	99
Figure 5.1: Workflow of the methodology followed in the current chapter exploiting Transmittance Function deviations (anomalies)	104
Figure 5.2: CFRP truss and excitation equipment	108
Figure 5.3: Indicative damage on the CFRP tube with 3-point bending (up) and one of the resulting damage scenarios (Damage 6) with damaged members mounted on the truss (bottom).....	109
Figure 5.4: Formed Damage scenarios on the Truss.....	110
Figure 5.5: Hierarchical separation of damages.....	110
Figure 5.6: Experimental time-response measured accelerations from sensor 1 of the CFRP truss for Healthy and Damage 1 cases.....	111
Figure 5.7: Experimental TFs between sensor locations 1-3 for a range of 60-200 Hz (above) and 70-90 Hz (below) for the Healthy and Damage 1, 2 and 3 cases.....	112
Figure 5.8: Experimental Power spectrum of signals from location 3 for the Healthy state	113
Figure 5.9: FE model of the CFRP truss	114
Figure 5.10: Experimental-Numerical (updated material properties of Table 1) TFs comparison between sensor locations 1-4 for a range of 70-90 Hz for the Healthy cases	115
Figure 5.11: Experimental and simulated DTFs comparison (with different r -values) for the locations 1-4 X and Z for the Damage 1 and 3 cases.....	116
Figure 5.12: Experimental and simulated DTFs comparison for the locations 1-4, 2-4 and 3-4 X for the Damaged 1 case. The simulated DTFs were generated with randomly sampled material parameters	118
Figure 5.13: CNN classifier architecture used	119
Figure 5.14: Accuracy (grey lines) and loss (gold lines) curves for randomly initialized backpropagations for the Stage I classifier. Black lines show the mean performance of accuracy and loss.....	121
Figure 5.15: Stage I Predictions on experimental measurements from D1-D6 states	121
Figure 5.16: Accuracy (grey lines) and loss (gold lines) curves for randomly initialized backpropagations for the Stage II classifiers. Black lines show the mean performance of accuracy and loss.....	122
Figure 5.17: Stage II Predictions on experimental measurements from D1-D6 states	123
Figure 5.18: Accuracy (grey lines) and loss (gold lines) curves for randomly initialized backpropagations for the Stage III classifiers. Black lines show the mean performance of accuracy and loss.....	124
Figure 5.19: Stage III Predictions on the experimental D1-D5 and D3-D5 states.....	124
Figure 5.20: Accuracy (grey lines) and loss (gold lines) curves for randomly initialized backpropagations for the Stage I classifiers using single damage approximation constants r . Black lines show the mean performance of accuracy and loss	126

Figure 5.21: Stage I Predictions on experimental measurements from D1-D6 states using single damage approximation constants = 0.6 and 0.7.....	127
Figure 5.22: Stage I Predictions on experimental measurements from D1-D6 states using single damage approximation constants = 0.8 and 0.9.....	128
Figure 5.23: Accuracy (grey lines) and loss (gold lines) curves for randomly initialized backpropagations for the Stage I classifiers using material uncertainty simulation of 3%. Black lines show the mean performance of accuracy and loss	130
Figure 5.24: Stage I Predictions on experimental measurements from D1-D6 states using material uncertainty simulation of 3%	131
Figure 5.25: ROC curves of the experimental class prediction performance in the Stage I comparison.....	133
Figure 6.1: Decision boundary for a binary classification problem where online testing data shows shifted feature maps towards the numerical that have been used in training.....	139
Figure 6.2: The experimental bridge structure with the accelerometer network and excitation hammer and measurement equipment. Below the basic external dimensions.....	143
Figure 6.3: Indicative Experimental Excitation and Acceleration Responses for the X direction	144
Figure 6.4: Indicative Experimental Frequency Responses for the X direction	145
Figure 6.5: Finite Element Model of the test structure	146
Figure 6.6: Experimental and Numerical response comparison in frequency the X-direction..	147
Figure 6.7: Experimental and Numerical response comparison in time for the X-direction.....	148
Figure 6.8: Depiction of the 1st to 4th vibration modes displacements.....	149
Figure 6.9: Damage scenario with Damage 1 (D1) and Damage 2 (D2) cases using a beam with a cut to replace a healthy one.....	150
Figure 6.10: Damage scenario with Damage 3 (D3) and Damage 4 (D4) cases where the healthy beam is completely missing.....	151
Figure 6.11: Comparison in Frequency with measured experimental responses in different locations for different health states of the structure.....	151
Figure 6.12: Comparison in time responses with FE simulated accelerations for different health states of the structure	152
Figure 6.13: Different excitation impact cases used in data generation	153
Figure 6.14: Indicative training signals for the damage identification problems	154
Figure 6.15: Training curves of accuracy and loss for 10 random start BPs for the networks associated with the D1-D2 damage identification. Mean performance with black line	156
Figure 6.16: Training curves of accuracy and loss for 10 random start BPs for the networks associated with the D3-D4 damage identification. Mean performance with black line	156
Figure 6.17: Class prediction histograms for the experimental D1-D2 identification/classification	158
Figure 6.18: Class prediction histograms for the experimental D3-D4 identification/classification	158

Figure 6.19: Convolutional feature map components for the D1-D2 damage identification network. Feature maps are plotted for numerical inputs used in training and experimental used for validation.....	159
Figure 6.20: Convolutional feature map components for the D3-D4 damage identification network. Feature maps are plotted for numerical inputs used in training and experimental used for validation.....	160
Figure 6.21: Simplified Truss model made of beam elements (left). Section sizing (right).....	161
Figure 6.22: Sample acceleration time response of the simplified Truss for some impact excitation.....	162
Figure 6.23: Indicative mode shapes of the simplified Truss	162
Figure 6.24: Training curves for 10 random start BPs networks trained on Set2 numerical data.....	164
Figure 6.25: Training curves for 10 random start BPs networks trained on Set3 numerical data.....	164
Figure 6.26: Training curves for 10 random start BPs networks trained on Set4 numerical data.....	165
Figure 6.27: Results on average class bias reflected on Set 1 data from networks trained on Set 2 to Set 4 numerical data.....	166
Figure 6.28: Indicative predictions for D2 (up) and D4 (down) inputs from corresponding networks trained on Set 4 data.....	166
Figure 6.29: Convolutional feature map components for a representative D1-D2 (up) and D3-D4 (down) damage identification network. Feature maps are plotted for numerical inputs used in training from Set 2 and numerical inputs from Set 1 where they are assed in genera.....	167
Figure 6.30: Convolutional feature map components for a representative D1-D2 (up) and D3-D4 (down) damage identification network. Feature maps are plotted for numerical inputs used in training from Set 4 and numerical inputs from Set 1 where they are assed in genera.....	168
Figure 6.31: Relationship of zero or healthy inputs feature maps difference to the classification bias for the network trained on D1-D2 damage identification on Set 4 data.....	169
Figure 6.32: Training curves of accuracy and loss for 10 random start BPs for the networks associated with the D3-D4 damage identification trained on 2 sensor locations	171
Figure 6.33: Class prediction histograms for the experimental D3-D4 identification/classification by networks trained on 2 sensor locations	171
Figure 6.34: Convolutional feature map components for the D3-D4 damage identification network trained on 2 sensor locations. Feature maps are plotted for numerical inputs used in training and experimental used for validation.....	172
Figure 6.35: Comparison in Frequency with measured experimental responses in all sensor locations for different health states of the structure in the D1-D2 problem	173
Figure 6.36: Comparison in Frequency with measured experimental responses in all sensor locations for different health states of the structure in the D3-D4 problem	174

Contents

Chapter 1	29
1.1 Problem Statement	29
1.2 Motivation of Research and Posed Questions.....	30
1.3 State of the Art	32
1.4 Objectives of Research and Contributions	34
1.5 Outline of Thesis.....	35
Chapter 2.....	38
2.1 Finite Element Model Updating.....	39
2.2 Numerical Training Dataset Generation	41
2.3 Classification with Convolutional Neural Networks	46
2.3.1 Deep learning feature extraction with convolutional neural networks	47
2.3.2 Deep learning classification	48
Chapter 3.....	53
3.1 Introduction.....	54
3.2 Experimental benchmark and Updated Finite Element Model	56
3.3 Labeled Data Generation	61
3.4 Neural Network Classification and Experimental Validation.....	63
3.4.1 Binary Damage Identification Training and experimental validation.....	65
3.4.2 Multiclass Damage Identification and experimental validation.....	68
3.5 Conclusions.....	71
Chapter 4.....	75
4.1 Introduction.....	76
4.2 Experimental Set-Up and Updated Finite Element Model	77
4.2.1 Updated Finite Element Model	78
4.3 Hierarchical Damage Identification and Faults Simulation	83
4.3.1 Damage Scenarios.....	83

4.3.2	Hierarchical Damage Identification	84
4.3.3	Finite Element Simulation of Connection Faults	85
4.4	Classifier Training and Experimental Generalization	87
4.4.1	Training Dataset generation	87
4.4.2	Training of Hierarchical Convolutional Neural Network Classifiers	89
4.4.3	Results on experimental generalization	93
4.5	Discussion	100
4.6	Conclusions	101
Chapter 5	103
5.1	Introduction	104
5.2	Transmittance deviations from a reference state using approximate stiffness reductions	105
5.3	Experimental Set-Up and Damage Scenarios	107
5.3.1	Impact-Like Damage and Hierarchical Identification Problem	108
5.3.2	Experimental Responses	111
5.4	FE Model and Transmittance Deviation Approximations	113
5.4.1	Transmittance Deviation from the Healthy State Approximation	115
5.5	Deep Learning Classifiers Training and Experimental Generalization	117
5.5.1	Training data Generation	117
5.5.2	Neural Network Training and Experimental Validation	119
5.5.3	Influence of Damage Magnitude Approximation value r	125
5.5.4	Influence of Material Uncertainty Simulation	129
5.6	Discussion	131
5.7	Conclusions	134
Chapter 6	136
6.1	Introduction	137
6.2	Bias Estimation with Feature Map Similarity Assessment	138
6.3	Experimental Set-up and Finite Element Model	142
6.3.1	Physical Test Structure	142
6.3.2	Finite Element Model	143
6.3.3	Damage scenarios of different magnitude	149
6.4	Data Generation, Training of Classifiers and Experimental Validation	153
6.4.1	Data generation	153
6.4.2	Classifier Training	155

6.4.3	Experimental Validation and Feature Maps.....	156
6.5	Bias as a Function of Model Error	161
6.5.1	Training Data with Progressive Distancing from the Reference.....	161
6.5.2	Classifier Training.....	163
6.5.3	Results on Dataset Generalization and Feature Maps.....	163
6.6	Discussion	169
6.7	Conclusions.....	173
Chapter 7	177
7.1	Conclusions of thesis	177
7.2	Future Work.....	178
8	181
	Bibliography	181

1

Introduction

1.1 Problem Statement

Structures of various sizes and complexities serve for a variety of tasks in everyday life or in specialized applications. Nevertheless, there are cases of structures where monitoring their health status is crucial to avoid catastrophic failures or plan maintenance schedules. A prominent field in engineering known as Structural Health Monitoring (SHM) deals with measurement and assessment of data related to the health condition of structures. This is usually performed by vibration measurements through a network of sensors on the structure [1-3] and processing of the acquired signals to assess the health status. The assessment of the response can indicate damage type and location [4-6] or detection of anomalies that imply degradation in structural properties [7-9]. The exact goal of each SHM application can be therefore case specific and the working principles can be categorized in physics and data-based approaches [10,11]. Physics based, aim to relate measured data with the corresponding state of a representative numerical model that approximates the dynamic behavior. That means solving the inverse problem. Data based on the other hand can conveniently avoid time consuming inverse numerical problems but their capabilities depend strongly on the available data or available health conditions to be measured in advance. Even though many different ways to handle and process responses exist in SHM data-based approaches, they follow a main workflow. First, measurement and creation of datasets. Second, training of a mathematical decision model with the dataset. Third, monitoring the structure with the trained models by providing new measured responses, on demand or constantly.

The key factor affecting the effectiveness of a data-based SHM system is access to appropriate data in order to create rich training sets. When damaged states of structures are available to be measured, subsequent damage detection methodologies can be organized in a so-called supervised way. With the term supervised, it is meant that measurement data is labeled in healthy or specific damage states. The mathematical model trained in a supervised way, may also perform direct

decision making on later monitoring states. Damage may be explicitly recognized or classified like that. For large and working structures however, access to damaged states is usually not possible. Limited literature exists on working structures with actual damage [12-14] where measurement was possible. The bulk of SHM development is confined for that reason in lab scale supervised approaches [15,16] or unsupervised methodologies [3,7]. Unsupervised approaches in SHM usually consider training data on the baseline or intact state. During the monitoring stage, the trained model calculates the way data contains differences from the baseline. Post processing of results is necessary in order to make decisions. Despite the core differences, both in supervised and unsupervised SHM the training data needs to cover different possible excitations and ambient conditions [17-19]. Therefore, experimental measurements for training datasets may be time consuming and expensive given demanding monitoring scenarios.

The problem on which the present thesis is directly based on and aims to provide solutions, is exactly the problem of data availability in vibration data-based SHM. The issue of adequate data, especially in working structures, is the main factor that defines whether a monitoring system covers possible operating conditions to perform effective unsupervised monitoring or may also proceed in more detailed recognition and location of damage. Focusing on supervised monitoring systems in order to exploit explicit identification of health states, the main question that the present thesis plans to answer is: how to classify specific damaged states when measurement is not possible for it in advance? The thesis therefore is interested in the SHM problem of identification, meaning decision making among possible states of a studied structure.

1.2 Motivation of Research and Posed Questions

The research in the proposed thesis is strongly motivated by the stated problem of vibration response availability for data-based SHM in supervised damage identification. The original inspiration therefore comes from the need of damaged states responses to perform straightforward recognition of health states. The solution investigated is the generation of labeled data with Finite Element (FE) models to be used for training of classifiers. In that way, SHM and damage identification can be realized in cases where experimental training data is not available, or too costly to be obtained. Simulated data of course does not come problem free and has to be evaluated for its applicability in substituting corresponding experiments. FE simulation error in numerical training data can be normally assumed to reduce data quality and techniques to minimize error are a legit addition. Optimal FE models [20,22] can be constructed for simple or complex structures using modal or time response experimental data. In a candidate structure for building a SHM system this requires an initial experimental cost for measurements which can happen on the intact state. After, the correct and accurate modeling of damage cases in order to generate the simulated vibration response is a task of the designer. Simulation of possible uncertainties in FE model parameters could also enhance the quality of synthetic data. A combination of numerical and experimental techniques is therefore to be studied for SHM data production.

The purpose of experimental measurements on the intact state should be highlighted that it falls within the optimal FE model structuring and should not be confused with the needs of an experimental unsupervised damage or anomaly detection monitoring. Even though the intact state may offer such a potential, the motivation and focus of the present work is given on the availability of damaged state responses.

In addition to the data availability problem, processing and decision making with data brings the equally important problem of what kind of mathematical damage identification model should be used, how does it process the signals and how it should be trained in order to focus on response characteristics that can be applied in practice. Usually, in practical SHM applications, training datasets usually comprise series of responses in different loading possibilities, fluctuations in environmental conditions and measurement uncertainties, along with health states when available. The data most of the times comes in multiple channels of a sensor network. The mathematical model applied for the monitoring task has to successfully be able to filter and keep useful information or patterns related to the health status. At the same time, it needs to ignore response components that are not relevant. The principle of vibration based SHM is therefore statistical and is founded on the effective training on the acquired dataset. The workflow follows as, train a model on the given dataset, accept new input data, process it and predict a score.

Statistical methods [23] form on one hand models for the pattern recognition problem in SHM. On the other hand, the SHM field is constantly complemented with different Machine Learning (ML) methodologies [24,25]. ML models which are also in essence statistical since they are trained on large datasets, differentiate in their way of training by not being explicitly programmed how to perform a task. Deep Learning (DL) Artificial Neural Network (ANN) models, a sub-category of ML methodologies, have been introduced in SHM tasks and noted for their high efficiency and performance on vibration based SHM [24,26]. Convolutional Neural Network (CNN) DL models [24,27-29] can directly process raw vibration data minimizing user effort, can be applied with multisensory inputs on a structure and can be easily tuned for supervised damage identification. To exploit such advantages, CNN classifiers will be the model of choice that handles the numerically produced datasets in the present work. Nevertheless, although literature is constantly renewed with DL-SHM methodologies, it is still left to be investigated how such models perform on the physical case when trained by FE simulated data.

In combination to the proposed thesis main motivation for numerical datasets, the problem of FE data generalization by a DL model on the experiment is an additional motivation. During training stage, a DL model learns to extract the so-called features which are a mapping from the inputs to a space of higher-level representation. In a damage identification task, this higher-level representation means useful information is extracted from the inputs that concerns the health status classification. The quality of learned features, or how well they may generalize on unseen inputs depends naturally on network architecture and the classification problem contained in the data. The effect of such parameters is yet to be investigated on how numerically trained classifiers perform on corresponding experimental states. Even though authors have reported different cases

of FE based training data, experimental validation of classifiers does not accompany most of such studies.

The following questions now rise after the motivations of utilizing FE generated training data and CNN classification:

- How to generate labeled training datasets by optimal FE models?
- How to consider modeling errors that simulated responses carry?
- What kind of classification strategy and CNN model structuring should be followed for best experimental generalization?
- How much can such a simulated training data methodology be finally trusted or can it be applied arbitrarily?

The present thesis aims to answer the above questions with results from different tested cases and provide the concluding remarks.

1.3 State of the Art

Methods to perform vibration based SHM and damage detection or identification have evolved in direct processing of frequency/modal data characteristics of structures or time-series responses in a data-based approach. Frequency Response domain data and Functions (FRF) [1,3,15,16,30,31] or Transmittance Functions (TF) [32] with statistical or ML/DL tools have been established as effective monitoring methodologies. Raw acceleration time-series on the other hand can also be directly used in DL models [2,33-36] to perform supervised or unsupervised monitoring. Artificial CNN architectures are widely applied in signal processing and classification tasks where minimal user processing of data is necessary. Application with frequency domain data [37] is also possible, making CNNs possibly the most flexible of models to be used in structured and unstructured data types, which follows in the choice of such classification models in the present work. Convolutional architectures are deployed in series of layers where progressive feature filtering is performed, while the intrinsic nature of information propagation has led to numerous studies investigating efficient dataset fitting. Efficient fitting is also known with the term generalization, meaning an ANN being able to work correctly on data it has not been used for training, or in other words data is has not seen. Active research on this field comprises architectural or training process parameters investigations in various fields [38-40], not strictly confined within SHM damage identification tasks.

To perform explicit decision making or specific damage identification, the SHM training datasets need to be provided in a supervised or labeled manner. That means series of measurements are necessary in different health conditions, which is usually not possible for large, expensive and working structures. The limited measured datasets in distinct health states of structures with practical interest that exist, are considered valuable and used as reference in different other studies. Characteristic are selected cases where deliberate damage was possible due to decommissioning [12,14] or retrofitting [1]. Acknowledging the problem of data acquisition for SHM training,

authors have tried to provide classifiers with numerically generated data by FE models. FE model responses have been used directly to substitute corresponding experimental states in numerous damage scenarios for a variety of structures. Examples in literature exist for digital models of simple frames [25] to bridge like infrastructure [11,15,41-43]. The bulk of this synthetic data however has never been tested on the physical cases with damage and therefore reliability of this kind of numerical source of data and the subsequent SHM classifiers is unknown. It is worth mentioning that the problem of synthetic data reliability has been acknowledged in the early attempts to utilize simulated data, by fabricating response features less prone to error [42]. Reliability depends of course on the model error contained in data with respect to the physical cases and how robust classification may be on inaccuracies [44].

However, while responses in the damaged conditions of structures may be difficult to be obtained, the intact or healthy state of the structure can be used to update FE models for damage simulation. FE model updating strategies aim in using measured data and minimize the disagreement with the numerical model through an optimization strategy. Up to this date FE model updating has been in applied in different small lab-scale [21], large [45,46], or aerospace structures [47]. Gradient free algorithms such as the Covariance Matrix Adaption Evolution Strategy (CMA-ES) [48,49] perform model optimization by random search of model parameters that best minimize the residual between FE model and measurements. CMA-ES successful applications include simple to large and complex structures for linear or non-linear problems [21,50]. The unknown damage responses may be additionally simulated as stochastic, since structural parameters and values acquired through measurements can be affected by various sources of uncertainties [20,22]. In practice it is also not uncommon to have problem specific reasons for challenging updating, such as quasi periodic structures where modes are clustered around an area of interest [51] or more general uncertainties [52] such as the constitutive law used or the FE simplifications.

Last but not least, after the dataset, numerical or experimental, has been formed and after the mathematical SHM model has been decided, goal of every monitoring system is detection and/or location of the smallest damage without false alarms. SHM comes with the purpose of early damage detection [53]. This of course depends strongly on how the statistical or ML/DL model is trained on the data, preprocessing of data to aid in the learning phase and adequate testing and benchmarking to validate the results. Authors up to this date have invested in different ML/DL tuning and architecture improvements [26,54-57], features preprocessing [43,58,59] and studies on sensor placement [60,61]. This is of most importance when numerical data has been used for training, since FE models, even updated will have differences from the corresponding measurement. How this affects the reliability of FE trained data lacks literature sources yet.

The presented State of the Art on vibration data-based SHM and FE model updating, was given with focus on the stated problem of data availability and the investigated methodology of FE generated training data and CNN-DL supervised classification.

1.4 Objectives of Research and Contributions

The overall objectives of the research presented in this thesis are to investigate, assess and propose an innovative state-of-the-art methodology for structural health monitoring (SHM) and damage identification of structures through numerically simulated data. For this purpose, Finite Element (FE) models are employed in generating structural vibration response datasets and deep learning (DL) Convolutional Neural Network (CNN) classifiers trained on such data are validated on the experimental structure.

Specific objectives that compose the main goal are:

- to develop a general approach for numerical simulation of health states that can be possibly used in cases where measurement of damaged states is not possible
- to acquire effective updated FE models by measured data on intact states, meaning FE models that can provide the necessary responses for numerical training data in unmeasured yet damages
- to train effective CNN DL models on simulated data sets and experimentally validate them on the corresponding physical states, where effective means accurate experimental generalization
- to identify efficient ways to define the damage identification problem in a candidate structure and separate damage scenarios
- to investigate CNN DL architectural and training parameters that impact on the experimental generalization
- to investigate training data preprocessing effects on experimental generalization
- to investigate the reliability of such numerically trained CNN DL classifiers for online damage detection and identification and propose a methodology to explore their practical limits
- to identify potential future research topics

The innovative contributions of the thesis in the literature may be identified specifically as:

- A labeled training data generation methodology by simulation of healthy and damaged states with FE models for supervised learning in vibration data-based monitoring and damage identification
- Evaluation of classifier training and data generation/processing parameters that affect numerical to experimental generalization
- Reliability estimation of numerically trained ANN classifiers for their potential in performing on the real structure monitoring

The research objectives and contributions are on par with the current need for structural responses of damaged conditions and lack of experimental validation in most of simulated cases in the literature, as explained in paragraphs 1.1, 1.2 and 1.3.

1.5 Outline of Thesis

The following outline of thesis briefly summarizes the contents of the following chapters. The chapters are set in the order of the progress made during research.

Chapter 2 In this chapter the theoretical basis behind the distinct steps followed in the proposed methodology is presented. A flow chart summarizes the order of actions and the theory behind FE model updating, data generation and CNN DL classification is presented.

Chapter 3 This chapter includes the first application of the methodology on a simple steel beam benchmark where two different artificial damages are imposed. Training data is generated by the nominal and the updated FE model and CNN DL classifiers trained by the simulated data are validated against the experimental measurements. It is demonstrated how reducing FE model error by updating leads to better experimental performance. It is also investigated how the CNN architecture applied affects the experimental performance. It is shown how smoothing or averaging of damage features can lead to better performance.

Chapter 4 In this chapter it is investigated how the damage detection problem may be organized hierarchically to improve experimental generalization. A lab-scale truss of composite materials is used for this purpose with multiple different damage scenarios. Impacts are used as excitation and the FE model is employed for the generation of labeled damaged cases to form the training set. Classifiers are trained on numerical data in a direct multiclass and a hierarchical way. The multiclass approach tries separation of all health states at once, while the hierarchical performs binary separation in stages. It is investigated how experimental generalization can potentially improve through a hierarchically organized damage identification

Chapter 5 This chapter deals with data preprocessing and conversion in the frequency domain for scenarios of small and difficult to simulate damage detection. The lab scale composite truss is subjected to impact like damages in different truss members. A damage approximation method is applied for the FE simulation of the damage cases while material and damage parameter uncertainties are included in the simulations. The vibration training data set is finally converted to transmittance functions (TF). DL classifiers trained on the datasets are validated on the experimental states investigating the effects of uncertainties simulation. The training data of TFs and their deviations from references is also tested for its applicability in simulating responses for damaged states.

Chapter 6 In this chapter important conclusions are made on the reliability of numerically trained classifiers. A methodology is presented on how such conclusions can be drawn, tested on a lab-scale bridge truss made of steel members. Two different scenarios of damaged cases are tested with the first being small and less distinct damages while the second larger and more distinct. It is found how the effect of FE model error in the baseline model used for training data generation affects experimental generalization and can lead to

Chapter 1-Outline of Thesis

classifiers in wrong results on the physical set-up. An innovative way of relating in advance the reliability of the numerically trained classifiers by evaluation of the feature maps of the intact state is tested and validated.

Chapter 7 The final chapter of the thesis contains the conclusions of the research presented. Future study on the topics of SHM with DL and data generation by FE models is given as well.

Theoretical Background

In this chapter the theoretical basis of the proposed thesis methodology is presented. The main goal, being evaluation of the experimental generalization of numerically trained classifiers as discussed in **Chapter 1** is made through different steps:

- 1) Optimal Numerical model of the candidate structure updated on the healthy state
- 2) Different health states scenarios simulation and extraction of the labeled learning datasets
- 3) Deployment of a suitable Convolutional Neural Network (CNN) classifier and learning on the previously simulated datasets
- 4) Experimental validation on real structural measurements

The flowchart of **Figure 2.1** summarizes the process. The main background of Finite Element (FE) model updating, dataset generation and neural network classification is given in the following sections.

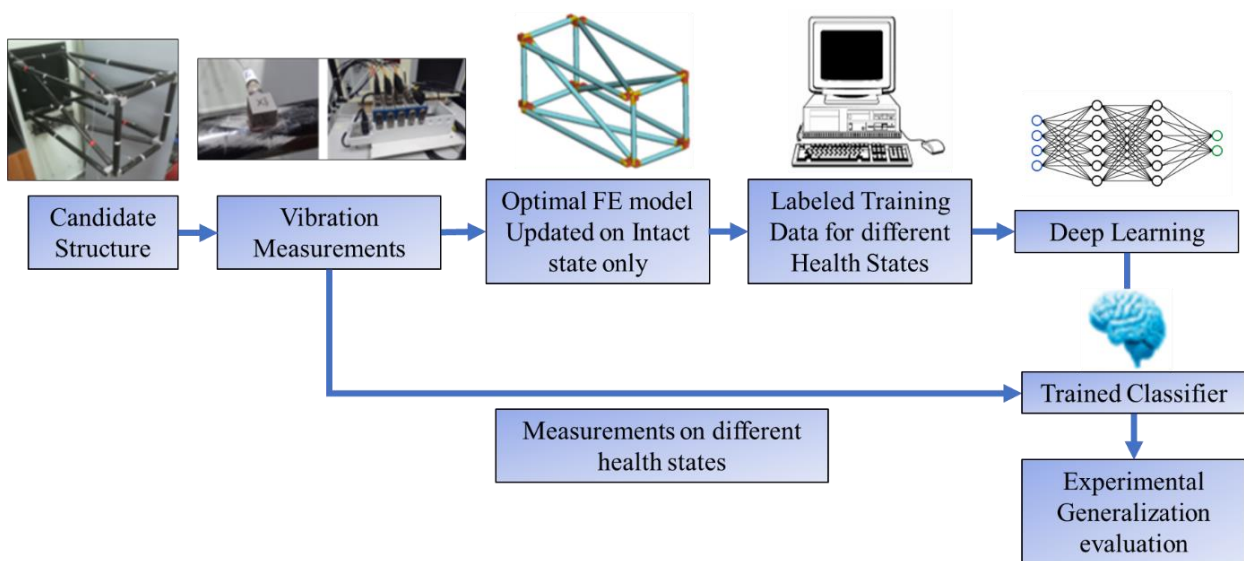


Figure 2.1: Flow chart of the proposed monitoring and damage identification by simulated damage responses

2.1 Finite Element Model Updating

Finite Element (FE) Model Updating constitutes a wide class of algorithms that use methodologies which try to minimize differences or residuals between experimental measurements and numerical responses from a FE model [21,45-47,50-52].

The measurement equipment such as the accelerometer network and the excitation components have to be deployed initially on the structure. The excitation equipment may have a dual purpose, first to create the appropriate response in order to generate the signals for the optimal FE model generation and second to create the responses for later Structural Health Monitoring (SHM) testing. In cases where the structure is investigated on-site [50] and excited by operating conditions no excitation equipment is necessary both for the model updating and SHM testing phase. In addition, for problems where large complex structures are considered but only certain components are of interest and should concentrate focus, FE sub-structuring and model reduction techniques can be applied [62]. With the measurements and the constructed FE model at hand, the updating of model parameters that best minimize experimental and numerical response mismatch can proceed further with an optimization algorithm. In the present thesis the algorithm used consistently is the Covariance Matrix Adaptation Evolution Strategy (CMA-ES). CMA-ES has been successfully applied in the past on FE updating of in various structures [21,46,50,63,64].

The measures of fit that are commonly used in dynamics may be defined now for linear FE models, usually as modal or response residuals. Let the measured modal data be represented as the set $\{\hat{\omega}_r, \hat{\phi}_r \in R^{N_0}, r = 1, \dots, m\}$ with $\hat{\omega}_r$ and $\hat{\phi}_r$ being the m total measured modal frequencies and mode shapes respectively, measured at N_0 DOFs. Now, let a parameterized class of linear structural models used to model the dynamic behavior of the structure and let $\underline{\theta} \in R^{N_\theta}$ be the set of free structural model parameters to be identified. The corresponding model calculated modal data is grouped in the set $\{\omega_r(\underline{\theta}), \phi_r(\underline{\theta}) \in R^{N_0}, r = 1, \dots, m\}$ with ω_r and ϕ_r being the m total calculated modal frequencies and mode shapes respectively, at N_0 corresponding DOFs. The modal residuals are formed now as:

$$\varepsilon_{\omega_r}(\underline{\theta}) = \frac{\omega_r^2(\underline{\theta}) - \hat{\omega}_r^2}{\hat{\omega}_r^2} \quad \text{and} \quad \varepsilon_{\phi_r}(\underline{\theta}) = \frac{\|\beta_r(\underline{\theta})\phi_r(\underline{\theta}) - \hat{\phi}_r\|}{\|\hat{\phi}_r\|} \quad (2.1)$$

where ε_{ω_r} and ε_{ϕ_r} are the modal frequency and shape residuals respectively. The $\|\underline{z}\|^2 = \underline{z}^T \underline{z}$ is the Euclidian norm and $\beta_r(\underline{\theta}) = \hat{\phi}_r^T \phi_r(\underline{\theta}) / \|\phi_r(\underline{\theta})\|^2$ a normalization constant that guarantees comparison between the measured and calculated mode shapes that have the best similarity. Therefore, the squares of 2 modal residuals $J_1(\underline{\theta})$ and $J_2(\underline{\theta})$ to be minimized are:

$$J_1(\underline{\theta}) = \sum_{r=1}^m \varepsilon_{\omega_r}^2(\underline{\theta}) \quad \text{and} \quad J_2(\underline{\theta}) = \sum_{r=1}^m \varepsilon_{\phi_r}^2(\underline{\theta}) = \sum_{r=1}^m [1 - MAC_r^2(\underline{\theta})] \quad (2.2)$$

where $MAC_r(\underline{\theta}) = \frac{\hat{\phi}_r^T \underline{\phi}_r(\underline{\theta})}{\|\underline{\phi}_r\| \|\hat{\phi}_r\|}$ is the Modal Assurance Criterion [21] between experimental and estimated mode shapes.

Response residuals on the other hand may also be defined based on correlation of response vectors as given in [21]. A global correlation coefficient $x_s(\omega_k)$ is defined as:

$$x_s(\omega_k) = \frac{\left| \{H_X(\omega_k)\}^H \{H_A(\omega_k)\} \right|^2}{\left(\{H_X(\omega_k)\}^H \{H_X(\omega_k)\} \right) \left(\{H_A(\omega_k)\}^H \{H_A(\omega_k)\} \right)} \quad (2.3)$$

where the $\{H_X(\omega_k)\}$ and $\{H_A(\omega_k)\}$ are the experimental and predicted response vectors at matching excitation-response locations respectively. When is derived as $x_s(\omega_k) = 1$ it indicates a perfect response correlation while $x_s(\omega_k) = 0$ shows that no correlation exists. The global correlation coefficient however cannot detect scaling errors but gives emphasis on shape [65] in the Frequency Response Functions (FRF) and an additional amplitude correlation coefficient $x_a(\omega_k)$ may be defined as:

$$x_a(\omega_k) = \frac{2 \left| \{H_X(\omega_k)\}^H \{H_A(\omega_k)\} \right|}{\left(\{H_X(\omega_k)\}^H \{H_X(\omega_k)\} \right) + \left(\{H_A(\omega_k)\}^H \{H_A(\omega_k)\} \right)} \quad (2.4)$$

using the same $\{H_X(\omega_k)\}$ and $\{H_A(\omega_k)\}$ experimental and predicted response vectors respectively. The coefficient $x_a(\omega_k)$ this time demands totally identical response vectors in phase and amplitude to reach unity. The response residuals $J_3(\underline{\theta})$ and $J_4(\underline{\theta})$ that can provide shape and amplitude correlations are formed as:

$$J_3(\underline{\theta}) = \sum_{r=1}^m \left[1 - x_s(\hat{\omega}_r, \underline{\theta}) \right]^2 \quad \text{and} \quad J_4(\underline{\theta}) = \sum_{r=1}^m \left[1 - x_a(\hat{\omega}_r, \underline{\theta}) \right]^2 \quad (2.5)$$

using $x_s(\hat{\omega}_r)$ and $x_a(\hat{\omega}_r)$ that correspond to the identified resonant frequencies of the system. A combined weighted residual $J(\underline{\theta}; \underline{w})$ can be given now by combining the modal and frequency response residuals:

$$J(\underline{\theta}; \underline{w}) = w_1 J_1(\underline{\theta}) + w_2 J_2(\underline{\theta}) + w_3 J_3(\underline{\theta}) + w_4 J_4(\underline{\theta}) \quad (2.6)$$

using weighting factors $w_i \geq 0$, $i = 1, 2, 3, 4$, with $w_1 + w_2 + w_3 + w_4 = 1$. The weights can be user selected depending on the importance of each measure of fit and the objective is to find the set of parameters $\underline{\theta} \in R^{N_\theta}$ which best minimizes $J(\underline{\theta}; \underline{w})$.

Additionally, parameter estimation of nonlinear models is based on response time history measurements such as acceleration and displacements. Time response formulation has the advantage of applicability over both linear and non-linear systems; it compares the measured raw data of the experimental arrangement to the equivalent predictions of the numerical model. In this

way, all available information is preserved and systematic errors of the identification procedure are alleviated. The measure of fit is given by:

$$J(\underline{\theta}) = \frac{1}{N} \sum_{i=1}^N \frac{\sum_{j=1}^M (\hat{y}(\underline{\theta})_{ij} - y_{ij})^2}{\sum_{j=1}^M (y_{ij})^2} \quad (2.7)$$

Where $\hat{y}(\underline{\theta})_{ij}$ is the acceleration time history computed from the numerical model and y_{ij} the experimental signal. The subscript i corresponds to the sensor and direction location out of a N total and j to the time step instant out of a total M . When the optimization algorithm converges to the requested accuracy corresponding to residuals in equations (2.1) or (2.7) minimization, the optimal model parameters $\underline{\theta}$ are acquired.

The CMA-ES works as a randomized black box algorithm using multivariate normal distributions to sample parameter search points in order to reach the minima of residuals in equations (2.6) or (2.7). Black box optimization refers to methods where the only accessible information on updating the parameters $\underline{\theta}$ is in the function values of the objective J . The workflow of Algorithm 2.1 is followed.

Algorithm 2.1: Randomized Black box search, $J : \mathbb{R}^n \rightarrow \mathbb{R}$ is the objective function with n number of search parameters

1. Initialize distribution parameters $\underline{\theta}^{(0)}$
2. for generation $g = 0, 1, 2, \dots$
3. sample independent points from distribution $P(\underline{\theta} | \underline{\theta}^g) \rightarrow \underline{\theta}_1, \dots, \underline{\theta}_\lambda$
4. evaluate the sample $\underline{\theta}_1, \dots, \underline{\theta}_\lambda$ on J
5. update parameters $\underline{\theta}^{(g+1)} = F_\theta(\underline{\theta}^{(g)}, (\underline{\theta}_1, J(\underline{\theta}_1)), \dots, (\underline{\theta}_\lambda, J(\underline{\theta}_\lambda)))$
6. Break if convergence is met

The core of the method lies in the update of the mean \underline{m} and covariance \underline{C} of the search distribution $N(\underline{m}, \underline{C})$ in each generation or step. Approximation of the optimum is therefore provided iteratively in parameter sampling generations. Details on the evolutionary path and the update can be found in [21,48,49]. Advantages of the method include the parallelization capabilities and better chances of global optima approximations compared to gradient-based algorithms.

2.2 Numerical Training Dataset Generation

With the optimal FE model acquired after the updating procedure, the training data for the classifiers can be generated. This step is highlighted as the main novelty of the present work. The goal is to simulate structural state scenarios, intact or damaged, exclusively with the FE models, which however were updated on the Healthy or intact state. The important question at this stage is

how to generate training data considering possible inaccuracies in the FE model and the real structure. In the present work, since a data-oriented SHM process based on a physics model is followed, it is aimed to simulate such inaccuracies as well.

The governing equations of motion in the FE solution are given as:

$$\mathbf{M}(\rho, g)\mathbf{A} + \mathbf{C}(\alpha, \beta)\mathbf{V} + \mathbf{K}(E, g)\mathbf{U} = \mathbf{F} \quad (2.8)$$

where \mathbf{A} , \mathbf{V} and \mathbf{U} are global the acceleration, velocity and displacement vectors respectively. \mathbf{M} , \mathbf{C} and \mathbf{K} represent the global mass, damping and stiffness matrices of the structure. The mass matrix \mathbf{M} is a function of the structural density parameters ρ and geometric parameters g (for example thickness of shell elements). The stiffness matrix \mathbf{K} is a function of the elasticity E parameters and geometry g . \mathbf{F} is the loading vector. The FE updating, as described in section 2.1, usually considers search of such parameters $\underline{\theta} = [E, \rho, a, \beta, g]$ which however can be inaccurate, since the experimental measurement values used for optimization can be subjected to various uncertainties [20,22,66-69]. The training dataset may therefore carry systematic errors on which the subsequent classifier may attach. A repetitive load case scheme algorithm is employed for that reason, generating training cases by random sampling of FE model parameters. It is expected that classifiers trained on such datasets can learn to avoid attaching on specific dynamics of a single set of structural parameters and generalize better, learning more robust patterns in the data.

In the ML\DL terminology this is similarly taken into account by techniques known as data augmentation. Applications include images, for example with geometric transformations [70] or in 1-D time series signals with simplest dataset enhancements like noise addition [71]. Data augmentation originally refers to enhancement of the given data and not physics-based creation of new data, however the literature terminology of augmentation is expanding with such model-based generated data as well [72-75]. Classifiers are taught to learn more general patterns in all of such approaches. In Algorithm 2.2 the proposed model-based labeled dataset generation used in this work is presented, providing solutions not attached on specific FE model parameters.

Data generation starts by deciding the number of total training examples n and the number of classes s that form the $[s \times 1]$ class vector \mathbf{Y} . The class vector corresponds to a specific label which is defined according to the damage scenario to be simulated as for example in **Figure 2.2**. The FE model is used to simulate the intact or Healthy state and different Damage scenarios in the form of cuts. It is appropriate to create balanced datasets and therefore the instances of each class should appear equally in the total number of cases n . Next model parameters as defined in equation (2.8) are sampled for the FE model within predefined bounds. The loading conditions have to be user decided in advance in order to cover the possible excitation or ambient conditions. Operation variability effects, such environmental excitations, temperature fluctuations or geometric distortions that can affect the response in a real structure [11,18,19] may also be simulated, if possible, when judged important.

Algorithm 2.2: Numerical model data generation algorithm

Input: Number of damage scenarios s , load cases n and bounds for parameters $\rho, \alpha, \beta, E, g$

Output: n number of labeled vibration responses

7. **for** $i=1:n$ **do**
8. select Health status label and get corresponding FE model $\rightarrow \mathbf{Y}_i$
9. sample $E, g \rightarrow \mathbf{K} = \mathbf{K}(E, g)$
10. sample $\rho \rightarrow \mathbf{M} = \mathbf{M}(\rho, g)$
11. sample $\alpha, \beta \rightarrow \mathbf{C} = \mathbf{C}(\mathbf{M}, \mathbf{K}, \alpha, \beta)$
12. select or sample loads $\rightarrow \mathbf{F}$
13. solve $\mathbf{M}\mathbf{A} + \mathbf{C}\mathbf{V} + \mathbf{K}\mathbf{X} = \mathbf{F}$
14. return \mathbf{A}_i and \mathbf{Y}_i

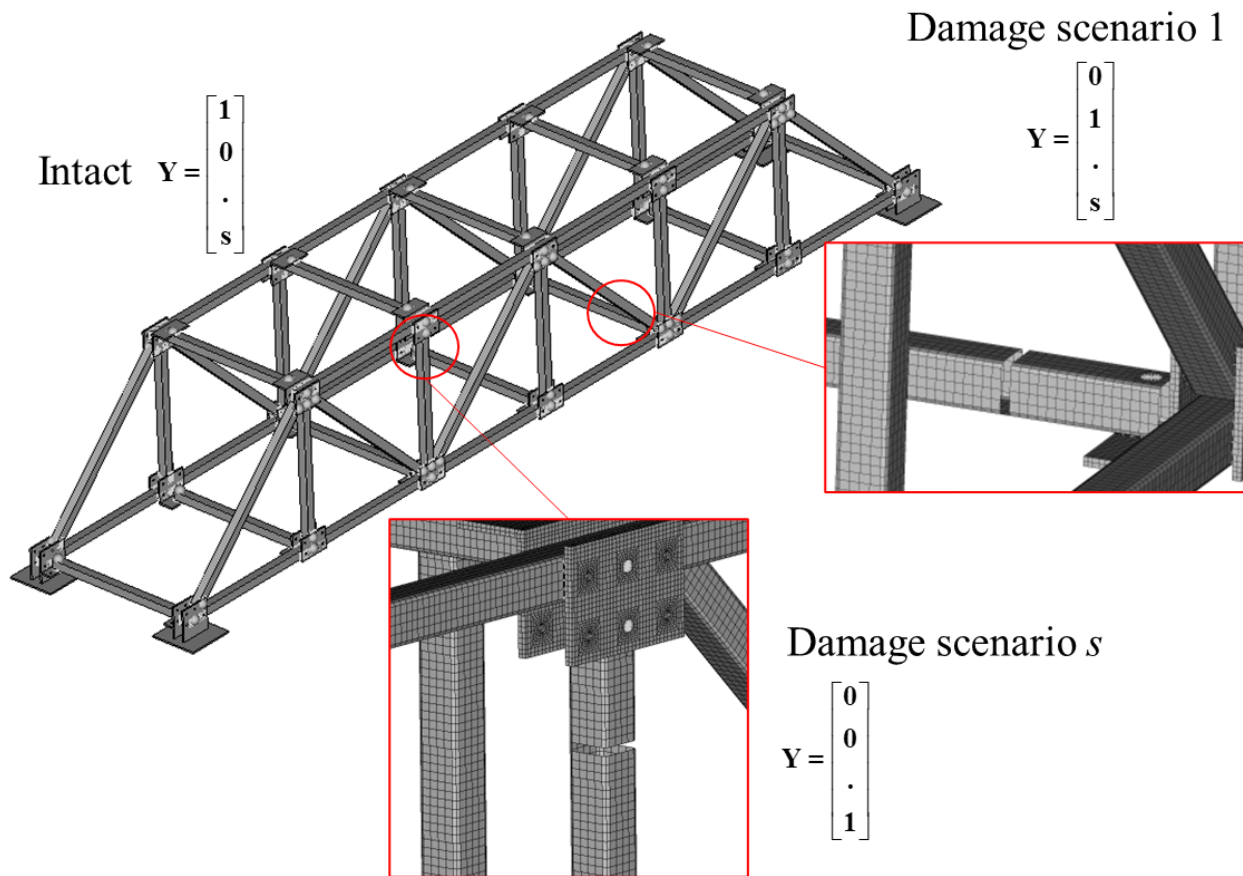


Figure 2.2: Example of Damage scenarios on FE model of truss and the corresponding entries in the label vector \mathbf{Y}

The solution of each iteration i of the algorithm is after appended in the labeled training set of equation (2.9):

$$\mathbf{Train_set} = \{(\mathbf{A}_1, \mathbf{Y}_1), (\mathbf{A}_2, \mathbf{Y}_2), \dots, (\mathbf{A}_n, \mathbf{Y}_n)\} \quad (2.9)$$

In the acceleration vectors \mathbf{A}_i which have been noted as the training data examples, it may be included only the responses of the DOFs of interest, which are of size $[t \times c]$. Where t the total number of time-samples used and c the number of channels or sensors.

Concluding, the procedure of Algorithm 2.2 is no different than a Monte Carlo procedure for stochastic FE simulations [76]. The algorithm may also be altered according to FE solver needs such as modal superposition solution [77]. The effectiveness of such a training data scheme generation will be demonstrated through validation of classifiers on experimental measurements. The influence of parameters sampling bounds will be shown as well. Consider now however the following simplified example to showcase the connections between uncertainty simulation in the training set and classification feature space enrichment already in this section. Feature space in the Machine Learning (ML) terminology refers to the collection of training points or values in the training examples that the classifier actually uses to separate labeled inputs. The purpose of the proposed methodology is that the unmeasured experimental damaged state features will be placed correctly on the feature space. This is demonstrated in the following example.

Simplified numerical example for data generation and feature space classification

A 2-DOF system of springs and mounted masses is shown in **Figure 2.3**. For this simplified system assume that its health status may be identified by its 2 eigenfrequencies, therefore a 2-dimensional feature space to be used by some classifier. Health status labels may be defined as damaged with a 10% increase of m_2 .

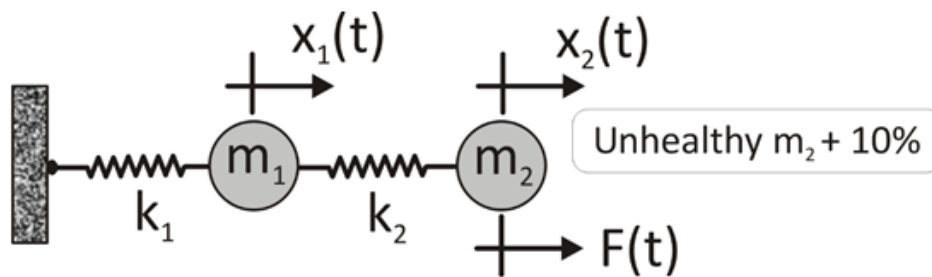


Figure 2.3: Simple linear spring system with 2 DOFs and damage simulated as 10% increased mass on the right edge

To generate the data for the above demonstration, the global equations of motion as a function of the model stiffness parameters k_1, k_2 and lumped masses m_1 and m_2 can be assembled as $\mathbf{M}(m_1, m_2)\mathbf{A} + \mathbf{K}(k_1, k_2)\mathbf{U} = \mathbf{F}$. \mathbf{A} , \mathbf{U} and \mathbf{F} are the global acceleration, displacement and force vectors respectively. \mathbf{M} and \mathbf{K} represent the global mass and stiffness matrices including the

boundary conditions. We may numerically solve the eigenproblem for the healthy and damaged (unhealthy) case that is formulated from the above equation as $[\mathbf{K} - \lambda\mathbf{M}]\mathbf{V} = 0$ where λ represents the eigenvalue and \mathbf{V} the corresponding eigenvector. The two eigenfrequencies are obtained as $\omega_1 = \sqrt{\lambda_1}$ and $\omega_2 = \sqrt{\lambda_2}$. Next, in an approach to show the influence of uncertainties on the health status recognition, assume that numerical eigenfrequencies can simulate measured quantities. The element stiffnesses k_1, k_2 and mounted masses m_1, m_2 may vary randomly by a small percentage from their nominal values in a real case scenario. In addition, uncertainties are simulated for the eigenfrequency calculation resulting in different possible combinations that could be measured in a real system. A random distribution can be followed and the possible eigenfrequencies measured are depicted in a 2D chart. Multiple combinations through random sampling are used by following Algorithm 2.3.

Algorithm 2.3: Data generation algorithm for the simplified example

Input: Number of load cases n and upper (up) and lower (lo) statistical bounds for each quantity

Output: n Eigenfrequencies of the system

1. **for** $i = 1:n$ **do**
2. $k_{1i}, k_{2i} = \text{Uni}(k_{up}, k_{lo}) \rightarrow \mathbf{K} = \mathbf{K}(k_{1i}, k_{2i})$ /Uni=Uniform distribution
3. $\mu_i^1, \mu_i^2 = \text{Uni}(\mu_{up}, \mu_{lo})$ for Healthy system $\rightarrow \mathbf{M} = \mathbf{M}(\mu_i^1, \mu_i^2)_{healthy}$
and $\mu_i^2 \rightarrow \mu_i^2 = \mu_i^2 + \mu_i^2 \cdot 10\%$ for Damaged system $\rightarrow \mathbf{M} = \mathbf{M}(\mu_i^1, \mu_i^2)_{damaged}$
4. solve $[\mathbf{K} - \lambda\mathbf{M}]\mathbf{V} = 0 \rightarrow \omega_1 = \sqrt{\lambda_1}, \omega_2 = \sqrt{\lambda_2}$
5. return $\omega_{1i} = \text{Uni}(\omega_{1up}, \omega_{1lo}), \omega_{2i} = \text{Uni}(\omega_{2up}, \omega_{2lo})$
6. end

The spread of the example data is shown in **Figure 2.4 (A)**. Red represents the case of healthy system and black the unhealthy. With the large square markers, the nominal frequencies and with small circles the simulated measurements that include uncertainties. More specifically, $\pm 1\%$ uncertainty from nominal values has been simulated as an example for the stiffness and mass, while $\pm 5\%$ and $\pm 1\%$ uncertainties were assumed as errors in the supposedly measured frequencies. The data spread in this potential feature space, indicates, that if the simulated cases would depict measurements and a potential classifier was informed only of the nominal values, the possible points in the blue circled areas could be misclassified.

On the other hand, a classifier trained with data that simulates the uncertainties, would have good chances of correctly classifying the measured cases by forming boundaries around the class variances. This is shown with blue dashed line in **Figure 2.4 (B)**. The question rises as how much the uncertainty magnitude should be in the FE data generation step. For that, the same calculations

are performed but with increasing uncertainty magnitude on the elements stiffnesses at $\pm 2\%$ in **Figure 2.4 (C)** and $\pm 3\%$ in **Figure 2.4 (D)**. A good classifier would not have any problem to calculate a boundary when presented with $\pm 2\%$ uncertainty data, however for $\pm 3\%$ the task becomes more difficult. The overlap between simulated cases marked in the blue circled area means that the potential 2 featured classifiers would start decreasing in learning accuracy. The classification accuracy of the simulated data could therefore be a good indicator about the magnitude of the uncertainties that could be implemented in simulations.

The described behavior of feature space enrichment and impact on classification difficulty and uncertainty simulation/data augmentation is also encountered in the studied cases of the present thesis. Even though vibration time-series were mostly used, the classifiers described in the next section have the ability to map time series in discrete low-dimension features. Therefore, a similar behavior can be expected to be followed already, where uncertainty simulation through random parameters sampling has positive effect on classifying the unknown experimental cases.

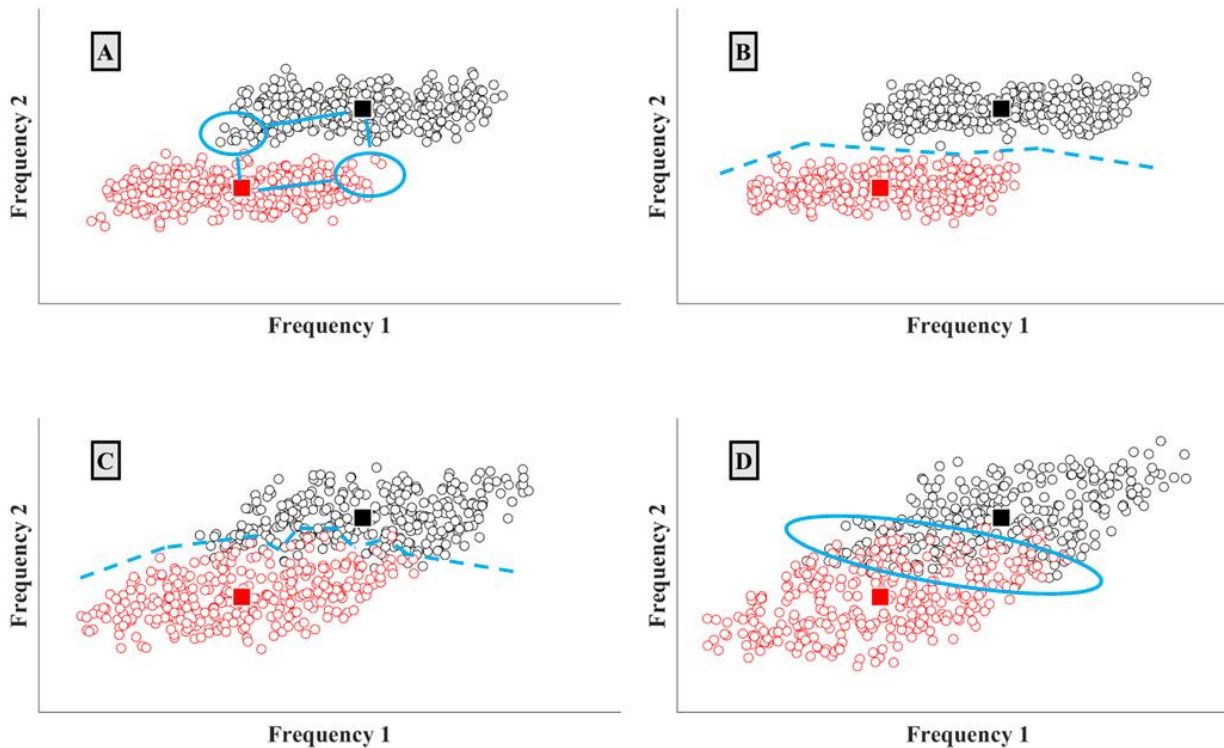


Figure 2.4: Eigenfrequency data generated with FE model and measurement uncertainties for the healthy and the damaged state of the 2 DOF linear system. Graphs A and B depict results for 1% uncertainty in stiffness, while C and D represent 2 and 3% respectively

2.3 Classification with Convolutional Neural Networks

In the present section the theoretical background behind 1-D supervised classification and learning with Convolutional Neural Networks (CNN) will be given. The function of such classifiers is presented, starting with convolutional feature extraction from the input signals which produce

feature maps for the classification part of the network. This is called Forward Propagation (FP) of information in Artificial Neural Networks (ANN).

A simplified description is shown in **Figure 2.5**. Notice, that the input signals and highest-level convolutional feature maps were taken from a real damage identification application. A CNN can therefore work like this on a raw signal and extract concentrated information.

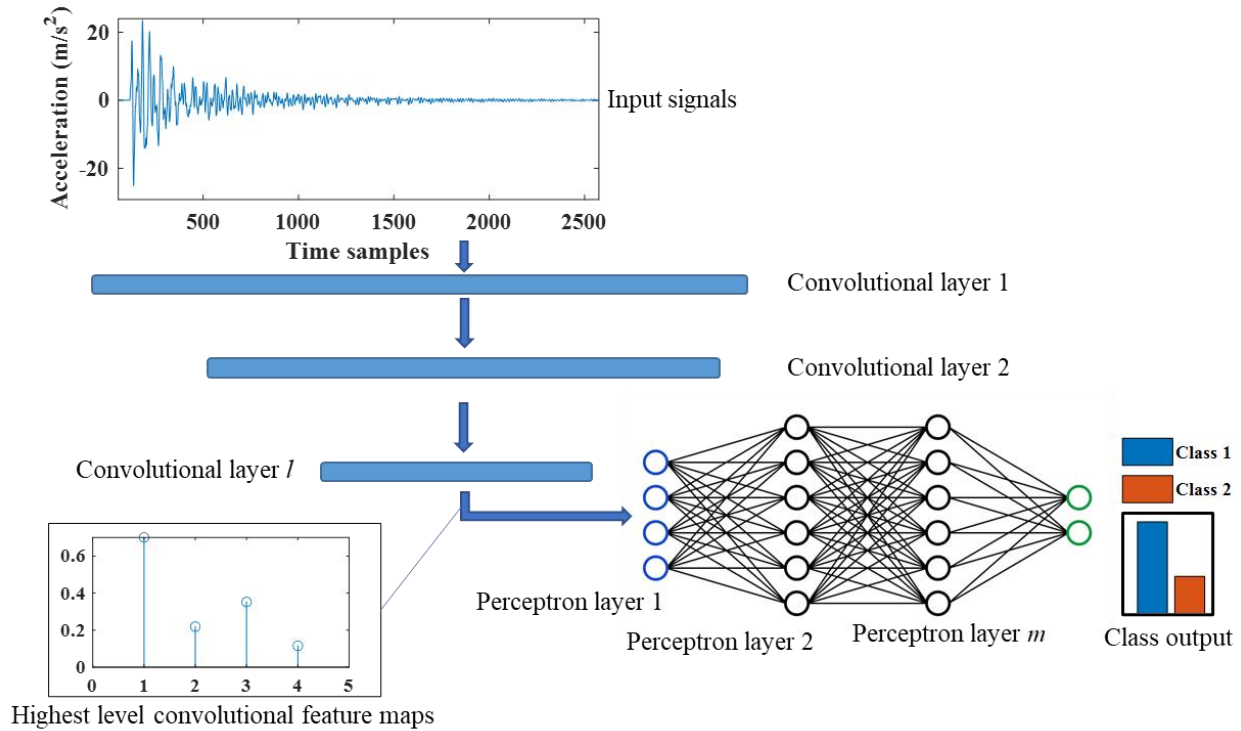


Figure 2.5: Example of Forward Propagation in a network with a Convolutional and Classification (fully connected perceptron) part

2.3.1 Deep learning feature extraction with convolutional neural networks

A one-dimensional (1D) CNN [33,78] is made of series of layers that process an input discrete 1D signal in of t_{in} time samples and therefore of size $[t_{in} \times 1]$ by applying a filter w_k of size $[t_w \times 1]$ with $t_w < t_{in}$. A single CNN neuron k produces therefore a filtered output f_k of size $[t_{out} \times 1]$ according to the convolution process:

$$f_k = w_k * in \quad \text{with} \quad (w_k * in)[t_{out}] = \sum_j in(j)w_k(t - j + 1) \quad (j \text{ takes all valid values}) \quad (2.10)$$

where $t_{out} = (t_{in} - (t_w - 1))$ in the so called no-zero-padding convolution. The filtered signal which contains higher level features is further processed by the neuron activation function $a_k = a(f_k)_k$ with bias b_k , to get the final neuron output as:

$$out_k = a_k(w_k * in + b_k) \quad (2.11)$$

The activation function in neurons is a user chosen parameter, usually among standard functions that have appeared in the literature [78]. It can be linear, or non-linear, affecting the effectiveness of the training process and it is regarded as a hyperparameter, meaning it needs to be tested for each specific problem. The output is after propagated to the next convolutional layers where it is used as input, repeating the aforementioned process. The reader should notice that previous layer outputs are summed up for the next layer input. For example, the output out_k^l of a neuron k of a successive convolutional layer l is:

$$out_k^l = a_k^l(x_k^l) \quad \text{with} \quad x_k^l = b_k^l + \sum_{i=1}^{N^{l-1}} f_{ik}^{l-1} \quad \text{and} \quad f_{ik}^{l-1} = w_{ik}^{l-1} * out_i^{l-1} \quad (2.12)$$

Where f_{ik}^{l-1} is the convolution of the output out_i^{l-1} of neuron i of the previous layer $l-1$ with the filter w_{ik}^{l-1} that neuron k of layer l uses on the neuron i of the previous layer. The previous layer $l-1$ has a number of N^{l-1} neurons. The notation as in [79] has been used.

Additionally, it is common to apply subsampling or different pooling [78,80,81] operations after each layer with the purpose to progressively reduce data size in high level information. A common example is the max-pooling operation where an overlapping or non-overlapping window scans the output signal of equations (2.11) or (2.12) and outputs the maximum values only, in a preselected sub-sampling value. For example [82] a max pooling operation of 2 with a non-overlapping window and no padding on a vector signal with entries [1 2 3 4 5] results in [2 4].

Finally, other techniques can also accompany convolutional layers such as dropout [83]. Dropout is a simple yet effective technique that randomly switches off neuron output (during training) in order to enhance neural network generalization. This can be achieved by multiplying a value r_i^{l-1} with the neuron outputs so equation (2.12) can be:

$$out_k^l = a_k^l(x_k^l) \quad \text{with} \quad x_k^l = b_k^l + \sum_{i=1}^{N^{l-1}} f_{ik}^{l-1} \quad \text{and} \quad f_{ik}^{l-1} = w_{ik}^{l-1} * (r_i^{l-1} \cdot out_i^{l-1}) \quad (2.13)$$

where r_i^{l-1} can be sampled from a predefined probability distribution to take the values of 0 or 1. Such approaches are found in the literature as regularization techniques, with dropout, early stopping and batch normalization all working towards less overfitting [84-86]. Explicit details are not given in the present work since except dropout they were not applied and are referenced for a more complete review of the reader. Concluding, the outputs of the final convolutional layer l are considered the highest output feature maps, symbolized as $h = [out_1^l \quad out_2^l \quad \dots \quad out_{N^l}^l]^T$, where the outputs of N^l number of neurons are concatenated. This extracted information from the original signal can now be processed for classification. The size of h depends on all previous inputs, filter lengths and pooling.

2.3.2 Deep learning classification

In supervised learning, after the convolutional component, classification neurons can be deployed. The classification neurons known as perceptrons is the standard and earliest form of ANNs

described in recent [78] and older textbooks [87]. A perceptron neuron acts as a product of a weight array and the inputs. The output of a perceptron neuron k is calculated as:

$$a_k = a_k(W_k h + b_k) \quad (2.14)$$

The neuron activation is again symbolized with a_k and W_k and b_k are the neuron weights and bias respectively. The inputs this time have been noted as h , which can be equal to the highest-level convolutional feature maps. Given that a single perceptron has a single scalar output, the dimensions of W_k and b_k are of $[1 \times \text{len}^h]$ and $[1 \times 1]$ respectively given a size of inputs h as $[\text{len}^h \times 1]$. A single perceptron neuron can learn to do a linear separation on the inputs $h = [h_1 \ h_2]^T$ according to a hyperplane defined by $W_k = [w_1 \ w_2]$ as shown in an example in **Figure 2.6** for a two-dimensional case. This is the fundamental principle of work for classification with perceptrons.

The classification or fitting power over the inputs is increased by employing more neurons and more layers, forming the so called Fully Connected (FC) layers which can learn complex patterns and non-linear separations over multiple labels of inputs [78,87]. Multilayered and multilineal perceptron output for a layer m can be conveniently written in matrix notation as:

$$\mathbf{a}^m = \mathbf{a}^m(\mathbf{W}^m \mathbf{a}^{m-1}(\mathbf{W}^{m-1} \mathbf{a}^{m-2}(\mathbf{W}^{m-2} \mathbf{a}^{m-3}(\dots) + \mathbf{b}^{m-2}) + \mathbf{b}^{m-2}) + \mathbf{b}^m) \quad (2.15)$$

where \mathbf{a}^m is the activation function of size $[N^m \times 1]$ of layer m with N^m number of neurons.

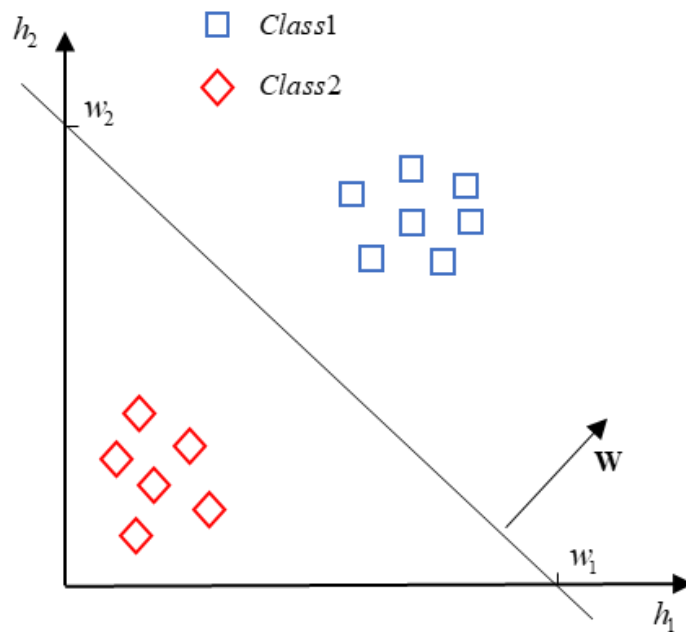


Figure 2.6: Example of a linear separation boundary with a single perceptron neuron

The matrix \mathbf{W} and vector \mathbf{b} represent this time the layer weights and bias as:

$$\mathbf{W}^m = \begin{bmatrix} w_{1,1} & w_{1,2} & \dots & w_{1,N^{m-1}} \\ w_{2,1} & w_{2,2} & \dots & w_{2,N^{m-1}} \\ \dots & \dots & \dots & \dots \\ w_{N^m,1} & w_{N^m,2} & \dots & w_{N^m,N^{m-1}} \end{bmatrix} \text{ and } \mathbf{b}^m = \begin{bmatrix} b_1^m \\ b_2^m \\ \dots \\ b_{N^{m-1}}^m \end{bmatrix} \quad (2.16)$$

In supervised learning, as considered in the present work, the outputs of the perceptron part are propagated to the final or classification layer. The number of neurons in the classification layer is equal to the number of classes. For example, in a binary problem the classification layer would have 2 neurons as in the example of **Figure 2.6**. The class vector σ as the softmax function gives the health label prediction on the initial inputs:

$$\sigma_i = \frac{e^{x_i^{lc}}}{\sum_{j=1}^{N^{class}} e^{x_j^{lc}}} \quad (i=1,2\dots N^{class}) \quad (2.17)$$

where lc denotes the classification layer with number of neurons N^{class} . The correct label will be predicted when the network has learned the appropriate values of convolutional filters described in section **2.3.1** and perceptron weights \mathbf{W} and bias \mathbf{b} .

Learning is achieved with Backpropagation (BP) on the labeled training data as in equation (2.9). The BP algorithm is the most widely used algorithm in training ANNs and has been established as the *de facto* since it was first popularized [88]. The algorithm uses gradient descent methods to minimize a loss function which could be the categorical cross entropy (CE) between the correct and the output health status labels Y_i and σ_i (for i number of classes) respectively:

$$CE(\underline{w}) = - \sum_{i=1}^{N^{class}} Y_i \ln \sigma_i(\underline{w}) \quad (2.18)$$

The convolutional filters and perceptron weights and biases values, grouped in parameters vector \underline{w} , that best minimize the loss are acquired iteratively in gradient descent steps. Neural network training can be regarded therefore as an optimization problem. The main disadvantage of BP is that as a gradient-based method it can be prone to convergence in local minima. Various techniques have been tested in the past to improve global minimum approximation such as noise injection [89], combination with gradient free methods [90] or adjustments in activation functions [91] or the loss [92]. In the present work, for all CNN formulations the open-source python library keras [82] was utilized and the stochastic gradient descent (SGD) BP algorithms contained within. Stochastic gradient descent updates the weights iteratively considering the data separated in random batches. This has been proved to increase generalization capabilities [38] and will be the standard throughout the present work.

Chapter 2-Classification with Convolutional Neural Networks

For the weights update let the total loss within a random batch of Q training examples from the

total number of n in the training set **(2.9)** be $L(\underline{w}) = -\sum_{q=1}^Q \sum_{i=1}^{N^{class}} Y_i \ln \sigma_i(\underline{w}) = -\sum_{q=1}^Q L_q(\underline{w})$ with $Q < n$.

The gradient descent update rule of \underline{w} for an iteration k is therefore:

$$\underline{w}(k+1) = \underline{w}(k) - a \nabla_{\underline{w}} L(\underline{w}) \quad (2.19)$$

where a is the learning rate. The most of BP efforts lie in computing the gradient $\nabla_{\underline{w}}$ (which is the average gradient of the training batch) and details from the computationally extensive process may be found in standard textbooks or the aforementioned works [78,87,88].

Furthermore, since BP starts with randomly initialized solutions for the general case, an ensembling scheme among different networks will be used in the present work, in order to compensate for different possible minima convergence due to different starting points. Ensembling or averaging in ANN prediction and classification are known techniques that increase performance [93,94]. Concluding, the details in all ANN architectures and training results that follow in the coming Chapters will be given based on the theory that has been presented.

Supervised Damage Identification with Updated Finite Element Model data and Deep Learning

Contents from Original Paper [95]: Seventekidis, P., Giagopoulos, D., Arailopoulos, A., & Markogiannaki, O. (2020). Structural Health Monitoring using deep learning with optimal finite element model generated data. *Mechanical Systems and Signal Processing*, 145. <https://doi.org/10.1016/j.ymsp.2020.106972>

ABSTRACT

Identifying damage through Structural Health Monitoring (SHM) methods is increasingly attracting attention due to multiple maintenance and failure prevention applications. In order to create reliable SHM systems for structural damage identification (DI) tasks, access to large amounts of data containing measured structural responses is usually necessary. The data acquisition is mostly based on direct experimental responses up to now and requires time consuming measurements in various working and ambient conditions of the structure. In the present work a novel SHM method is tested where all data is solely derived from FE calculated responses after an initial experimental cost, for FE model updating on the healthy structure state. The proposed method can be especially applied in cases where specific damage types are expected or anomalies are adequately defined so they can be effectively simulated by FE models originating from the healthy experimental status. To test the proposed SHM system, the optimal FE model of an experimental benchmark linear beam structure is constructed, simulating an undamaged condition. In order to check the robustness of the proposed method the damage magnitudes imposed on the benchmark are kept small and combined with random excitations. Next, the optimal FE model is used for generating labeled SHM vibration data through a repetitive load case scheme, which also includes uncertainties simulation. The data derived from the optimal FE model is finally used to train a Deep Learning (DL) Convolutional Neural Network (CNN) classifier which is after experimentally validated on the benchmark structure. The optimal FE generated data proves to be able to train an accurate CNN that can predict adequately the experimental benchmark states. A comparison is also given with a CNN trained by the corresponding nominal FE model data which is found not reliable on the experimental validations. The presented combination of optimal FE and DL is a potential solution for future SHM tools and further investigation is encouraged.

Keywords: Structural Health Monitoring, Deep learning, Neural networks, Damage identification, FE model updating

3.1 Introduction

Goal of the current chapter is to investigate the feasibility of numerically trained classifiers and study the influence of Finite Element (FE) model updating (accuracy) and neural network parameters on the experimental generalization of corresponding health states.

Structural health monitoring (SHM) is a general term referring to engineering analysis methods that study the presence and characteristics of changes in a structure's integrity with an indirect way, meaning without observing directly the physical changes. In mechanical systems that include moving parts the anomalies identification process is usually known as Condition Monitoring (CM) instead of SHM. The procedures however in SHM or CM systems are similar. A SHM or CM process includes structural response data acquisition over time and processing of the data in order to identify features that may contain information about possible damage presence and extend. Significant attention has recently been drawn on various SHM and CM techniques in order to reduce maintenance costs and prevent catastrophic failures in mechanical systems and structures. Potential applications of SHM and CM methods may include large structures such as bridges [96-98] and wind generators [13, 99], to smaller but more complex, like transmission systems [100, 101] or aircraft components [102]. The equipment necessary to monitor a system's condition relies mainly on vibration or acoustic emissions which are captured by a network of sensors. The information can be processed continuously in real-time or on demand. SHM systems usually undergo through a phase of training or equivalently known also as learning, where a mathematical model learns to distinguish between normal or faulty operating conditions based on measured structural responses. Two main types of learning, supervised and unsupervised are used to train SHM systems. Choosing between them depends on the complexity of the problem, the availability of learning and testing data, the type of the mathematical models involved and the specific requirements of each problem.

In the present chapter a methodology is proposed for the solution of the data availability problem by generating labeled training data with Updated (FE) models as has been described in **Chapter 1**. Data acquisition or data generation is the most important stage of a SHM process since it affects the effectiveness of the subsequent steps. For a mechanical system, the structure's response could be obtained through experimental measurements like an accelerometer network or computationally via numerical methods like the FE method. The data has of course to be as representative as possible of the structure's labeled status and adequate numbers of data sets must be available depending on the nature of the problem and uncertainties involved. This inherently poses experimentally acquired data more attractive for most problems, since standard nominal FE models will have significant differences from the real structural response as the problem complexity rises. Nevertheless, due to practical limitations there are only few cases [12-13] with real-life structures where the actual expected damage can be measured. For this reason, data acquisition usually happens on lab-scale substitutes or purely unsupervised learning SHM systems are applied. CM data might be easier to be experimentally obtained for different damage types [103, 104] however large number of measurements should again be necessary.

On the other hand, given FE models accurate enough, arbitrary number of load cases, damage types and uncertainties could be simulated at virtually no cost and effort. Updated model techniques [20, 50] can offer solutions to the problem of FE accuracy by using experimental measurements of the actual structure to numerically modify the physical parameters of a FE model. The high-fidelity updated or optimal FE model may well be really close to the experimental structure responses for which it was fit on for linear or non-linear [21] problems and different model scales with large numbers of degrees of freedom [46]. At an initial FE updating cost on the healthy structure states, labeled SHM data can easily be generated also accounting for cases that are not possible to simulate in real conditions. Main prerequisite is of course that the optimal FE model developed on the healthy status can be used to simulate damaged statuses as well. In this chapter, a novel supervised learning method is proposed where all necessary SHM training data is derived from optimal FE simulations by model data fit on the healthy experimental status responses. For SHM applications where specific damage types are expected, such as loose bolts on a structure or cracks in certain locations, which constitute defined stiffness reductions on the original healthy optimal model, the proposed method could effectively provide an alternative to the current experimentally oriented SHM systems. Therefore, main advantage except avoidance of strenuous and time-consuming measurement procedures would be the direct labeling of damage types. In addition, for cases where ambient conditions are important and depend on seasonal characteristics, for example temperature or traffic conditions on bridge structures, the proposed method would be beneficial by simulating the appropriate ambient conditions or excitations [105,106]. Data could be gathered relatively quickly compared to real waiting times for experimental measurements. Finally, the data for damage types that are too expensive or not possible to be simulated outside lab conditions may be generated.

Next, for the mathematical classification models to handle the damage identification, Convolutional Neural Networks (CNN) are applied. As discussed in **Chapter 1** and **2**, such classifiers filter the original signal input producing useful characteristics, yet sometimes too abstract for a human designer to identify or describe and a SHM or CM CNN classifier [27,28,33,107] when fed in with appropriate data may perform supervised, unsupervised damage recognition and quantification, while operating literally on raw measurements. We follow therefore the approach of CNN based supervised classifiers to minimize data pre-processing and tackle the SHM in a global way, handled by the self-learning capabilities of CNNs. The large number of data sets usually required by CNNs to learn effectively will be generated by using the optimal FE models which were fit on the healthy status and were modified accordingly to account for damaged cases.

The robustness of the proposed optimal FE-CNN SHM system is finally tested on a benchmark linear steel beam setup. Two distinct and small magnitude artificial damage types are imposed using random excitations. Task of the CNNs is to identify the experimental benchmark structure states having been previously trained on FE simulated data. The damage identification (DI) problem will be evaluated in two stages with increasing difficulty. First, a binary form of the DI

problem will be evaluated, meaning considering a single undamaged and a damaged class during training and experimental evaluation. Second, a multiclass DI problem with three different benchmark states is tested, based again on labeled data of purely numerical origin. Results about the accuracy and damage assessment capabilities are discussed. The optimal FE trained CNN-SHM system is also compared with a nominal FE trained model to test the importance of accurate FE simulations. Additionally, architectural parameters such as multifilter averaging are tested. A *multi-headed* or *multi-filter* CNN architecture is benchmarked against a standard CNN in order to study the effect of ensemble in experimental generalization of numerically trained CNNs.

The presentation follows in section 3.2 with a description of the experimental setup along with the measuring and excitation equipment. Section 3.2 also contains the optimal FE model development on the experimental healthy structure. Section 3.3 describes the FE load case algorithm for the data generation which is to be fed in the classifiers. Section 3.4 contains the CNNs architectures tested in this work, data training results and experimental generalization validation of the proposed methodology. Finally, in section 3.5 the conclusions of the present chapter are presented. The workflow is as was shown in **Figure 2.1**.

3.2 Experimental benchmark and Updated Finite Element Model

A depiction of the experimental setup of a linear steel beam with the excitation and measuring equipment is shown in **Figure 3.1**.

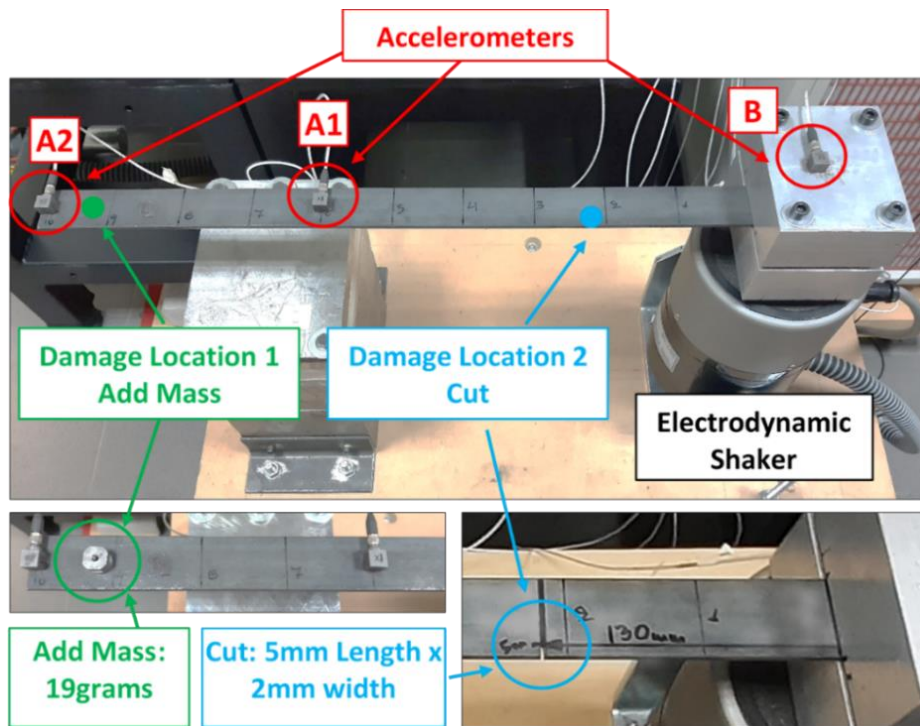


Figure 3.1: Experimental set-up with accelerometer and excitation equipment (up). Damage case 1 (down left) simulated as mounted mass on the beam. Damaged case 2 (down right) with a cut on the beam

The linear steel beam is clamped on one edge with an electrodynamic shaker which serves as the base excitation while the other end is free to oscillate. Artificial damage is introduced on the beam edge by first mounting a mass via a magnet and in a second instance inducing a cut on the beam in order to simulate a crack. The first damage case, from now on referred as Damage 1 includes a mounted mass of 19g (around 2% of total benchmark weight) while the second damage case, referred as Damage 2 contains a cut (5mm length x 2mm width) on the beam. The healthy beam state containing no damage, but the solid beam alone will be referred as the Healthy case. The DI problem to be tested with the proposed SHM method will be evaluated in two stages. First, in a binary classification form, with goal to separate measurements from Damage 1 and 2 benchmark instances from the Healthy benchmark state. As a result, two classes will be considered in the SHM system, a Damaged and a Healthy one. Second, in a more demanding multiclass form where each of the 3 benchmark states forms a separate class and the SHM system considers also 3 classes. The goal this time is to test the ability of damage separation. In addition, to test the robustness of the proposed SHM method, random base excitations are applied to increase the complexity of the DI problem.

Acceleration signals throughout this work were measured by $\pm 50g$ Brüel & Kjær accelerometers, using a data acquisition system of National Instruments (CDAQ 9178 chassis and CDAQ-9234, 4-Channel Accelerometer Input Modules). The electrodynamic shaker is the Model ET-140 with Amplifier ET-141 of Labworks Instrument. The sampling frequency was chosen at 2048 Hz for all measurements. The accelerometer network used is comprised of sensors in two (2) different locations on the beam (A1, A2) and one (1) at the base (B). The detailed dimensions of the experimental set-up along with the corresponding optimal FE model are shown in **Figure 3.2**.

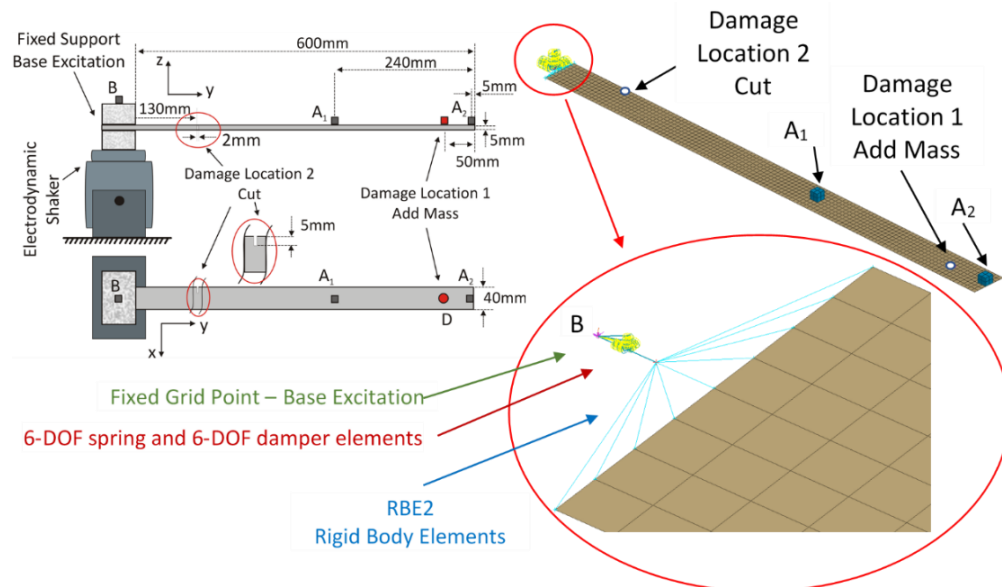


Figure 3.2: Sketch of the experimental setup (left) and the optimal FE model (right) including also modeling of the base support

All accelerometers A1, A2 and B are used for the model updating scheme. Accelerometer B serves the purpose of capturing the random gaussian base excitation forced by the electrodynamic shaker and the measured acceleration time histories are used as base excitation in the FE model. On the other hand, acceleration histories for experimental measurements during the testing phase of the proposed SHM method are recorded at the accelerometer sensors A1, A2 shown in **Figure 3.2**. The previously described binary and multiclass DI problems are tested with purely numerically trained CNN-SHM classifiers as already described in the Introduction. Therefore, acceleration measurements are first conducted for the optimal FE modeling of the benchmark on the healthy beam status.

The base is additionally modeled in the optimal FE design, using for clamping rigid body elements and for the support a 6-degrees of freedom (DOF) linear spring and damper. Higher accuracy is expected in that way compared to a nominal FE model which just restrains the DOFs at the clamping. The body of the beam was modeled with 960 CQUAD shell elements with $5mm$ discretization length and $5mm$ nominal thickness. The accelerometers with dimensions $10 \times 10 \times 10mm$ were modeled with 24 CHEXA solid elements with $.5mm$ discretization length.

The model parameters in search to be updated for the optimal FE structure are presented in **Figure 3.3**. The initial or nominal parameters for the beam are Young's modulus $E = 210GPa$, Poisson's ratio $\nu = 0.3$ and density $\rho = 7850kg / m^3$. While for the accelerometers are $E = 69GPa$ for the Young's modulus and $\rho = 2750kg / m^3$. Nominal damping on the other hand is used as constant $\zeta = 0.01$ at all frequencies resulting in Rayleigh coefficients $\alpha = 0.01998$ and $\beta = 1.9998$.

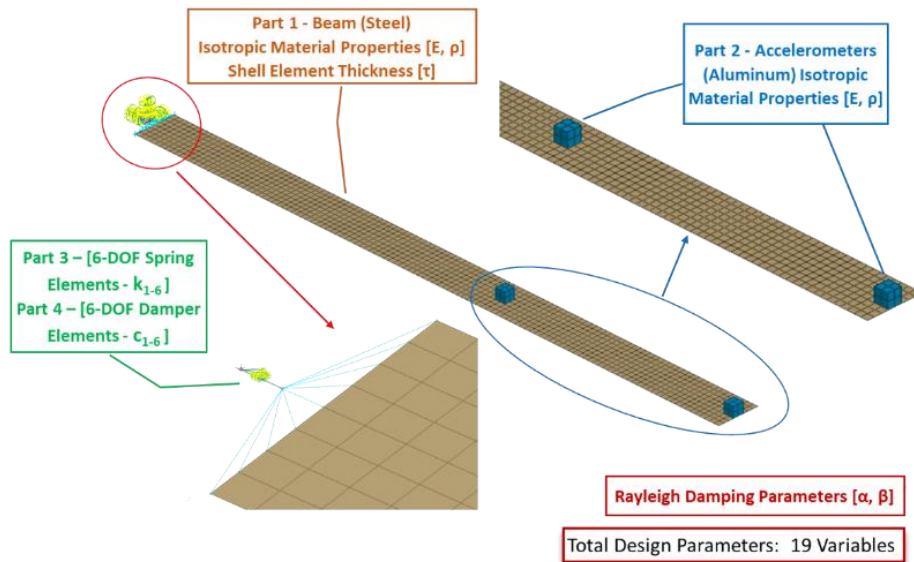


Figure 3.3: FE model parameters to be updated for the FE optimal model construction

The Covariance Matrix Adaptation Evolution Strategy (CMA-ES) algorithm was used to update the model to most probable structural parameters by comparing experimental and numerical time

histories, therefore using the residual of equation (2.7). The details about the specific computational framework behind the updating strategy using the CMA-ES algorithm can be found in **Chapter 2**. The results from the updating procedure for the structural parameters are summarized in **Table 3.1**. UB and LB denote the possible upper and lower bounds for each parameter in search with the CMA-ES algorithm, while the Result shows the final parameter value converged. Values in **Table 3.1** are arranged according to the parts shown in **Figure 3.3**. Additionally, as structural damping plays a key role in the response, Rayleigh damping coefficients corresponding to low and high frequencies were also included in the inferred parameters with a wide range of $(\zeta_1, \zeta_2) = [0.1\%, 9.9\%]$ in order to fulfill an adequate correlation between the experimental and numerical acceleration time histories. The damping coefficients for Rayleigh damping were calculated as $\alpha = 1.9607$ and $\beta = 1.14780$. A sample time response for random excitation is depicted in **Figure 3.4** where the good correspondence of the optimal model to the experimental set-up is observed. The nominal model response is also included for comparison.

Table 3.1: Optimal FE model structural parameters after model updating

Part	Density			Young's Modulus			Thickness			Spring stiffness			Damper		
	ρ			E			τ			K			C		
	$[kg/m^3]$			$[GPa]$			$[mm]$			$\cdot 10^5 kN/m$			$\cdot 10^{-2} kNs/m$		
	LB	UB	Result	LB	UB	Result	LB	UB	Result	LB	UB	Result	LB	UB	Result
P1	7065	8635	8487.47	189	231	226.75	4.5	5.5	5.48	-	-	-	-	-	-
P2	2475	3025	2832.50	62.1	75.9	65.55	-	-	-	-	-	-	-	-	-
P3	-	-	-	-	-	-	-	-	-	-	-	12.01	-	-	-
	-	-	-	-	-	-	-	-	-	-	-	11.58	-	-	-
	-	-	-	-	-	-	-	-	-	9	15	11.24	-	-	-
	-	-	-	-	-	-	-	-	-	-	-	9.22	-	-	-
	-	-	-	-	-	-	-	-	-	-	-	10.57	-	-	-
	-	-	-	-	-	-	-	-	-	-	-	13.59	-	-	-
P4	-	-	-	-	-	-	-	-	-	-	-	-	-	-	4.37
	-	-	-	-	-	-	-	-	-	-	-	-	-	-	2.61
	-	-	-	-	-	-	-	-	-	-	-	-	-	-	7.10
	-	-	-	-	-	-	-	-	-	-	-	-	1	9	5.68
	-	-	-	-	-	-	-	-	-	-	-	-	-	-	7.06
	-	-	-	-	-	-	-	-	-	-	-	-	-	-	4.16

Concluding this section, the eigenfrequencies of the system are calculated with the optimal FE model for the healthy and the Damage 1 and 2 cases, shown in **Table 3.2**. Both Damage cases in the optimal models originate from the Healthy model parameters and the mass or cut was designed according to **Figure 3.2**. The results show that only four eigenfrequencies (1, 2, 3 and 7) in the frequency range 0-1000Hz are disturbed more than $\pm 1\%$ for damage 1. For damage 2 the disturbance is even smaller with less than 0.15% on the calculated eigenfrequencies. The eigenfrequencies might not be the only possible features that a CNN can be based on, however the calculated values indeed show that the DI problem in the benchmark case is a demanding one, also

combined with the random excitation to be used as a system working condition. A high robustness can therefore be shown with the proposed SHM method, provided that damage is classified successfully for the given excitation and damage magnitude conditions.

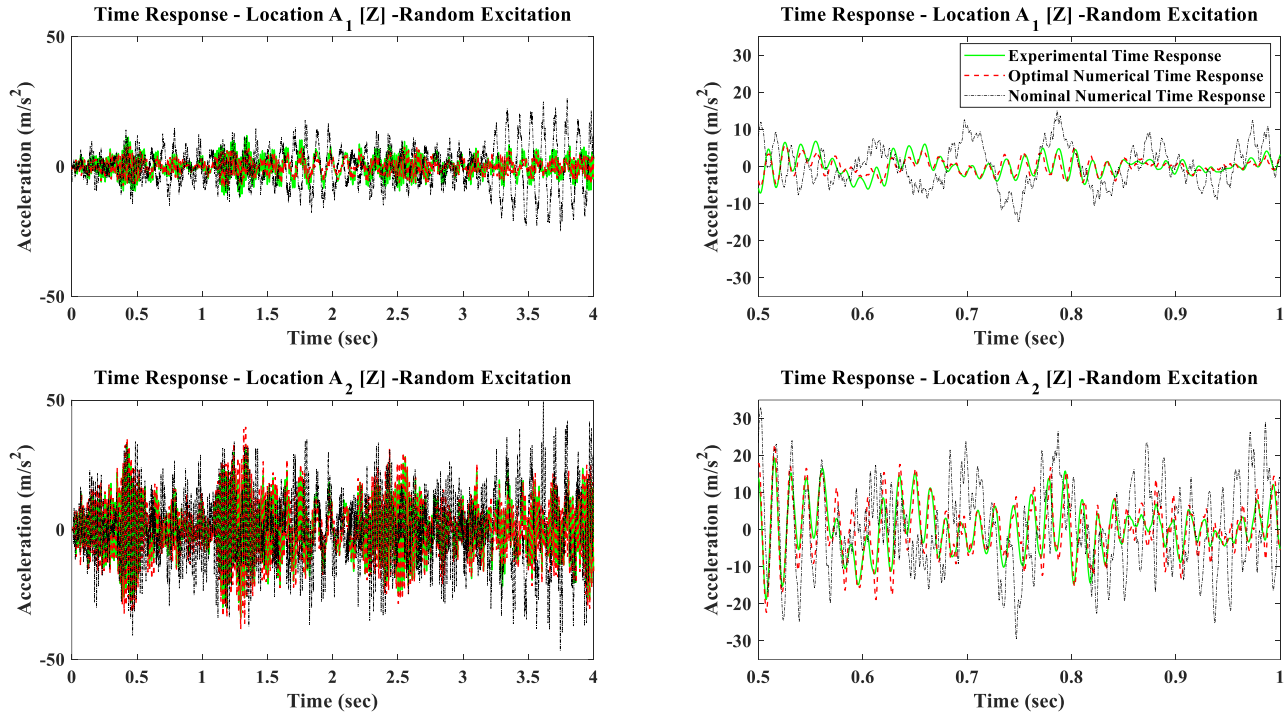


Figure 3.4: Comparison of acceleration time responses for the optimal and nominal FE models against the experimental measurement for accelerometer locations A1 (up) and A2 (down)

Table 3.2: Computed eigenfrequencies of healthy and damaged states using optimal FE model along with the difference compared to the healthy state

	Frequency Healthy [Hz]	Frequency Damage 1 [Hz]	Difference 1 (%)	Frequency Damage 2 [Hz]	Difference 2 (%)
1	8.97	8.77	2.24	8.96	0.14
2	15.31	15.00	2.00	15.30	0.03
3	63.42	62.69	1.15	63.42	0.00
4	187.24	186.45	0.42	187.05	0.10
5	274.92	274.29	0.23	274.58	0.12
6	379.54	379.29	0.07	378.94	0.16
7	392.53	387.47	1.29	390.85	0.43
8	636.30	635.93	0.06	635.62	0.11
9	862.23	860.47	0.20	863.09	0.10
10	968.82	965.89	0.30	968.53	0.03

3.3 Labeled Data Generation

Using the optimal FE model presented in section 3.2 the training data generation procedure is ready to begin. Data will also be generated by the nominal FE model of the benchmark, in order to show potential differences on the trained CNNs behavior.

The equations of motion of the FE discretized continuum of the beam structure are:

$$\mathbf{M}(\rho, \mu)\mathbf{A} + \mathbf{C}(\mathbf{K}, \mathbf{M}, \alpha, \beta)\mathbf{V} + \mathbf{K}(E, E_s)\mathbf{U} = \mathbf{F} \quad (3.1)$$

Where \mathbf{A} , \mathbf{V} and \mathbf{U} are global the acceleration, velocity and displacement vectors respectively. \mathbf{M} , \mathbf{C} and \mathbf{K} represent the global mass, damping and stiffness matrices of the structure. The mass matrix \mathbf{M} is a function of the structure's density ρ and mounted mass μ on the beam for the Damage 1 case. The stiffness matrix \mathbf{K} is a function of the structure's and support's modulus of elasticity E and E_s respectively. For the Damage 2 case, $\mu = 0$ and the cut directly results in separate mass and stiffness matrices, constructed however with the same way in material uncertainties. Finally, the damping matrix \mathbf{C} is a function of the system's stiffness, mass and damping coefficients α and β for the continuum and the support.

Once the number of load cases to be created and the statistical bounds for the uncertainties of each parameter are decided, Algorithm 3.1 can be followed in order to create labeled acceleration histories. The repetitive load case scheme is based on the Algorithm 2.2 as presented in section 2.2 data generation procedures. The vector \mathbf{Y} extracted from the algorithm each time contains the classification label according to damage scenario.

Algorithm 3.1: Finite Element model data generation algorithm

Input: Number of load cases n and upper (up) and lower (lo) statistical bounds for each quantity

Output: n number of labeled acceleration vectors at preselected FE nodes

for $i = 1 : n$ **do**

$E_i^s = \text{Uni}(E_{up}^s, E_{lo}^s), E_i = \text{Uni}(E_{up}, E_{lo}) \rightarrow \mathbf{K} = \mathbf{K}(E_i, E_i^s)$ /Uni=Uniform distribution

$\rho_i^1 = \text{Uni}(\rho_{up}, \rho_{lo}), \mu_i = \text{Uni}(\mu_{up}, \mu_{lo}) \rightarrow \mathbf{M} = \mathbf{M}(\rho_i, \mu_i)$ **form** $y = y(\mu_i)$

$a_i = \text{Uni}(a_{up}, a_{lo})$ $\beta_i = \text{Uni}(\beta_{up}, \beta_{lo}) \rightarrow \mathbf{C} = \mathbf{C}(\mathbf{K}, \mathbf{M}, a_i, \beta_i)$

define random \mathbf{F}

Solve $\mathbf{M}\mathbf{A} + \mathbf{C}\mathbf{U} + \mathbf{K}\mathbf{U} = \mathbf{F}$

return \mathbf{A} and \mathbf{Y}

end

Different numerically generated random excitations from a normal distribution with zero mean were used at the support of the FE model simulating the shaker. The total excitation time was 8

seconds for each load case. The number and characteristics of the generated data are summarized in **Table 3.3**. The same uncertainty was simulated for all FE model parameters being the Young's modulus, density, stiffness of the support and all damping parameters. Uniform distribution was used with upper and lower bounds $\pm 5\%$ of the original values respectively. To increase DI sensitivity and generalization, the mounted mass for the damaged cases was varied with values picked randomly at both directions from a uniform distribution as well. The same way of uncertainty simulation was also performed for the cut on the beam. Cases were simulated for the benchmark states being Healthy and Damage 1 and 2 both for the optimal and the nominal FE model. The FE optimal and nominal models are solved with the commercial FE code NASTRAN on an intel i7-8700 PC with 32GB of RAM

Table 3.3: FE generated data for SHM classifiers learning

FE model	Optimal	Nominal	Optimal	Nominal	Optimal	Nominal
Uncertainty simulation for FE model parameters	$\pm 5\%$	$\pm 5\%$	$\pm 5\%$	$\pm 5\%$	$\pm 5\%$	$\pm 5\%$
Case	Healthy	Healthy	Damage1	Damage1	Damage2	Damage2
Variation on added mass or cut length	0	0	$\pm 15\%$	$\pm 15\%$	$\pm 25\%$	$\pm 25\%$
Number of cases n	2500	2500	2500	2500	2500	2500

An average time of 20 seconds was required for the solution of one of the load cases, which were run on 5 parallel executables resulting in approximately 8.33 hours for the optimal or nominal data set. For each case i the vertical accelerations histories \mathbf{S}_i at the sensor points of the FE models were extracted, along with the corresponding labeling data \mathbf{Y}_i for the DI tasks. As mentioned in section 3.1 the first DI approach includes a binary separation of the Healthy and both Damaged conditions combined. Data labeling for the binary classification problem includes a separation in the form of 0 or 1 as targets for each class, so \mathbf{Y}_i^{bin} is a two-dimensional vector in the binary DI case. Healthy labeled responses form the Healthy class while combined Damage 1 and 2 cases form the Damaged class. For the multiclass DI problem to be tested, each simulated benchmark instance forms a single class so \mathbf{Y}_i^{multi} becomes a three-dimensional vector. Finally, the initial acceleration signals \mathbf{S}_i were reduced to randomly sampled windows of 0.334 seconds starting at the same time point for both sensors, being \mathbf{S}_i^1 and \mathbf{S}_i^2 respectively. The final accelerations are stacked sequentially in the vector \mathbf{A}_i as $\mathbf{A}_i = [\mathbf{S}_i^1 \ \mathbf{S}_i^2]$ symbolized finally as \mathbf{A}_i^{opt} and \mathbf{A}_i^{nom} according to model type derivation, being optimally and nominally FE derived accelerations respectively. The sets of DI learning data from the optimal model and the nominal model data are formed as:

$$S_{optBin} = \{(\mathbf{A}_1^{opt}, \mathbf{Y}_1^{bin}), (\mathbf{A}_1^{opt}, \mathbf{Y}_2^{bin}), \dots, (\mathbf{A}_n^{opt}, \mathbf{Y}_n^{bin})\}^{opt} \quad (3.2)$$

$$SoptMulti = \{(\mathbf{A}_1^{opt}, \mathbf{Y}_1^{multi}), (\mathbf{A}_2^{opt}, \mathbf{Y}_2^{multi}), \dots, (\mathbf{A}_{n^{multi}}^{opt}, \mathbf{Y}_{n^{multi}}^{multi})\}^{opt} \quad (3.3)$$

$$SnomBin = \{(\mathbf{A}_1^{nom}, \mathbf{Y}_1^{bin}), (\mathbf{A}_2^{nom}, \mathbf{Y}_2^{bin}), \dots, (\mathbf{A}_{n^{bin}}^{nom}, \mathbf{Y}_{n^{bin}}^{bin})\}^{nom} \quad (3.4)$$

$$SnomMulti = \{(\mathbf{A}_1^{nom}, \mathbf{Y}_1^{bin}), (\mathbf{A}_2^{nom}, \mathbf{Y}_2^{bin}), \dots, (\mathbf{A}_{n^{multi}}^{nom}, \mathbf{Y}_{n^{multi}}^{bin})\}^{nom} \quad (3.5)$$

Where $n^{bin}=5000$ for the binary DI consisting of 2500 Healthy and equally combined 1250 Damage 1 and 2 cases together and $n^{multi} = 7500$ for the multiclass DI consisting of 2500 cases of all three states.

For the experimental validation data, measurements were performed on the benchmark set-up of section 3.2 for the different damage scenarios. In total 300 measurements were performed for a random excitation with duration of 10 seconds. 100 measurements were performed for the Healthy beam structure and 100 measurements each for each Damage 1 and 2 cases. The measured accelerations for each sensor were also reduced to randomly sampled windows of 0.334 seconds to match the learning data lengths. The final testing inputs for a measurement i are \mathbf{A}_i^{Test} formed as $\mathbf{A}_i^{Test} = [\mathbf{S}_{test_i^1} \quad \mathbf{S}_{test_i^2}]$ where $\mathbf{S}_{test_i^1}$ and $\mathbf{S}_{test_i^2}$ are the experimental sensor accelerations. The test measurements are separated as follows:

$$\mathbf{A}h_i^{Test} \quad i=1-100 \text{ Healthy benchmark measurements} \quad (3.6)$$

$$\mathbf{A}d1_i^{Test} \quad i=1-100 \text{ Damage 1 benchmark measurements} \quad (3.7)$$

$$\mathbf{A}d2_i^{Test} \quad i=1-100 \text{ Damage 2 benchmark measurements} \quad (3.8)$$

At this point, with the complete FE simulated learning data and experimental measurements, the CNN learning procedure design and real validation follows.

3.4 Neural Network Classification and Experimental Validation

The general CNN feature extraction and classification function was presented in section 2.3. In the current section, the specific CNN architectures are to be trained on the simulated responses of section 3.3. As described in the Introduction section 3.1 a standard CNN and a *multi-head* CNN architecture are to be tested in order to investigate ensembling effects on later experimental generalization. The standard (*single-head*) and *multi-head* networks that have been used are depicted in **Figure 3.5**. The *multi-head* network can simultaneously handle the input signals with different convolutional filter lengths. This is expected to enhance generalization by averaging the information acquired by different filters and this effect is studied for experimental generalization.

Generally, in CNNs the user must decide on the number of layers, filters and the perceptron classifiers. There is no specific way to do that in advance, so the process has to rely on trial-and-error based on the network learning accuracy. In the present work, different combinations are examined between the network hyperparameters which are the filter length, filter and perceptron numbers as well as the dropout and pooling values. The combinations are formed over a predefined

range for each hyperparameter, also called as grid. This way of testing a network by trial-and-error is known as grid search. The grid-search ranges for both the *multi-headed* and *single-head* CNNs are shown in **Table 3.4** and **Table 3.5** respectively. For every network hyperparameter, the range of tested values appears in brackets. Each value is tested with all combinations with values shown in the other brackets. Every combination is restarted 10 times to minimize the effect of random BP initializations (described in section 2.3).

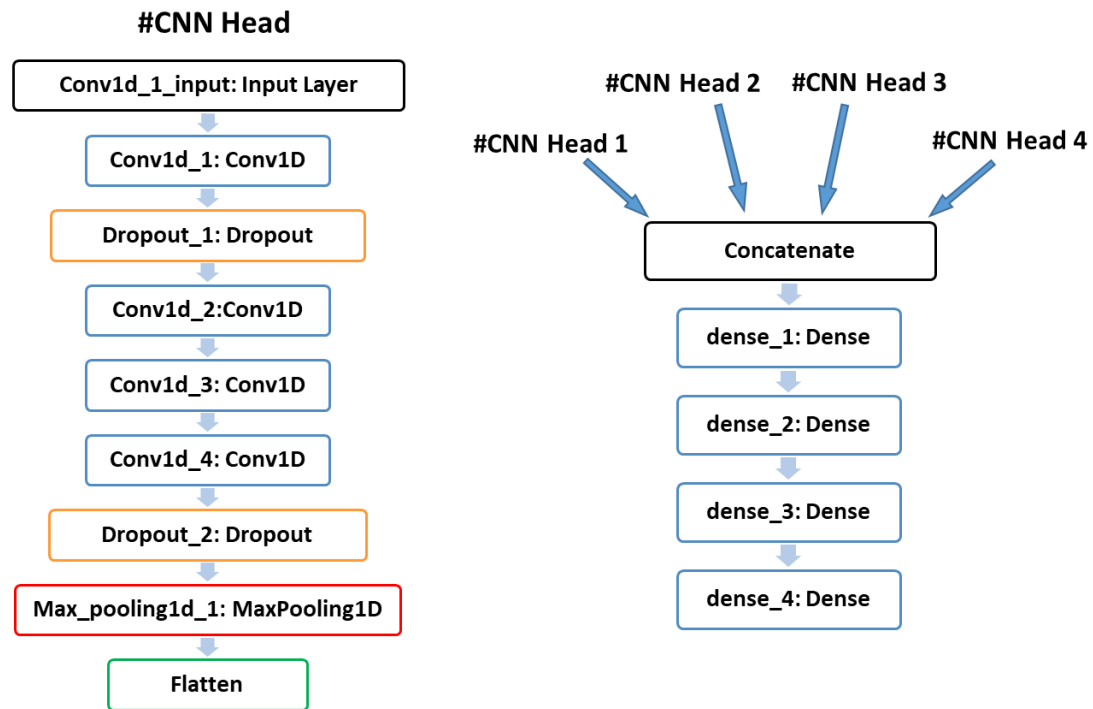


Figure 3.5: CNN head architecture (left) and 4-headed CNN (right)

For the *multi-headed* CNN, it has to be highlighted that the allowed filter length ranges were deliberately chosen different between the first and second “head” pair. The first pair can have a filter length of 12, 10 or 8 time steps while the second one 6, 4 or 2. That results in possible filter length differences between 10 and 2 time steps between the heads, forcing the network to learn DL features from different signal scales. The full range of 12 to 2 steps filter length was chosen after preliminary testing. CNNs made of *single-heads* were found to effectively learn the FE simulated problem within these values. The filter length range however should depend every time on the specific problem response and it cannot be generalized to all SHM applications. The values of **Table 3.4** and **Table 3.5** are therefore a grid-search fine tuning rather an initial crude approach.

Results from the best 20 networks of the grid search are to be considered though a *committee of machines* averaging, meaning final prediction averaging between multiple trained networks. The candidate CNNs are picked based on their validation accuracy on a randomly chosen set extracted from the learning data. Categorical Cross Entropy was used as learning accuracy metric and stochastic gradient descent was applied with a randomly picked mini-batch size of 50 learning examples and 30 epochs (iterations). Learning was performed on a GTX 1660Ti Graphics

Processing Unit (GPU) with a mean time of 2 minutes for each grid search run. The results of learning on the FE generated data sets of equations (3.2)-(3.5) are presented in the next paragraphs according the DI problem type. The predictions on the corresponding experimental states for the numerically trained CNN classifiers follow both damage problem training results.

Table 3.4: 1D-CNN Grid-Search hyperparameter ranges for the multi-head CNNs

Layer type	Filter length (time steps)	Filter/Neuron numbers	Magnitude/Activation
Convolutional head1	[12, 10, 8]	[12,36]	ReLu
Convolutional head2	[12, 10, 8]		ReLu
Convolutional head3	[6, 4, 2]		ReLu
Convolutional head4	[6, 4, 2]		ReLu
Dropout	-	-	[0.5, 0.4]
Pooling	-	-	[4, 5, 6]
Perceptrons (Dense)	-	[100, 150, 200]	ReLu

Table 3.5: 1D-CNN Grid-Search hyperparameter ranges for the single-head CNNs

Layer type	Filter length (time steps)	Filter/Neuron numbers	Magnitude/Activation
Convolutional	[12, 10, 8, 6, 4, 2]	[12,36]	ReLu
Dropout	-	-	[0.5, 0.4]
Pooling	-	-	[4, 5, 6]
Perceptrons (Dense)	-	[25, 50, 100]	ReLu

3.4.1 Binary Damage Identification Training and experimental validation

In this paragraph the learning results and experimental validations from *multi-head* and *single-head* 1D CNNs with parameters tuned by Grid-Search are shown. Results are presented for the binary DI problem where the task is to separate the Healthy from Damage (1 and 2) states of the beam. The CNN learning results for the data derived from the optimal and the nominal FE are shown in **Table 3.6**. The values reveal a very high learning validation accuracy for all cases indicating that the networks have successfully learned the FE task. The goal is that the FE trained networks generalize well on real measurements as well.

Continuing to the experimental validations, the trained network class predictions scores are shown in **Figure 3.6** and **Figure 3.7** according the FE model learning data. All inputs for the class prediction scores are derived from sets (3.6)-(3.8) as follows.

Table 3.6: Learning results for the multi-head and single-head 1D CNN architectures on the binary DI problem

Learning data set	Number of learning examples	Number of validation examples	Mean learning validation accuracy of best 20 grid-search runs for the “multi -headed” CNNs	Mean learning validation accuracy of best 20 grid-search runs for the “single -headed” CNNs
<i>SoptBin</i> set (3.2)	4500	500	91.56%	91.75%
<i>SnomBin</i> set (3.4)	4500	500	91.85%	92.18%

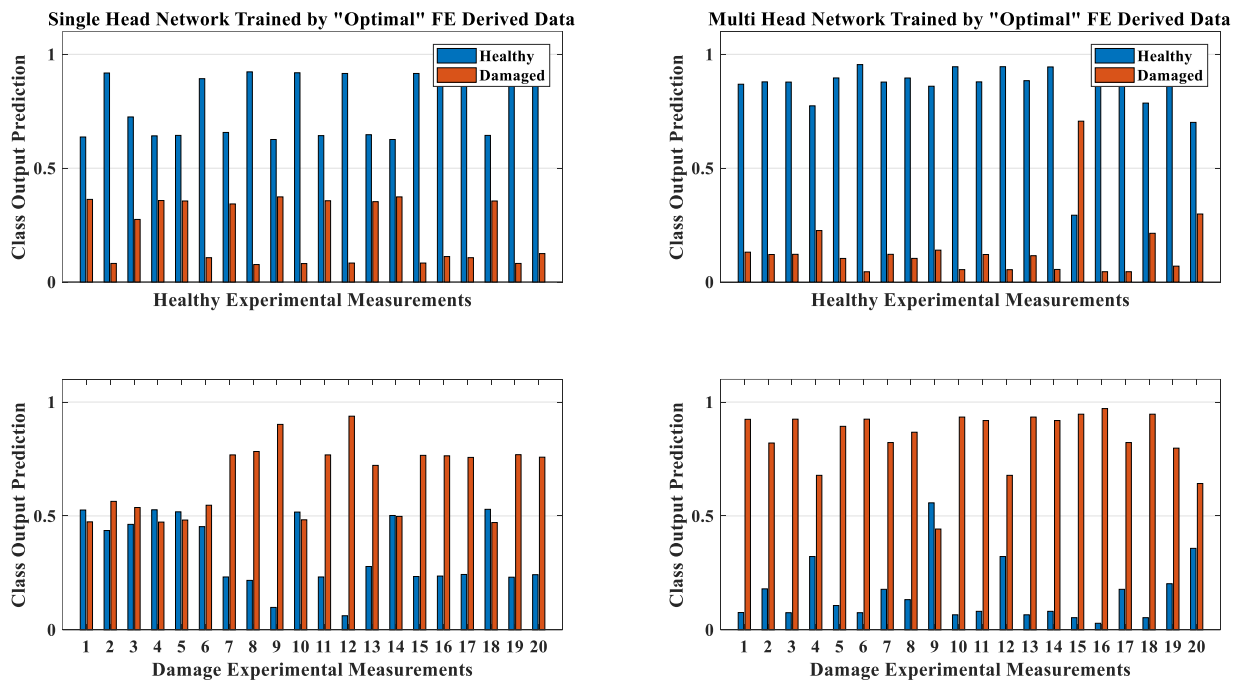


Figure 3.6: Class predictions on experimental Healthy (up) and Damaged (below) inputs. Results on single (left) and multi (right) filter architectures from optimal FE training data

The top charts in each of figures, show the class prediction scores for inputs fed from the experimental measurements set 14, which are Healthy benchmark states. Bottom charts, show class predictions from the Damaged benchmark state measurements, drawn equally from experimental sets (3.7) and (3.8). Left and right results are separated by the network type, “single” or “multi-head” respectively. The network prediction scores come in values between 0 and 1, with 0.5 being the class threshold. Blue is used for the Healthy class score that the network predicts and red for the Damaged. The sum of the blue and red column is always equal to 1 in the network output.

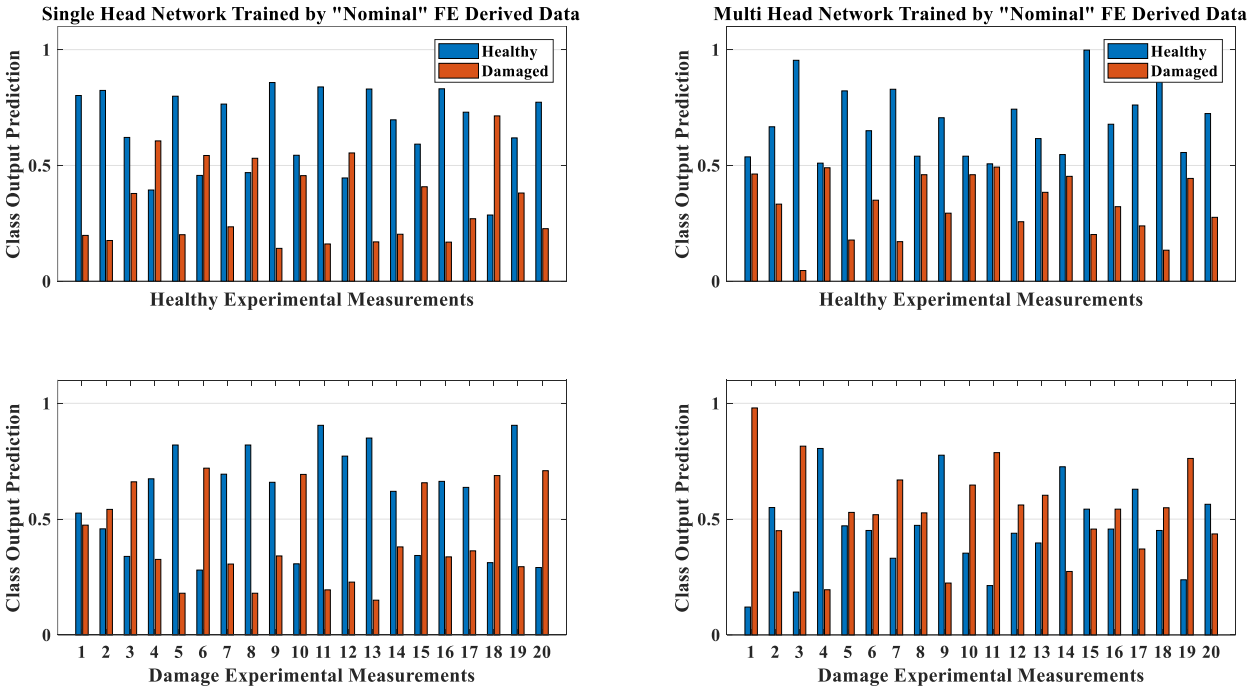


Figure 3.7: Class predictions on experimental Healthy (up) and Damaged (below) inputs. Results on single (left) and multi (right) filter architectures from nominal FE training data

Except the visualized 20 measurements, the complete class prediction scores for 100 experimental inputs are summarized in the confusion matrices of **Figure 3.8**. The correspondence of class predictions and inputs in the matrices is the same as in **Figure 3.6-Figure 3.7**. Healthy class targets correspond to 100 inputs from set (3.6) while damaged from sets (3.7) and (3.8) in 50 measurements each. The elements of the confusion matrices can be explained as follows. Diagonal elements contain the numbers of correctly classified cases (along with their percentage) while off-diagonal elements always show misclassified ones. Bottom diagonal element shows the overall accuracy (in green) and loss (in red). Right columns show precision (in green) and false discovery rate (in red). Bottom rows show recall (in green) and false negative rate (in red).

The *multi-headed* networks trained by the optimal FE data set *SoptBin* recorded the best scores and “single-head” trained by the nominal set *SnomBin* the worst as expected. The latter produced highly biased predictions towards the Healthy class. Having an optimal model showed to be more important than a *multi-head* architecture for this binary problem. The *single-head* network trained by *SoptBin* recorded slightly better scores than *multi-headed* by *SnomBin*. Nevertheless, the *multi-headed* DL classifier managed to give acceptable results, with a lowest accuracy of 67% even when trained with nominal FE derived data. It has to be highlighted again that the small magnitudes of damage imposed on the benchmark and the combination of random base excitations pose a difficult DI problem. The multiple filter length architecture however, showed to be learning adequately representative features, even with nominal FE data, compared to the unreliable results when single filter classifiers were used.



Figure 3.8: Confusion matrices of the network class predictions on the experimental measurements for the binary DI problem according to FE model learning data and network architecture

The reader should also notice that the network learning validation accuracy is not in line with the experimental prediction accuracy. Especially for the *single-head* network trained by nominal FE data, where the high learning accuracy of 93% shows that it has learned successfully the FE task, however this is not reflected at all on the real set-up. Optimal FE model and wider DL features by multiple filter lengths can therefore close the gap between real and simulated responses.

3.4.2 Multiclass Damage Identification and experimental validation

In this paragraph, the learning and experimental validations from the *multi-headed* 1D CNN with parameters tuned by Grid-Search is shown for the multiclass DI problem. After the FE data training, the task this time is to separate all 3 benchmark states, Healthy, Damaged 1 and Damaged 2 in a corresponding 3 class problem. The learning results for data derived from the optimal and the nominal FE are shown in **Table 3.7**.

Table 3.7: Learning results for the 1D-CNN for the multi and single head architectures on the multiclass DI problem

Learning data set	Number of learning examples	Number of validation examples	Mean learning validation accuracy best 20 grid-search runs for the “multi -headed” CNNs	Mean learning validation accuracy best 20 grid-search runs for the “single -headed” CNNs
<i>SoptMulti</i> set (3.2)	6750	750	78.66%	67.35%
<i>SnomMulti</i> set (3.4)	6750	750	78.47%	83.57%

The values calculated show immediately that the multiclass DI is more demanding than the binary of paragraph 3.4.1 with CNNs having lower learning validation accuracy on the FE derived datasets. However, validation accuracies close to 80% are recorded (except the optimal FE data “single-head” CNN) meaning that networks have adequately learned the task and can potentially perform well on problem. The experimental data sets this time are the full (3.5-3.7) sets containing each 100 measurements of each benchmark state. Class prediction scores from the trained CNNs on the measurements are shown in **Figure 3.9** and **Figure 3.10** according to FE model learning data derivation. The interpretation of the figures is similar as in paragraph 3.4.1. Top charts represent class scores from Healthy benchmark experimental inputs (set 3.5). Middle charts and bottom charts represent class prediction results from Damage 1 (set 3.6) and 2 (set 3.7) experimental inputs respectively. Left charts show *single-head* network predictions while right ones *multi-head*. Class score this time is again between 0 and 1, while the total sum of the 3 classes is equal to one. The class is predicted according to highest score. Except the visualized 20 measurements, the confusion matrices for the total of 300 measurements, 100 of each set (3.5-3.7), are also shown in **Figure 3.11**. The results in the matrices are presented in the same way as in paragraph 3.4.1.

The *multi-headed* network trained from the optimally FE derived set *SoptMulti* manages to record again the best predictions, with 83.3% global accuracy. Separating the Healthy state from the Damage 2 state appears as the most demanding and difficult, with false Damage 2 predictions of 16% in the Healthy benchmark measurements and 29% false Healthy in the Damage 2 measurements. Damage 1 measurements on the other hand, appear to be predicted in a solid manner with a true positive accuracy of 96%. For the *multi-headed* network trained by the nominal FE derived data set *SnomMulti* the predictions picture is substantially different. The total accuracy on the experimental data is 65.3% and even though the Damage 1 states are predicted with 100% accuracy the network cannot separate states in an acceptable degree. A false Damage 1 prediction rate of 56% exists in Healthy measurements while a false rate of 31% Healthy predictions is included in the Damage 1 measurements. Single head networks on the other hand, for both FE data combinations, showed poor performance in all cases. The reader may also notice that the *single-*

head networks had problem predicting the class in a decisive way, with low calculated scores for most cases. Therefore, both optimal FE data and *multi-headed* architecture for the multiclass DI appears to be essential.

Useful metrics for comparison may additionally be given with the Receiver Operating Characteristic (ROC) curves [31,138,139] that encapsulate the performance of classifiers on the corresponding problems. The ROC curves of damage detection and macro-average [140,141] for the multiclass problem are given in **Figure 3.12** showing the True Positive against the False Positive Rate as the decision threshold changes. A perfect classifier will have a curve located on the upper left corner of the graph while a curve on the diagonal indicates a classifier that essentially makes random predictions. The ROC curves sum up the previous results showing increase in performance with optimal training data or *multi-head* architecture, indicating their combination as the optimal solution.

Finally, the differences in the FE data learning validation and experimental prediction scores indicate, as in paragraph 3.4.1 that only the *multi-head* networks trained with optimal FE data set manage to generalize correctly on experimental measurements. The *single-head* networks especially, showed high inconsistency between learning and experimental validation scores when trained with the nominal FE data set. It is proved again that learning on the simulated FE problem does not automatically mean good generalization on the real experiment.

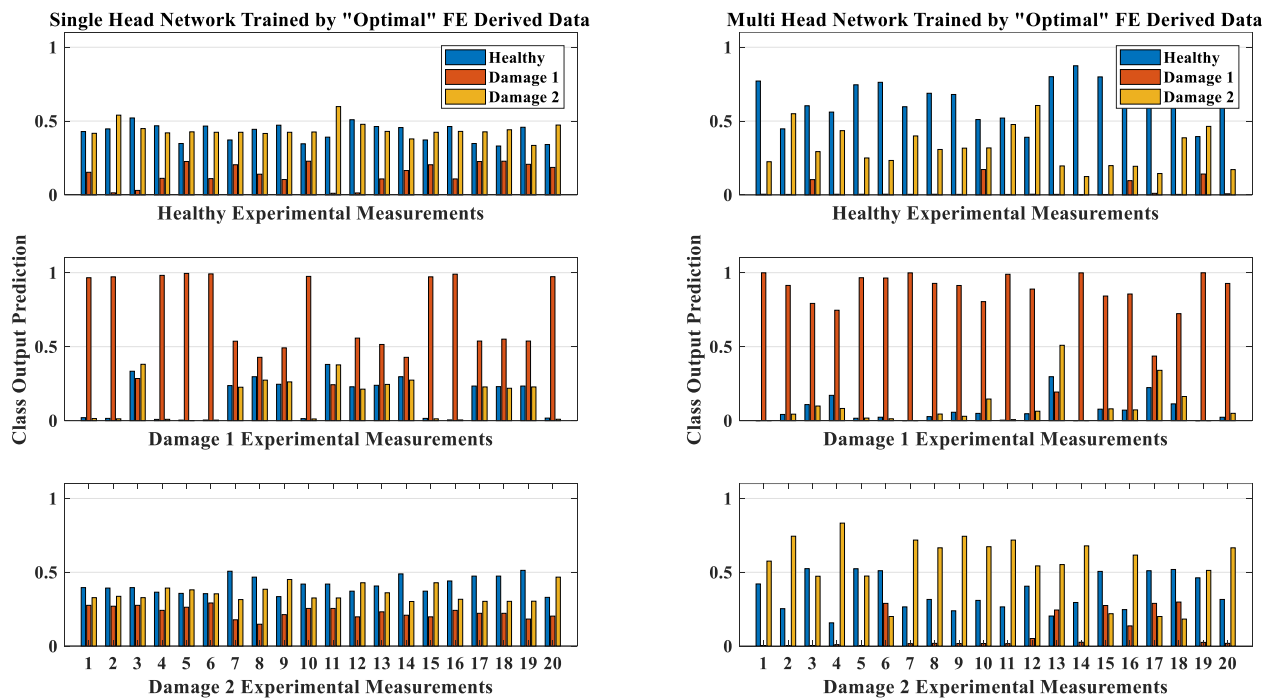


Figure 3.9: Class predictions on experimental Healthy (up), Damaged 1 (middle) and Damaged 2 (below) inputs. Results on single (left) and multi (right) filter architectures from optimal FE training data

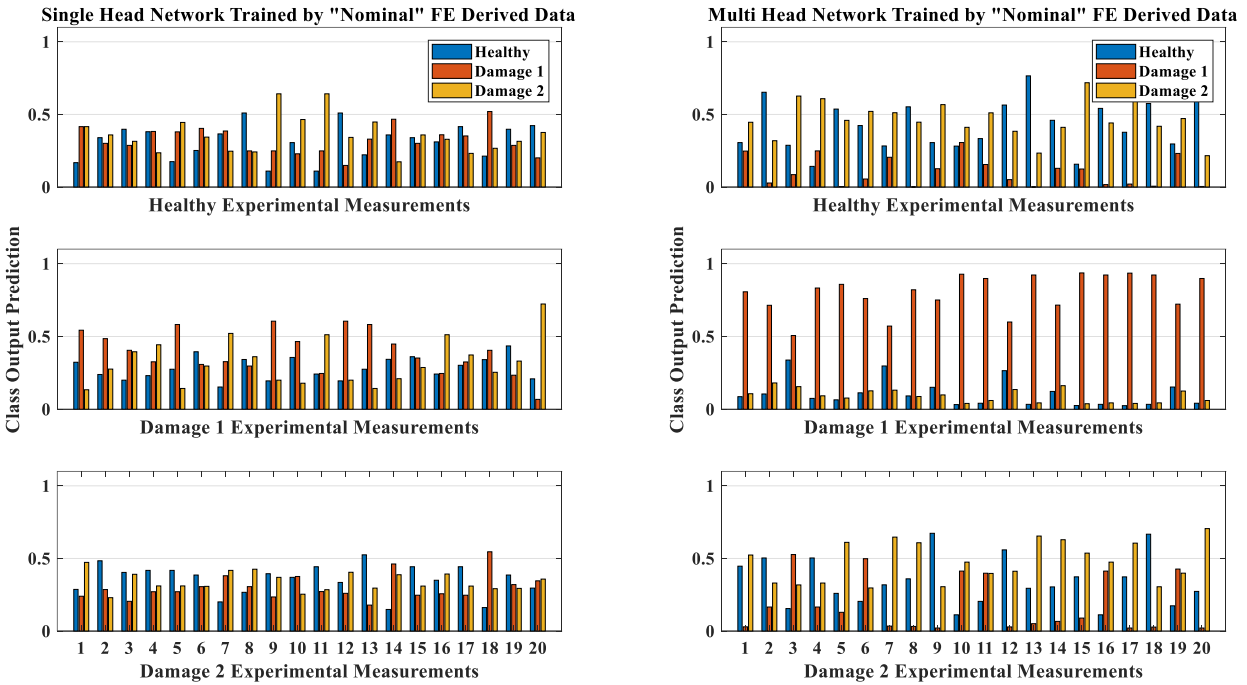


Figure 3.10: Class predictions on experimental Healthy (up), Damaged 1 (middle) and Damaged 2 (below) inputs. Results on single (left) and multi (right) filter architectures from nominal FE training data

3.5 Conclusions

In conclusion, in this chapter a novel SHM method was presented where monitoring and identification of the possible damage is handled by CNN DL classifiers, exclusively trained by numerically generated structural responses. The goal was to showcase the influence of CNN architecture and FE model updating on final experimental generalization.

The trained CNNs were validated on the real benchmark set-up by experimental measurements, in binary and multiclass DI problems. The proposed SHM method was divided in distinct data generation steps and CNN learning. The *multi-headed* CNNs, comprised of multiple parallel filters, can learn useful signal characteristics and can generalize better compared to *single-head* conventional CNN architectures. More specifically, *multi-headed* CNNs trained by simulated data were able to learn features that were validated on experimental measurements, outperforming *single-headed* CNNs.

An expected performance gain on predictions was found when simulated data was derived from optimal FE models that were previously fit to the experimental benchmark. Considering the random excitation and low artificial damage types on the benchmark, demanding DI problems were formed. The necessary learning data however was generated by the optimal FE model of the benchmark replacing demand in experiments and resulting in a robust SHM system. The nominal FE derived data on the other hand, appeared to be inadequate for the demanding multiclass DI

Chapter 3-Conclusions

problem. It was shown that the CNNs trained with nominal FE models can be applied on different data types up to a certain problem difficulty.

Therefore, the initial experimental and computational cost of FE model updating on the healthy states cost of FE model updating can consequently enhance the SHM system performance and aid in reliability. A degree of difference in CNN validation and experimental prediction accuracy was observed in all cases of the DI problems. This indicates that experimental validations are necessary for the moment and the proposed SHM system's accuracy cannot be evaluated from the learning stage for the time being, even for optimally FE derived data. The proposed SHM method will also be tested in larger benchmark structures in the following chapters.



Figure 3.11: Confusion matrices of the network class predictions on the experimental measurements for the multiclass DI problem according to FE model learning data and network architecture

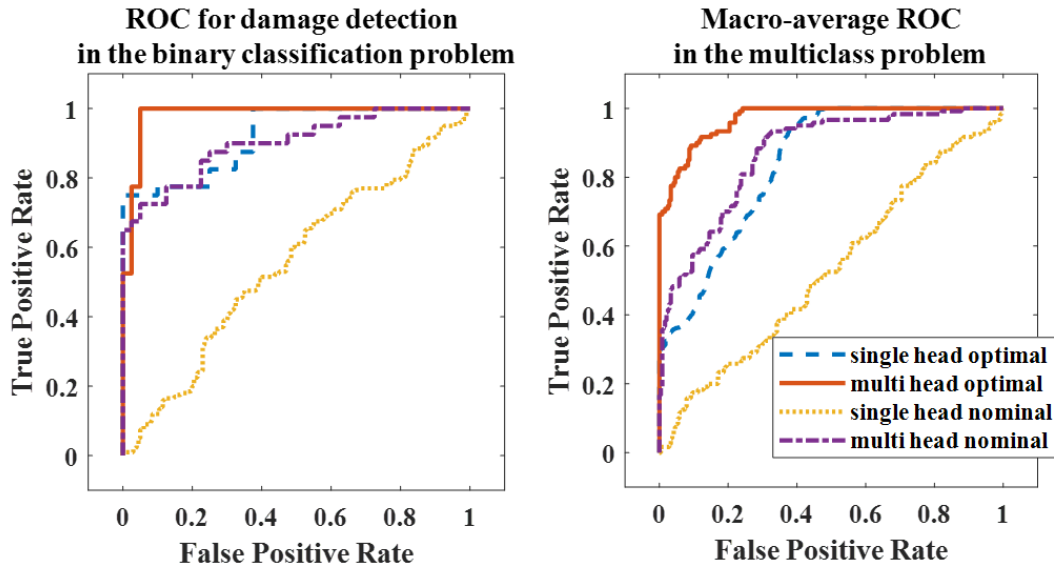


Figure 3.12: Receiver Operating Characteristic (ROC) curves of classifiers on experimental state recognition

Hierarchical Damage Identification with Numerical Data trained Classifiers

Contents from Original Paper [108]: Seventekidis, P., & Giagopoulos, D. (2021). A combined finite element and hierarchical Deep learning approach for structural health monitoring: Test on a pin-joint composite truss structure. *Mechanical Systems and Signal Processing*, 157. <https://doi.org/10.1016/j.ymssp.2021.107735>

ABSTRACT

Structural Health Monitoring (SHM) is an emerging field of engineering with a wide range of applications. The most common SHM strategies operate on structural responses through vibration measurements and focus on training mathematical classifiers which are used after to identify damage in unknown responses. Classifiers may additionally locate damage when adequate labeled damaged data is available. In the present work, a novel SHM method is presented where labeled damaged data is generated through FE models for a pin-joint composite truss structure employing a model-based approach for the problem of data acquisition. The truss is made of carbon fiber reinforced polymer (CFRP) members joint on aluminum connections forming a complex and large FE problem. A Deep Learning (DL) Convolutional Neural Network (CNN) classifier is trained on the FE generated vibration data combined with a hierarchical multiple damage identification and location scheme. The numerically trained CNN is after validated on experimental statuses of the truss in both damage detection and location, proving to be robust and accurate for the considered test case. The potential of hierarchical CNNs with FE based SHM data for multiple damages is investigated in this work and a comparison is given between hierarchical and direct multiclass CNNs. The large performance gains of the former are proven for the studied experimental case highlighting also the importance of SHM system architectures with CNNs

Keywords: Structural Health Monitoring, Deep Learning, Damage Identification, System Identification, FE Model Updating, Carbon Fiber Reinforced Polymers

4.1 Introduction

Goal of the current Chapter is to investigate the method of Finite element (FE) data generation and Deep Learning (DL) classification for damage identification in a more complex structure compared to the simple beam benchmarks of **Chapter 1** or literature sources [109]. A pin-joint truss of carbon fiber reinforced polymer (CFRP) is used, excited by external impacts in multiple damage scenarios. The damage identification problem formulation is investigated with a hierarchical separation to study potential improvements of numerically trained classifiers on experimental generalization.

The healthy state and different damages in terms of compromised pin connections are simulated with FE models of the CFRP truss, previously fit on healthy experimental vibration measurements. The simulated vibration data sets are then used to train a 1D Convolutional Neural Network (CNN) which is trained in a hierarchical damage detection and location approach. A comparison is provided with classifiers trained by direct multiclass damage detection and location to highlight the performance gains of the hierarchical separation. The trained networks are validated on the real structure. The workflow is shown in **Figure 4.1**.

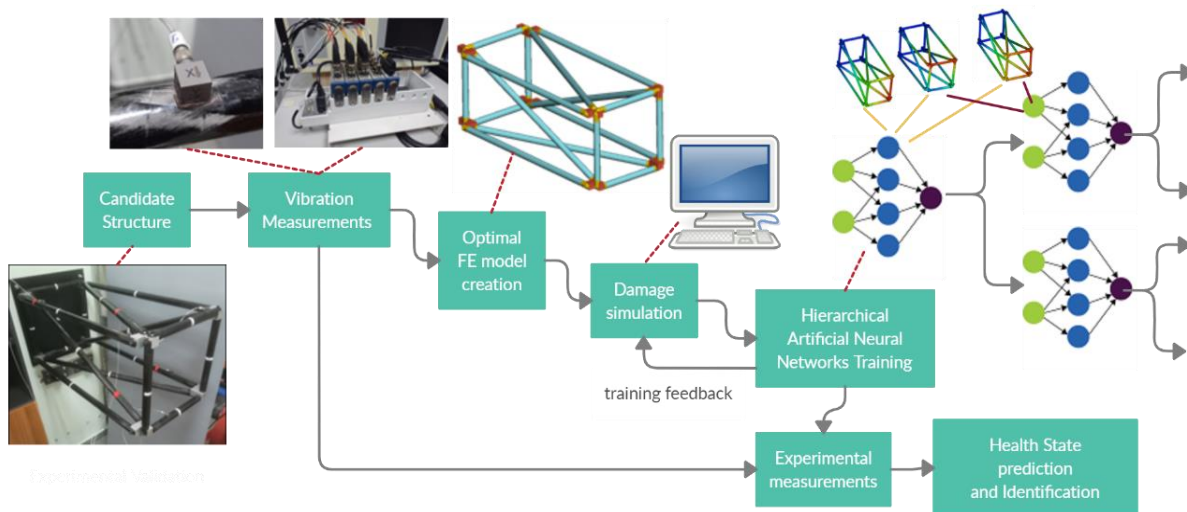


Figure 4.1: Flow chart of the proposed damage detection and identification by simulated damage responses

The chapter follows in section **4.2** that contains the experimental set-up and the process of system identification and updated FE model construction. In section **4.3** the chosen artificial damage types on the physical benchmark are given and the hierarchical SHM problem formulation is also provided. Together, the numerical approximation of faulty pin connections that comprise the damage scenarios in the FE simulations is presented. In section **4.4**, the data generation and the SHM-CNN learning on the simulated vibration data sets are presented. The experimental generalization validations are following. Results are discussed in section **4.5**. The conclusions and findings of this chapter are presented in section **4.6**.

4.2 Experimental Set-Up and Updated Finite Element Model

In this section the experimental SHM set-up is described. The set-up includes a truss structure, which is made by CFRP tubes connected with aluminum joints. On each tube end, aluminum connection parts are glued permanently forming a complete truss element. Finally, the truss elements are bolted on aluminum joints using steel fasteners and the structure is anchored on flat steel plate parallel to the ground, on a vertical concrete column, shown in **Figure 4.2**.

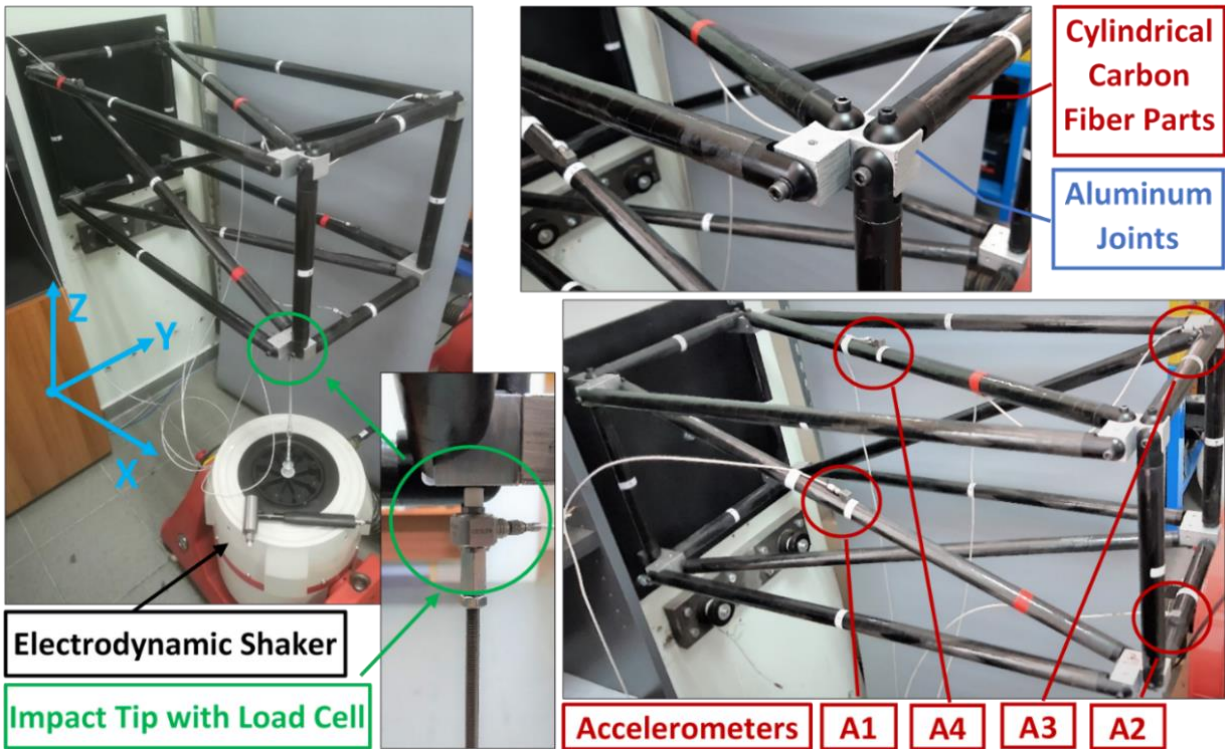


Figure 4.2: Truss structure set-up along with the measuring and excitation equipment

An electromagnetic shaker was mounted on a free end of the frame where a load cell sensor was placed to record the imposed multiple impact forces.

The CFRP tubes were produced by the filament winding process and are consisted of a stack of seven (7) plies with equal thickness and orientation angles apart from one ply. Specifically, plies 1 to 2 and 4 to 7 have a nominal thickness of $t = 0.26\text{ mm}$ at $\theta = 8^\circ$ and $\theta = -8^\circ$ nominal orientation angles consecutively. Ply 3 has a nominal thickness of $t = 0.16\text{ mm}$ at $\theta = 86^\circ$. The nominal material parameters of the 2D orthotropic material used to model the CFRP was $E_1 = 140.360\text{ GPa}$ and $E_2 = 8.684\text{ GPa}$ for the modulus of elasticity in X and Y direction respectively, $\nu = 0.27$ is the Poisson's ration for in-plane bi-axial loading, and $G_{12} = 4.61\text{ GPa}$, $G_{1z} = 4.61\text{ GPa}$, $G_{2z} = 3.035\text{ GPa}$ are the in-plane, transverse for shear in XZ plane and transverse for shear in YZ plane shear moduli and $\rho = 1525\text{ kgr} / \text{m}^3$ is the density.

For the measuring equipment of the set-up, four (4) triaxial accelerometers are placed on different tubes of the truss. No detailed sensor placement methodology was followed however and the deployed network aims to capture the main bending and torsional mode dynamics. The electrodynamic shaker which serves as the excitation source of the structure is placed below the truss and is mechanically connected with a rod. The rod is connected on one end with the load cell which forms a small gap with the lower left aluminum joint of the truss. The shaker may then excite the truss with impacts. An indicative time-force curve for multiple impacts measured at the load cell tip is shown in **Figure 4.3** along with recorded accelerations. The recorded signals may be also used for system identification and model updating on the healthy state. All measurements in this work were performed with a sampling rate of 2048 Hz.

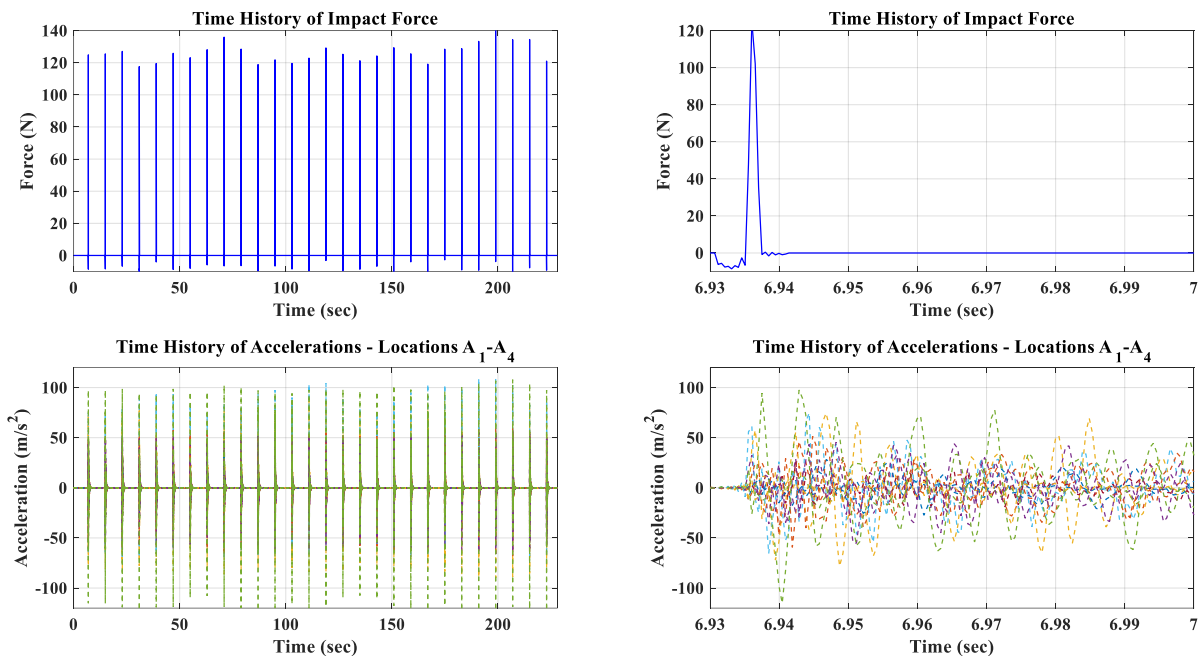


Figure 4.3: Recorded consecutive impact forces on the truss

The system is additionally identified in terms of its natural frequencies and damping after recording the accelerations and input force during a single impact test. The measurements are then used to produce the Frequency Response Functions (FRFs) at different sensor locations. Graphs of the experimental FRFs are shown in **Figure 4.4** for a range of frequencies of 50-200 Hz. The graph reveals that frequencies are not equally spread but are instead grouped between 50-120 Hz and 180-200 Hz.

4.2.1 Updated Finite Element Model

The FE model of the structure was also built in parallel to the measurements using a total of 205.240 triangular shell elements for the CFRP tubes and 1.730.616 tetrahedral elements for the metallic parts, glue and foam that connects them with the tubes. The bolts are modeled as rigid elements that connect the truss connections with the joints. A depiction of the FE model is shown

in **Figure 4.5**. A detailed parametrization of the FE model is also depicted in **Figure 4.6**. The similar truss components are grouped according to their material type and are presented in the same color. The parametrization forms the (13) design variable problem for update with the CMA-ES.

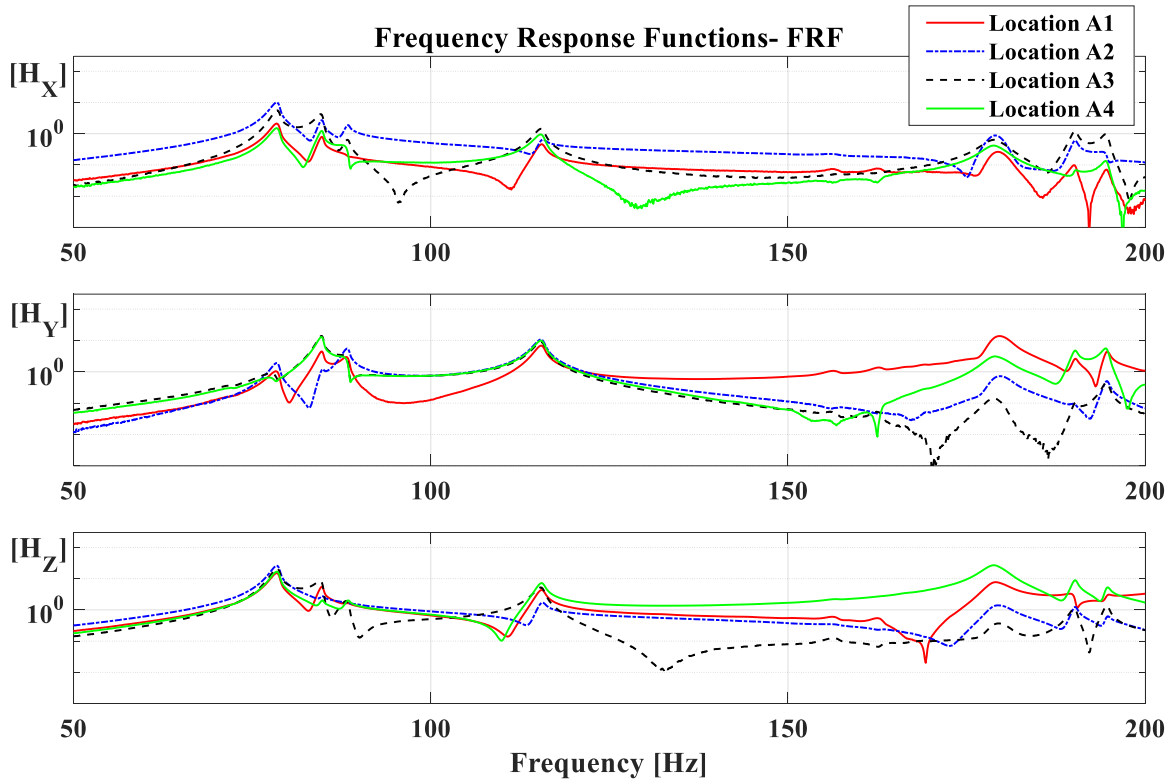


Figure 4.4: Frequency response functions of the healthy truss structure.

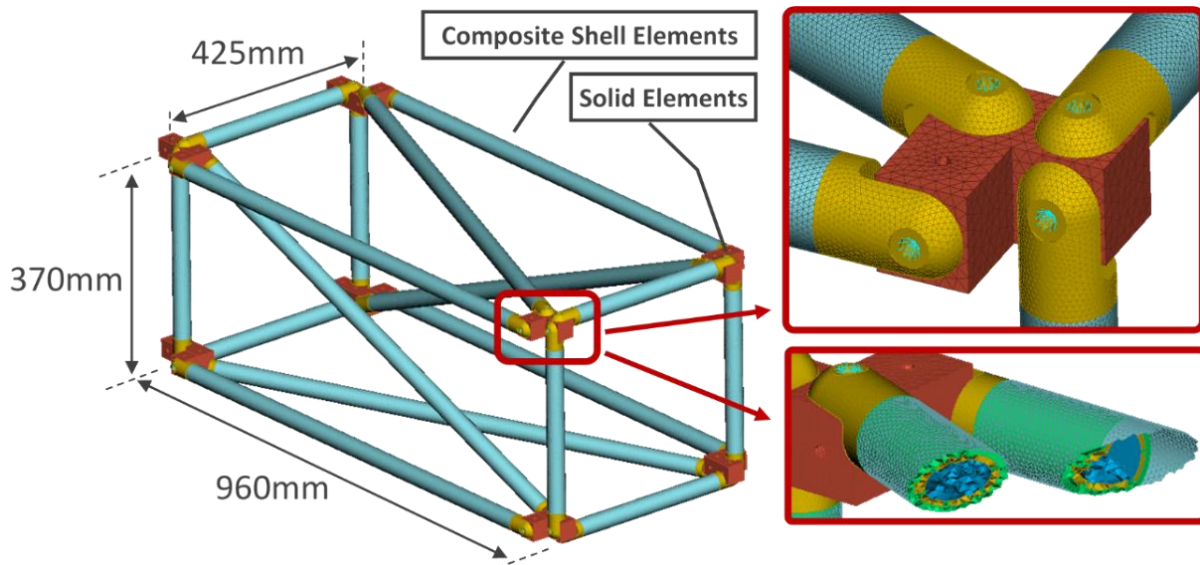


Figure 4.5: FE model of the truss

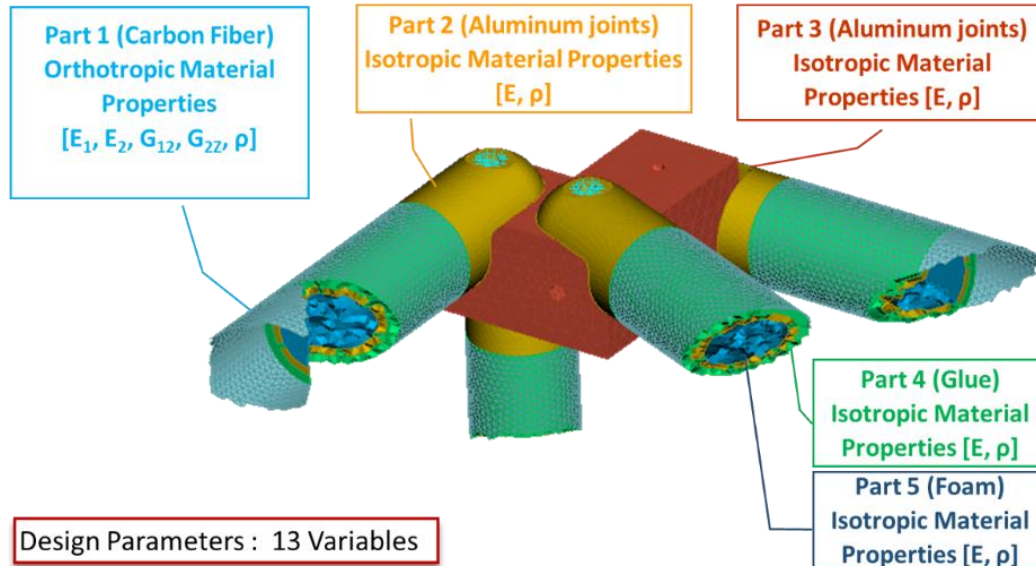


Figure 4.6: Parametrized FE model in different parts according to color and design variables

The parametrized nominal FE model is updated based on the fit with the experimental acceleration time responses according to the minimization problem described in equation (2.7) of Chapter 2. A single experimental impact and response as in **Figure 4.3** were recorded for the updating. The commercial FE code Nastran solver SOL112 for transient modal analysis was used in combination with CMA-ES. The converged material values that represent the best fit to the experimental results are presented in **Table 4.1** for each part of the assembly. A comparison between experimentally identified and updated frequency values along with the calculated difference is finally given in **Table 4.2**. Errors less than 5% on the frequencies are noted for the updated FE model. Also, the experimentally identified modal damping ratios pertaining to the first seven (7) eigenmodes are shown in Table 4.2. The damping ratio used in the FE analysis, without loss of accuracy is 0.5% for the frequency range 0-200Hz. The Modal Assurance Criterion Analysis (MAC) analysis is used to determine the similarity of the first seven (7) mode shapes between Optimal and Nominal FE models. The MAC matrix is presented in **Figure 4.7**, and it appears that the modes 1-4 are identical, while the modes 5-7 are different.

The updated FE model is finally validated on experimental time response measurements on acceleration histories, as will be used in the later data generation and CNN classification stage. A measured impact time-force history is used as input to the updated FE model and the comparison between experimental and numerical responses for two sensor positions is shown in **Figure 4.8**: Time response comparison between experimental and updated FE time histories for the same impact excitation. The numerical predictions seem to be in good accordance with the experimental values for the directions of motion X and Z. However, for the Y direction the numerical predictions do not follow as closely the experimental measurements. Model error is to be expected of course for such a complex structure of 13 material parameters as well as idealizations that were made for the bolted joints.

The workflow of the proposed methodology follows in the damage problem formulation and faults approximation in the next section.

Table 4.1: Updated FE model material parameters

Part		P1	
Parameter	Bounds	Result	
Modulus of Elasticity in X E_1 [GPa]	[90, 150]	110	
Modulus of Elasticity in Y E_2 [GPa]	[5.00, 10.00]	7.09	
In-plane Shear Modulus & Transverse Shear Modulus 1-Z plane $G_{12} = G_{1Z}$ [GPa]	[4.00, 6.00]	5.34	
Transverse Shear Modulus 2-Z plane G_{2Z} [GPa]	[2.00, 4.00]	2.29	
Density ρ [kg / m ³]	[1200, 1650]	1540	

Part	P2		P3		P4		P5	
Parameter	Bounds	Result	Bounds	Result	Bounds	Result	Bounds	Result
Young's Modulus E [GPa]	[60, 80]	75.80	[60, 80]	62.10	[0.85, 1.15]	1.14	[0.85, 1.15]x10 ⁻³	1.0x10⁻³
Density ρ [kg / m ³]	[2450, 2950]	2650	[2450, 2950]	2482.5	[850, 1150]	983	[85, 115]	100

Table 4.2: Comparison between identified, nominal and updated FE predicted modal frequencies

Mode	Identified		Numerical (before updating)		Numerical (after updating)	
	Frequency (Hz)	Damping (%)	Frequency (Hz)	Error (%)	Frequency (Hz)	Error (%)
1	78.46	0.46	74.96	4.45	77.20	1.60
2	84.93	0.57	80.54	5.18	82.85	2.45
3	87.65	0.67	94.65	7.99	91.70	4.62
4	113.54	0.61	115.7	1.90	114.71	1.03
5	185.58	0.27	204.2	10.03	188.91	1.79
6	190.74	0.24	204.84	7.39	189.60	0.60
7	195.50	0.31	204.87	4.79	194.66	0.43

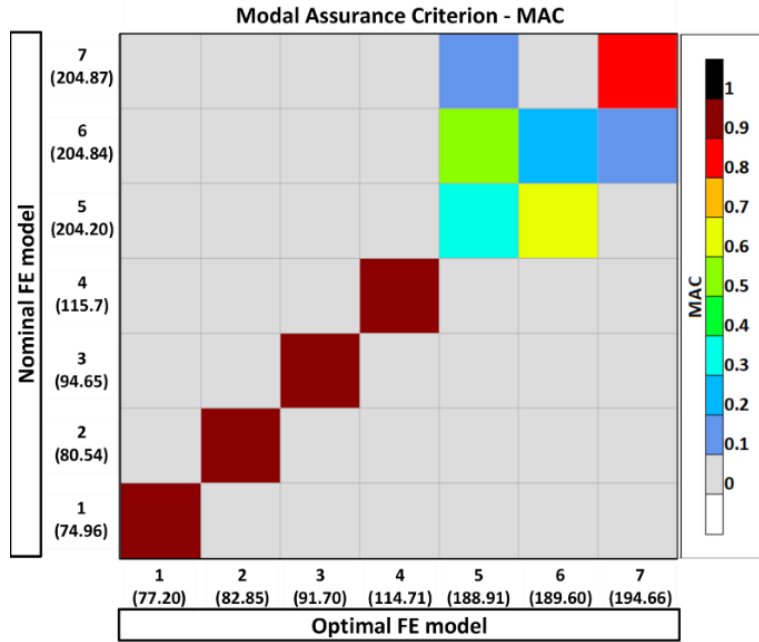


Figure 4.7: MAC Matrix between optimal FE model and nominal FE model mode shapes

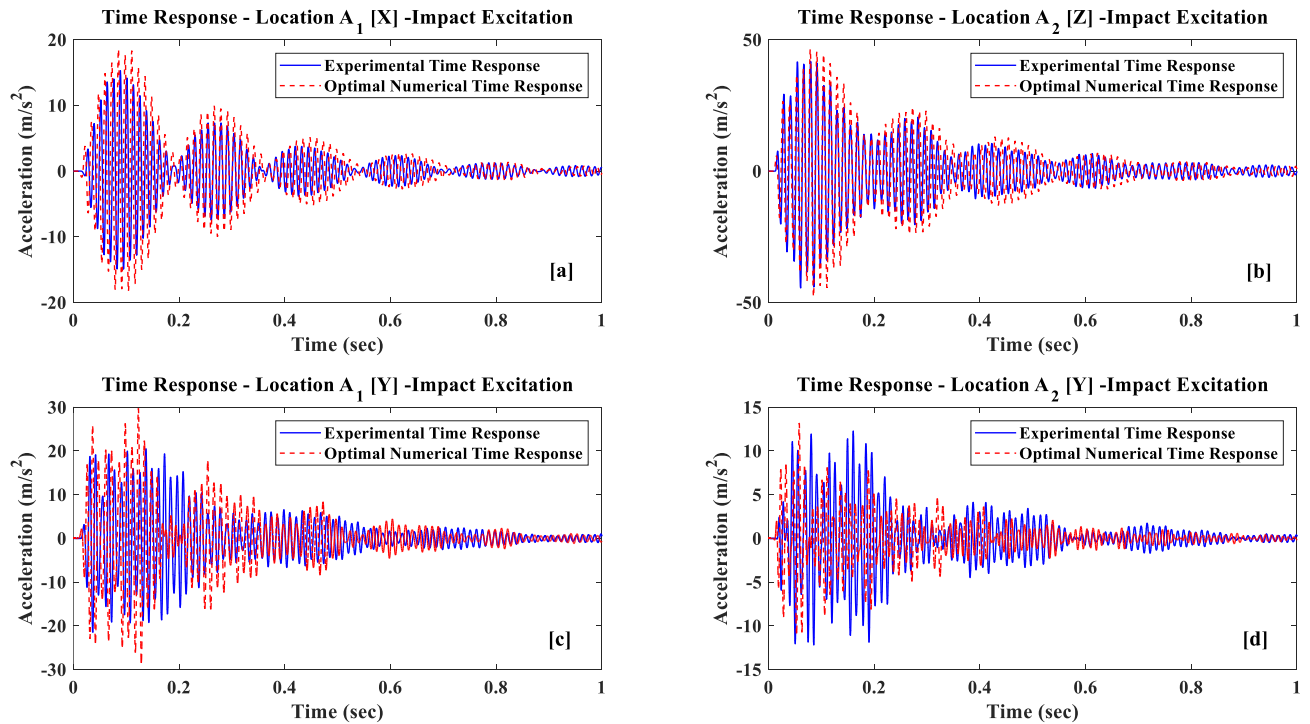


Figure 4.8: Time response comparison between experimental and updated FE time histories for the same impact excitation

4.3 Hierarchical Damage Identification and Faults Simulation

Artificial damage is chosen to be applied on the test truss structure as loose bolts. Bolted connections in SHM [110, 111] and numerical modeling [112, 113] have been already an important and complex subject of study. In a simple way in this work, in order to emulate a faulty connection that also retains some stiffness in a manner of early loosening, rubber O-rings have been used as an interface between the fastener and aluminum connection and joints.

4.3.1 Damage Scenarios

The damage cases considered are synthesized by 8 different fasteners from F1 to F8 on the truss set-up as shown in **Figure 4.9**.

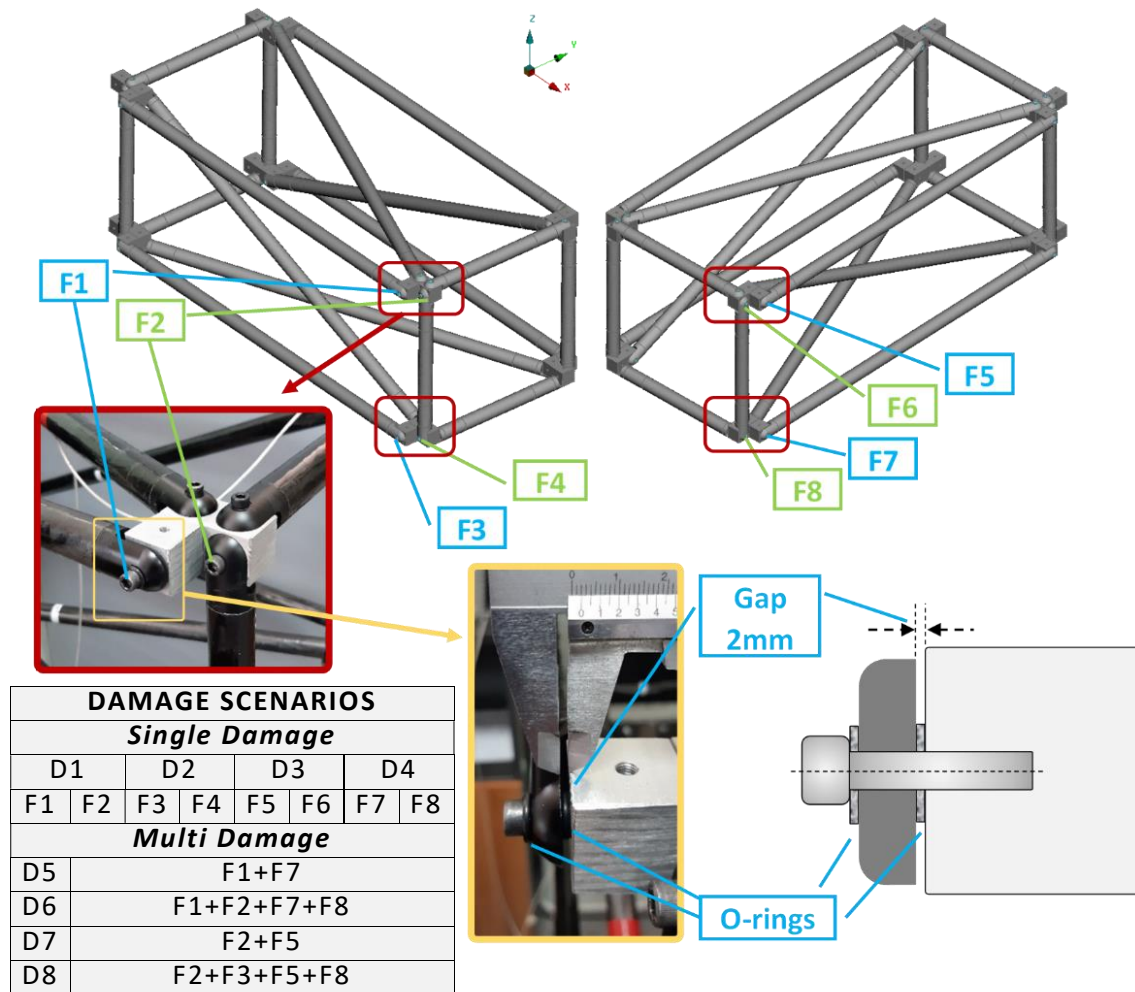


Figure 4.9: Damage scenarios and location description on the truss structure

To examine the performance of the proposed method for the identification of damages of different magnitudes two main damage types are considered. Individual fastener interference with O-rings is applied for the Single Damage scenarios while multiple simultaneous fastener interference is applied for the Multi Damage cases. A gap of 2mm is set for each case to approximate the same

preload on all damage cases. A total number of 8 different damaged state classes is considered, named as D1-D4 for the Single Damage cases and D5-D8 for the Multi Damage cases. For the Single Damage cases, compromised fasteners on the same joint belong in the same D1-D4 class. For example, either F1 or F2 compromised fasteners, appearing therefore one at a time, belong to the D1 damage class as shown in the table contained in **Figure 4.9**. The explained terminology of classes will be used throughout this work.

4.3.2 Hierarchical Damage Identification

The SHM and damage identification problem to be studied is formulated afterwards hierarchically in four stages as shown in **Figure 4.10**. First the SHM classifier performs binary damage detection meaning separating the properly fastened Healthy state class from the Damaged state class. The Damaged state class may be comprised of any of the 8 damaged classes D1-D8. In the second stage, in case the Damage class is flagged true a consecutive SHM classifier is employed which performs damage separation on whether a Single or a Multi Damage case has been identified. The third and fourth stage classifiers afterwards work independently for Single or Multi Damage cases filtering further groups of classes in a binary separation again until a single prediction from D1-D8 is reached. The same acceleration input signal may be used from the first to the final fourth stage where the exact D1-D8 damage is predicted.

It is worth mentioning that the described hierarchical classification using simple binary separation classifiers instead of a more powerful one with multiple class outputs, has been chosen for its advantages in simpler training and optimization. This may potentially lead in improved prediction performance as reported in different classification problems in the literature [114, 115]. The approach has already drawn attention for SHM applications [116] since SHM is by nature hierarchical in terms of detecting damage in low level diagnostics [117] and providing details for higher level predictions. In this work a multiclass damage detection classifier will also be compared to the hierarchical one in order to investigate the expected performance gains of the former in the proposed framework.

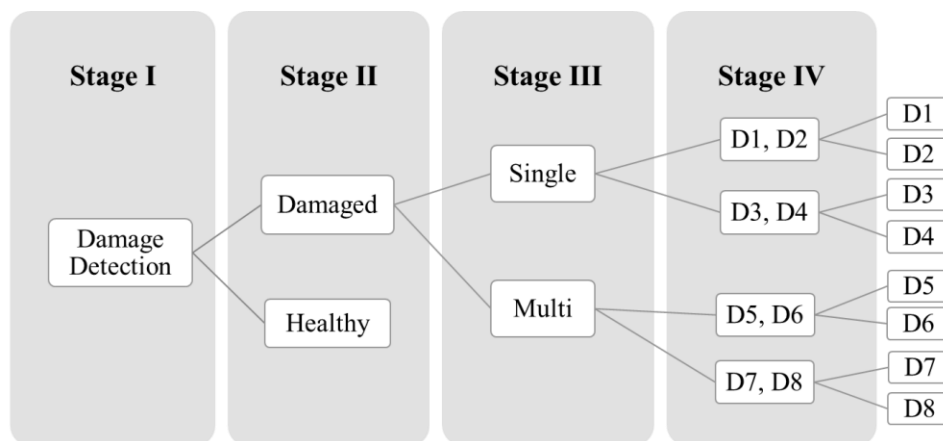


Figure 4.10: SHM hierarchical problem formulation

4.3.3 Finite Element Simulation of Connection Faults

For the simulation of the damages with the optimal FE model, the exact stiffness of the O-ring interface connection would require a complex contact analysis FEM simulation. However, the effect of the connection stiffness may be reflected on the structure's natural frequencies and modes [31,111,118-120] which will diverge from the healthy condition. To account for the lowered connection stiffness, the rigid elements that originally represent the fastener are replaced with a spring element on each of the DOFs on the corresponding bolt according to the damage case (D1-D8). The non-damaged bolt connections are left always as rigid body elements. A wide range of the same value stiffnesses every time on each of DOFs as $k_1 = k_2 = k_3 = k_4 = k_5 = k_6 = k = 0-1000$ (N/mm for translational DOFs and Nmm/rad for rotational DOFs) is to be simulated in the data generation step in order to approximate the damage and teach the subsequent classifier to generalize better. That range was chosen after a typical study of the experimentally measured first four natural frequencies for the case of F6 damage given in **Table 4.3**, compared with model predicted frequencies. The values may suggest that the simulated spring stiffness can be approximated at around $k = 300 N/mm$. However, also up to $k = 1000 N/mm$ the frequencies are diverging from the healthy FE model predictions (**Table 4.2**) which can be approximated at an order of $k = 10^7 N/mm$.

Table 4.3: Comparison between identified F6 damage case and FE calculated frequencies for different simulated connection stiffnesses

	Identified Frequency [Hz]	Frequency FE [Hz] $k = 300 N/mm$	Frequency FE [Hz] $k = 1000 N/mm$	Frequency FE [Hz] $k = 10^7 N/mm$
1	69.9	69.88	76.36	77.15
2	80.38	80.90	82.35	82.8
3	86.7	91.2	91.54	91.7
4	105.7	107.26	108.19	113.7

Figure 4.11 shows a comparison for the first four mode shapes of the truss for healthy state and F6 damage with $k = 1000 N/mm$. The main 4 modes of the truss are still retained as bending and torsion in a similar way as in the healthy state, even though distorted in some degree. A wide sensitivity margin is therefore kept with cases of $k = 0-1000 N/mm$ while still away from the rigid connector stiffness. Finally, to keep a clearer effect of the first four modes in the response, a lowpass filter at 150Hz is used after for all measurements and simulated data that follow in this work.

Except the frequency comparison, the applied damage approximation dynamics are also demonstrated and verified in time responses. In **Figure 4.12** cases of acceleration time series for simulated and experimental F6 damages are shown. In Figure 4.12 (a) the simulated responses are shown while in Figure 4.12 (b) experimental F6 damage is also presented for different gaps other than 2mm, which is the one used throughout this work, in order to show the effect of the O-ring

preload on the real response. Direct comparison in Figure 4.12 (a) between numerical healthy time response with numerical damage with $k = 10^7 \text{ N/mm}$ confirms the very good approximation of the healthy model with a 6 DOF spring at an order of $k = 10^7 \text{ N/mm}$. With reduced order stiffness k the simulated time responses start diverging from the healthy state as expected. The O-ring preload effect in Figure 4.12 (b) shows that using 1mm gap would give a time response that resembles the healthy one and thus will present a much more difficult problem of damage detection and identification. Gaps of 1mm would require further increase of the simulated k stiffness range as shown in Figure 4.12 (c) compared to the $k = 1000 \text{ N/mm}$ simulated case. On the other hand, comparison in Figure 4.12 (d) between numerical damage time response with $k = 300 \text{ N/mm}$ and the experimental 2 mm case confirms the good approximation of the damage model with a 6 DOF spring at an order of $k = 300 \text{ N/mm}$. The more pronounced damage case of 3mm gap may also be simulated with less stiffness k approximated at $k = 50 \text{ N/mm}$ as shown in Figure 4.12 (e). The use of 2mm gaps for the experimental damages is therefore justified as the most suitable case for later stage validations.

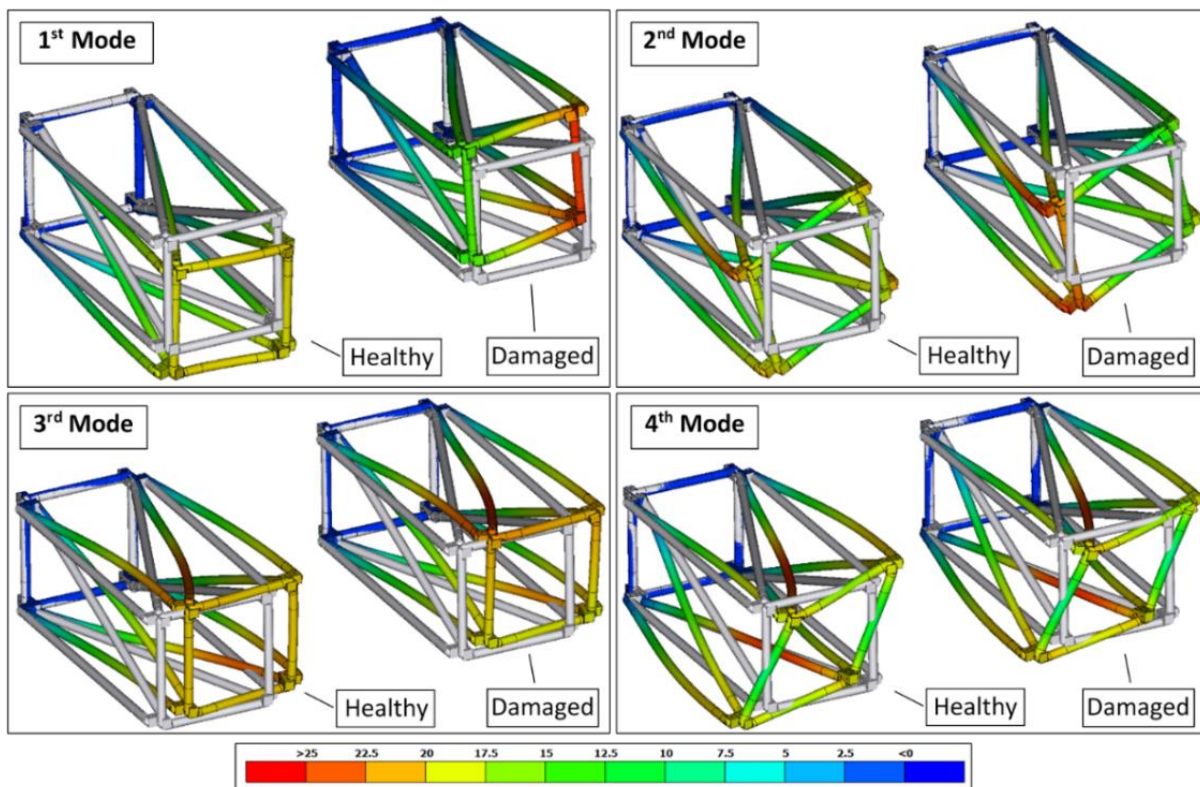


Figure 4.11: First four modes of the truss for healthy state and F6 damage with $k=1000 \text{ N/mm}$

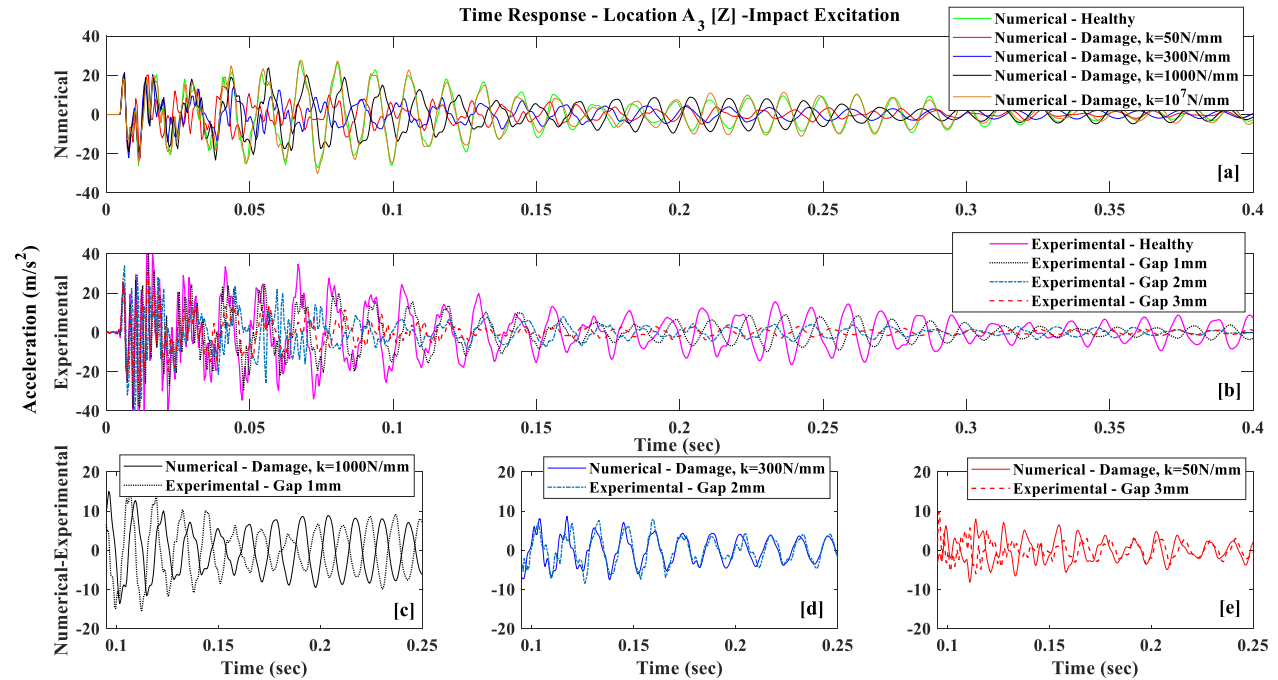


Figure 4.12: Comparison between (numerical and experimental) healthy and F6 damage for different simulated connection stiffnesses and experimental o-ring preload gaps

4.4 Classifier Training and Experimental Generalization

The present section deals with the numerical training data generation with the help of the optimal FE model of the test truss structure. The learning scheme and DL architecture of the proposed SHM classifier is presented after and finally validated on experimental state measurements.

4.4.1 Training Dataset generation

The simulated health condition data is generated with the corresponding status labels for the healthy and damage cases following Algorithm 4.1. The presented algorithm is based on random FE parameters sampling in order to provide uncertainty simulation and enhance generalization as was explained in **Chapter 2**. A transient modal solution is followed on the commercial FE code Nastran SOL 112. Uncertainty is included in all material parameters of the truss parts, being the elasticities and densities, as shown in **Figure 4.6** which are sampled in Algorithm 4.1 from a random uniform distribution with a $\pm 10\%$ deviation from the optimal FE data of **Table 4.1**. Errors of less than 5% were observed in the natural frequencies between the optimal FE and the experimental data of **Table 4.2** and since the considered structure is linear a $\pm 10\%$ deviation is assumed sufficient

A uniform distribution is also chosen as a starting point to sample each parameter with the same probability in order to exclude possible data biases. The parameters are organized in vectors as per part of the structure in Elasticity moduli $\bar{E} = [E_1^1 \ E_2^1 \ G_{12}^1 \ G_{13}^1 \ E^2 \ E^3 \ E^4 \ E^5]$ and densities

$\bar{\rho} = [\rho^1 \rho^2 \rho^3 \rho^4 \rho^5]$. The superscript denotes the part number every time. The same uncertainty simulation of $\pm 10\%$ deviation is used also in Algorithm 4.1 for the modal damping ratios of the FE model which were approximated at 0.5% for each of the eigenfrequencies according to Table 4.2. Damping ratios are included as $\bar{\zeta} = [\zeta_1 \zeta_2 \zeta_3 \zeta_4 \zeta_5 \zeta_6 \zeta_7]$ for each of the identified modes ζ_i of the structure. For the damaged cases F1-F8 the simulated connection stiffness k (see Section 4.3.3) is the final parameter and is sampled from a range of $k = 0 - 1000 \text{ N/mm}$ on the appropriate bolt positions according to the corresponding damage case. The impact excitation is finally created before solving each load case by simulating an impact force peak uniformly sampled between 80-120N and a duration of 0.02-0.03 seconds.

Algorithm 4.1: Numerical model data generation algorithm

Input: Number of load cases n and statistical bounds for each quantity $\bar{E}_j, \bar{\rho}_k, \bar{\zeta}_m, k$

Output: n number of labeled acceleration vectors at preselected FE nodes

for $i = 1 : n$ **do**

define health status y according to FE model $\rightarrow \mathbf{Y}$

If health status damaged replace corresponding bolt/s with spring k

sample \bar{E}_j ($j=1,2..8$) and $k \rightarrow \mathbf{K} = \mathbf{K}(\bar{\mathbf{E}}, k)$

Else

sample \bar{E}_j ($j=1,2..8$) $\rightarrow \mathbf{K} = \mathbf{K}(\bar{\mathbf{E}})$

End if

sample $\bar{\rho}_k$ ($k = 1, 2..5$) $\rightarrow \mathbf{M} = \mathbf{M}(\bar{\rho})$

calculate natural frequencies ω_m and modes Φ_m ($m=1,2..7$) of the structure

sample $\bar{\zeta}_m$

Create excitation force

Solve modal equations of motion [121] and return physical accelerations \mathbf{A} and \mathbf{Y}

end

The extracted acceleration histories \mathbf{A} at the sensor locations are grouped with the status labels \mathbf{Y} . The total simulation time for each load case was 4 seconds. However, signals were reduced to segments of 0.24 seconds corresponding to 500 time steps, sampled randomly between the first 0-600 time steps of the response. An indicative case is shown in **Figure 4.13**. Acceleration signals are also normalized, divided with the maximum value. The status labels on the other hand are organized to binary labels according to the hierarchical classification stage where the learning example is used shown in **Table 4.4**. The labeling corresponds directly to the hierarchical problem formulation described in paragraph 4.3.2. In total 608 cases were simulated for the Healthy class and 400 cases for each D1-D8 class individually. Every classification stage is provided with a balanced number of labels. The learning sets are after used for training of the CNN classifiers.

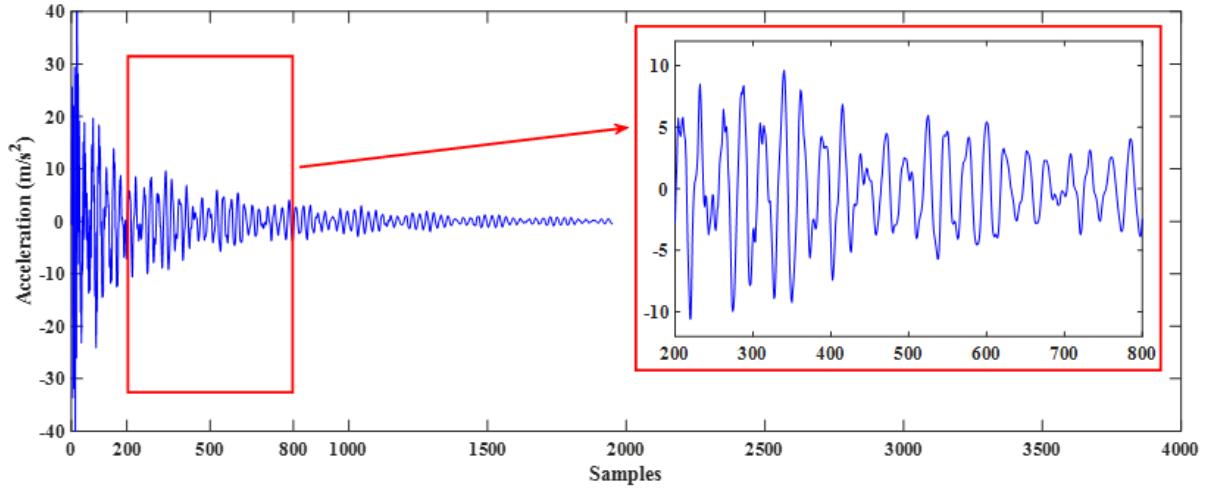


Figure 4.13: Signal training window sampled during the free structure response

Table 4.4: Data sets and classification labels according to hierarchical SHM stage classifiers

SHM	Label	Label
Stage I	608 x Healthy	76 x (D1+D2+D3+D4+D5+D6+D7+D8)
Stage II	400 x (D1+D2+D3+D4)	400 x (D5+D6+D7+D8)
Stage III D1/2/3/4	400 x (D1+D2)	400 x (D3+D4)
Stage IV D1/2	200 x D1	200 x D2
Stage IV D3/4	200 x D3	200 x D4
Stage III D5/6/7/8	400 x (D5+D6)	400 x (D7+D8)
Stage IV D5/6	200 x D5	200 x D6
Stage IV D7/8	200 x D7	200 x D8

4.4.2 Training of Hierarchical Convolutional Neural Network Classifiers

Using the training sets described in paragraph 4.4.1, a CNN classifier is trained for each stage of the hierarchical SHM problem. A *multihead* CNN is used that is made of four (4) independent convolutional filters. A similar architecture was proposed again in [108]. The characteristics of the network are shown in **Figure 4.14** and **Table 4.5**.

The network characteristics such as the number of neurons, filters and filter lengths were chosen over a wide range of parameters through grid search. The simpler or less “powerful” network, using the lowest number of parameters, to achieve good learning scores on the training sets of **Table 4.4** was chosen. The results are presented in **Table 4.6** in terms of mean validation accuracy between 20 randomly initialized backpropagations for each damage detection and identification stage. Gradient descent with 300 epochs with model checkpoint to prevent overfitting and unstable solutions was used throughout. The reader may also notice that only 3 filters per convolutional layer were deployed, however the learning scores indicate that the CNN has successfully learned to classify the FE generated data at all SHM stages with scores exceeding 88% in validation.

The detailed dynamics of training are also given in the curves of accuracy/loss for both the learning and validation datasets in **Figure 4.15** to **Figure 4.16** for each classification Stage. It may be noted in the loss graphs how much more unstable the learning process was for the Stage II and Stage III Single Damage classifiers. That possibly indicates more difficult classification problems for the specific tasks with the given sensors since network capacity and architecture changes did not seem to affect to smoothness of the learning process when different neuron/layer combinations were used. The mean scores of every 20 CNN aggregate is to be employed however as the prediction of each SHM problem Stage to smoothen out results. The trained networks are after validated on experimentally measured inputs in the next paragraph.

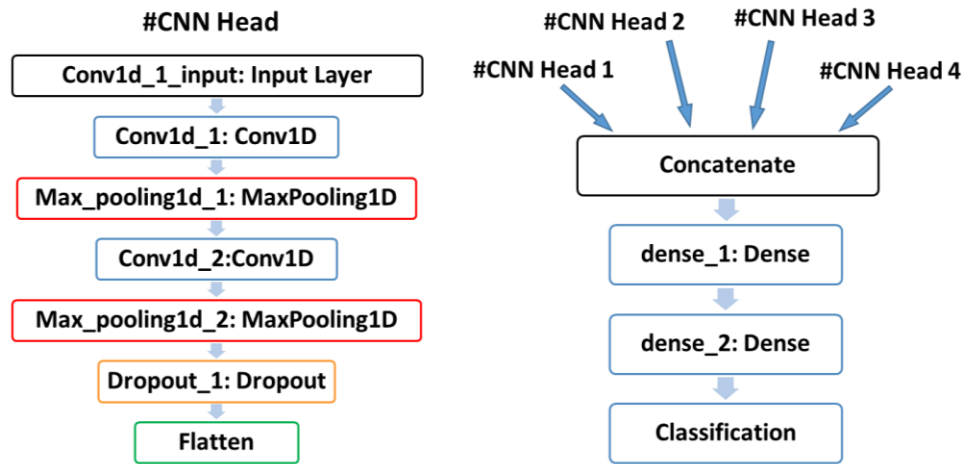


Figure 4.14: *Multihead* CNN architecture of the hierarchical classifiers. Convolutional Head layers (left) and perceptron classifiers (right)

Table 4.5: *Multihead* CNN filters, neuron numbers, activations and loss function for the for the hierarchical classifiers

Layer type	Filter length (time steps)	Filter/Neuron numbers	Magnitude/Activation
Convolutional head1	4	3	ReLu
Convolutional head2	6		ReLu
Convolutional head3	8		ReLu
Convolutional head4	10		ReLu
Dropout	-	-	0.5
Pooling	-	-	2
Perceptron Layers (Dense)	-	20	ReLu
Classification Layer	-	-	Sigmoid/Softmax
Loss Function	Categorical Cross-entropy		

Table 4.6: Learning scores on different SHM classification stages

Learning data set	Number of learning examples	Number of validation examples	Mean learning validation accuracy best 20 CNNs
Stage I	608	608	94.29%
Stage II	1600	1600	93.82%
Stage III D1/2/3/4	1600	1600	95.7%
Stage IV D1/2	800	800	88.83%
Stage IV D3/4	800	800	90.76%
Stage III D5/6/7/8	1600	1600	99.6%
Stage IV D5/6	800	800	98.66%
Stage IV D7/8	800	800	99.5%

Concluding, a multiclass classifier was also trained for comparison with the hierarchical one. The comparison will be given for Single Damage detection and identification since is expected to be the most demanding. All Stages I, II, III and IV are substituted this time by a single CNN which performs the Healthy and D1, D2, D3, D4 identification directly, formulating therefore a 5-class problem. The minimum corresponding CNN architecture increased compared to the hierarchical one in order to achieve again high validation scores. The number of convolutional filters was increased to five (5) instead of (3) per head with the same number of layers, while the number of Dense perceptron layers increased to five (5) instead of (2). In addition, 50 neurons were used instead of 20 per Dense layer. Activation functions remain identical. The same aggregate scheme was used again with a learning set of 600 cases for each class or a total of 3000 as noted in **Table 4.7**. A number of up to 300 epochs were used combined with model checkpoint. The multiclass classifier achieved again a validation accuracy of more than 90%. The comparison with the hierarchical SHM classifiers with therefore be given on how good the generalization to the experimental states is. An unstable loss curve was noted on the learning curves of **Figure 4.17** showing peaks in different epochs in some of the randomly initialized backpropagations. Network capacity and architecture changes did not seem to positively affect the smoothness of the learning process again.

Table 4.7: Learning score of the multiclass classifier

Learning data set	Number of learning examples	Number of validation examples	Mean learning validation accuracy best 20 CNNs
Multiclass separation for Healthy, D1, D2, D3, D4 classes	1500	1500	91.5%

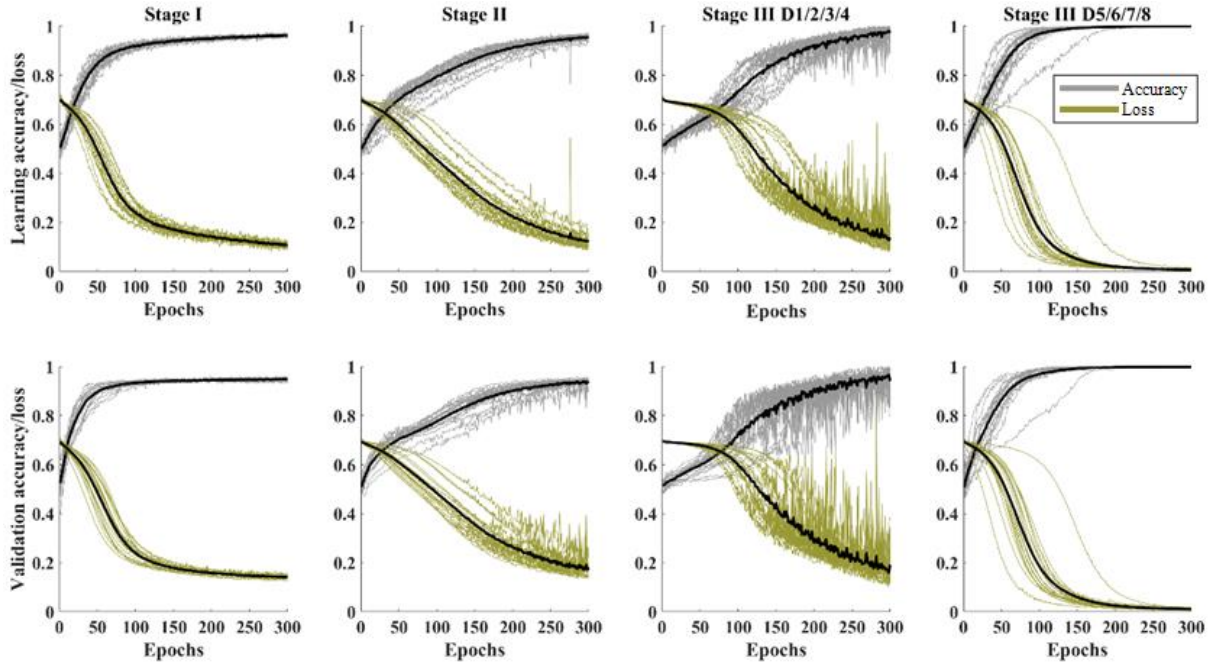


Figure 4.15: Accuracy (grey lines) and loss (gold lines) curves for randomly initialized backpropagations for Stage I, II and III networks

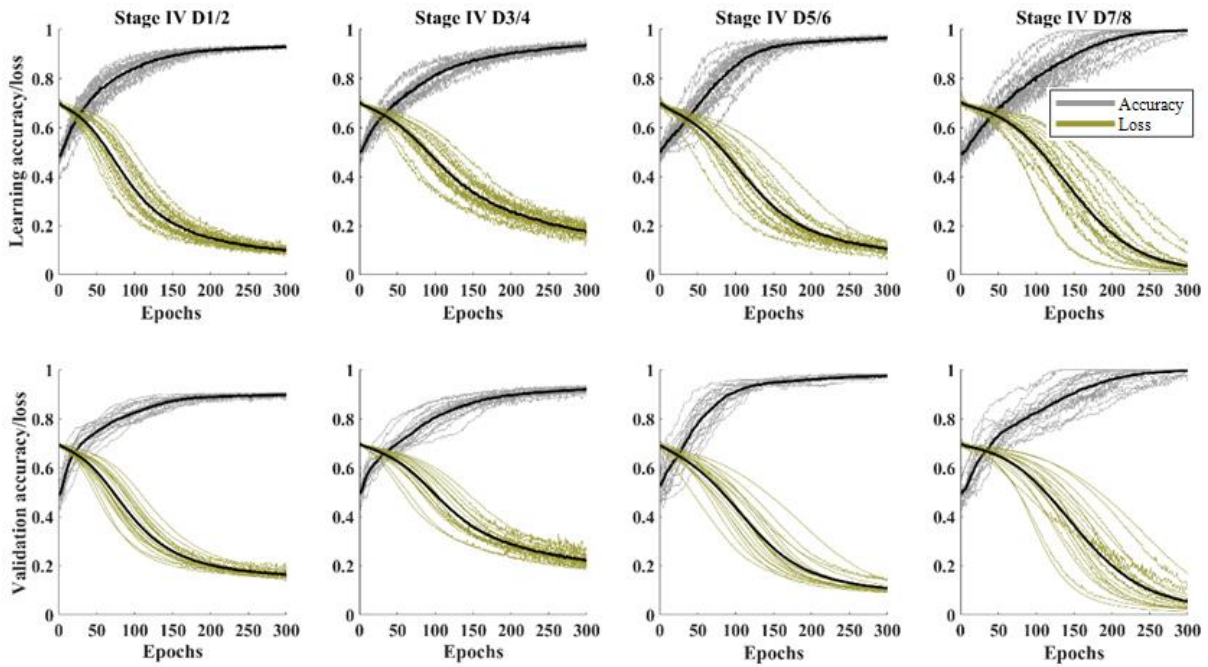


Figure 4.16: Accuracy (grey lines) and loss (gold lines) curves for randomly initialized backpropagations for Stage IV networks

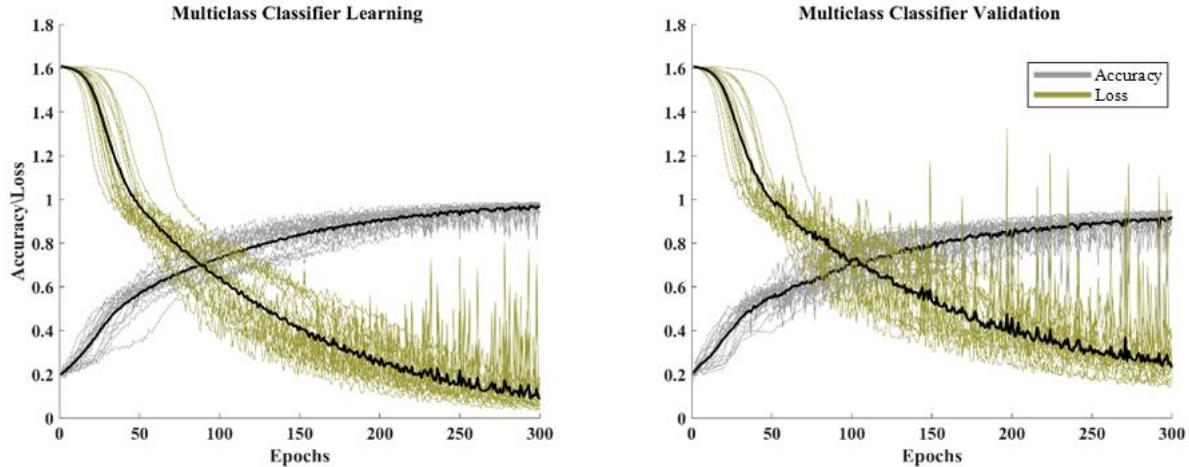


Figure 4.17: Accuracy (grey lines) and loss (gold lines) curves for randomly initialized backpropagations for the multiclass classifier

4.4.3 Results on experimental generalization

The trained CNNs of paragraph 4.4.2 are finally used to predict the experimental status of the truss setup. For Stage I validations the task is separating Healthy from Damaged experimental structure states. Indicative predictions of the Stage I networks on corresponding experimental measurements are shown in **Figure 4.18**. A number of 20 predictions for the same number of experimental inputs are indicatively shown for the Healthy (a) and 10 of each D1-D8 case (b)-(e). For the single Damage classes D1-D4, each of the 10 experimental inputs set consists of equal 5+5 measurements of the two possible individual fastener conditions as was explained in paragraph 4.3.2. The D1-D4 cases predictions are shown in the same manner for the other Stages as well, with equal measurements of both candidate fasteners of each joint. The network prediction scores on the experimental inputs come in values between 0 and 1, with 0.5 being the class threshold. Blue is used for the Healthy class score that the network predicts on the input and red for the Damaged score. The sum of the blue and red column is always equal to 1. The same prediction code is used throughout this work.

For Stage II validations the task is separating Single from Multi Damage states. Indicative predictions on 20 experimental inputs of each D1-D8 state corresponding to Single Damage (D1-D4) and Multi Damage (D5-D8) are presented in **Figure 4.19**. Continuing, for Stage III and IV validations the tasks are separating groups in the Single and Multi Damage cases and finally predict the exact D1-D8 cases respectively. For the Single Damage classifiers, the Stage III and IV predictions for 20 D1-D4 experimental states inputs are shown in **Figure 4.20** and **Figure 4.21**. Damage is grouped in D1/2 -D3/4 groups on Stage III and finally filtered in the individual classes on Stage IV. For the Multi Damage predictions on the other hand the corresponding results are shown in **Figure 4.22** and **Figure 4.23** where damage is initially grouped in the D5/6-D7/8 groups on Stage III before each class is output on Stage IV.

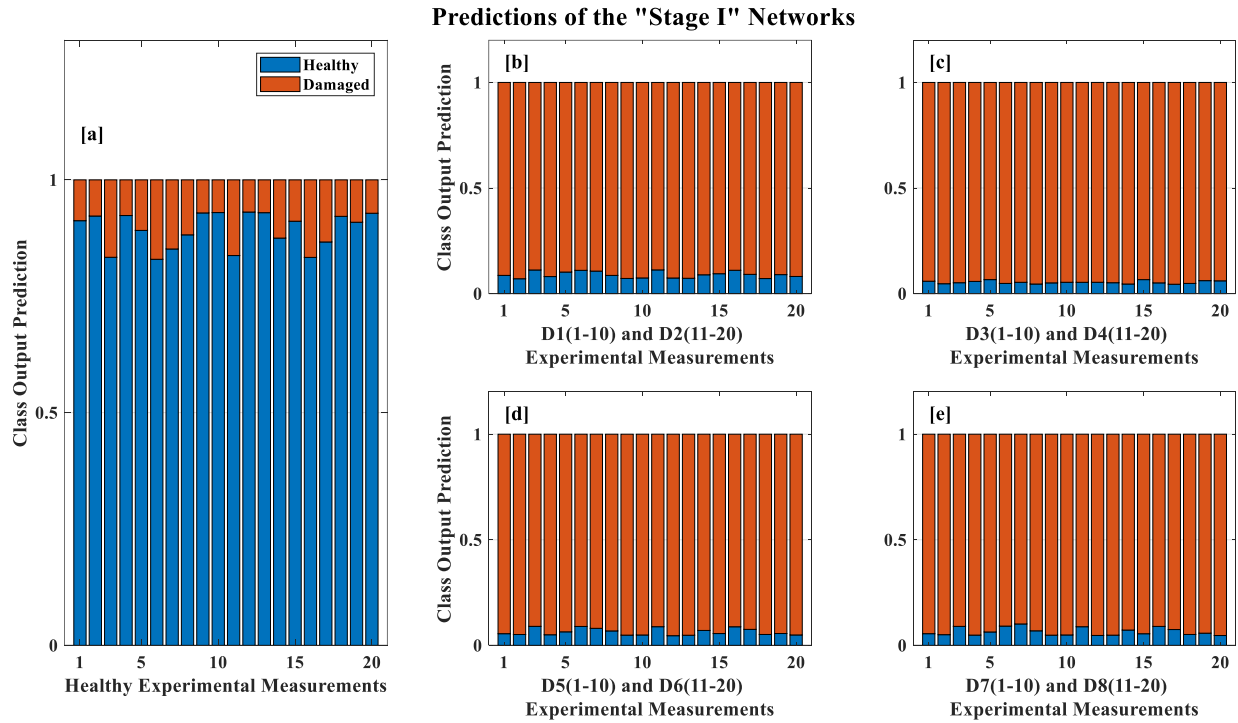


Figure 4.18: Stage I Predictions on the experimental, (a) Healthy and (b)-(e) Damaged state inputs

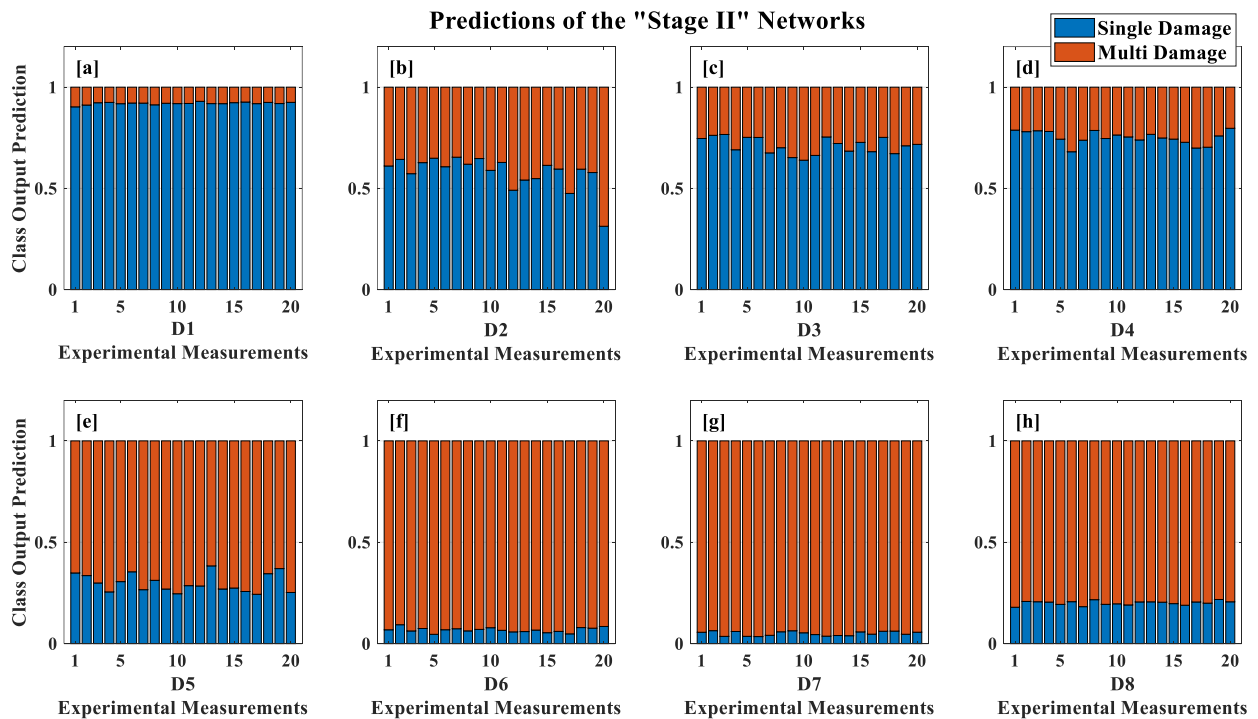


Figure 4.19: Stage II Predictions on the experimental, Single and Multi Damage inputs

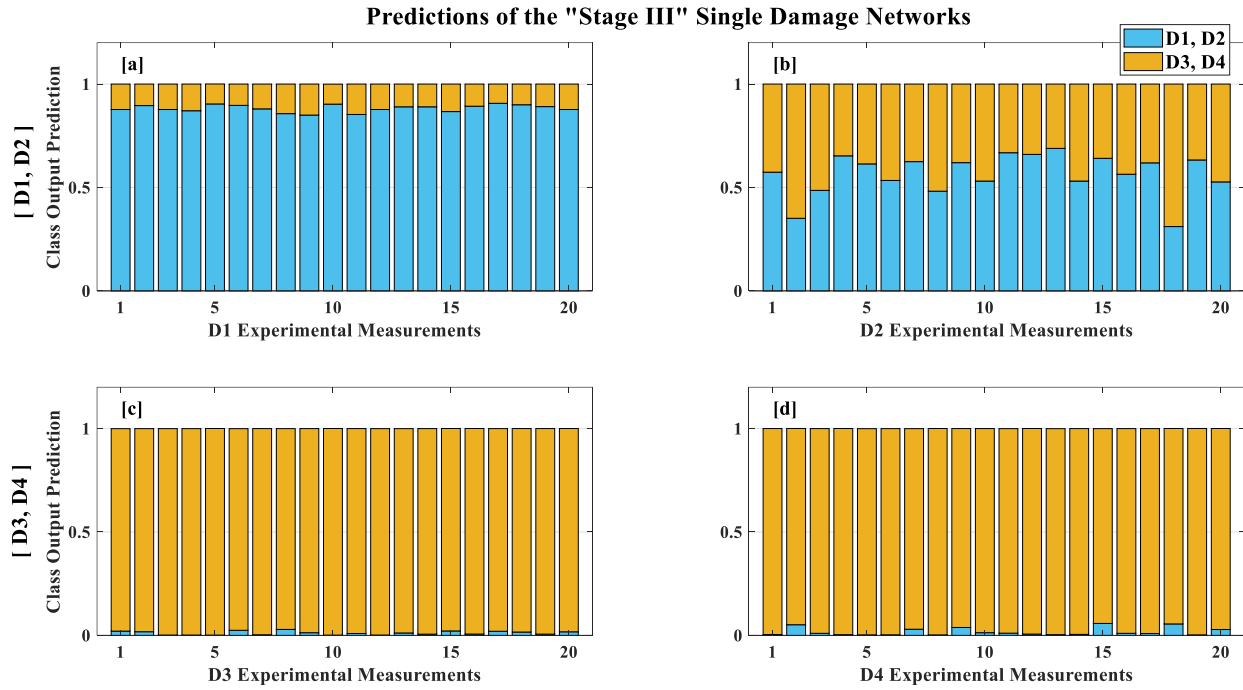


Figure 4.20: Stage III Predictions on the (a) D1, (b) D2, (c) D3 and (e) D4 cases

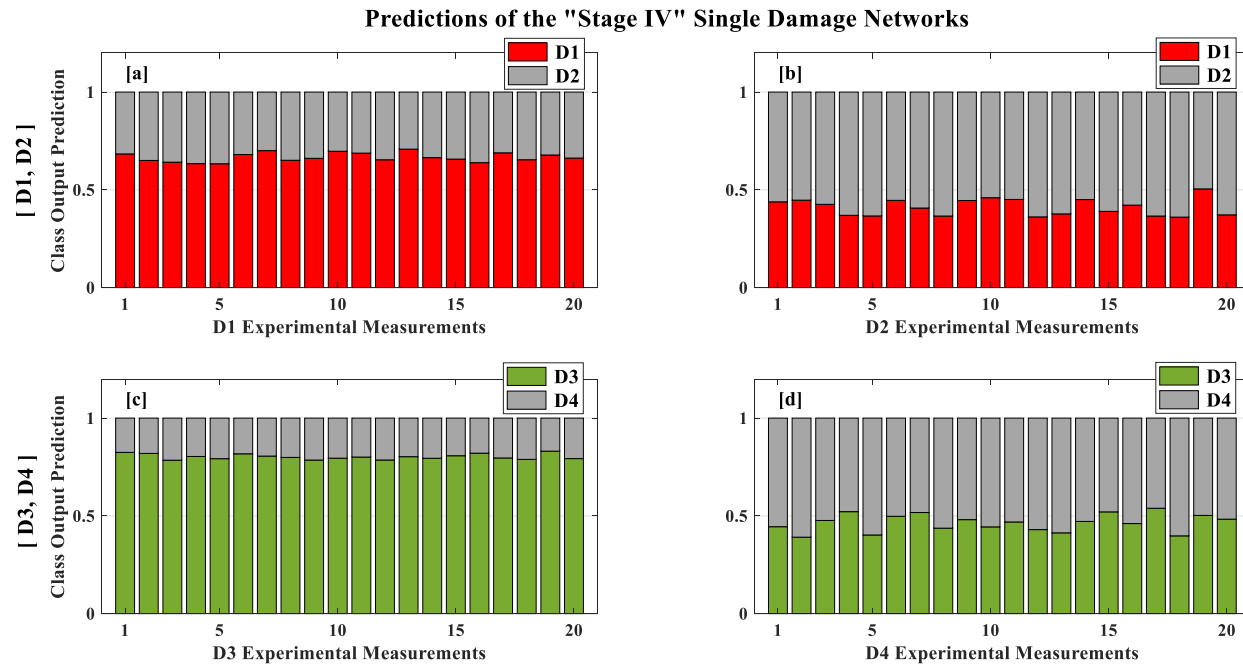


Figure 4.21: Stage IV Predictions on the (a) D1, (b) D2, (c) D3 and (e) D4 cases

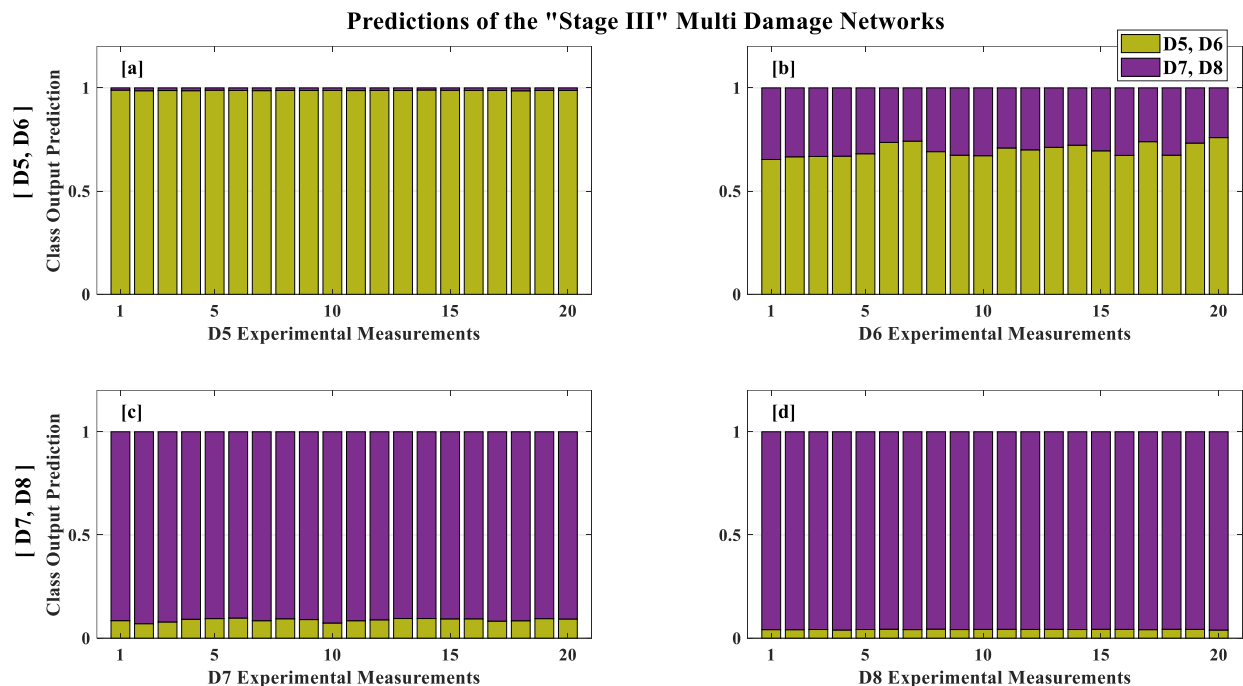


Figure 4.22: Stage III Predictions on the (a) D5, (b), D6, (c) D7 and (e) D8 cases

Finally, for the multiclass predictions the task is separating 5 states of the truss being the Healthy and D1, D2, D3, D4 cases. The results are shown in **Figure 4.24** for 20 inputs for each experimental state as in the same manner as in the hierarchical SHM validations. The total sum of the predicted scores of each class is again equal to one but a 5-color code is used instead.

In addition, the confusion matrices for the hierarchical predictions of all Stages and the multiclass SHM formulation are also presented in **Figure 4.25-Figure 4.28** for 100 measurements for each experimental state. Again, an equal number of each of the possible damaged fasteners on each joint was used for the Single Damage cases inputs D1-D4. The confusion matrices are read as follows. Diagonal elements in bold contain the amount of correctly classified cases while off-diagonal elements in bold always show wrong ones. The percentage of the outputs with respect to the total amount of inputs is contained also below each element. The bottom diagonal element on the other hand shows the overall accuracy (in green) and loss (in red). The auxiliary right column show precision (in green) and false discovery rate (in red). The bottom row finally shows recall (in green) and false negative rate (in red).

The shown scores reveal great differences between the hierarchical and the multiclass SHM problem formulations. The former was able to classify correctly all or almost all of the cases in the various Stages while the latter showed to be unreliable and not able to generalize correctly on the experimental states even though training validation scores were above 90%. The results are discussed in section 4.5. The Receiver Operating Characteristic (ROC) curves are provided additionally in **Figure 4.29** for comparison between the hierarchical and the multiclass approaches. The True Positive to False Positive Ratio in classifiers as the decision threshold changes is summed

up. Curves on the upper left corner indicate the optimal classifier compared to curves approaching the diagonal, that shows a random prediction classifier. Macro-averaging has been used to compare the binary problems with the multiclass.

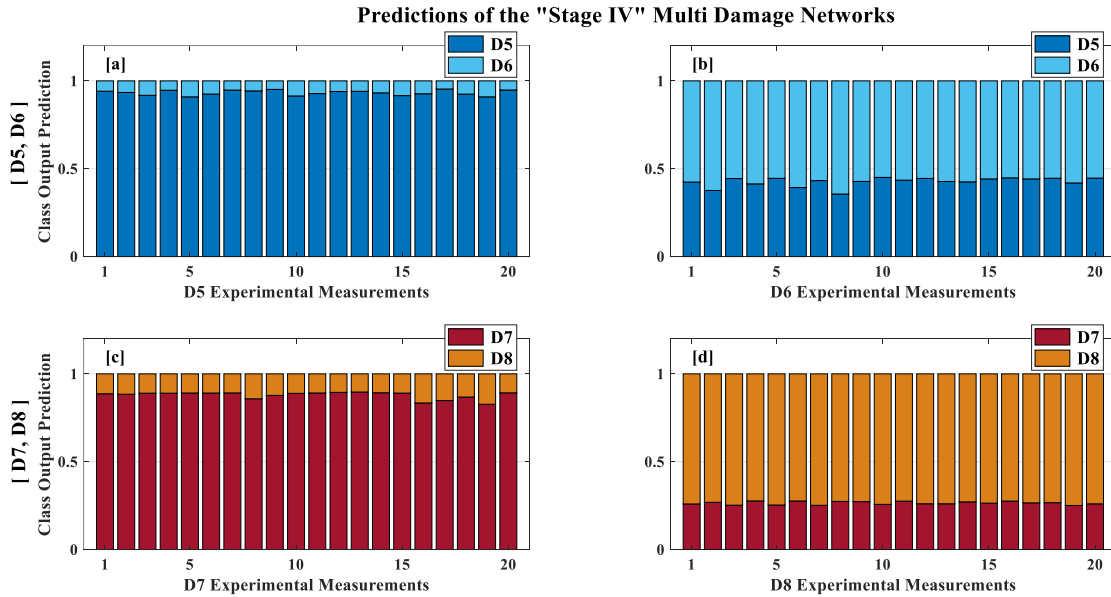


Figure 4.23: Stage IV Predictions on the (a) D5, (b) D6, (c) D7 and (e) D8 cases

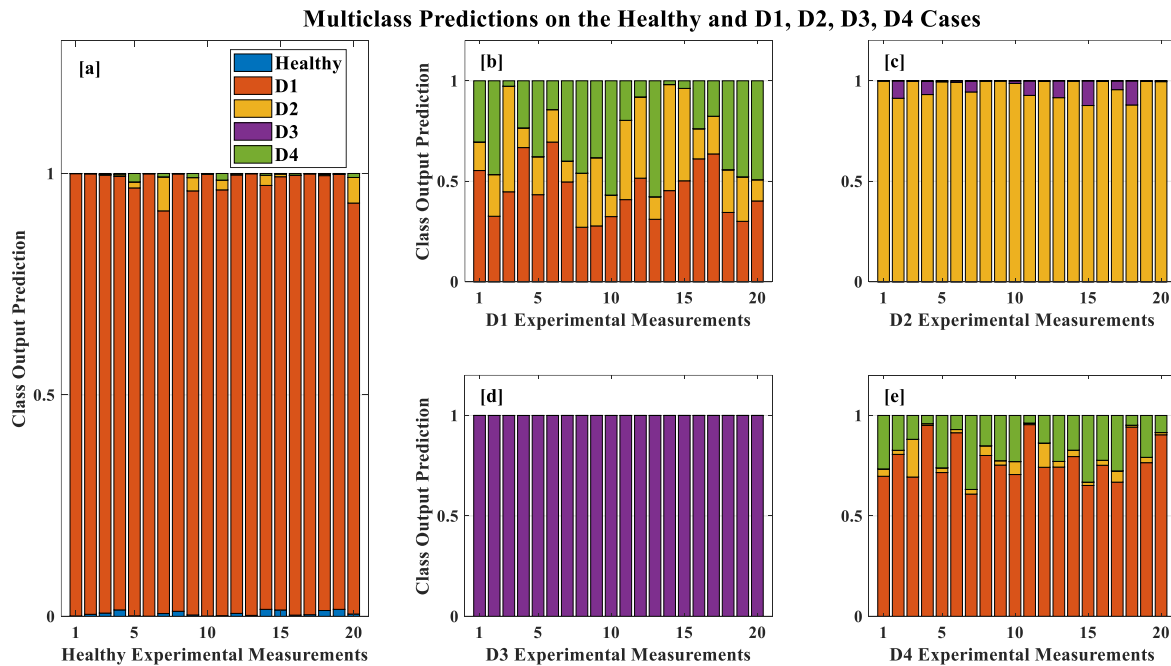


Figure 4.24: Multiclass predictions on the, (a) Healthy and (b)-(e) D1, D2, D3, D4 cases

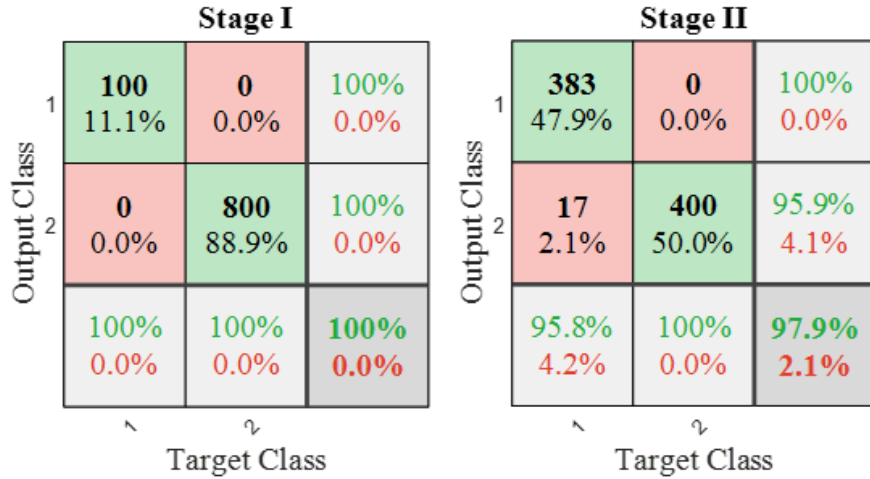


Figure 4.25: Confusion matrices for the Stage I and II experimental inputs

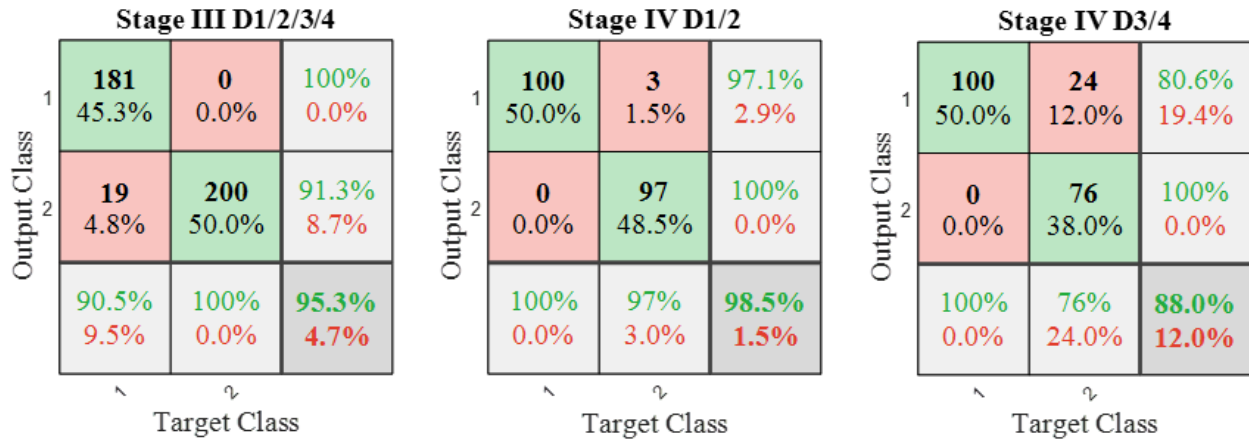


Figure 4.26: Confusion matrices for the Stage III and IV experimental inputs of Single Damage cases

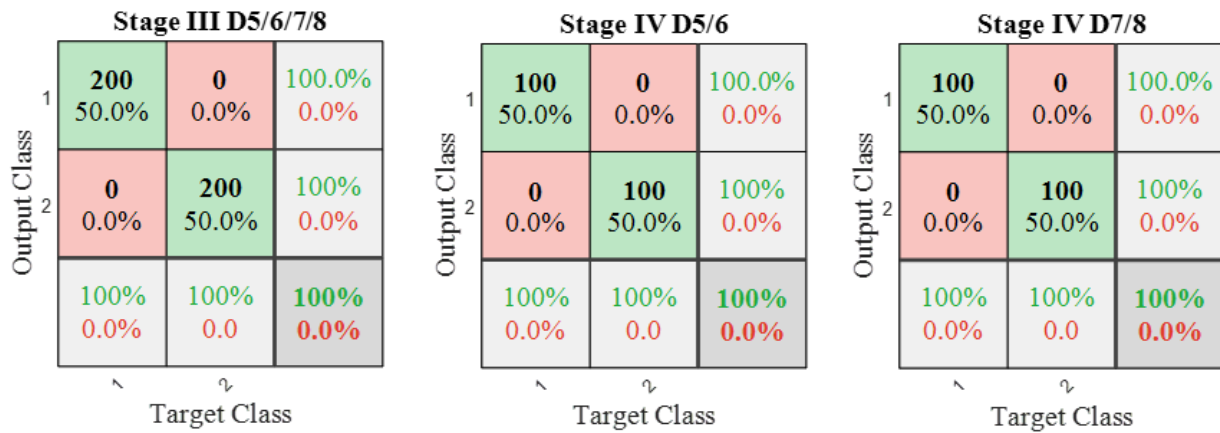


Figure 4.27: Confusion matrices for the Stage III and IV experimental inputs of Multi Damage cases

Multiclass predictions

1	0 0.0%	0 0.0%	0 0.0%	0 0.0%	0 0.0%	NaN% NaN%
2	100 20.0%	55 11.0%	0 0.0%	0 0.0%	100 20.0%	21.6% 78.4%
3	0 0.0%	10 2.0%	100 20.0%	0 0.0%	0 0.0%	90.9% 9.1%
4	0 0.0%	0 0.0%	0 0.0%	100 20.0%	0 0.0%	100% 0.0%
5	0 0.0%	35 7.0%	0 0.0%	0 0.0%	0 0.0%	0.0% 100%
	0.0% 100%	55.0% 45.0%	100% 0.0%	100% 0.0%	0.0% 100%	51.0% 49.0%
	1	2	3	4	5	
	Target Class					

Figure 4.28: Confusion matrix for the multiclass predictions on the experimental measurements

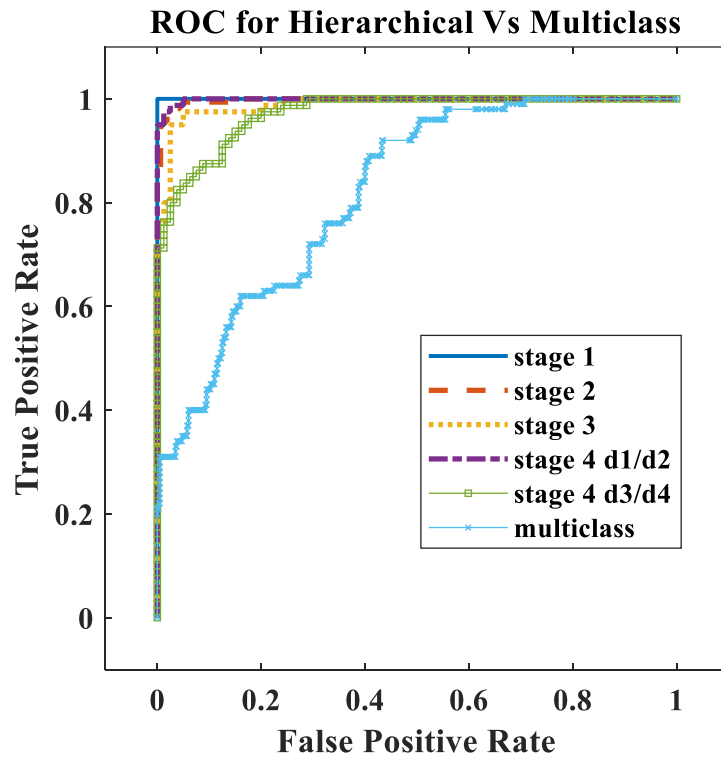


Figure 4.29: ROC curves of the class prediction performance on the experimental states

4.5 Discussion

In this section discussion on the results and the methodology of solving the presented SHM test case is given. As shown in section 4.4, FE generated labeled datasets were used to successfully train CNN classifiers in two different SHM problem schemes. The first SHM problem formulation used a hierarchical approach by separating Healthy from Damaged states and identifying a total of 8 damaged classes in 4 Stages, meaning a sum of 9 classes formed the problem. The second SHM problem on the other hand was tested in the expected most demanding part of the former in a direct multiclass way separating 5 health states in total. During the training phase both ways scored high learning validation values of around 90% on the learning sets. However, as noted also in [108] learning validation on the FE data does not guarantee the same scores on the experimental states due to the model error factor. This of course is the main limitation of the FE generated data for SHM training instead of directly acquiring experimental learning sets. The applicability of the proposed method for the problem of data acquisition by simulations therefore depends on how accurate the FE models can be to simulate various health states.

To minimize the effect of disagreement between FE and experimental responses, data was generated by creating an optimal model fit on the healthy state and uncertainty was simulated on material parameters. An additional step was to separate the SHM problem in different stages through a hierarchical approach in order to exploit its advantages as discussed in paragraph 4.3.2 which proved to have a huge impact on the experimental accuracy. The hierarchical approach showed clearly a more robust and accurate SHM damage detection and location system for the studied test case. This is summed up in the ROC curve comparisons of **Figure 4.29** where the experimental prediction scores produce curves closer to the ideal at the top left corner for the hierarchical classifiers, compared to the multiclass one. Interestingly, the chosen SHM hierarchical categorization showed more confident prediction scores on Stage I than Stage II, III and IV meaning that the predicted class by the network was calculated consistently with enough margin between the Healthy and Damaged class (**Figure 4.18, Figure 4.25**). This may be attributed to the fact that the Healthy state is in fact better “known” to the network since the updated FE model was fit on the experimental Healthy state. A more accurate and confident prediction is therefore to be expected on Stage I. In addition, the Multi Damage scenarios which were expected to have larger impact on the structural response, in contrast to the Single Damage cases, were predicted in a solid 100% accuracy in all classification Stages confirming that larger anomalies are naturally expected to be easier detected and identified. Nevertheless, Single Damage identification networks scored accurate prediction scores with Stage IV D3/4 being the lowest with an 88% overall accuracy (**Figure 4.21, Figure 4.26**). However, that is still not far from the training validation score of 90.76% indicating that the classifier generalizes correctly on the experiment. Furthermore, in case the hierarchical SHM system uses the average of multiple predictions to progress from one Stage to the following, a score of 100% accuracy may be achieved.

On the other hand, the direct multiclass approach showed that the considered SHM problem is a difficult case of generalization from FE to experimental data. A large difference between the

learning stage validation of 90% and experimental of 51% is noted with the classifier failing to predict correctly even the Healthy states. A high bias towards the D1 class was also noted for Healthy and D4 experimental measurements while the experimental D1 class itself was accurately predicted with only 55%. Studying the exact source of not appropriately learned features is not purpose of this work since the whole DL concept is avoiding user defined signal features. The possibility of tuning a multiclass network that generalizes correctly still exists, however complex multiclass networks should be avoided and simpler networks assigned with simpler tasks should be preferred. An indication of the more demanding tasks in the multiclass considered approach was already observed with the much more unstable learning process of the classifier. The loss curves indicated not smooth enough loss surfaces. In the same way, the lowest scores for the hierarchical classifiers were recorded for the ones with the most unstable learning curves being Stage II and Stage III and IV D3/4 for the Single Damage classes with 97.9, 95.3 and 88 % accuracies as in **Figure 4.25** and **Figure 4.26** respectively. The systematic study of this connection however is not considered in the present work.

A final fact to be observed in present study is the influence of the structure's dynamics, excitation and measurement method. The reader may notice that even though the same amount of data is equally used for every class and therefore no data bias is to be expected, the structure is not symmetric and not symmetrically excited and measured by the placed sensors. Therefore, the D1, D2, D3 and D4 identification problems even though they may initially seem as symmetric they form not identical but individual neural network problems. This physical non-symmetry may afterwards influence the experimental validations where the trained networks on Stage IV seem to generalize better on the D1-D2 separation rather than D3-D4 in the confusion matrices of **Figure 4.26** with accuracies of 98.5 % compared to 88% respectively.

4.6 Conclusions

In this chapter a SHM framework using simulated FE models and hierarchical DL CNN classifiers was shown for a test CFRP pin-joined truss structure. The goal was to investigate the method of FE data generation and DL classification for damage identification in multiple damage scenarios. The damage identification problem was investigated with a hierarchical separation to study potential improvements of numerically trained classifiers on experimental generalization

The presented hierarchical SHM classification method proved to be accurate and robust for the studied test case, showing that FE trained CNNs may also generalize correctly on experimental states with greater confidence in larger magnitude damages as expected. In comparison, the non-hierarchical but direct multiclass classifier showed to be inadequate for the test structure and not be able to generalize correctly on experimental states. Simpler classifiers with simpler SHM problem formulations should be therefore preferred against direct multiclass in future works.

Damaged State Responses Approximation with Transmittance Anomalies

Contents from Original Paper [122]: Seventekidis, P., & Giagopoulos, D. (2022). Model-based damage identification with simulated transmittance deviations and deep learning classification. *Structural Health Monitoring*. <https://doi.org/10.1177/14759217211054348>

ABSTRACT

Damage detection and identification is one of the main tasks in vibration based Structural Health Monitoring (SHM). The robustness of such SHM applications depends among others on the amount and quality of data that can be acquired. Model based SHM methods may offer such data in unlimited numbers by simulating different structural states, however the main drawback remains the accuracy of models especially for small damages and early detection scenarios. In the present work a method is presented where SHM data is generated through Finite Element (FE) models, simulating transmittance deviations from reference healthy states. The method is tested on a Carbon Fiber Reinforced Polymer (CFRP) truss for multiple damage scenarios of relatively realistic and small magnitude, affecting different truss members. The transmittance deviations for each scenario are approximated in the FE model by reducing the stiffness of the corresponding components simulating in parallel different uncertainties, resulting in a rich training dataset. The simulated data is finally passed to a Deep Learning (DL) classifier which is later validated on the experimental damages. The dataset is proven to provide to the DL classifier the appropriate information to generalize on the experimental states and the method has potential to contribute to model based SHM applications. The numerical to experimental generalization is proven to depend on the uncertainty simulation of various model parameters.

Keywords: Structural Health Monitoring, Damage Detection, Data-Driven, Finite Element Modeling, Deep Learning

5.1 Introduction

In this chapter, a test setup of a carbon fiber reinforced polymer (CFRP) truss is investigated for small and realistic impact-like damage identification. The set-up is identical to the one in Chapter 4, except that random excitation is used now. The impact-like damage affects the outer layers of the CFRP in a small area, presenting a challenging case for classifiers trained with simulated data. A novel methodology is investigated where instead of vibration time responses, Transmittance Function (TF) deviations from a reference state are used as input features in a Convolutional Neural Network (CNN) classifier. Goal of the present chapter is to investigate the feasibility of TF anomalies as pre-processed input features and study the effect uncertainty in parameters simulation during the data generation state.

Transmittance functions (TF) have been already used in various SHM applications [32,123,124] since they can inherently capture the changes in relationships between different sensors on a structure and do not require excitation measurement. To approximate the specific transmittance deviations or anomalies that correspond to a different truss member damage, the FE models are adapted with lowered stiffness on the affected members for their full length. For this approximation, a range of CFRP tube stiffness values and material uncertainties are simulated covering the feature space in a wide range. The resulting set of transmittance deviations is used after as inputs for the training of DL classifiers which have the task to find the appropriate trends in data that characterize each damage scenario. In that way, the proposed approach operates supervised by simulated transmittance deviations and finally is validated on its generalization on real physical damages. The workflow followed is in essence the same as in Chapters 2, 3 and 4. An updated flowchart is given however in Figure 5.1 to highlight that TFs are used instead of vibration time-responses.

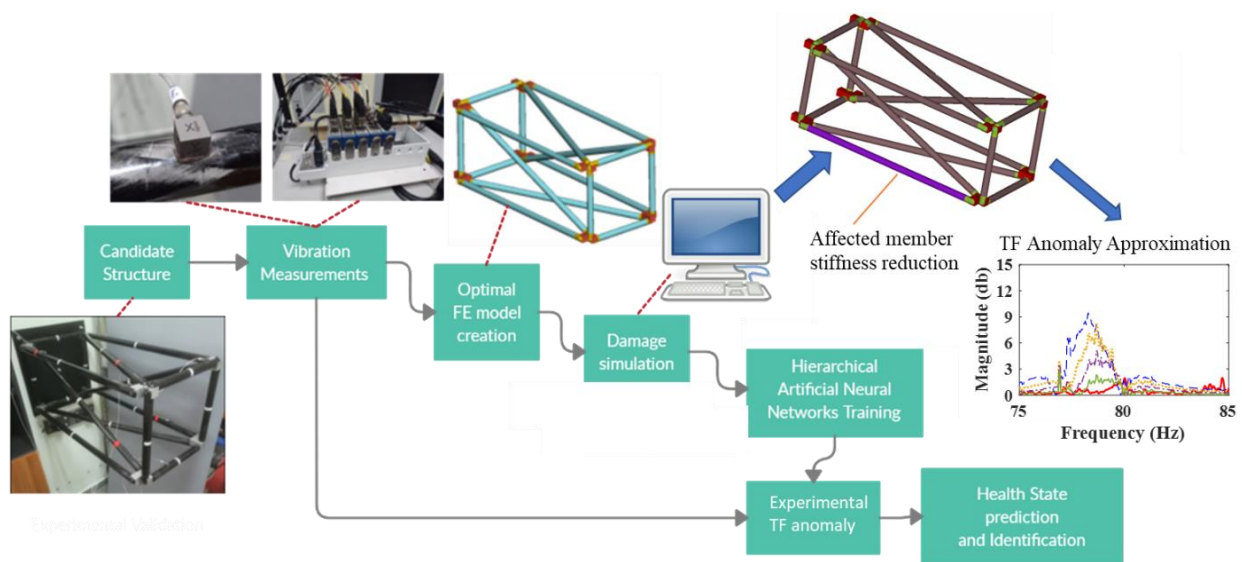


Figure 5.1: Workflow of the methodology followed in the current chapter exploiting Transmittance Function deviations (anomalies)

The text follows in section 5.2 where the concepts behind the FE modeling of TFs deviations with uncertainty on parameters for data generation is given. Next in section 5.3 the physical test set-up of the CFRP truss is presented along with the excitation equipment and the accelerometer network used. The damage on the truss members is also described and the identification problem is formulated with different state scenarios. Next, in section 5.4 the FE model of the truss is presented together with the material parameters, calculated with update on the healthy structural state. A comparison is given between healthy and damaged state transmittance functions for the approximate numerical and the experimental data. The methodology behind model parameter uncertainty and classification features that aid in DL generalization is explained as well. In section 5.5 the DL classifier architecture and training dynamics are presented with validation on the experimental states. The effect of damage magnitude and material uncertainty on the generalization is provided by comparing results from corresponding datasets. Sections 5.6 and 5.7 include the Discussions and Conclusions of this chapter.

5.2 Transmittance deviations from a reference state using approximate stiffness reductions

Transmittance functions (TF) have previously found application in different SHM and damage detection methodologies since they can capture the relationship between sensor pairs without the need of measuring the excitation force. The TF between two sensor pairs y_1 and y_2 is defined [123] as the ratio:

$$TF_{y_1 y_2}(\omega) = \frac{S_{y_1 y_2}(\omega)}{S_{y_2 y_2}(\omega)} = \frac{x_{y_1}(\omega) x_{y_2}^*(\omega)}{x_{y_1}(\omega) x_{y_1}^*(\omega)} \quad (5.1)$$

where the $S_{y_1 y_2}$ is the cross spectral density and $S_{y_2 y_2}$ the auto spectral density of the signals y_1 and y_2 , while x and x^* represent the respective Fourier and conjugate Fourier transform of the corresponding signals. For the triaxial accelerometer sensor network used in this work the calculated TFs are grouped according to measurement axis with the TF matrices:

$$TF^X = \begin{bmatrix} 1 & T_{12}^X & \cdots & T_{1w}^X \\ T_{21}^X & 1 & & T_{2w}^X \\ \vdots & & \ddots & \vdots \\ T_{w1}^X & T_{w1}^X & \cdots & 1 \end{bmatrix}_{w \times w} \quad TF^Y = \begin{bmatrix} 1 & T_{12}^Y & \cdots & T_{1w}^Y \\ T_{21}^Y & 1 & & T_{2w}^Y \\ \vdots & & \ddots & \vdots \\ T_{w1}^Y & T_{w1}^Y & \cdots & 1 \end{bmatrix}_{w \times w} \quad TF^Z = \begin{bmatrix} 1 & T_{12}^Z & \cdots & T_{1w}^Z \\ T_{21}^Z & 1 & & T_{2w}^Z \\ \vdots & & \ddots & \vdots \\ T_{w1}^Z & T_{w1}^Z & \cdots & 1 \end{bmatrix}_{w \times w} \quad (5.2)$$

Where w represents the total number of sensors used. Of course, any other combination between channels can be calculated as desired. The deviation between a healthy state reference and a test state TF, named as DTF, which is used as the classification feature for training and validation of the DL classifiers is defined as:

$$\begin{aligned}
 DTF^X &= \left| TF_{healthy}^X - TF_{test}^X \right|_{wxw} & DTF^Y &= \left| TF_{healthy}^Y - TF_{test}^Y \right|_{wxw} \\
 DTF^Z &= \left| TF_{healthy}^Z - TF_{test}^Z \right|_{wxw}
 \end{aligned}
 \tag{5.3}$$

where $T_{healthy}$ and T_{test} represent the corresponding TFs of each structural health state. This specific difference is not restrictive and except the absolute difference other measures might be tested such as the mean square difference. In this work only the formulation of equation (5.3) will be considered for simplicity. In addition, components of the DTF matrices might be dropped during the design of the DL training process if they do not offer information for damage classification, this however this is problem specific.

To obtain now the simulated TFs and calculate the DTFs that form the DL training set a suitable numerical FE data generation scheme has to be applied. The FE equations of motion are given as:

$$\mathbf{M}(\rho)\mathbf{A} + \mathbf{C}(\mathbf{K}, \mathbf{M}, \alpha, \beta)\mathbf{V} + \mathbf{K}(E)\mathbf{U} = \mathbf{F}
 \tag{5.4}$$

where \mathbf{A}, \mathbf{V} and \mathbf{U} are the global acceleration, velocity and displacement vectors respectively. \mathbf{M} , \mathbf{C} and \mathbf{K} represent the global mass, damping and stiffness matrices of the structure that depend on the model physical parameters of density ρ , damping α and β and elasticity E . In previous works a repetitive load case algorithm has been used [108, 122] that samples randomly material parameters to compensate for uncertainties of the numerical model. The logic behind this respective load scheme data generation was explained in **Chapter 2** section 2.2. The same approach is followed in this chapter as well.

For each load case a health status classification label \mathbf{Y} is defined, which corresponds to stiffness parameters reduction of the respective CFRP truss member. The stiffness parameters of the FE equations may therefore be separated in parts as $E = [E^1 E^2 \dots E^p]$ for a p number of parts where in each damage scenario only one of the E^1 to E^p is reduced. The reduced stiffness E^d of the member is calculated as a percentage r of the member's original healthy $E^{healthy}$ as $E^d = rE^{healthy}$. For composite parts E may generally be given per ply as $E = [E_1 E_2 G_{12} G_{1z} G_{2z}]$ containing the moduli of elasticity E_1 and E_2 as well the in-plane and transverse shear moduli G_{12} , G_{1z} and G_{2z} . A uniform stiffness reduction approximation is considered meaning all moduli are reduced by the same degree r for simplicity. For this approximate way of CFRP damage simulation in the test case of this work a range of percentages r are simulated for each damage scenario. Goal of the present chapter is to investigate the effect and performance of the stiffness reduction approximation and material uncertainty simulation on the generalization capability to the real experiment of the subsequently trained DL classifiers.

The complete FE data generation algorithm for DL training is presented finally in Algorithm 5.1.

Algorithm 5.1: Numerical model data generation algorithm**Input:** Number of load cases n and statistical bounds for each quantity ρ , α , β , E , r **Output:** n number of labeled DTFs and health labels

```

for  $i = 1:n$  do
  sample  $E \rightarrow \mathbf{K} = \mathbf{K}(E)$ 
  sample  $\rho \rightarrow \mathbf{M} = \mathbf{M}(\rho)$ 
  sample  $\alpha, \beta \rightarrow \mathbf{C} = \mathbf{C}(\mathbf{K}, \mathbf{M}, a_i, \beta_i)$ 
  solve  $\mathbf{MA} + \mathbf{CU} + \mathbf{KU} = \mathbf{F}$ 
  calculate  $T_{healthy}$  from  $\mathbf{A}$ 
  define Health status  $\rightarrow \mathbf{Y}_n$ 
  sample  $r \rightarrow$  recalculate  $E$ 
  Solve  $\mathbf{MA} + \mathbf{CU} + \mathbf{KU} = \mathbf{F}$ 
  calculate  $T_{damage}$  from  $\mathbf{A}$ 
  return  $DTF_n = |T_{healthy} - T_{damage}|$  and  $\mathbf{Y}_n$ 
end

```

After the desired number of n load cases is achieved, the data is organized in training examples forming the training set (5.5) which is passed to the DL classifiers for damage identification training.

$$Train_set = \{(DTF_1, \mathbf{Y}_1), (DTF_2, \mathbf{Y}_2), \dots, (DTF_n, \mathbf{Y}_n)\} \quad (5.5)$$

It is worth noting that Algorithm 5.1 may be altered to suit the needs of the FE solver used, such as modal a solution. This has been noted again in the previous chapters.

5.3 Experimental Set-Up and Damage Scenarios

In this Section the experimental set-up is described. The CFRP tube truss structure pin-joint with aluminum connections and the excitation and measurement equipment is shown in **Figure 5.2**. The CFRP tubes are permanently glued on aluminum connections which are bolted on intermediate aluminum parts. The complete structure is permanently clamped on a steel base which is attached on a concrete wall.

The CFRP tubes were produced with filament winding and are made of a stack of seven (7) plies. The details of the ply orientation, thickness and nominal material properties have been given already in [108] and **Chapter 4**. The electrodynamic shaker and the accelerometer network of four (4) triaxial sensors as shown in **Figure 5.2** is also the same, however the shaker is permanently attached on the truss and random excitation is forced. A low lateral stiffness stinger rod is used for

connection in order to minimize effect of the shaker's stiffness on the dynamic response. The connecting rod with the bolted dynamometer on the low left corner aluminum connection is shown.

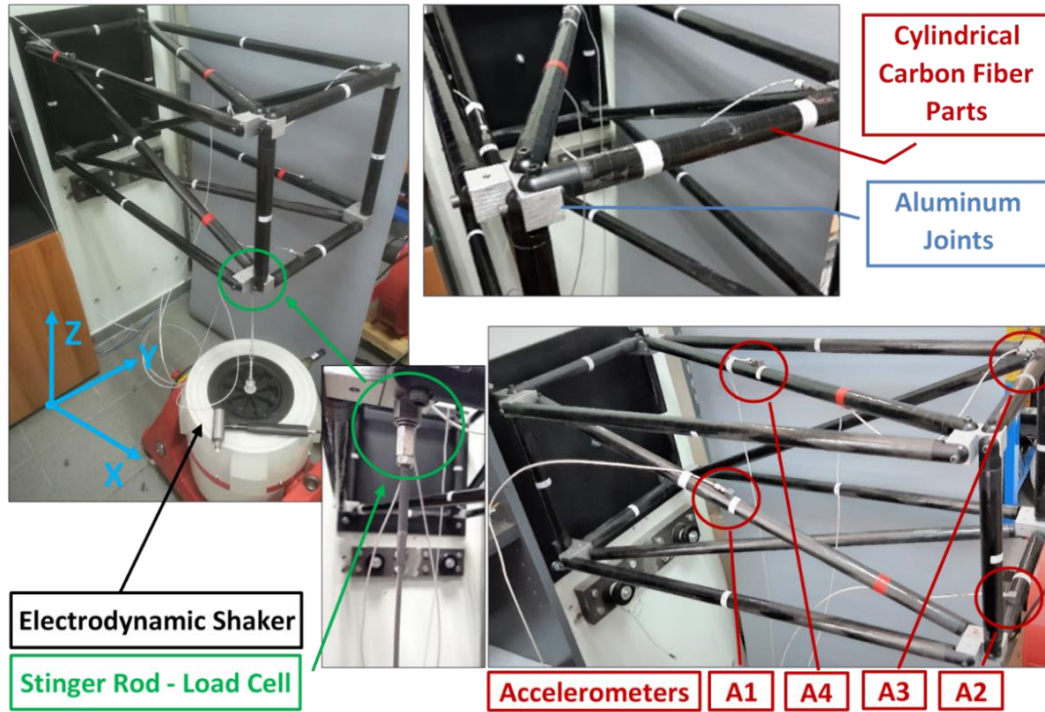


Figure 5.2: CFRP truss and excitation equipment

5.3.1 Impact-Like Damage and Hierarchical Identification Problem

The experimental damage in this work is applied directly in a form of 3-point bending test on a CFRP tube for a bending depth of 10 mm resulting in a relatively realistic damage case. In **Figure 5.3** it is shown how the 3-point bending test is performed using a tension-compression machine. The resulting damage that affects a small part of the CFRP tube can be seen to have caused failure of the outer layers resin of the CFRP. The exact condition and calculation/modeling of the damage of the tube is not studied, as purpose of this work is to account for not precisely defined damages of the truss. It is however shown later in this section that the magnitude of the damage affects only slightly the stiffness of the structure, and a challenging damage identification problem is formed, especially when model-based data is intended to be used.

The damage scenarios can now be formed with substitution of healthy CFRP tubes with damaged ones. The proposed methodology may not be limited theoretically in the number and combinations of damage cases considered. However, the performance of damage approximation and each individual damage on the tubes may affect the separation of related cases. For that reason, cases are also investigated with damaged truss member combinations that may be hard to separate. In total six (6) different scenarios are considered in this work. Four (4) cases, namely D1, D2, D3 and D4 consider single tube damages around the truss. The other two (2) cases D5 and D6 were formulated with combinations of pairs of tubes. To help the reader understand the damage cases

and which tube is involved in which scenario **Figure 5.4** is presented which shows the naming conventions used. An indicative picture of a real damage case (Damage 6) is shown already in **Figure 5.3**, the other cases are formed accordingly. In total two damaged beams were necessary to synthesize the cases, applied on the corresponding member every time. The first beam was used for the D1-D4 cases combined with the second beam in the D5 and D6 cases.

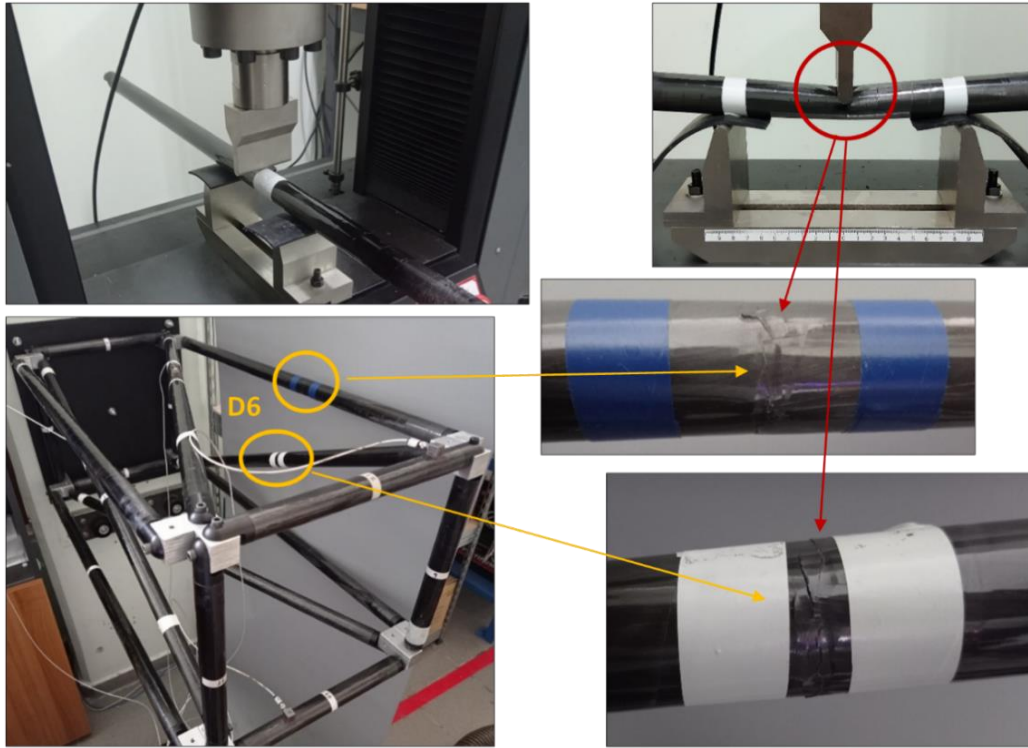


Figure 5.3: Indicative damage on the CFRP tube with 3-point bending (up) and one of the resulting damage scenarios (Damage 6) with damaged members mounted on the truss (bottom)

The chosen scenarios may offer insight on the effectiveness of the proposed methodology to investigate the smallest possible damage magnitudes with the D1-D4 cases which consider damages in single locations. It is worth noticing that the structure is not symmetric and not excited or measured symmetrically creating therefore different expected states for all cases even though the same damaged beam was used. The D5 and D6 cases on the other hand were included for additional validation, to investigate further the damage separation effectiveness and robustness. Notice that the D5 case differs from D1 by the addition of damaged tube 5 while D6 differs from D3 by the addition of damaged tube 6. Therefore, D5 and D6 are closely related with D1 and D3 cases and comprise small damage separation problems. For damages which may not appear in a predefined way and not with the same magnitude on different members, as in the present work, it would be important to assess the capability of identification for such cases as well. That is the logic behind the D5 and D6 cases which can resemble D1 and D3 cases respectively.

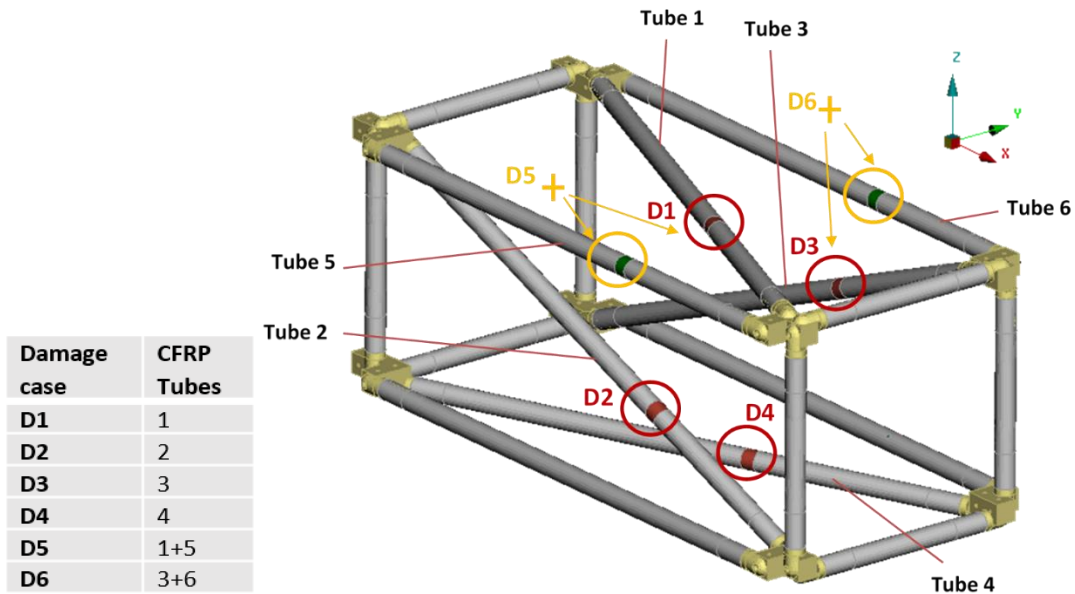


Figure 5.4: Formed Damage scenarios on the Truss

Finally, the damage identification procedure is organized hierarchically. The idea behind hierarchical classification is that damage cases are grouped and identification is performed progressively in stages, with each stage providing more details than the previous one until the final diagnosis is made. This way, also found in the literature as binary decomposition, has been found to increase the performance of classifiers compared to giving results directly in one stage from input to output [108, 125]. The organization of the classes and separation stages is as follows, depicted in **Figure 5.5**.

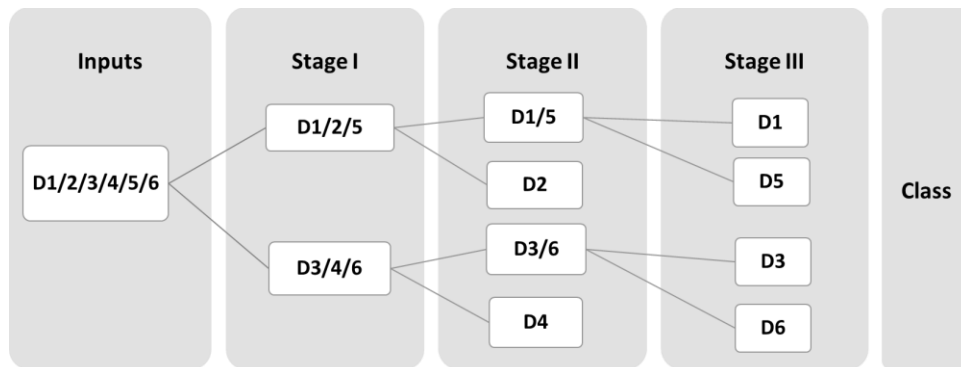


Figure 5.5: Hierarchical separation of damages

The first stage uses one classifier that receives the inputs which can be D1,2,3,4,5 or 6 and provides output in 2 classes that contain either the damages D1, D2 and D5 or the D3, D4 and D6. On the second stage, for the inputs that were flagged in the D1/2/5 class previously, further separation is provided by using the same initial inputs about whether the damage belongs to the D1 and D5 class or D2 class. For the inputs flagged as D3/4/6 damages a different classifier on the second stage

may provide a separation between D3 and D6 or D4 class. Finally, on the third stage, prediction between D1 and D5 is performed by one classifier and between D3 and D6 with another classifier. A total of five (5) binary classifiers are therefore used. The choice between the class grouping through the different stages is not restrictive. The damages with expected similarity such as D1, D5 and D3, D6 have been grouped together until the final stage.

5.3.2 Experimental Responses

Indicative experimental responses are presented in this paragraph to provide an insight on the damage cases. For all measurements in this work a sampling rate of 2048 hz has been used and random gaussian excitation was imposed on the shaker connected with the CFRP truss as was shown in **Figure 5.2**. **Figure 5.6** presents recorded accelerations from sensor location 1 for the X6 and Z directions. Responses are shown for the Healthy and D1 case.

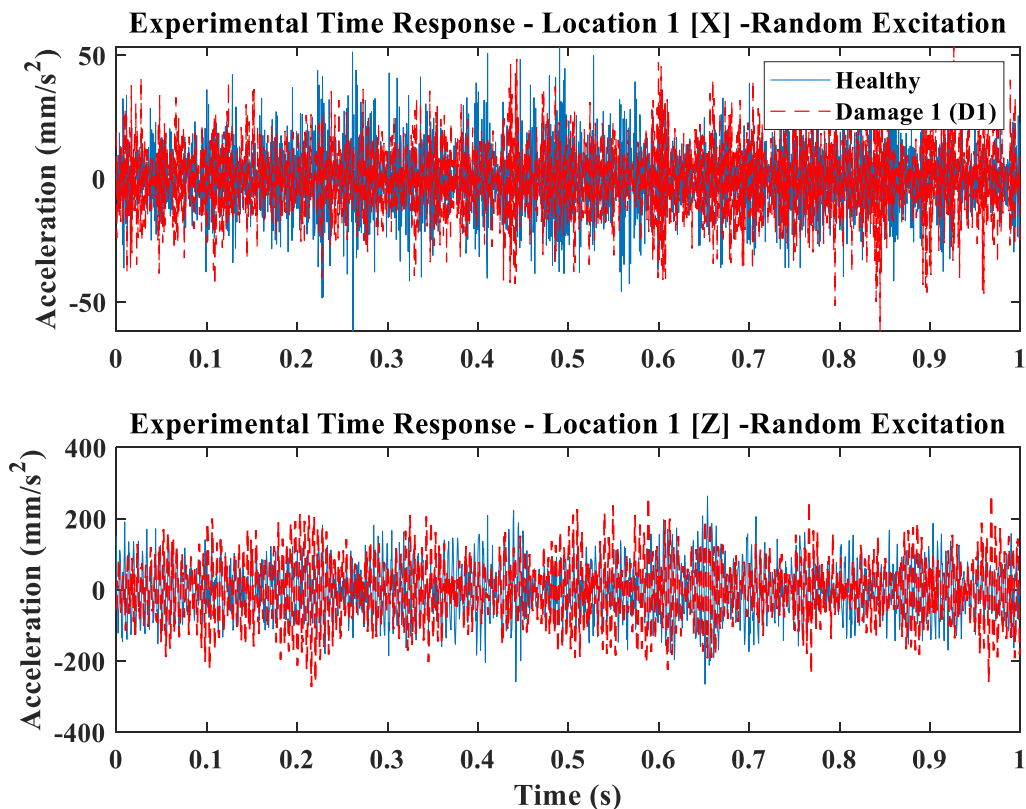


Figure 5.6: Experimental time-response measured accelerations from sensor 1 of the CFRP truss for Healthy and Damage 1 cases

On the other hand, **Figure 5.7** contains the calculated TFs between locations 1-3 and 1-4 for a range of 60-200 Hz of the Healthy and D1, D3 and D6 states.

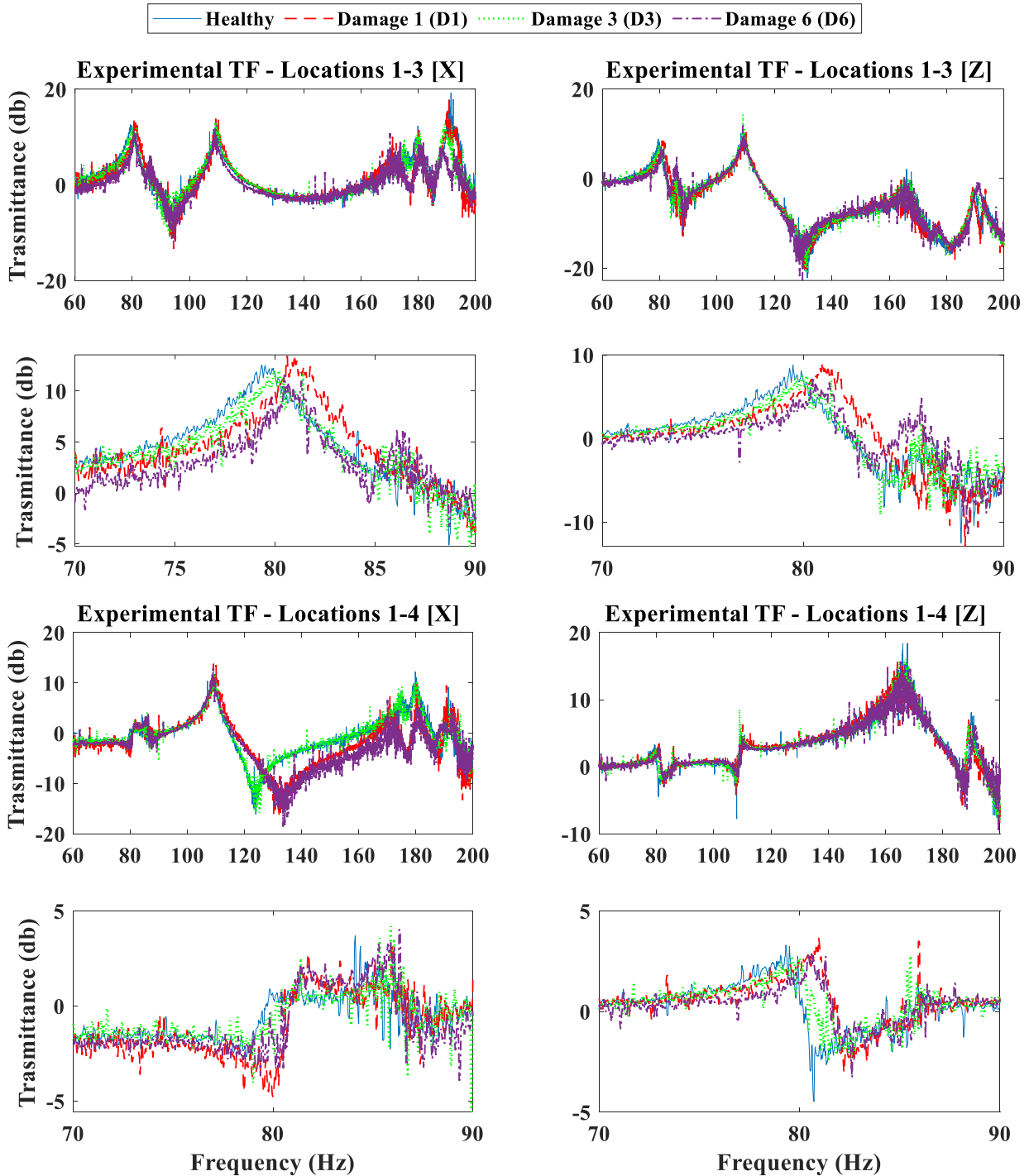


Figure 5.7: Experimental TFs between sensor locations 1-3 for a range of 60-200 Hz (above) and 70-90 Hz (below) for the Healthy and Damage 1, 2 and 3 cases

Focus on a lower frequency area of the TFs is shown as well for a range of 70-90 Hz. TFs were calculated by equation (2.7) using a total of 70000 time samples, corresponding to approximately 34 seconds. The range 60-200 Hz was found to accommodate more than seven (7) natural frequencies of the same CFRP in a previous FRF identification study [108] using however a

slightly different setup with the shaker not permanently connected. The first four (4) main modes of the truss, containing bending or torsion were contained up to 114 Hz approximately and the more complex higher modes were grouped tightly above approximately 185 Hz. The same behavior is repeated in the present work which can be observed in the power spectrum of the recorded signals as shown in **Figure 5.8** for the healthy state.

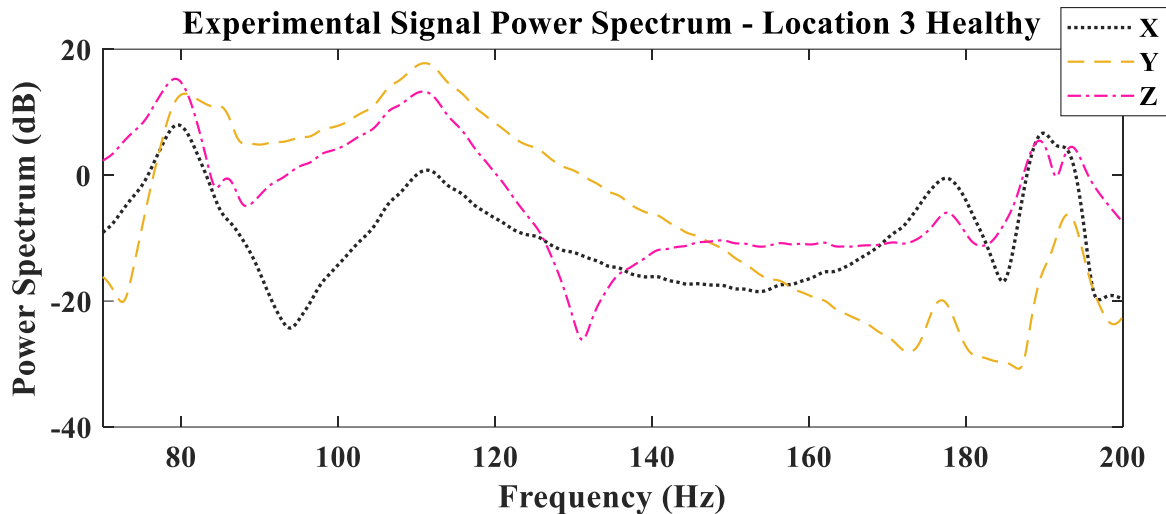


Figure 5.8: Experimental Power spectrum of signals from location 3 for the Healthy state

The damage cases show different deviations from the healthy state. The deviation is pronounced for the double CFRP damage case D6, while D3 with a single CFRP tube damage presents the smallest deviation. D1 which is also formed by single CFRP tube presents larger TF deviation than D3, highlighting that the structure and therefore single tube damages are not symmetric or identical. Nevertheless, all cases present small changes in the total stiffness of the structure without disrupting the shape of the TFs. The damage identification or SHM of the considered scenarios can therefore be challenging, especially with simulated approaches.

5.4 FE Model and Transmittance Deviation Approximations

The FE model of the CFRP truss is shown in **Figure 5.9**. In total the model is made of 480155 elements resulting in 1888956 degrees of freedom. Modeling of the aluminum joints, connections and glue is performed with solid elements while for the CFRP shell elements have been used. The pin-joint connections are modeled with rigid body elements between the aluminum joints and connections. The FE model is a remeshed copy of the one used in [108] and the same material properties are used. The material values were updated on the healthy state using impacts with the CMA-ES optimization algorithm. They are repeated here for the sake of completeness in **Table 5.1**.

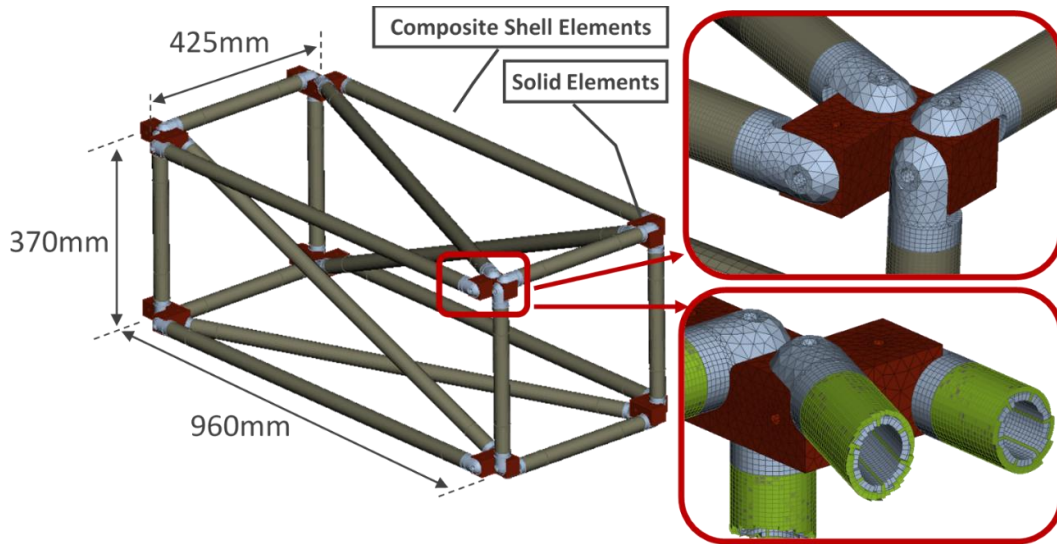


Figure 5.9: FE model of the CFRP truss

Table 5.1: Material parameter values used in the FE model which were updated on the healthy state

CFRP material properties		Aluminum joints	Aluminum connections	Glue	
Modulus of Elasticity in X E_1 [GPa]	110				
Modulus of Elasticity in Y E_2 [GPa]	7.09				
In-plane Shear Modulus & Transverse Shear Modulus 1-Z plane $G_{12} = G_{1z}$ [GPa]	5.34				
Transverse Shear Modulus 2-Z plane G_{2z} [GPa]	2.29				
Density ρ [kg / m^3]	1540				
		Young's Modulus E [GPa]	75.80	62.10	1.14
		Density ρ [kg / m^3]	2650	2482.5	983

The accordance of the FE model with the experimental healthy state is tested again, this time however for the TFs on the healthy state. In **Figure 5.10** indicative comparison between the healthy experimental and numerical TFs is given separated in X, Z between locations 1-3 and 1-4. The model is seen to follow the peaks and valleys of the experimental data although not with perfect accordance. It is left now to see how the deviations from the healthy TFs are reproduced by the model.

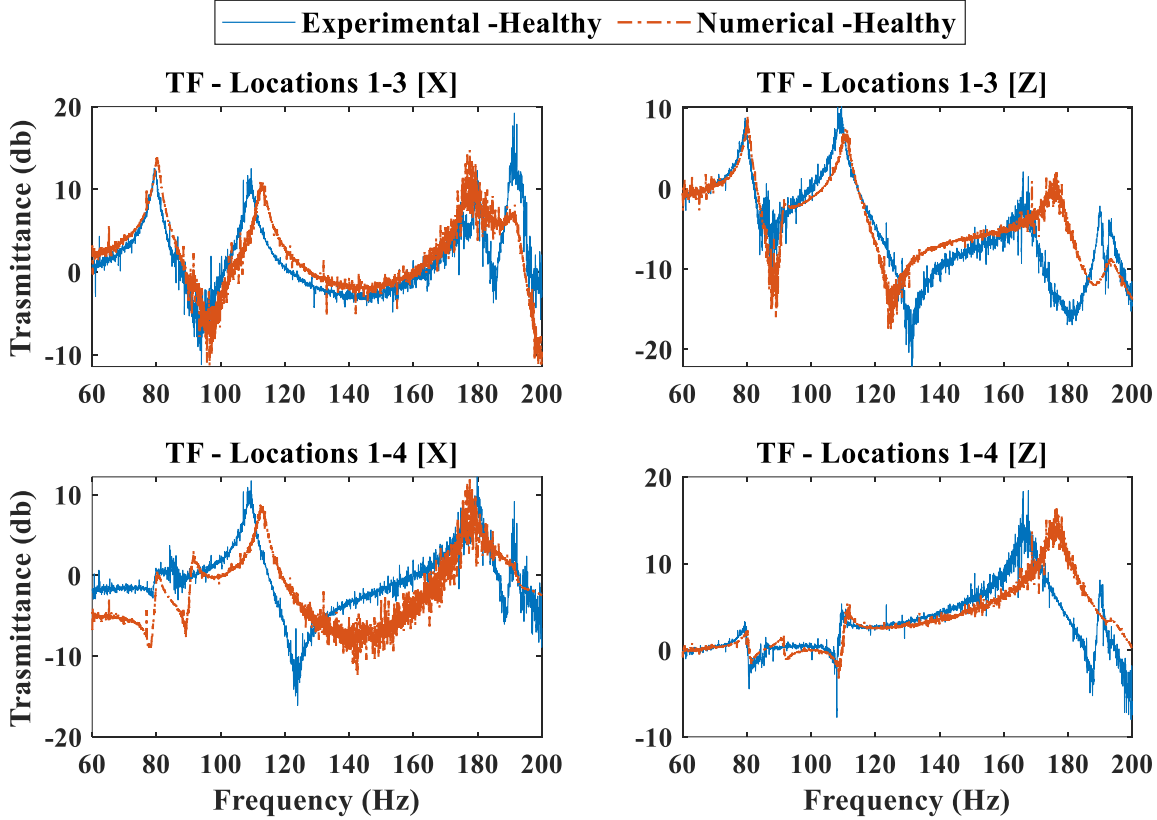


Figure 5.10: Experimental-Numerical (updated material properties of Table 1) TFs comparison between sensor locations 1-4 for a range of 70-90 Hz for the Healthy cases

5.4.1 Transmittance Deviation from the Healthy State Approximation

In section 5.2 the deviation from the healthy state $TF_{healthy}$ and a damage state TF_{damage} was defined as $DTF = |TF_{healthy} - TF_{damage}|$ and will be the damage detection feature used. The logic behind is that a FE model that is not perfectly fit to the experimental state, can simulate the changes even for small damages with better accuracy if the dynamic behavior is reproduced correctly. By using differences from a reference state instead of the state response, it is expected that the influence of the offset between the experimental and the numerical structure will be less important.

Suppose that for a state A the modeled TF_A^m is related to the experimental TF_A^e as $TF_A^m = TF_A^e + R_A(X_A)$ with an unknown error $R_A(X_A)$ that depends on the model parameters X_A . The same for a state B where $TF_B^m = TF_B^e + R_B(X_B)$. Their difference therefore is calculated as $TF_A^m - TF_B^m = TF_A^e - TF_B^e + R_{AB}$ with error $R_{AB} = [R_A(X_A) - R_B(X_B)]$ smaller in absolute value than R_A or R_B providing in that way the refined $DTF = |TF_A^e - TF_B^e|$. For each damage scenario as discussed in sections 5.2 and 5.3, the affected truss member is to be modeled with reduced stiffness $E^d = rE^{healthy}$ where $E^{healthy}$ is the healthy state stiffness and r the percentage reduction. For the case of CFRP damage considered in this work the E^d contains the parameters

$E^d = [E_1 \ E_2 \ G_{12} \ G_{1z} \ G_{2z}]$ for the CFRP which are reduced by the same degree r in the present approximation. The subsequent question that rises is what would be the r value to be used and how well the models can reproduce the experimental DTF.

An indicative model response of the approximation is given in **Figure 5.11** for the D1 and D3 scenarios with the locations 1-4 X and Z DTFs compared with the corresponding experimental using different r values.

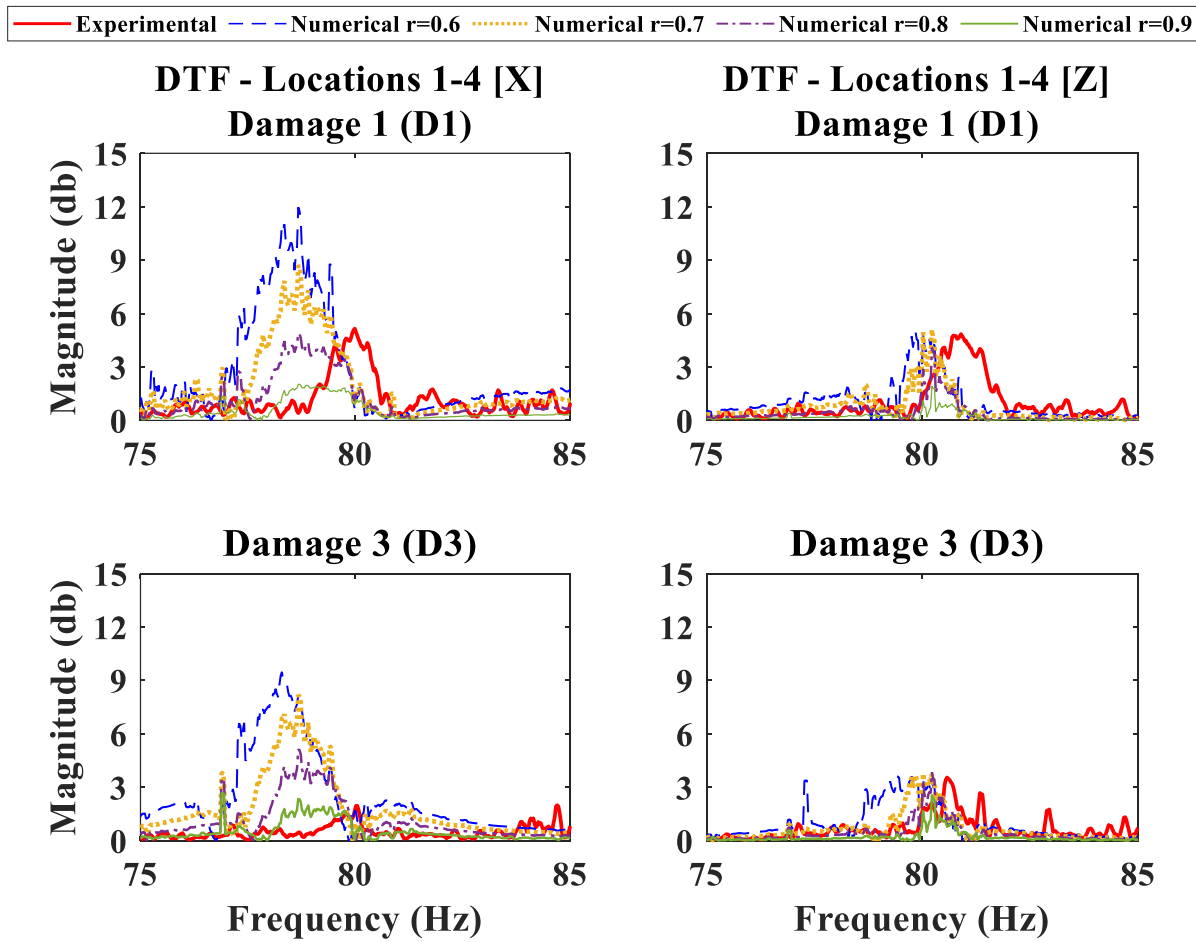


Figure 5.11: Experimental and simulated DTFs comparison (with different r -values) for the locations 1-4 X and Z for the Damage 1 and 3 cases

The model is seen to reproduce the peaks of the experimental DTFs, in a possibly better way than the TF comparisons and also react differently to the r values on X and Z directions. For example, in **Figure 5.11** and **Figure 5.10** the location 1-4 X DTF compared to location 1-X TF presents better agreement in the frequency range shown. That means the model-experiment initial offset may have less influence on the experimental generalization of classifiers trained with DTF data. However, how consistent will be the hypothesis of smaller DTF error $R_{AB} = [R_A(X_A) - R_B(X_B)]$ compared to TF errors R_A and R_B for the general case will not be further studied and could be subject of future work.

Continuing, in the results of **Figure 5.11**, the X direction different damage magnitudes with r - value change showed a model responding in the deviation direction, while the Z direction remained stiffer to changes. The experimental DTF as expected presented higher magnitude for the D1 compared to the D3 case, which seemed to be closer to the $r=0.8$ and $r=0.9$ numerical cases respectively. It is therefore evident that a good strategy for the approximations would be to simulate a range of damage magnitudes rather a single r value approximation while keeping only the simulated DTF directions which are sensitive in that magnitude approximation.

Classifiers provided with such simulated datasets can possibly generalize better on different unknown damage magnitudes and non-linearities of the dynamic behavior. Since this is a data-driven method the expected outcome is that even though a single simulated DTF might not precisely validate the experimental, the combined trends in the simulated data will provide to a trained classifier the appropriate feature extraction function. To test this hypothesis, comparison is given in section 5.5 between classifiers trained with a range of r values and classifiers trained with a single percentage, investigating the possible effects on generalization and the performance of the approximations. The reliability of the methodology will be judged on how well the performance on the simulated dataset is generalized on the experimental states.

In the same manner, simulating material uncertainties has positive effect in producing richer features. In **Figure 5.12** simulated DTFs for the locations 1-4, 2-4 and 3-4 X are indicatively shown for the Damage 1 case, produced with randomly sampled material parameters as per Algorithm 5.1. The locations presented have been chosen to be sensitive to model parameter changes and will be the ones used thought this work. In section 5.5 additional comparison will be given to investigate the effect of material parameters uncertainty simulation.

Concluding, data sets are formed in that way following the steps of Algorithm 5.1, enriching the DTF feature space with random sampling on the material parameters and damage approximation values r . Classifiers that can achieve good scores on such augmented data sets can potentially generalize better on experimental states as well, which is the main study of the present chapter.

5.5 Deep Learning Classifiers Training and Experimental Generalization

In this Section the numerical data generation and the training procedure of the DL classifiers are presented along with validation results on the experimental states of the test set-up. The results will be presented per damage detection Stage as described in paragraph 5.3.1 for the different damage scenarios.

5.5.1 Training data Generation

All learning data was simulated by following Algorithm 5.1 using a +/- 15% uniform random deviation from the nominal material values per case, while for each damage scenario the stiffness

approximation value was sampled in a range of $r = 0.6 - 0.9$. A total of 2000 examples were simulated by the FE models for each damage scenario using the FE solver MSC Nastran on an Intel i7-8700 processor with an approximate time of 4 minutes per case. Only balanced classification data sets were considered, created in the labeled form of equation 6. The number of training examples for each classification Stage is presented in **Table 5.2**.

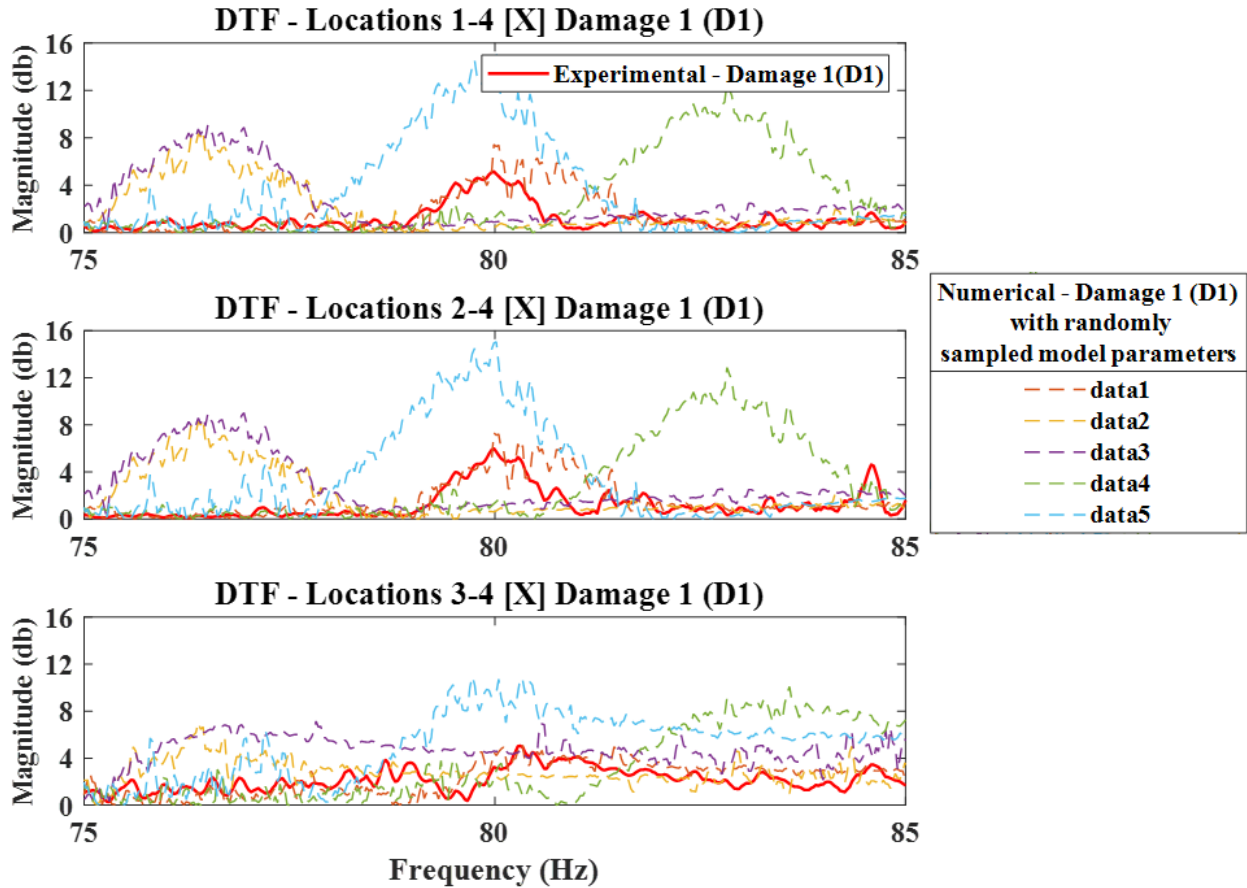


Figure 5.12: Experimental and simulated DTFs comparison for the locations 1-4, 2-4 and 3-4 X for the Damaged 1 case. The simulated DTFs were generated with randomly sampled material parameters

Table 5.2: Organization of learning data

Learning data set	Number of learning examples	Number of validation examples	Class 1 Labels	Class 2 labels
Stage I D1/2/5-D3/4/6	4200	1800	1000 x (D1+D2+D5)	1000 x (D3+D4+D6)
Stage II D1/5-D2	2800	1200	2000 x (D1+D5)	2000 x D2
Stage II D3/6-D4	2800	1200	2000 x (D1+D5)	2000 x D2
Stage III D1-D5	2800	1200	2000 x D1	2000 x D5
Stage III D3-D6	2800	1200	2000 x D4	2000 x D6

5.5.2 Neural Network Training and Experimental Validation

The network architecture used is shown in **Figure 5.13**.

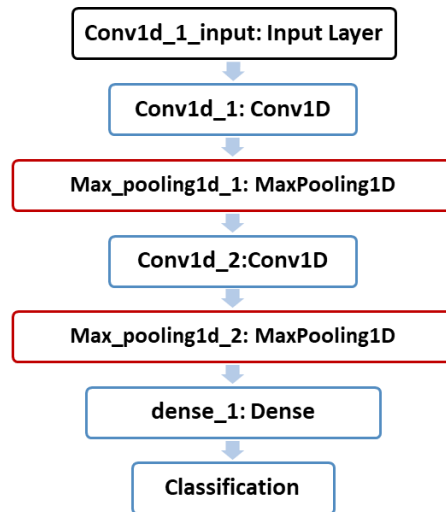


Figure 5.13: CNN classifier architecture used

The simplest architecture was chosen that performed well in training through preliminary tests. The number of neurons per layer has been kept to minimum to reduce the network parameters while retaining good leaning scores. Less parametrized networks can have a direct positive effect on the generalization capabilities [38] which of course is sought in this work, especially since transition from simulated to experimental states is pursued. In particular, 4 and 2 neurons were used for the first and second CNN layer, while only 3 neurons for the dense perceptron. For activation the hyperbolic tangent function was chosen. The pooling size has been chosen with a value of 10. The focus on the subsequent predictions is on a range of 75-85 Hz resulting in DTF lengths of 1000 steps, which is also the input dimension of the first CNN layer. A relatively large kernel size of 50 has been chosen to capture the primary gradients of the DTFs. Finally for the CNN training, backpropagation (BP) with model checkpoint to prevent overfitting was employed using the adaptive stochastic gradient descent algorithm Adam with default learning rate (0.001) and moment (first moment decay 0.9, second 0.999) parameter values. Categorical Cross entropy loss was implemented as the loss function.

First Stage Training and Classifications

The first Stage training curves are provided in **Figure 5.14** by leaning and validation accuracy and loss for 30 random start BPs. The network achieves good scores with over 95% in learning and validation accuracy suggesting that the correct information from the rich feature space is extracted and the classes can be separated in good degree.

In **Figure 5.15** the predictions of an ensemble of the 30 networks are shown for the six (6) different experimental states where measured DTFs were used as input. A number of 20 predictions on each state are indicatively shown for each D1-D6 states. The network prediction

scores come in values between 0 and 1, with 0.5 being the class threshold. Blue is used for the first class score that the network predicts on the input and red for the second class. The sum of the blue and red column is always equal to 1. The same prediction code and ensembles scheme (with the corresponding neural networks) is used throughout this work. According to the formulated damage identification problem experimental states were classified correctly. D1, D2 and D5 were separated successfully from the D3, D4 and D6 cases suggesting that the features learned from the simulated data validate the experimental state as well.

Second Stage Training and Classifications

Moving on to the second Stage classifications the training dynamics are presented in **Figure 5.16**. For both classification tasks, one separating D1 and D5 from D2 and the other D3 and D6 from D4 the networks achieve again very good scores with validation exceeding 97% in accuracy. The picture is reflected on the experimental validations as well, shown in **Figure 5.17**. Except minor cases in the D3 and D4 scenarios the classifiers managed to separate successfully D2 and D4 from their corresponding pairs.

Third Stage Training and Classifications

Finally, for the Stage III classification which aims to separate D1 from D5 and D3 from D6 the training dynamics are shown in **Figure 5.18**. This time however the picture is different and the classifier with the task to separate D1 from D5 has difficulty to reach good training and validation, achieving a score of around 84% for the first while the latter does not seem to reach over 65% suggesting an overfit. The loss curves as well follow the ill-conditioned classification problem. Adjusting the number of data examples and network parameters did not show to affect the results. The classifier with the task to separate D3 from D6 on the other hand showed a different picture resembling the training dynamics of the earlier Stages. The experimental validations are shown in **Figure 5.19**. The networks show a biased behavior towards the D1 class with all experimental cases of D5 misclassified. For the D3 and D6 separation however the networks were able to classify correctly both experimental states except for minor D3 misclassifications. As a complete picture, results from Stage I to Stage III showed that the classifiers were able to extract the correct trends from the rich feature space, simulating damage magnitude and material uncertainty with DTFs except the D1-D5 separation. Nevertheless, the learning results were reflected on the experimental validation for all cases.

In **Table 5.3** the correct and wrong classification scores are given for a total of 100 experimental inputs per case in the corresponding damage detection Stages of each case. **Table 5.4** is also given which contains predictions of the trained classifiers on numerical data for comparison.

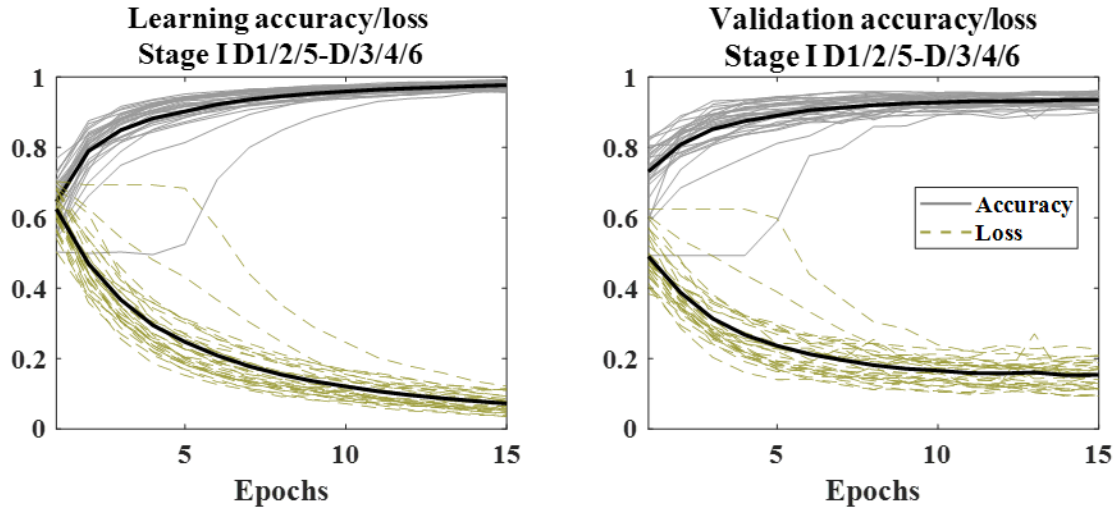


Figure 5.14: Accuracy (grey lines) and loss (gold lines) curves for randomly initialized backpropagations for the Stage I classifier. Black lines show the mean performance of accuracy and loss

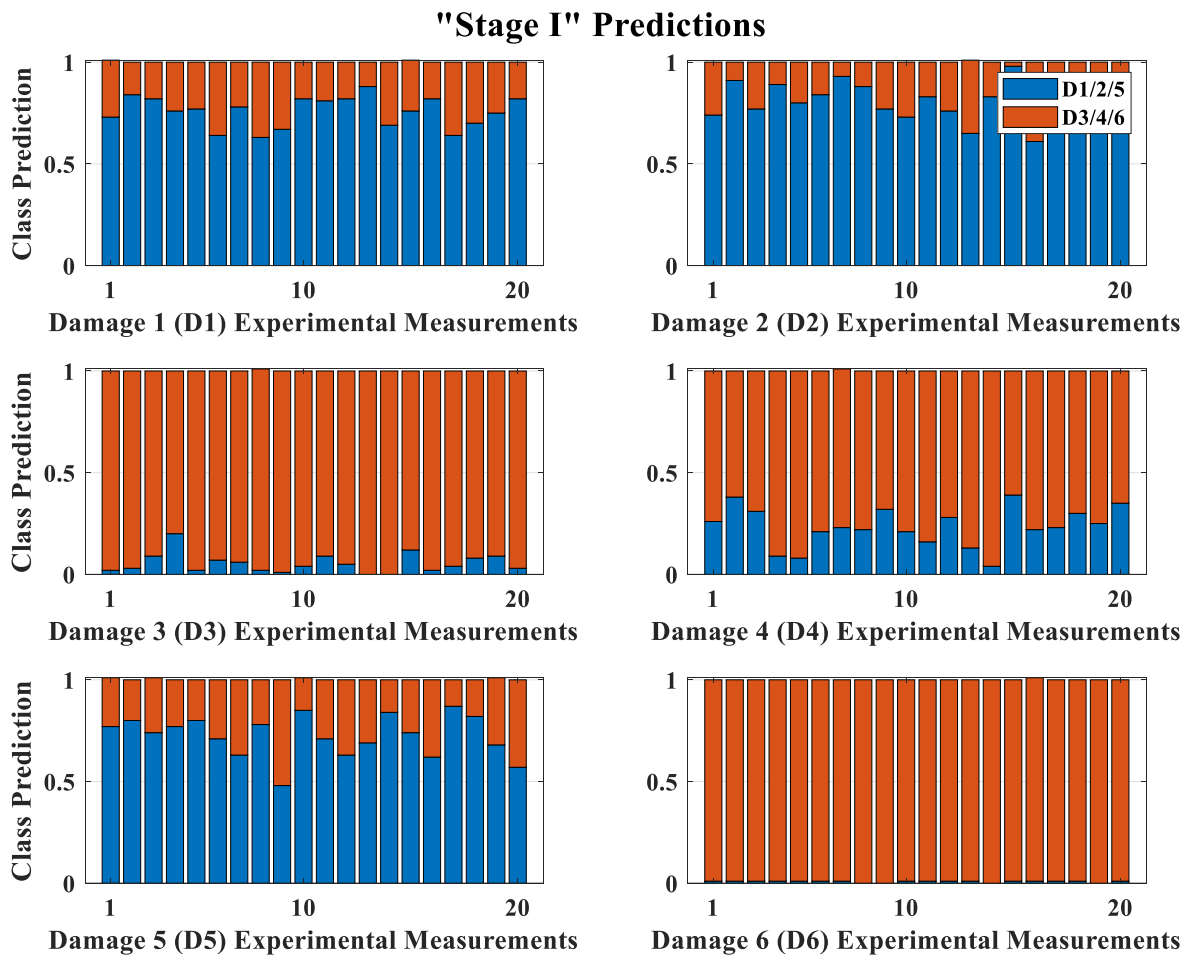


Figure 5.15: Stage I Predictions on experimental measurements from D1-D6 states

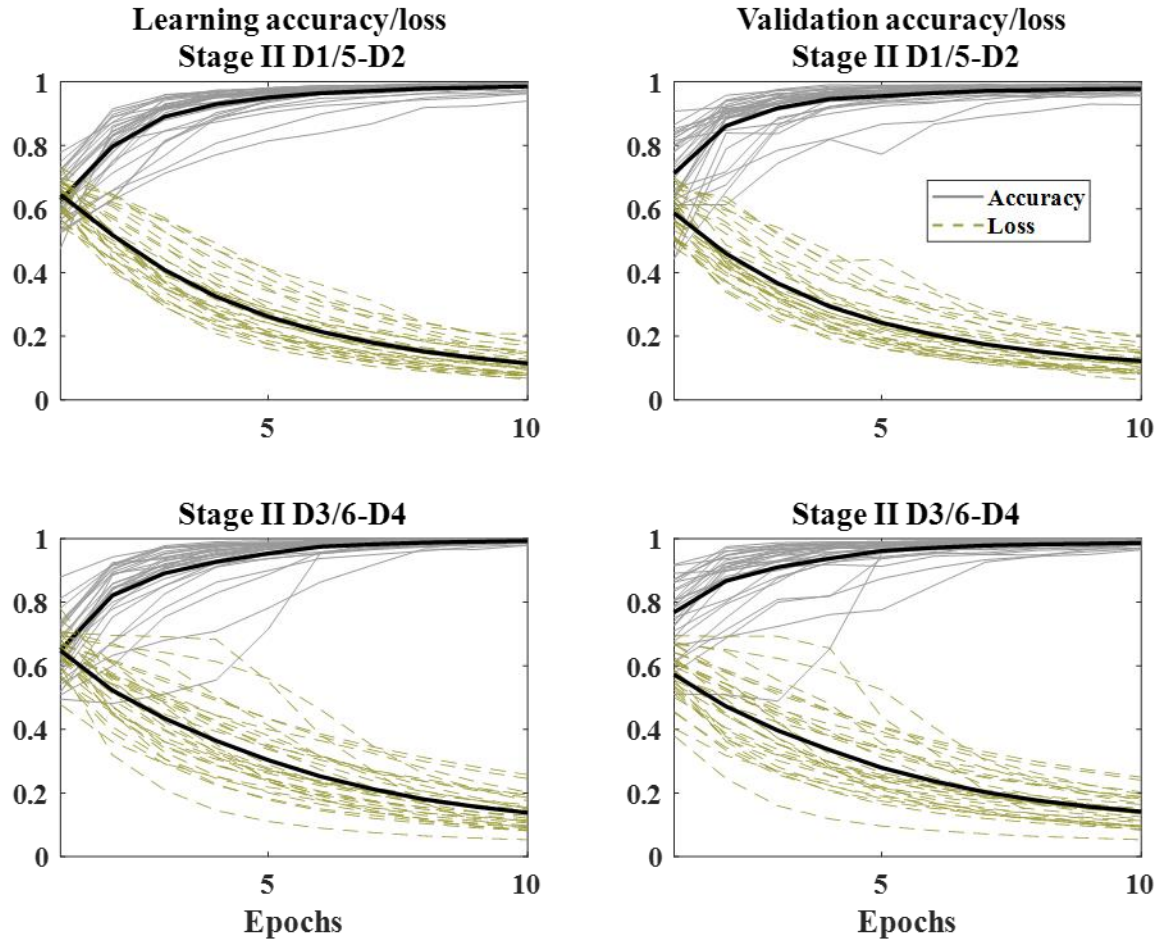


Figure 5.16: Accuracy (grey lines) and loss (gold lines) curves for randomly initialized backpropagations for the Stage II classifiers. Black lines show the mean performance of accuracy and loss

Table 5.3: Scores on experimental states predictions by trained classifier ensembles for a total of 100 inputs for each case

Experimental Input	Classified experimental inputs					
	Stage I		Stage II		Stage III	
	Correct	Wrong	Correct	Wrong	Correct	Wrong
Damage 1	100	0	100	0	100	0
Damage 2	100	0	100	0	-	-
Damage 3	100	0	96	4	92	8
Damage 4	100	0	88	12	-	-
Damage 5	100	0	100	0	0	100
Damage 6	100	0	100	0	100	0

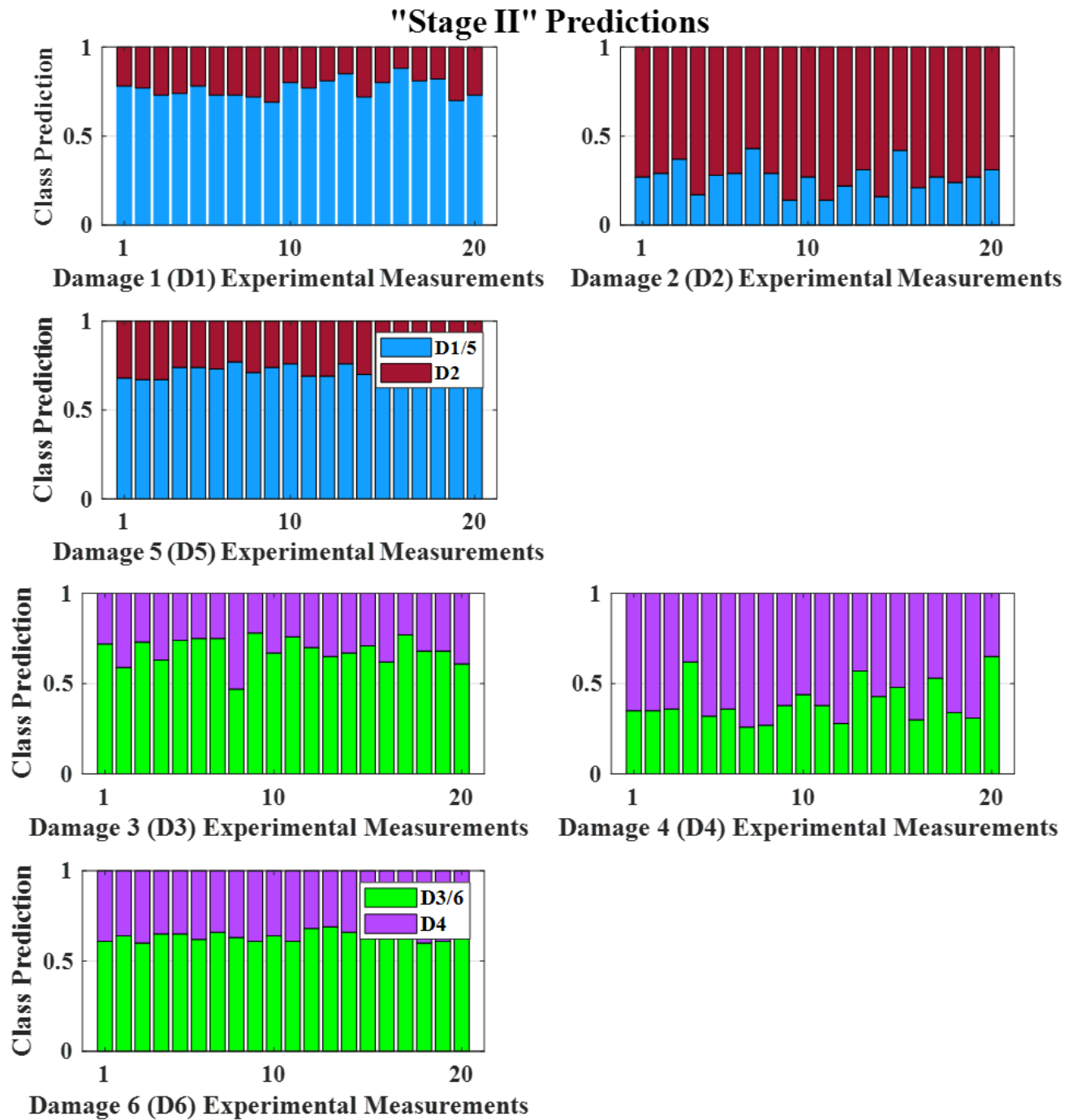


Figure 5.17: Stage II Predictions on experimental measurements from D1-D6 states

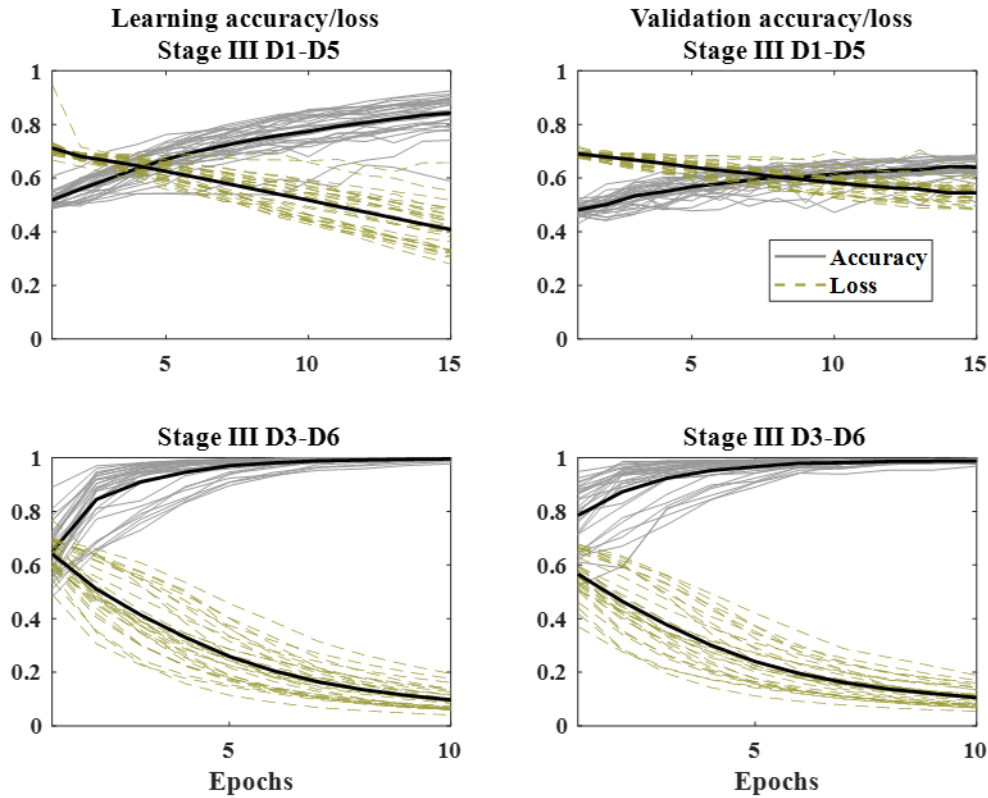


Figure 5.18: Accuracy (grey lines) and loss (gold lines) curves for randomly initialized backpropagations for the Stage III classifiers. Black lines show the mean performance of accuracy and loss

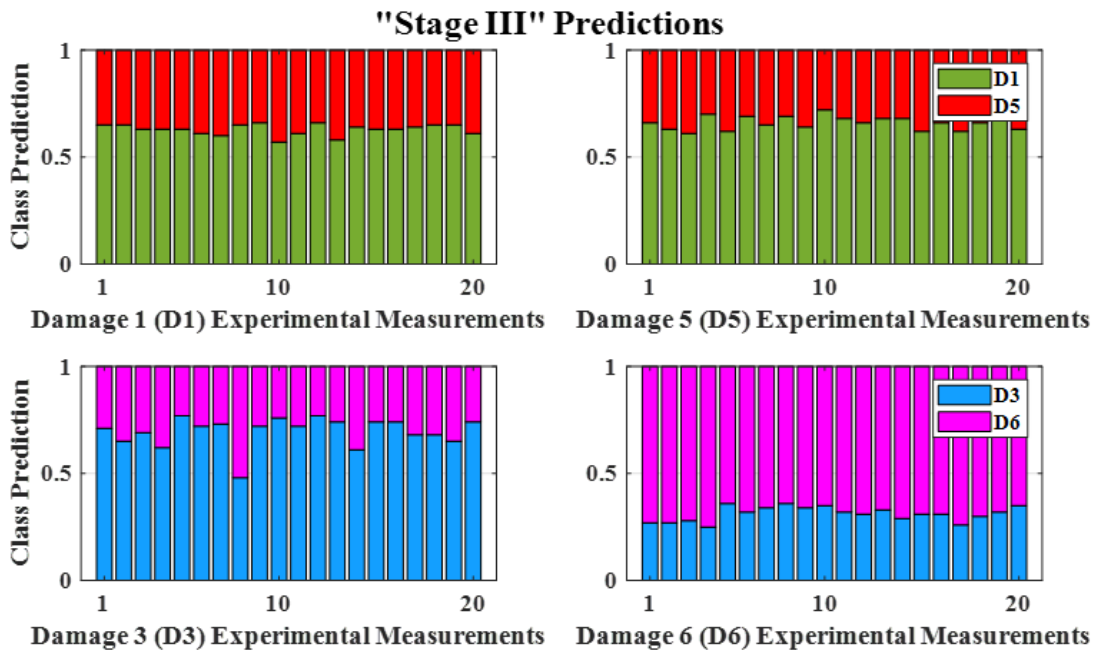


Figure 5.19: Stage III Predictions on the experimental D1-D5 and D3-D5 states

It has to be noted that the **Table 5.4** values are calculated by ensembles as well therefore the results may not be identical with the mean validations scores in the learning curves. The best generalization in terms of correct predictions difference between numerical and experimental classifications was observed for the first Stage. The largest differences were observed in the third Stage for the D1 to D5 separation. The training dynamics revealed however that the learning process was not as reliable as the others and that the asymmetric structure and loading conditions create different problems, meaning separating the D3 from D6 and D1 from D5.

Table 5.4: Scores on FE simulated states by trained classifier ensembles for a total of 100 inputs for each case

Numerical Input	Classified numerical inputs					
	Stage I		Stage II		Stage III	
	Correct	Wrong	Correct	Wrong	Correct	Wrong
Damage 1	98	2	98	2	88	12
Damage 2	97	3	100	0	-	-
Damage 3	100	0	98	2	96	4
Damage 4	98	2	100	0	-	-
Damage 5	98	2	99	1	63	37
Damage 6	98	2	100	0	100	0

5.5.3 Influence of Damage Magnitude Approximation value r

As discussed in paragraph 5.4.1 in order to investigate the effect of the simulated r value on the generalization the learning process is repeated, considering this time however data sets produced with a single r value rather than a range. The material uncertainty simulation is still kept at a +/- 15% uniform random deviation from the nominal material values. The training dynamics for data sets of $r = 0.6, 0.7, 0.8$ and 0.9 in Stage I classification are shown in **Figure 5.20**. The number of learning and validation examples has been kept the same as when a range of r was simulated in 5.5.1. The corresponding predictions on the experimental states are shown in **Figure 5.21** and **Figure 5.22**.

The training dynamics reveal that the learning problem is of less demand for the classifiers which could reach high learning and validation accuracies in less epochs than the classifiers of paragraph 5.5.2. The less populated input space when using single damage approximation constants r results as expected in less demanding classification problems for the simulated data sets. Exception is the dataset of $r = 0.9$ which showed that a damage separation problem cannot be established as good for such small damage magnitudes and resulted in overfitting and lower validation accuracy and loss. The predictions on the experimental inputs on the other hands show that the classifiers did not perform as well compared to the classifiers of paragraph 5.5.2. The best scores on the experimental states were recorded for $r = 0.6$ and $r = 0.7$ and gradually worsened from $r = 0.8$ to the completely biased $r = 0.9$. The total scores are given for 100 experimental inputs for each

case in **Table 5.5**. **Table 5.6** is given as well containing the predictions scores on numerical inputs from the trained classifiers.

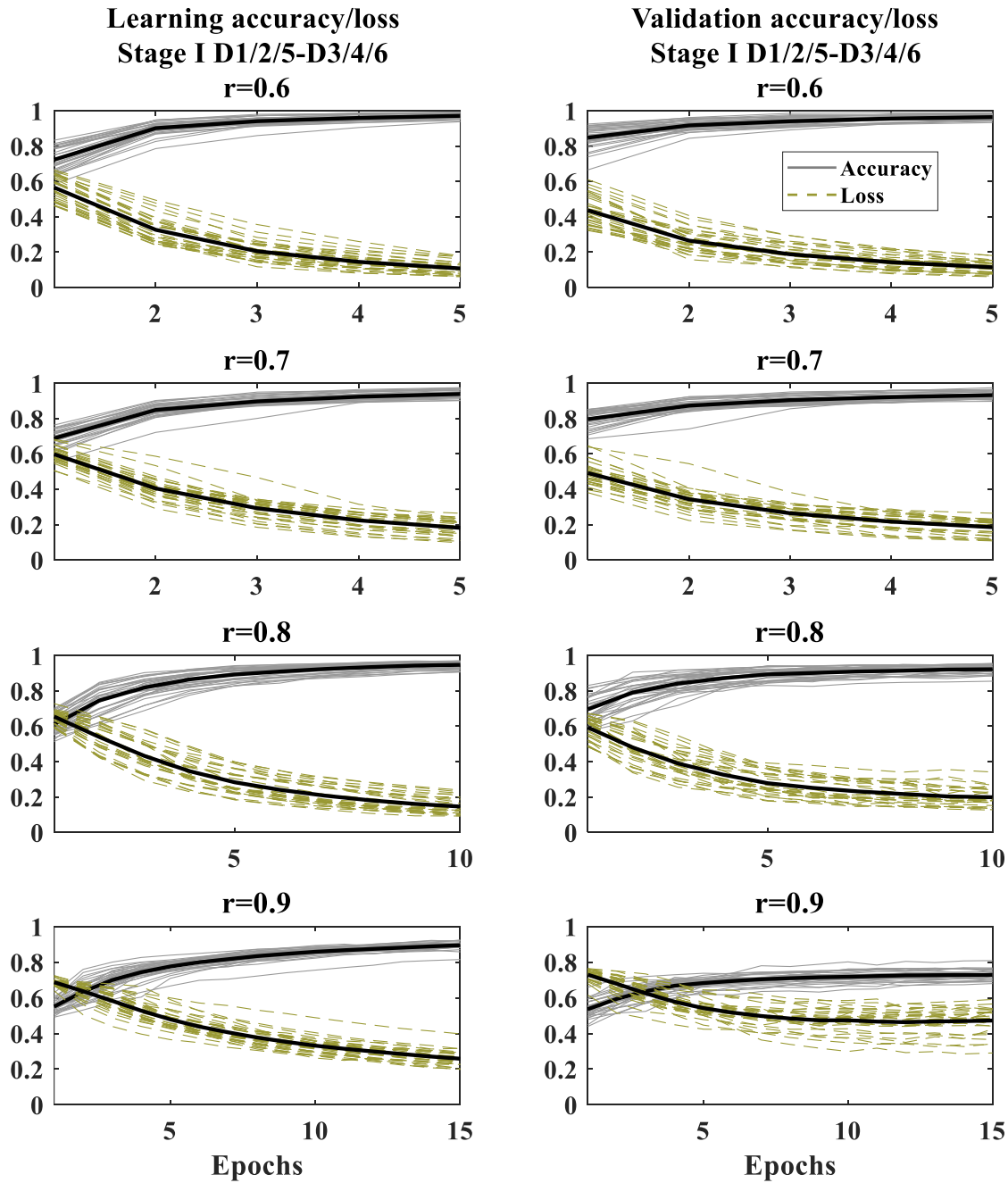


Figure 5.20: Accuracy (grey lines) and loss (gold lines) curves for randomly initialized backpropagations for the Stage I classifiers using single damage approximation constants r . Black lines show the mean performance of accuracy and loss

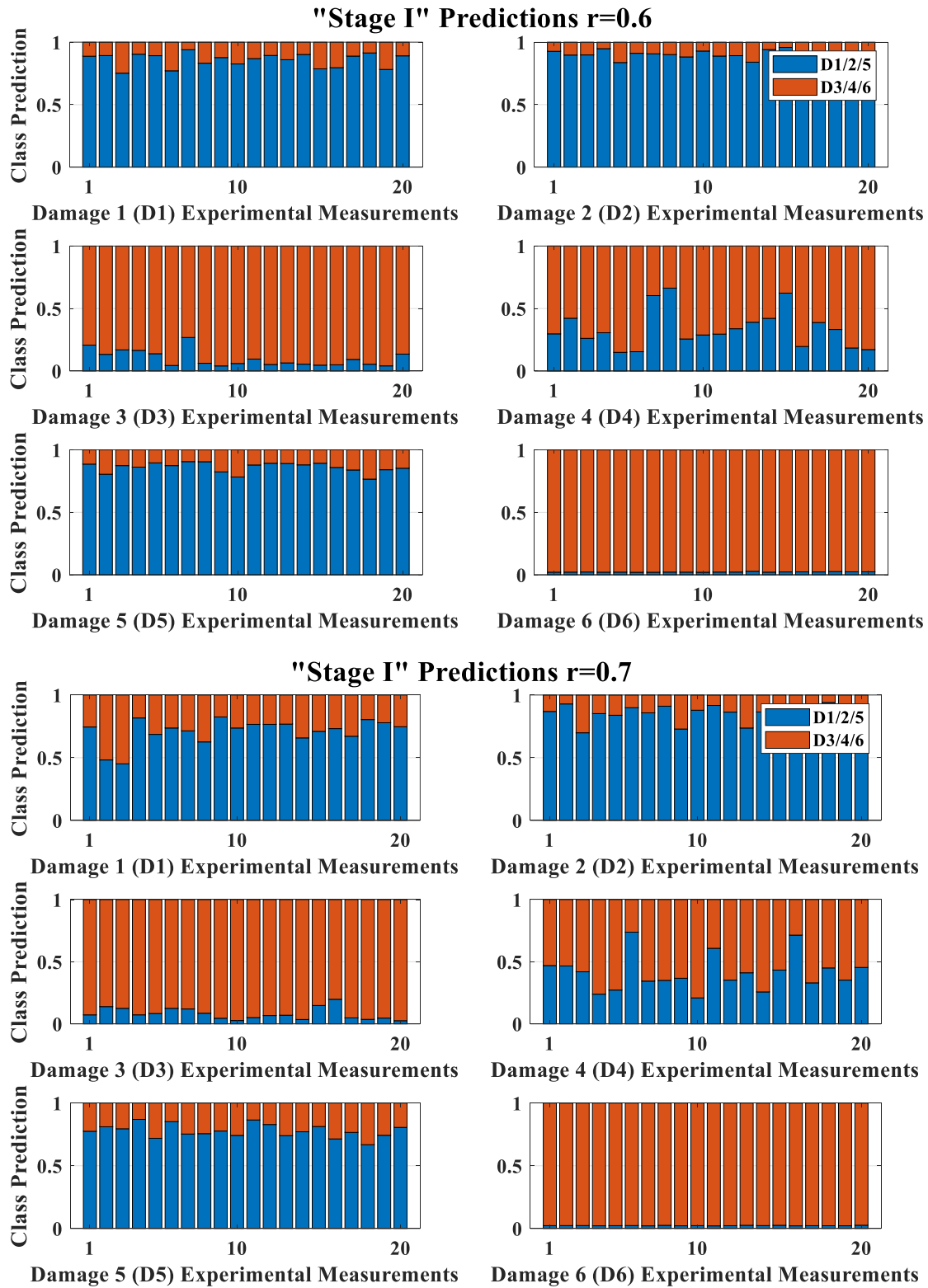


Figure 5.21: Stage I Predictions on experimental measurements from D1-D6 states using single damage approximation constants = 0.6 and 0.7

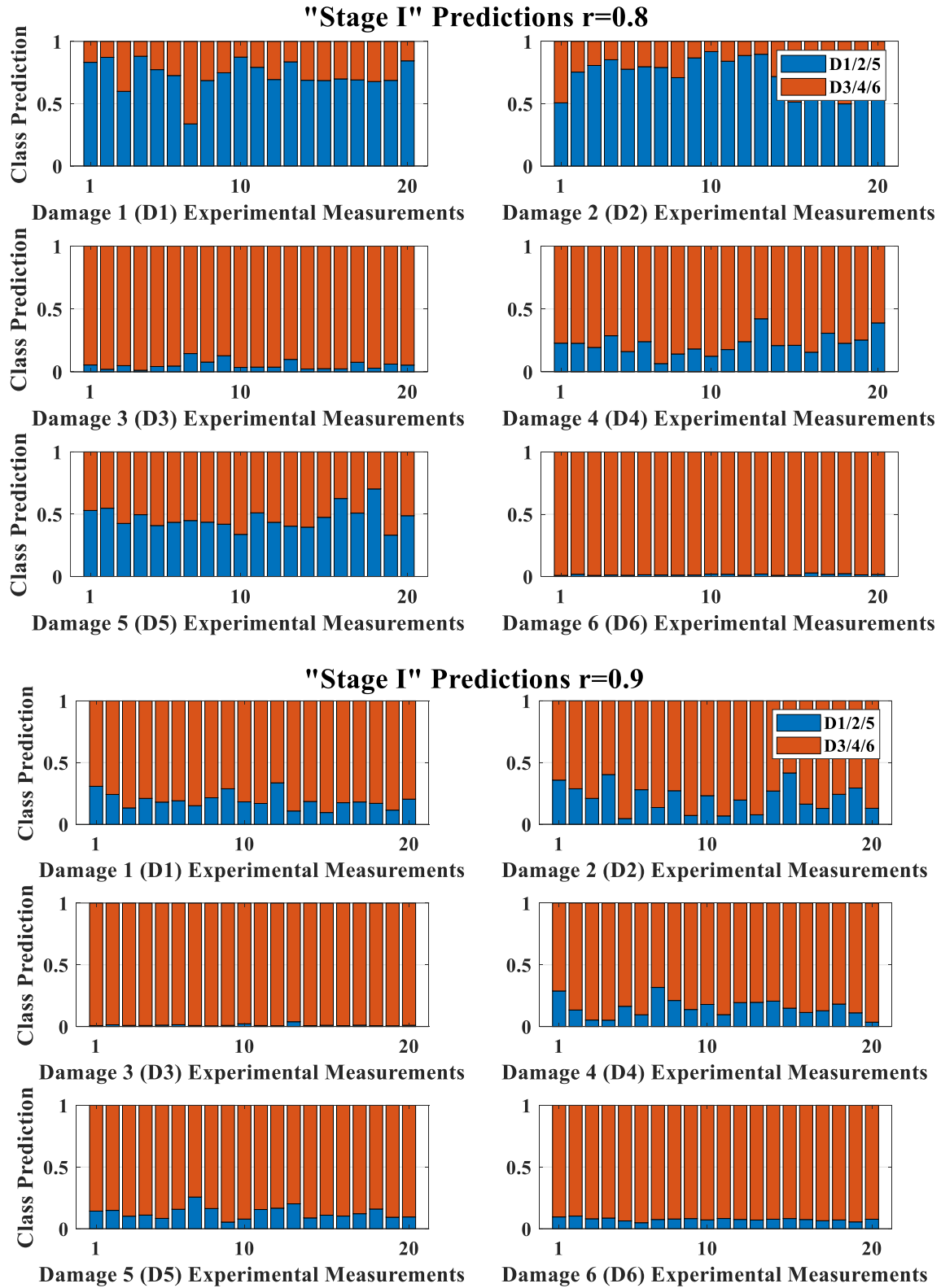


Figure 5.22: Stage I Predictions on experimental measurements from D1-D6 states using single damage approximation constants = 0.8 and 0.9

Table 5.5: Scores on experimental states predictions by trained classifier ensembles with single damage approximation constants r for a total of 100 inputs for each case

Experimental Input	Classified experimental inputs for Stage I							
	r=0.6		r=0.7		r=0.8		r=0.9	
	Correct	Wrong	Correct	Wrong	Correct	Wrong	Correct	Wrong
Damage 1	100	0	98	2	96	4	0	100
Damage 2	100	0	100	0	95	5	0	100
Damage 3	100	0	100	0	100	0	100	0
Damage 4	87	13	88	12	100	0	100	0
Damage 5	100	0	100	0	66	34	0	100
Damage 6	100	0	100	0	100	0	100	0

Table 5.6: Scores on FE simulated states by trained classifier ensembles for a total of 100 inputs for each case with single damage approximation constants r for a total of 100 inputs for each case

Numerical Input	Classified numerical inputs for Stage I							
	r=0.6		r=0.7		r=0.8		r=0.9	
	Correct	Wrong	Correct	Wrong	Correct	Wrong	Correct	Wrong
Damage 1	100	0	97	3	96	4	84	16
Damage 2	100	0	99	1	96	4	80	20
Damage 3	98	2	98	2	95	5	81	19
Damage 4	93	7	94	6	97	3	68	32
Damage 5	100	0	97	3	99	1	76	24
Damage 6	99	1	100	0	98	2	84	16

The generalization is showing to decline with increasing r value, with $r = 0.9$ being the worst as expected from the training dynamics and $r = 0.6$ and 0.7 the best with similar performance. However, marginally not as good as the classifiers trained with a range of damage magnitude approximation in paragraph 5.5.2.

5.5.4 Influence of Material Uncertainty Simulation

To investigate the effect of the simulated material uncertainty magnitude on the generalization, as discussed in paragraph 5.4.1, the learning process is repeated considering this time however a data set produced with simulation of 3% instead of 15% material uncertainty as per Algorithm 5.1. Training dynamics are given in Figure 5.23. The number of training examples have been kept the same as in paragraph 5.5.1.

The predictions on the experimental states for Stage I are given in Figure 5.24. The classification problem is shown again to be less demanding compared to the 15% material uncertainty simulation datasets of paragraph 5.5.1, operating now on a less populated and complicated input space. The classifiers were able to reach within 10 epochs high accuracy and low loss. The performance on the experimental validation however suffers with less confident and accurate predictions on the experimental states, except the D3 and D6 cases which showed to be the most confident predictions

for the classifiers throughout this work. The total performance on the experimental inputs classifications is given in **Table 5.7**.

Table 5.8 is finally given showing the predictions on numerical inputs from the trained classifiers. The specific case of less material uncertainty simulation presents the worst generalization from numerical to experimental data for all scenarios except D3 and D6, which however did not seem to be predicted wrongly thought all datasets.

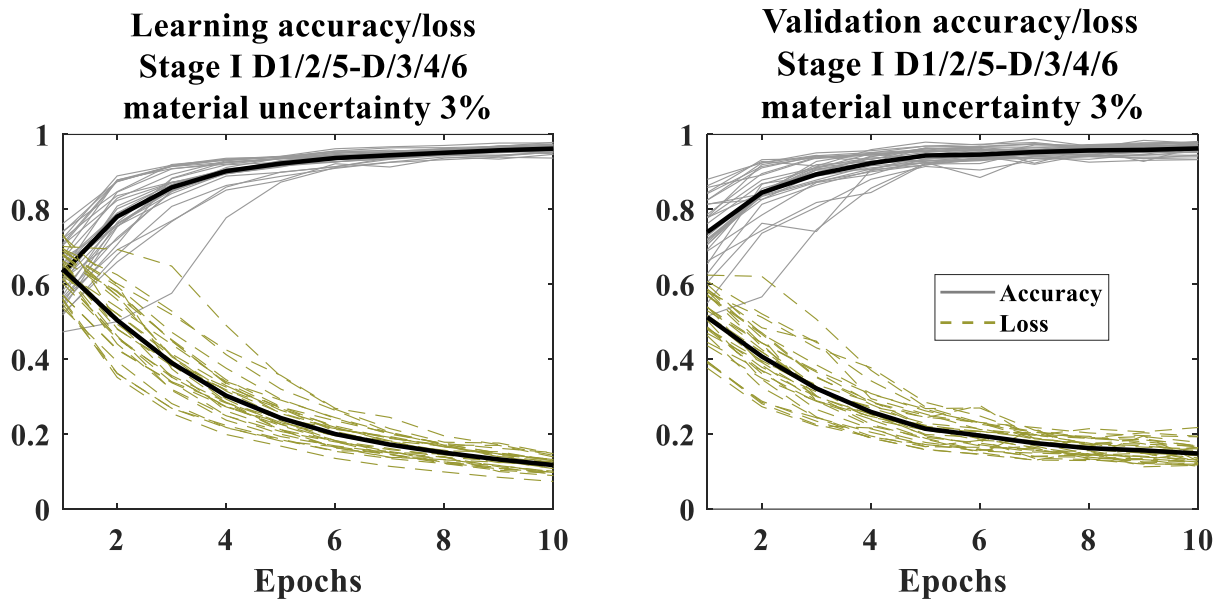


Figure 5.23: Accuracy (grey lines) and loss (gold lines) curves for randomly initialized backpropagations for the Stage I classifiers using material uncertainty simulation of 3%. Black lines show the mean performance of accuracy and loss

Table 5.7: Scores on experimental states predictions by the trained classifier ensemble with 3% material uncertainty simulation for a total of 100 inputs for each case

Experimental Input	Classified experimental inputs for Stage I	
	Material uncertainty 3%	
	Correct	Wrong
Damage 1	68	32
Damage 2	70	30
Damage 3	100	0
Damage 4	79	21
Damage 5	77	23
Damage 6	100	0

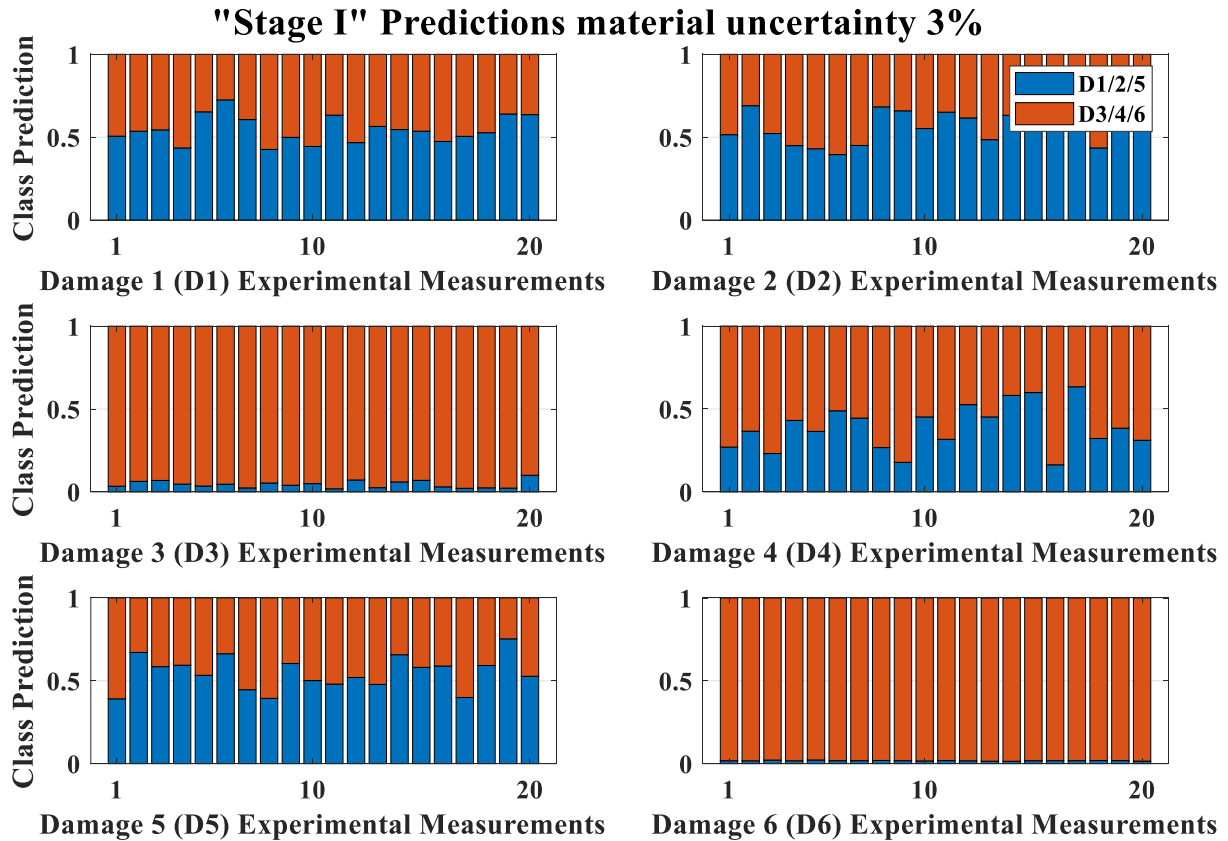


Figure 5.24: Stage I Predictions on experimental measurements from D1-D6 states using material uncertainty simulation of 3%

Table 5.8: Scores on FE simulated states by the trained classifier ensemble with 3% material uncertainty simulation for a total of 100 inputs for each case

Experimental Input	Classified experimental inputs for Stage I	
	Material uncertainty 3%	
	Correct	Wrong
Damage 1	99	2
Damage 2	95	5
Damage 3	99	1
Damage 4	97	3
Damage 5	100	0
Damage 6	100	0

5.6 Discussion

In the considered damage identification problem of the test structure in this chapter, different results of various aspects were obtained. First and foremost, it was shown that a FEM model can reproduce the trends of experimental DTFs for small and not precisely defined damages on the CFRP members by simulating lowered stiffness on the affected members, as in **Figure 5.11**.

However, this approximation alone was not enough to achieve the best performance and generalization on the predictions of the corresponding experimental states. Two independent factors affect the predictions, namely the exact damage magnitude and the model error. Both factors were proposed to be tackled by simulating different stiffness reductions on the affected members and material uncertainty resulting in labeled multi-example datasets. The repetitive variation of model parameters resulted in a populated input space as shown in **Figure 5.12** which tasked CNN classifiers to find the appropriate features that validate damage identification on the simulated datasets. The effect of variation in damage magnitude and material uncertainty showed to be critical for better experimental generalization according to the hypothesis formulated in paragraph **5.4.1**. The comparison was given for Stage I damage identification.

The classifier trained by a range of stiffness approximation constants r , shown in **Figure 5.14** and **Figure 5.15**, outperformed the classifiers trained by single r values, in **Figure 5.21-Figure 5.23**, which showed classification boundaries shifting in some scenarios. For example, r values from 0.6 to 0.7 showed some problems in classifying correctly Damage 4 while $r=0.8$ had difficulties in the Damage 5 case. It can be regarded therefore that the dataset with a range of values provided the correct combination of features, also with included values of $r = 0.9$ which did not provide any useful information when used individually in the dataset. Material uncertainty on the other hand played a crucial role and when simulated with 3% instead of 15%. As shown in **Figure 5.23** and **Figure 5.24**, generalization to experimental states suffered. In terms of mismatch between numerical and experimental inputs predictions the generalization is presented in **Table 5.9** to complete such a picture of comparison. The values in the table were calculated from the results of **Table 5.3-Table 5.8** as:

$$mismatch = \frac{|Correct_{Experimental} - Correct_{Numerical}|}{Correct_{Numerical}} \quad (5.6)$$

Table 5.9: Generalization from numerical to experimental data in terms of mismatch between correct classification scores for numerical and experimental inputs

	Highest mismatch in correct predictions between numerical and experimental inputs for Stage I	
Dataset used	Mismatch %	Damage case
$r = 0.6-0.9$ and 15% material uncertainty	3	D2
$r = 0.6$ and 15% material uncertainty	6	D4
$r = 0.7$ and 15% material uncertainty	6	D4
$r = 0.8$ and 15% material uncertainty	33	D5
$r = 0.9$ and 15% material uncertainty	100	D1
$r = 0.6-0.9$ and 3% material uncertainty	31	D1

Additionally, the Receiver Operating Characteristics (ROC) curves are provided in **Figure 5.25** that sum up the classification comparisons in experimental state prediction between the different

training datasets. The ROC curves are used to show the True Positive to False Positive Ratio potential in classification for different decision thresholds. The ideal classifier has a curve following the top left corner while a random prediction classifier follows the diagonal. Classifiers trained with either less material or r-value uncertainty simulation diverge from the ideal in this useful straightforward comparison. Therefore, the classification with simulated training datasets that include deviations from the healthy state TF functions can be greatly improved when including a rich input feature space, as validated in the mismatch values and ROC curves.

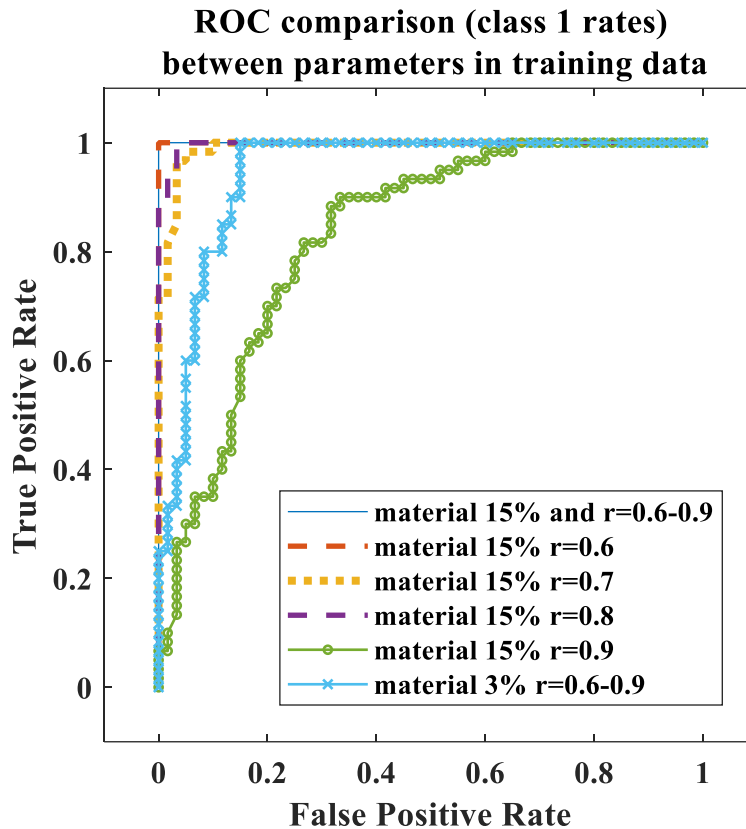


Figure 5.25: ROC curves of the experimental class prediction performance in the Stage I comparison

It is worth finally mentioning that the datasets simulated with uncertainty proved to generalize well even in cases where the classifier failed to separate the simulated data correctly as in Stage III D1 from D5. Overfitting was observed in the training dynamics of **Figure 5.18** and was directly reflected in the predictions of **Figure 5.19** showing a bias towards D1 class. The simulated D1 to D5 classes were considered closely similar for the classifier which failed to find a robust solution. The limitations of the methodology may therefore appear in cases where separation of similar damages is requested. The training dynamics curves can contain useful information on that aspect as was shown in the results of paragraph 5.5.1. The reader may also notice the effect of asymmetry in the structure and loading with the D3 and D6 cases of Stage III classification which might initially seem to resemble D1 and D5, establish a more robust separation. Finally, the tested

simplified damage approximation by evenly reducing the material parameters E_1 E_2 G_{12} G_{1z} G_{2z} could possibly be applied with different reduction percentages per material value that could fit other types of problems as a subject of future studies.

5.7 Conclusions

In the present chapter a model-based methodology was presented where a damage identification problem was formulated on a test CFRP truss structure. The damages were created by a three-point bending test on the CFRP members that affect the total stiffness of the structure in a small degree. Goal was to investigate the feasibility of DTF as pre-processed input features and study the effect of uncertainty in parameters simulation during the data generation state

Training data in the form of deviations (DTF) from the healthy state TF functions by FEM simulations showed to carry the appropriate information to the DL CNN classifier in order to perform the damage identification tasks, finally validated on corresponding experimental responses.

Both damage magnitude approximation and material parameters uncertainty simulation affected positively the numerical to experimental generalization. A high degree of reliability of the methodology was observed when the dataset was enriched correctly, concluding that FEM simulated responses have potential to provide SHM training data for small and not precisely defined damages.

The exact influence of simulating deviations in TFs instead of providing TFs directly was not studied in the present chapter and could be a suggestion for future work.

Effect of Model Error in Reliability of Supervised Classifiers for Damage Identification Trained by Finite Element Simulations

Contents from Original Paper: Seventekidis, P., & Giagopoulos, D. Model Error Effects in Supervised Damage Identification of Structures with Numerically Trained Classifiers (Under Review, *Mechanical Systems and Signal Processing*)

ABSTRACT

Advances in the field of Structural Health Monitoring (SHM) include model-based approaches with numerically generated responses by Finite Element (FE) simulations. The simulated data may be used for supervised training of Machine Learning classifiers to perform damage identification on some later experimental state. The reliability of the numerically trained classifiers depends on the quality of the training data in terms of the model error contained. Even though FE models can be updated on the intact state for better accordance with the experiment, some model error still remains for most complex structures. This error can limit the ability of generalization to the unmeasured yet damaged experimental states according to how distinct they are. In the present work, the effect of model error on subsequent classification of experimental damaged states is tested for a lab-scale bridge truss. A Convolutional Neural Network classifier is applied, trained by FE responses. Results show that larger and more distinct damages can be classified with more accuracy compared to small and less distinct, with the latter showing higher prediction bias. The numerical data reliability is found to be indicated when comparing the intact state numerical and experimental feature map shifts

Keywords: Damage Identification, Deep Learning, Machine Learning, Structural Health Monitoring, Vibration Measurements, Structural Dynamics

6.1 Introduction

The present chapter addresses probably the most important point in simulation-based data Structural Health Monitoring (SHM) and damage identification, which is the reliability assessment of classifiers trained on numerical data due to model error. In the previous chapters different techniques were tested in order to improve experimental generalization for damage identification. However, it would be of most importance to investigate a potential reliability estimation before the actual damage occurs. Goal of the present chapter is to study how model error contained in the simulated training data reflects to experimental generalization and how the reliability may be estimated in advance.

Model error in data will be the main cause of mismatch between numerical training data stage and experimental validation with corresponding damages. Minimizing the model error, meaning improving the agreement of a model generated response with the corresponding experimental with model updating, was described in **Chapter 1** and **2**. Model updating is a major engineering field and literature already contains reported cases in lab scale [21] or large civil [45] and aerospace structures [47]. In practice however, it might not be feasible to acquire an updated FE model that is perfectly fit to the experimental set up for all kind of structures. Reasons can be problem specific, such as quasi periodic structures where modes clustered around an area of interest make model updating challenging [51] or more general uncertainties [52] such as the constitutive law used or the FE simplifications. Therefore, great effort and computational time might be necessary to acquire a model capable of generating data for arbitrary SHM tasks. In such cases, the engineer might have to exploit the potential of the available model for numerical data production acknowledging the model error it carries. This fact was considered already in the early model-based approaches with Artificial Neural Networks (ANNs) where the authors tried to fabricate input features less prone to error for damage detection [42]. The question therefore rises as how small of damage magnitude can be detected with a model-based approach of a certain model accuracy, or in other words how reliable is the numerically generated data in order to generalize to the experiment. A rigorous mathematical formulation was presented in [44] that connected model error in training data to expected performance on the corresponding experimental classification problem. Measures of robustness to data uncertainties were proposed, that if calculated for a classification problem, the relation of error magnitude to the online or experimental performance can be estimated.

In the present chapter, the case of supervised FE model-based damage identification of a structure with DL is studied. The FE model is updated on the experimental intact or healthy state and used for simulating the unmeasured yet experimental damages. The trained classifier is finally tested on the real experimental states. It is investigated how the model error and distinct damage magnitude relate to the reliability of the numerical data. For supervised learning, meaning that vibration data is provided along with damage status labels, the model error included in the vibration signals can introduce classification error or bias when the DL model tries to generalize to the experiment. Improving generalization is one of the early fields of research in ANNs [126]. This concerns also

more recent works that test different techniques and network architectures [39,127,128], while others study the phenomenon in detail with metrics for expected generalization [38]. However, generalization from model to unknown experimental data is a more complex task as it contains the effect of model error. That means SHM problems with simulated data are in essence problems of extrapolation from the numerical to the experimental state.

In case the error present in the numerical data consistently shifts the feature maps of the later tested experimental inputs, bias phenomena will be become important as acknowledged also and explained in [44]. Such a problem is investigated in the current chapter for an experimental lab-scale bridge structure for which a not so perfect FE model is used for data generation. One task is the identification of small damages and another task the identification of larger ones. The relation of the similarity between the reference healthy states of the numerical and experimental systems with the data reliability is studied. The margin of allowed model error is evaluated in that way assuming that the intact states will be more similar to each other when a larger damage is present. It may be already natural to think that the greater the damage, the less perfectly fit model is necessary. Alternatively, classification boundaries [44] may be trained to be more robust to errors in more distinct separation cases. This is specifically tested for the presented lab-scale truss. The novelty of the present chapter is given therefore as the study of model error phenomena on the experimental generalization for numerically based DL damage identification, based on healthy state similarity and difficulty of the classification problem.

The manuscript continues in the following Sections. In section 6.2 where the description of biased behavior due to model error in the numerical to experimental generalization with an ANN classifier is described. It is shown also how similarity between the intact states is proposed to be evaluated. Next, in the section 6.3, the lab-scale physical structure along with the corresponding detailed FE model is presented. The damage scenarios are provided as well. In section 6.4, the data generation and classification results are given when a numerically trained DL classifier is validated against the experimental measurements for the small and large damage magnitude problems. Further, in section 6.5, a simplified numerical model is benchmarked in different data sets that progressively distance from a reference set. The purpose is to validate additionally the bias evolution effects and index as we move further from an “exact” solution space, to a space of solutions with increasing errors. Sections 6.6 and 6.7 are the discussions and conclusions of the chapter.

6.2 Bias Estimation with Feature Map Similarity Assessment

In section 2.3 it was explained how a Convolutional Neural Network (CNN) in Forward Propagation (FP) filters inputs signals and produces high level feature maps h that are used after as inputs in the perceptron layers for classification of the possible damage.

The FE generated training data for damage classification however contains model error, meaning that the expected feature maps of the numerical data used in training may not overlap with

subsequent experimental or online feature maps. The behavior of the numerical and experimental feature map disagreement can induce therefore classification errors during the online stage and biased behavior when the feature map shift is presented consistently in one direction. Bias is meant this time as the tendency of the model to favor a specific class prediction, not to be confused with neuron bias in equations (2.11) and (2.14) (which is a learnable network parameter). In other words, it is meant that a model-based data set may not generalize correctly on the experiment.

For example, assume a binary classification problem where training data generated by simulations with expected feature maps h_{model} forms a decision boundary [87] given by equation $\mathbf{W}h + b = 0$, shown in **Figure 6.1**. \mathbf{W} and b are the classification weights and neuron bias respectively, learned during training on the numerical data. During the online or experimental data testing stage, depending on the mismatch between the numerical training responses and the unknown up to this stage experimental, the feature maps h_{exp} can have a shift towards the class boundary. This shift can induce biased predictions. A simplified depiction in **Figure 6.1** shows an example of biased predictions when the numerically trained classifier may try to generalize on the physical states. The shift, appears as a smaller distance d_2 of the Class 2 experimental feature maps to the decision boundary, compared to the expected feature maps d_1 . This inherits a Class 1 bias towards the online testing. According to the simplified example presented the following questions may rise in applications of model-based data for training.

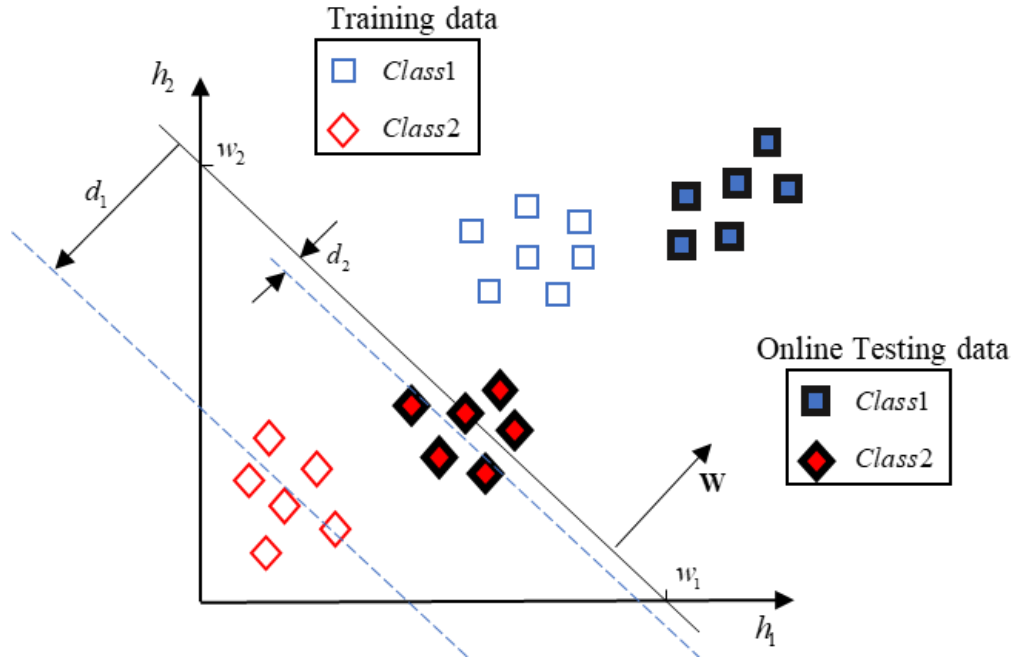


Figure 6.1: Decision boundary for a binary classification problem where online testing data shows shifted feature maps towards the numerical that have been used in training

First, whether or not model error will always inherit a consistent shift behavior on experimental feature maps and not some inconsistent disagreement. Given the fact that the learned convolutional weights that produce the feature maps together with the classification boundaries depend on the characteristics of the labelled numerical signals (which in turn have unknown model error compared to the unmeasured candidate damage) there can be no analytical formulation to answer that in advance. Results in previous chapters, for example **Figure 3.7**, **Figure 4.24** and **Figure 5.22**, have shown that when numerical classifiers were tasked difficult damage identification problems, biased experimental generalization was common. That means the expected feature maps between the classification boundary did not leave much space for feature map shift which happened in a consistent direction. A probabilistic error and bias analysis have been provided rigorously in [44]. In the present chapter, the feature map shift behavior is studied posteriori and is validated for a large number of cases in the tested damage scenarios. It cannot be however assumed that the same behavior will be followed unconditionally in all kind of simulation databased approaches. Further research can be encouraged on that to obtain more data on such problems.

Second, an important fact to consider is whether or not a comparison on the intact state responses between model and physical structure can provide estimates on the online feature map shift. This may indicate the “effective” model error as a function of the difficulty of the damage classification problem. It can be though that more distinct damages can actually allow more model error or in other words induce less feature map shift. For that reason, the feature maps of the healthy states produced by the damage separation classifiers are compared. It is expected to reveal a relation between shift in healthy states with shift in damage states. The logic is that healthy states used as input in damage separation classifiers carry no damage information and can be considered as a measure of a starting point for model and experimental responses. The basis of the methodology is as follows.

For a binary classification problem again, in the separation of two damage states D_1 and D_2 a CNN can be trained on dataset (6.1) originating from a repetitive load case algorithm, such as Algorithm 6.1.

$$\mathbf{Train_set} = \{(\mathbf{A}_{1,1}, \mathbf{Y}_{1,1}), (\mathbf{A}_{1,2}, \mathbf{Y}_{1,2}), \dots, (\mathbf{A}_{n,s}, \mathbf{Y}_{n,s})\} \quad (6.1)$$

The Algorithm operates on the FE equations of motion (6.2) as was described in section 2.2 (and used throughout **Chapters 3, 4** and **5**) for a solution of:

$$\mathbf{M}(\rho)\mathbf{A} + \mathbf{C}(\mathbf{M}, \mathbf{K}, \alpha, \beta)\mathbf{V} + \mathbf{K}(E)\mathbf{U} = \mathbf{F} \quad (6.2)$$

where \mathbf{A} , \mathbf{V} and \mathbf{U} are the global acceleration, velocity and displacement vectors respectively. \mathbf{M} , \mathbf{C} and \mathbf{K} represent the global mass, damping and stiffness matrices of the structure that depend on the model parameters of density ρ , damping α, β and elasticity E . \mathbf{F} is the loading vector. According to Algorithm 6.2, the data will consist of $n \cdot 2$ responses (for the binary separation $s = 2$) in total, or n models that have the same sampled properties to generate 2 cases, namely

D_1 and D_2 . The damage cases can be thought therefore as the responses from a common Healthy case model that is altered accordingly with deviations $\Delta\mathbf{M}$, $\Delta\mathbf{C}$ and $\Delta\mathbf{K}$ on the equations of motion of (6.3) as:

$$\begin{aligned} \mathbf{M}\ddot{\mathbf{X}}(\mathbf{t}) + \mathbf{C}\dot{\mathbf{X}}(\mathbf{t}) + \mathbf{K}\mathbf{X}(\mathbf{t}) &= \mathbf{F}(\mathbf{t}) \rightarrow \ddot{\mathbf{X}}(\mathbf{t})_{\text{healthy}} \\ (\mathbf{M} + \Delta\mathbf{M}_D)\ddot{\mathbf{X}}(\mathbf{t}) + (\mathbf{C} + \Delta\mathbf{C}_D)\dot{\mathbf{X}}(\mathbf{t}) + (\mathbf{K} + \Delta\mathbf{K}_D)\mathbf{X}(\mathbf{t}) &= \mathbf{F}(\mathbf{t}) \rightarrow \ddot{\mathbf{X}}(\mathbf{t})_D \end{aligned} \quad (6.3)$$

The response signals of D_1 and D_2 can decompose also in a Healthy response signal $\ddot{\mathbf{X}}(\mathbf{t})_{\text{healthy}}$ and a deviation $\Delta(\mathbf{t})$ as $\ddot{\mathbf{X}}(\mathbf{t})_D = \ddot{\mathbf{X}}(\mathbf{t})_{\text{healthy}} + \Delta(\mathbf{t})$. A well-trained CNN, will be able to extract the useful characteristics which lie in the signal deviation $\Delta(\mathbf{t})$ and not contained in the common for both classes healthy state $\ddot{\mathbf{X}}(\mathbf{t})_{\text{healthy}}$.

Algorithm 6.1: Numerical model data generation algorithm

Input: Number of load cases n and statistical bounds for each parameter

$\rho, \zeta, E, \alpha, \beta$

Output: n number of vibration responses and health labels s

```

15. for  $i = 1 : n$  do
16.   sample  $E \rightarrow \mathbf{K} = \mathbf{K}(E)$ 
17.   sample  $\rho \rightarrow \mathbf{M} = \mathbf{M}(\rho)$ 
18.   sample damping  $\alpha, \beta \rightarrow \mathbf{C}(\mathbf{M}, \mathbf{K}, \alpha, \beta)$ 
19.   for  $j = 1 : s$  do
20.     define Health status  $\rightarrow \mathbf{Y}_{i,j}$ 
21.     define loads  $\rightarrow \mathbf{F}$ 
22.     solve  $\mathbf{M}\mathbf{A} + \mathbf{C}\mathbf{V} + \mathbf{K}\mathbf{U} = \mathbf{F}$  and calculate accelerations  $\rightarrow \mathbf{A}$ 
23.     return  $\mathbf{A}_{i,j}$  and  $\mathbf{Y}_{i,j}$ 
24.   end
    
```

The highest level feature map h out of the convolutional component (explained in section 2.3) will follow the mapping $H(\ddot{\mathbf{X}})$ of the input signal as:

$$H(\ddot{\mathbf{X}}(\mathbf{t})_{\text{healthy}} + \Delta(\mathbf{t})) = h \quad (6.4)$$

where with H the complete convolutional layers processing is noted. Using a Healthy case signal in a network trained for Damage separation, the “zero” input or bias feature map h_0 is calculated for the selected case since there is absence of $\Delta(\mathbf{t})$ that would carry the classification information:

$$h_0 = H(\ddot{\mathbf{X}}(\mathbf{t})_{\text{healthy}}) \quad (6.5)$$

The comparison of zero input feature maps in equation (6.5) is benchmarked as an indicator of subsequent feature map shift in damage states. Results are provided in the present chapter in that

way as how the network perceives the model error for small and more distinct damages. Feature maps will be compared for a large number of FE solutions, as well as the available experimental, to validate a common behavior that can be useful in working towards a future reliability index. The reader should also notice that how distinct damage cases might be does not only depend on the magnitudes but on the sensor network as well. The SHM literature reports different cases of sensor network optimization for this cause on simple perceptron ANNs [129] or more complex graph neural networks that may pay more attention in the spatial relations between sensors [34]. Optimal sensor placement is considered a fundamental component of monitoring systems design [61,130] in any case.

6.3 Experimental Set-up and Finite Element Model

In the present Section the experimental set-up, the FE model used and the damage scenarios are presented.

6.3.1 Physical Test Structure

The test structure consists of a bridge like truss of steel beam members with nominal thickness of 2 mm, bolted on steel connections and mounted finally on cement blocks. A picture is shown in **Figure 6.2** with the basic external dimensions noted. The installed accelerometer sensor network and the excitation equipment is also shown. Excitation is provided with impacts on the noted location along direction X. The coordinate system orientation is provided as well and the X axis is considered perpendicular to the length direction of the structure. The sensor network was chosen with the available equipment in order to capture main bending and torsion modes of the truss. No detailed placement methodology was followed.

An indicative experimental raw time response after impact is given in **Figure 6.3** for the X direction responses. The frequency response functions (FRF) are given as well in **Figure 6.4** for a range up to 120 Hz which contains 7 natural frequencies and modes. These modes consider mostly movement in the X direction which is shown later with the FE model. The identified natural frequencies and modal damping values are given in **Table 6.1**. These values describe the intact or Healthy case of the bridge. For all experimental data shown in the present work a sampling rate of 2048 Hz is used.

Table 6.1: Identified modal values for the experimental intact or Healthy case of the bridge

Mode order	1	2	3	4	5	6	7
Frequency (Hz)	15.2	35.5	37.5	61.8	71	103.5	114.5
Damping	0.0213	0.0240	0.0232	0.0137	0.0499	0.0054	0.0098

6.3.2 Finite Element Model

A detailed FE model is developed, made in total of 217096 shell elements to model the truss members and 176365 solid elements for the truss joints and connections. A depiction of the FE model is given in **Figure 6.5**. The structure is idealized as a combination of 3 parts with the same properties. Part 1 is the main component of the truss member beams modeled with shell elements, Part 2 is the connections between beams, modeled with solids and Part 3 serves as the contact stiffness made also with solid elements.

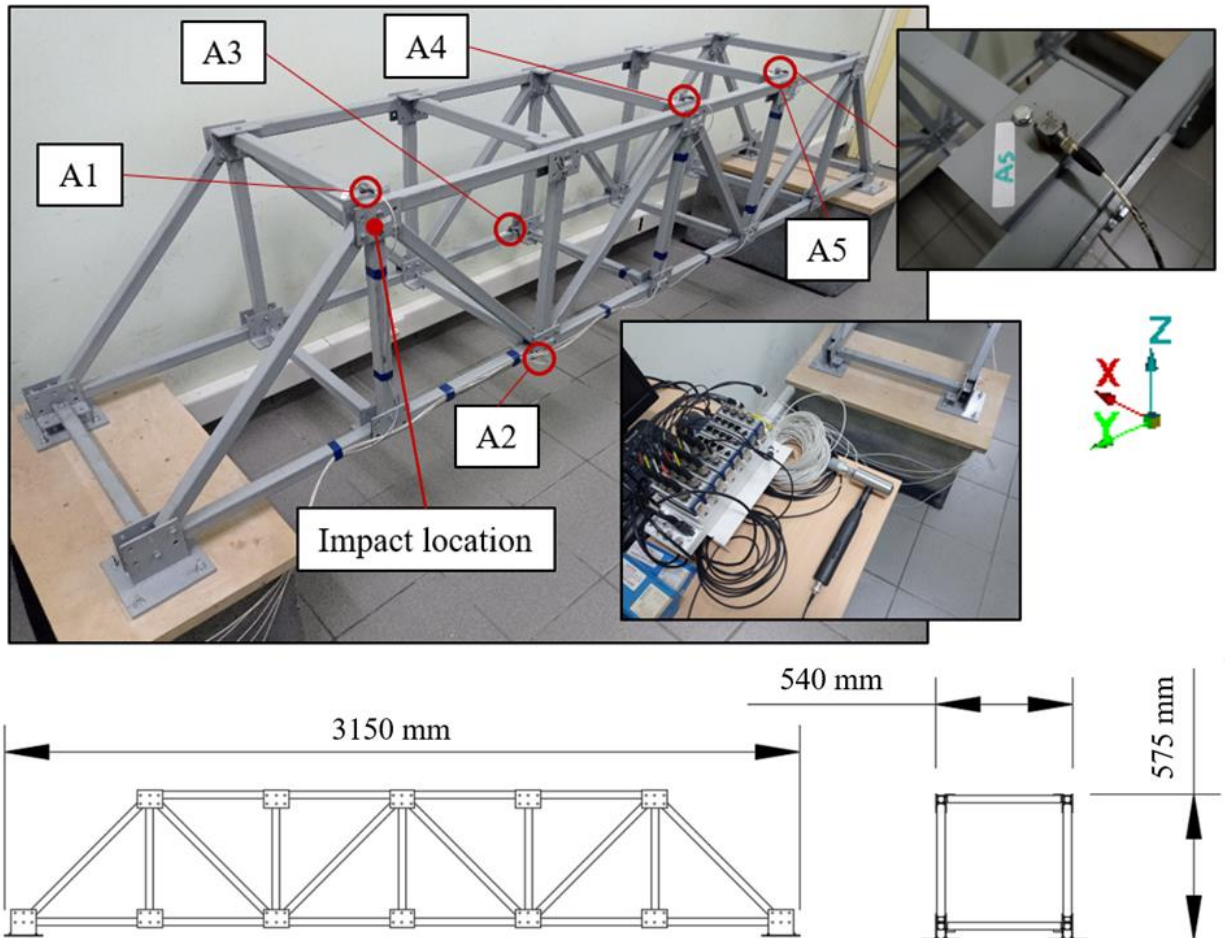


Figure 6.2: The experimental bridge structure with the accelerometer network and excitation hammer and measurement equipment. Below the basic external dimensions

The parameters for FE model updating are the stiffness and density for each part with addition to shell thickness for Part 1. In total, it is therefore a FE update problem of 7 parameters. For the damping values the experimentally identified of **Table 6.1** are applied and the transient modal analysis of MSC Nastran is used in all FE simulations in the present work. equation (2.7) is used for minimizing the residual between recorded experimental response for the 5 sensor locations in direction X and the numerically produced one using the CMA-ES algorithm. The results of the

update are summarized in **Table 6.2**. A single experimental impact and response as in **Figure 6.3** were recorded for the updating.

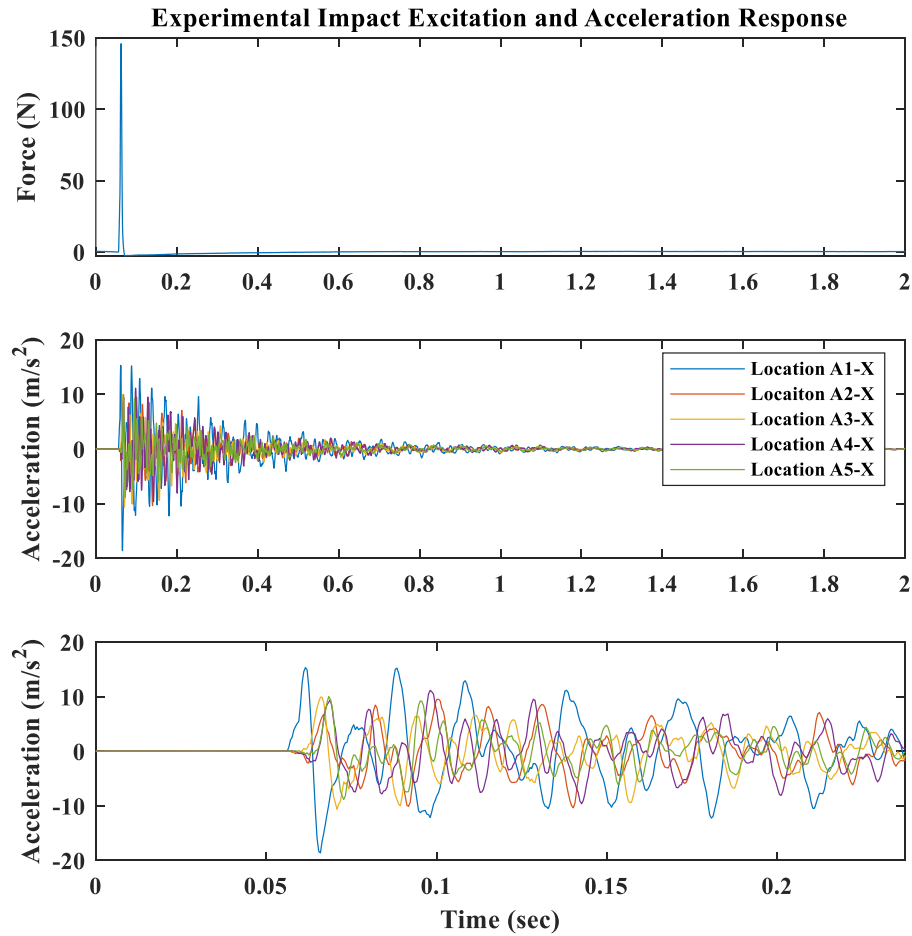


Figure 6.3: Indicative Experimental Excitation and Acceleration Responses for the X direction

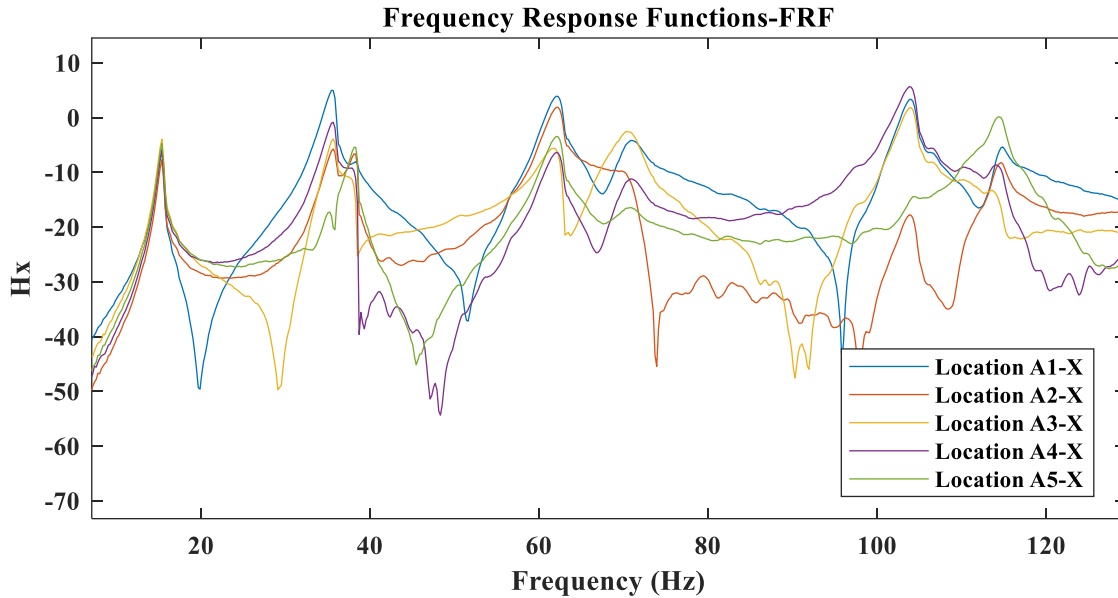


Figure 6.4: Indicative Experimental Frequency Responses for the X direction

The initial search points for the parameters of Part 1 and 2 were the nominal ones, given briefly as $E = 210GPa$, $\rho = 7800kg / m^3$ and $t = 2mm$. For Part 1 and 2 the search bounds were chosen at $\pm 10\%$ deviation from nominal stiffness and $\pm 15\%$ from nominal density, while $\pm 20\%$ on nominal thickness was used. For Part 3 that simulates the contacts, the initial search point of $E = 0.005GPa$ and $\rho = 5000kg / m^3$ was used. The search bounds this time were simulated wider at 100% of the initial points. The initial points for Part 3 were approximated at low stiffness and density values (thin elements as well) in order to employ the optimizer in evaluating the contacts starting from a point that does not affect the structure properties greatly. Convergence within that range showed that contacts simulated in such a way were indeed of low physical properties. A comparison of the updated FE model in terms of natural frequencies with respect to the identified in given in **Table 6.3**.

Table 6.2: FE Model Parameters Updating

Part	1		2		3	
Parameter	Bounds	Result	Bounds	Result	Bounds	Result
Young's Modulus						
E [GPa]	[189, 235]	230.77	[189, 235]	189.44	[0.001, 0.1]	0.0313
Density ρ [kg / m ³]	[7000, 9000]	7700	[7000, 9000]	8912	[1000, 10000]	3530
Thickness t [mm]	[1.8, 2.2]	1.81	-	-	-	-

Table 6.3: Updated FE model natural frequencies comparison with the experimentally identified

Mode order	Updated FE model [Hz]	Updated FE model [%] difference with the identified frequencies
1	16.0	-5.26
2	35.4	0.28
3	37.02	1.28
4	62.35	-0.88
5	65.3	8.02
6	103.7	0.19
7	107.8	5.85

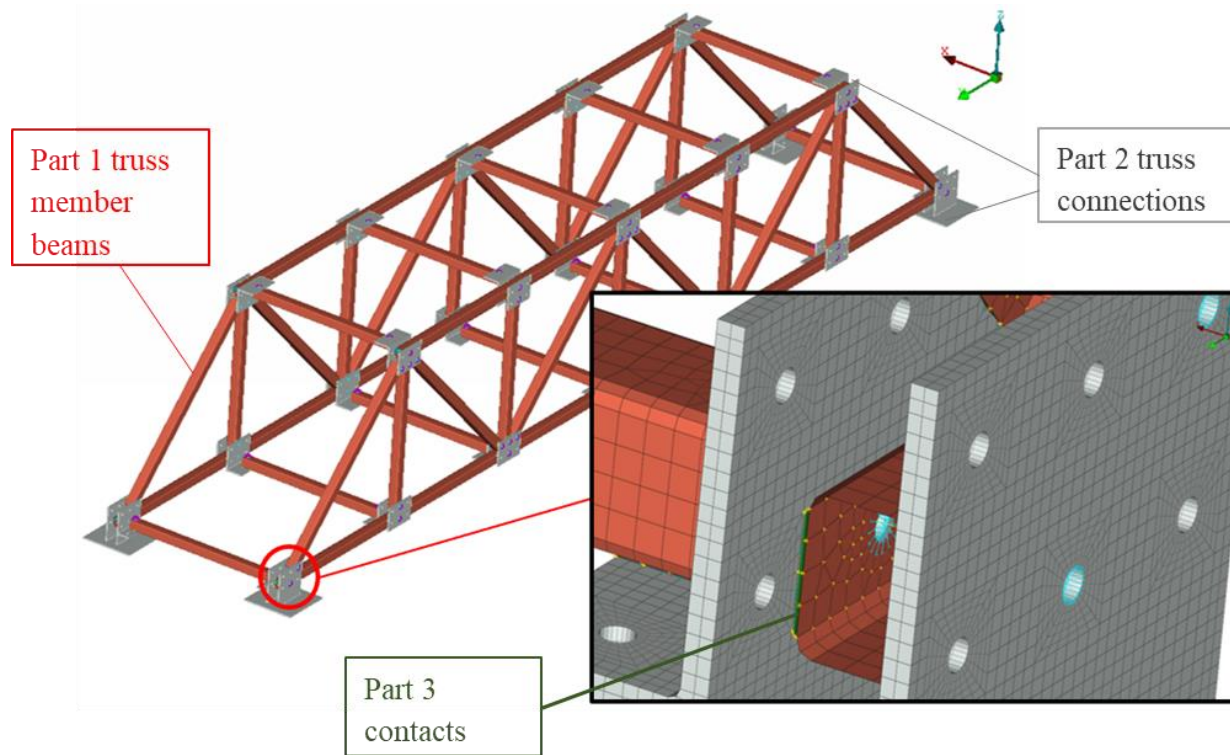


Figure 6.5: Finite Element Model of the test structure

Additionally, the accordance of the updated FE model with the experimental structure is given in **Figure 6.6**. The frequency components of the response are shown with the magnitude of the Fourier transform for the locations A1 and A2 for the X direction. The updated FE model shows to be able to represent the dynamics even though not perfectly reproduced. It will be actually the purpose of the following Sections classifiers to index the quality of accordance and more detailed measures of agreement such as Modal Assurance Criterion (MAC) are not investigated. The accordance results are shown indicatively.

Also, in **Figure 6.7** an indicative acceleration time response comparison for the same locations is provided with a low pass filter at 70 Hz. Such a filter will be used throughout this work since the accordance was the best for this range of frequencies. Again, in time responses the model shows to be able to reproduce the main dynamics, however not the details. The reasons for a not perfect update could be found in physical model uncertainties such as exact dimensions of different parts or different material properties of parts modeled as the same. A more detailed update process could be followed, for example separating the structure with more parts, however the purpose of this work is to study the limits of the numerical data with the model error it carries. Therefore, more detailed FE updating is not further considered. Finally indicative pictures of the 1st to 4th mode are shown in **Figure 6.8**.

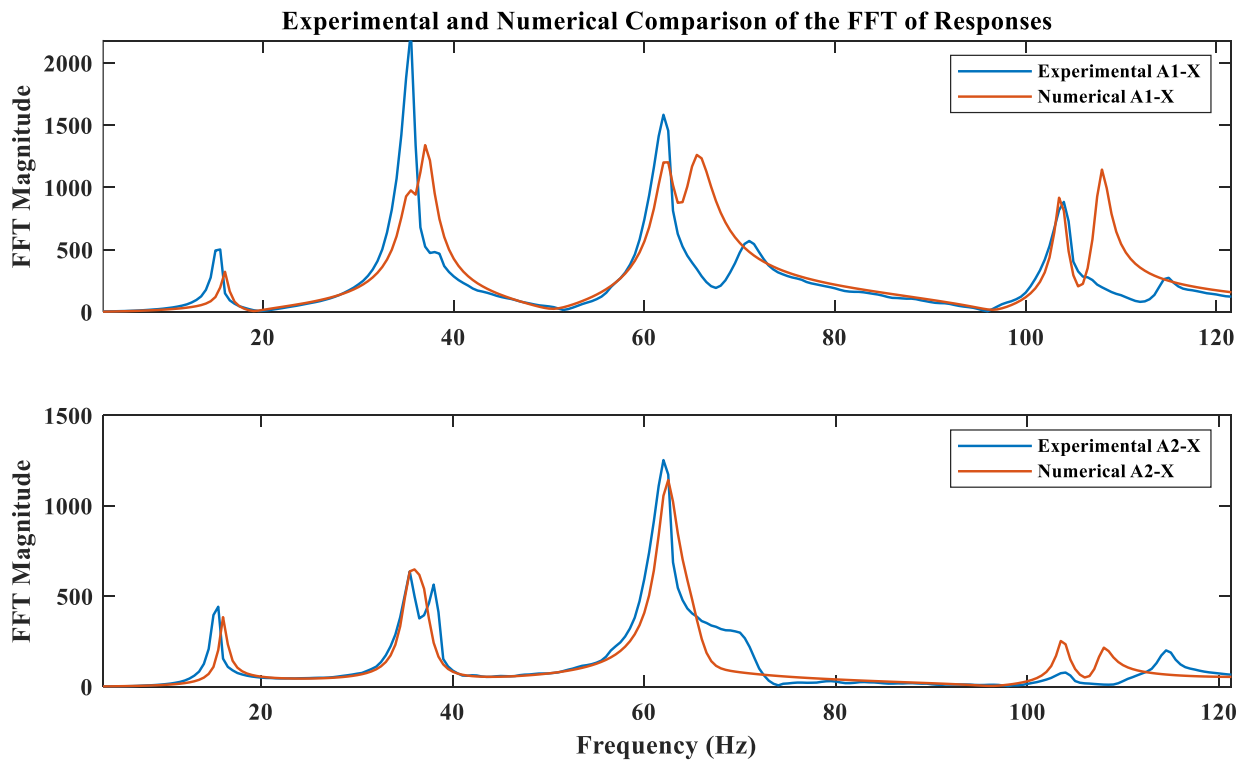


Figure 6.6: Experimental and Numerical response comparison in frequency the X-direction

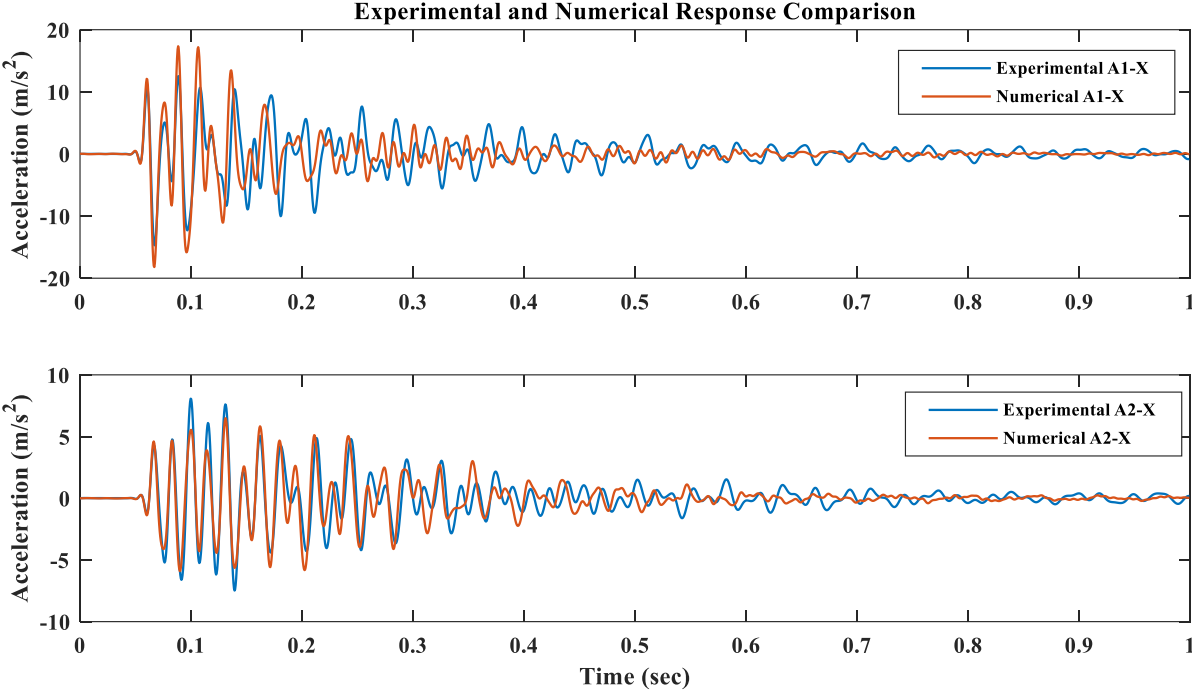


Figure 6.7: Experimental and Numerical response comparison in time for the X-direction

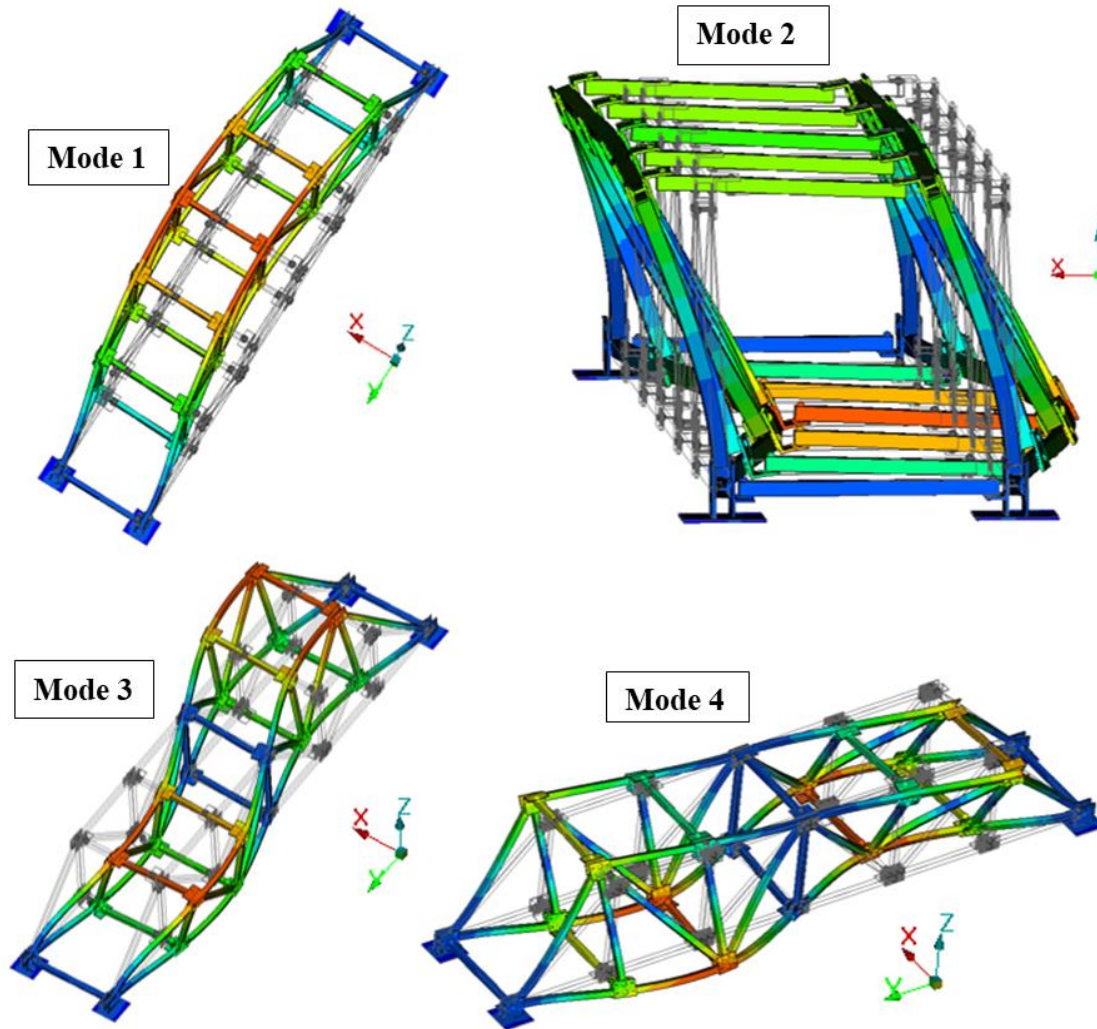


Figure 6.8: Depiction of the 1st to 4th vibration modes displacements

6.3.3 Damage scenarios of different magnitude

For the damage scenarios in the present chapter a binary damage identification problem is formulated. Focus is given on separating damage cases from each other on a structure that has been already flagged as damaged. This is considered as second level monitoring [25,108] while the first level, meaning identifying that there is deviation from the healthy state will not be considered in this work and can be realized also with different other techniques including unsupervised learning [3]. The first scenario of damages has been chosen to be the most demanding. A cut is induced on single truss beam member and a healthy beam is replaced on two specific locations. A depiction of the Damage 1 (D_1) and Damage 2 (D_2) cases, is shown in **Figure 6.9**. The damaged beam has been colored in red. For the second scenario of damage identification the beams at D_1 and D_2 locations are removed completely in order to impose damages of higher magnitude forming the corresponding Damage 3 (D_3) and Damage 4 (D_4) cases. A picture is shown for the D_3 and D_4

cases in **Figure 6.10**. The chosen locations do not have a special meaning other than simulating possible scenarios in a horizontal and a vertical member.

To get a notion of the damage magnitude in the structural response, a comparison in the experimental frequency range is given in **Figure 6.11** and a simulated acceleration time response in **Figure 6.12**. Identified modal parameters in D₁ and D₃ scenarios are given briefly as well in **Table 6.4** for comparison. As expected, the case of damage with the cut presents small changes from the reference healthy state. This might be indeed a very demanding damage identification problem that does not allow significant model error in the training data. The complete removal of the beam on the other hand disrupts the frequencies below 70 Hz, however not a dramatic change or collapse is taken.

It is left now for the classifiers trained with numerical data by the FE model (updated on the healthy state only) to show how good they may generalize on the experimental damage classification. It should be highlighted for the reader that the subsequent CNNs operate on the acceleration time responses only. A frequency data scheme could be fed and tested as well, however in the present work acceleration time series processing will be used to exploit as much the potential of raw feature learning in DL models. The FFT comparisons were given for indicative purposes.

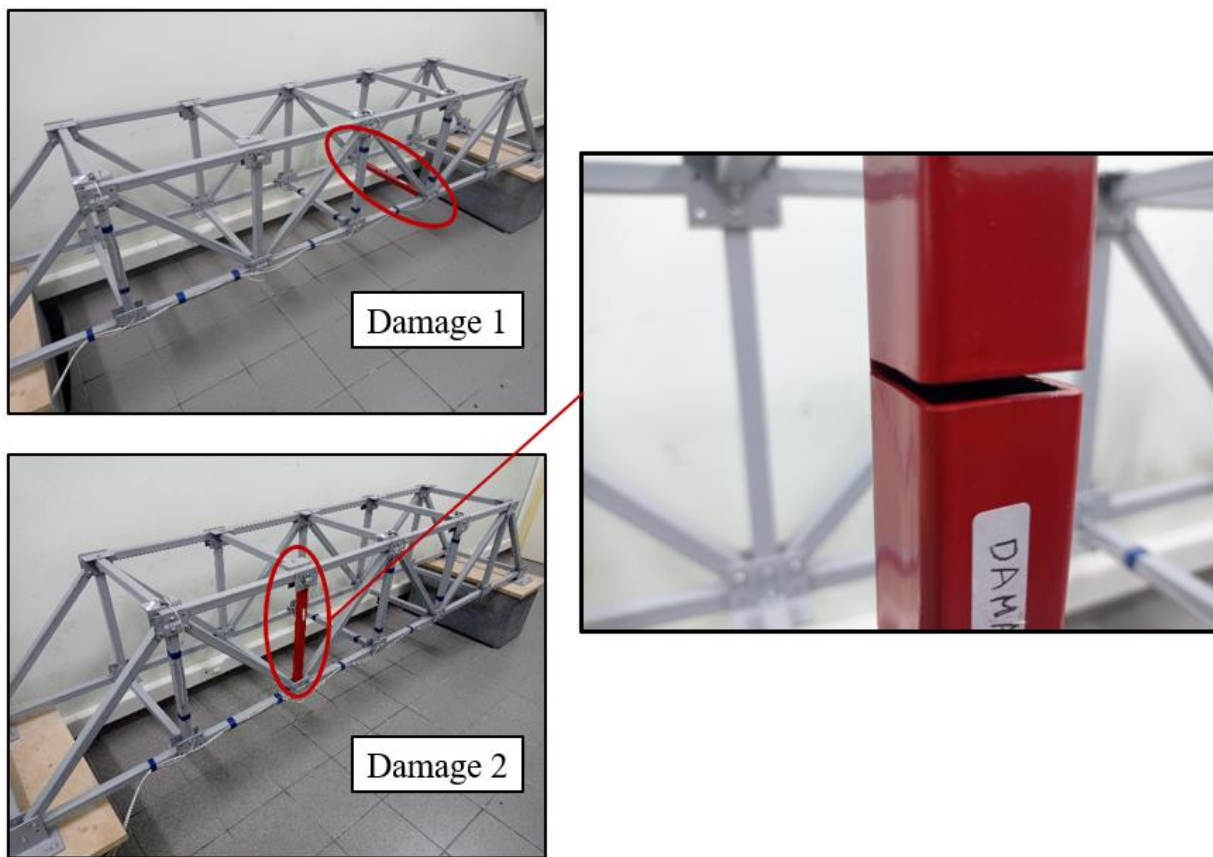


Figure 6.9: Damage scenario with Damage 1 (D1) and Damage 2 (D2) cases using a beam with a cut to replace a healthy one

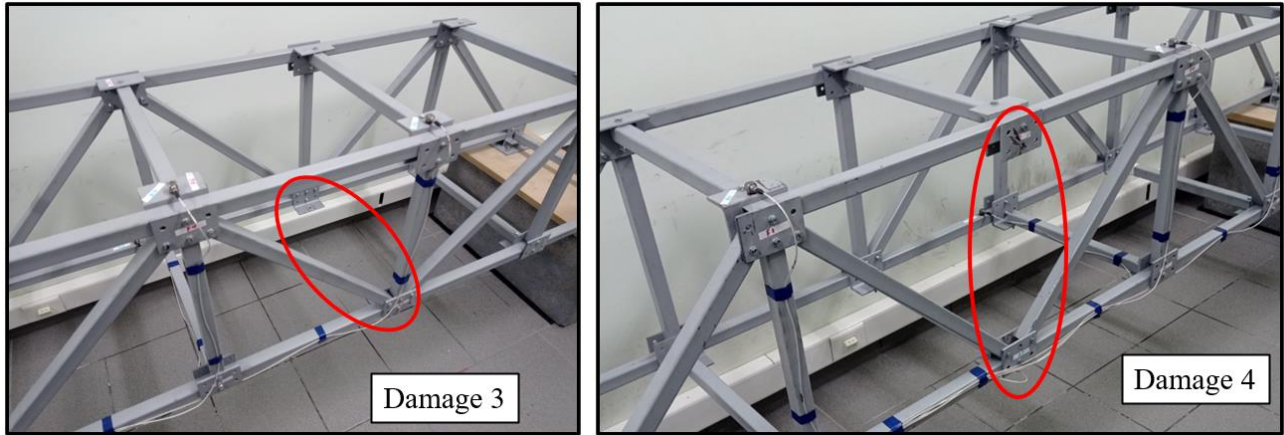


Figure 6.10: Damage scenario with Damage 3 (D3) and Damage 4 (D4) cases where the healthy beam is completely missing

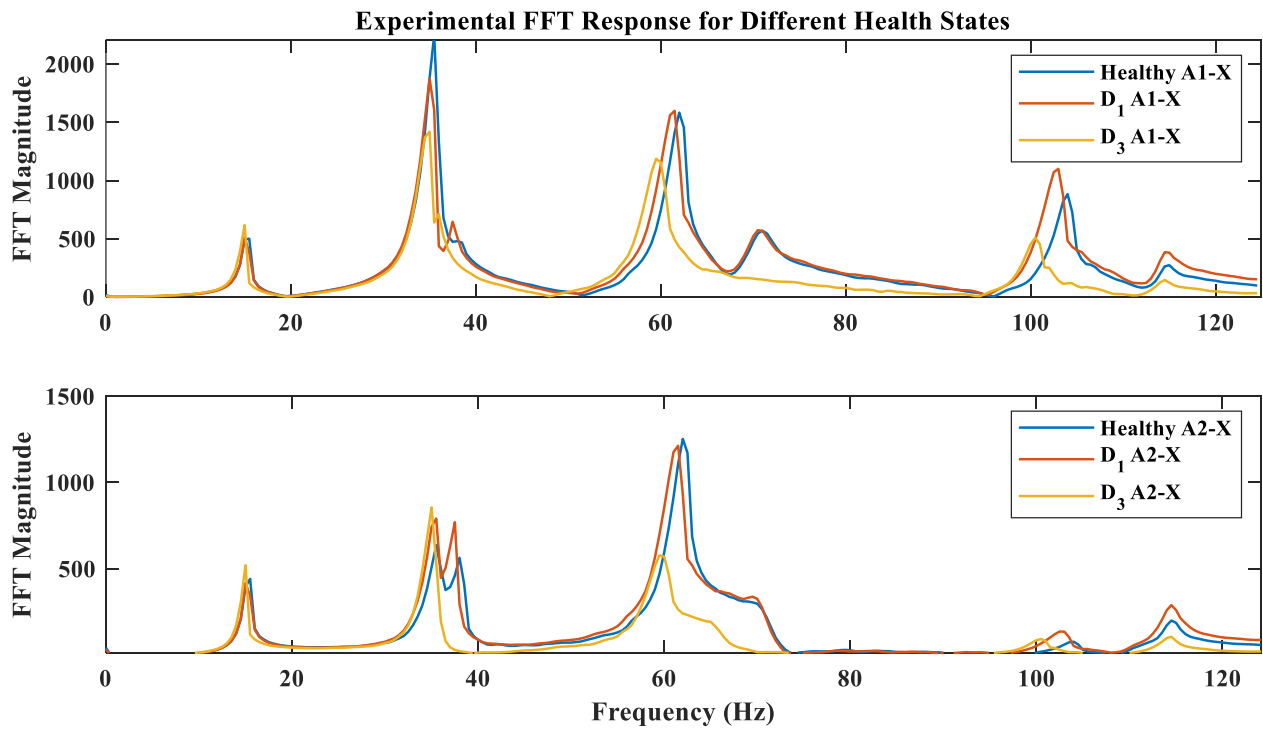


Figure 6.11: Comparison in Frequency with measured experimental responses in different locations for different health states of the structure

Table 6.4: Identified modal values for the experimental D1 and D3 cases of the bridge

Mode order	1		2		3	
Damage case	D ₁	D ₃	D ₁	D ₃	D ₁	D ₃
Frequency (Hz)	15.14	14.8	35.12	34.6	38.03	34.7
[%] difference with the identified on Healthy	-0.39	-2.63	-1.07	-2.25	1.41	-7.46

Mode order	4		5		6		7	
Damage case	D ₁	D ₃						
Frequency (Hz)	61.27	59.6	71.05	65.9	102.8	100.2	115	114.5
[%] difference with the identified on Healthy	-0.85	-3.5	0.07	-7.18	-1.37	-3.18	0.43	0

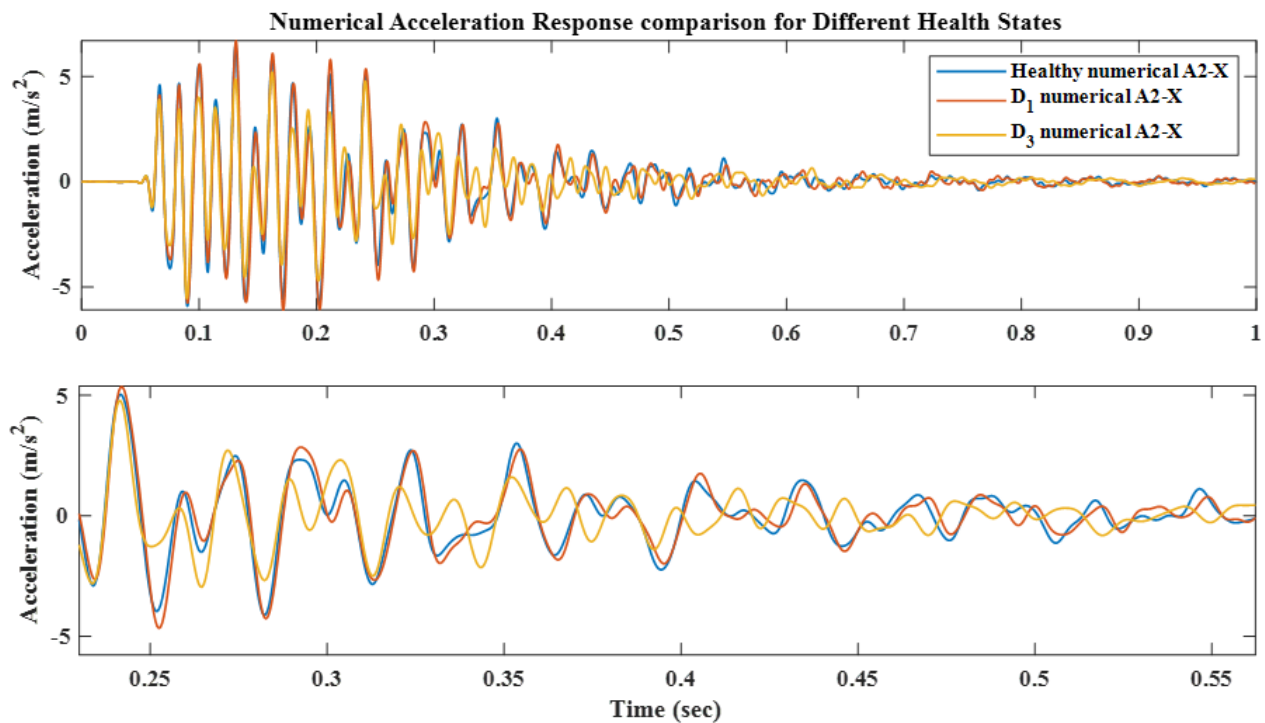


Figure 6.12: Comparison in time responses with FE simulated accelerations for different health states of the structure

6.4 Data Generation, Training of Classifiers and Experimental Validation

In the present section the numerical training data generation and classification results for the damage detection problems of the scenarios formulated in paragraph 6.3.3 are given. First a vibration training data set is generated by the FE model of paragraph 6.3.2 and a CNN is trained on the numerical data. The CNN classifier is validated finally on corresponding experimental measurements.

6.4.1 Data generation

To generate the training data for the classification problem, Algorithm 6.1 is used, adapted for modal superposition solution. As described in section 2.2, such an algorithm uses a repetitive load case scheme generation with random sampling on model parameters to aid in numerical to experimental generalization. The data characteristics are a $\pm 10\%$ uniform random deviation from the updated FE parameters of **Table 6.2** (including modal damping) for a total number of 1000 cases per label. For the excitation, in every load case an impact force is randomly selected from a total number of 10 cases, shown in **Figure 6.13**. Since impacts are hand driven in the experiment there is no way to achieve a completely identical curve. For this reason, 10 different impact curves were recorded and used in the FE simulations. The recorded impacts were chosen with variance in duration, peak and starting time in order to teach the classifier not to get attached on these specific parameters.

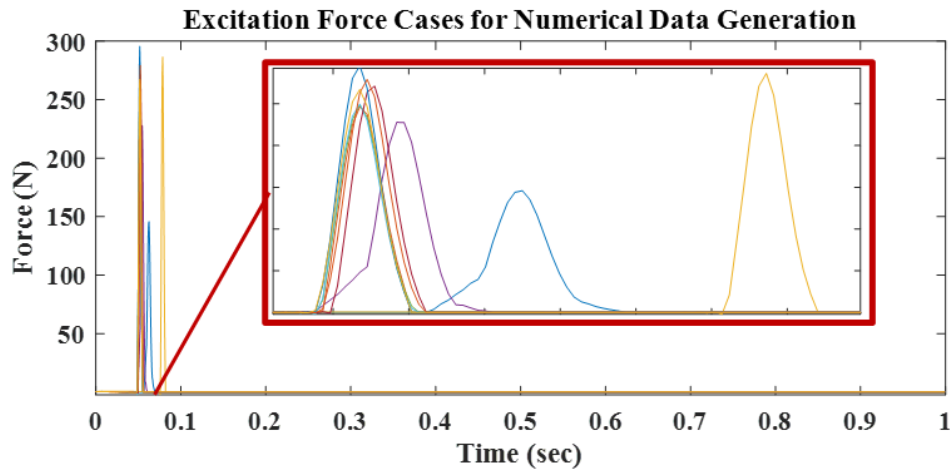


Figure 6.13: Different excitation impact cases used in data generation

After each run a time window of 500 time samples in the first 1000 of the simulated acceleration is kept and the final training set for each damage identification problem are formed as:

$$\begin{aligned} \text{Train_set}^{D_1-D_2} &= \{(A_{1,1}^{D_1}, Y_{1,1}), (A_{1,2}^{D_2}, Y_{1,2}), \dots, (A_{1000,2}^{D_2}, Y_{1000,2})\} \\ \text{Train_set}^{D_3-D_4} &= \{(A_{1,1}^{D_3}, Y_{1,1}), (A_{1,2}^{D_4}, Y_{1,2}), \dots, (A_{1000,2}^{D_4}, Y_{1000,2})\} \end{aligned} \quad (6.6)$$

where \mathbf{A} is the simulated accelerations vector of one training example with dimensions of 500×5 (time samples \times sensor channels) and \mathbf{Y} is the corresponding label vector. For all FE simulations MSC Nastran was used with a time step of $1/2048$ seconds matching the experimental sampling rate of 2048 Hz. The 5 acceleration channels used in training consist of the corresponding X direction sensors, as placed on the experimental structure (**Figure 6.2**). The training data characteristics for each damage identification problem are summarized in **Table 6.5**. Indicative training example responses are provided in **Figure 6.14**. Simulation time was noted approximately 9 minutes per load case on an Intel Xeon E5-2630 resulting in a total CPU time of 6.25 days for every one of the four damage cases. This can be distributed among different processors, however the computational cost in numerical data generation can become prohibitive when many different excitation types and working conditions need to be simulated. The reader may follow relevant works on model reduction techniques [[11](#),[26](#),[131](#),[132](#)] to explore possibilities of reducing the computational burden if need be.

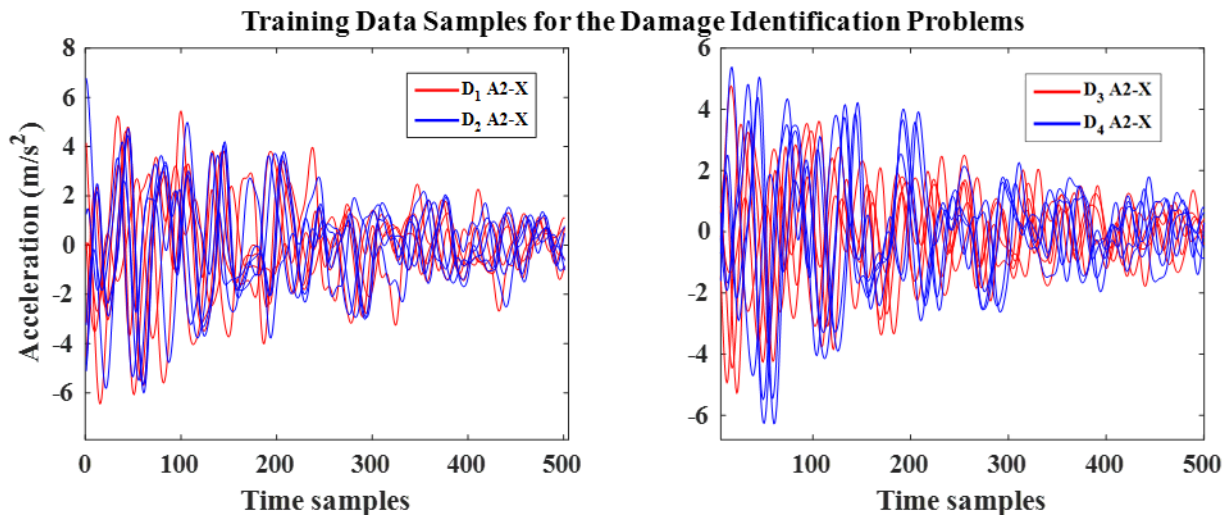


Figure 6.14: Indicative training signals for the damage identification problems

Table 6.5: Training cases per class in each Damage Identification Problem

Damage Identification Problem	Number of training examples				Validation split
	Class 1	Class 2	Total	Training example dimensions	
D ₁ -D ₂	1000	1000	2000	500x5	1600 training cases + 400 validation cases
D ₃ -D ₄	1000	1000	2000	500x5	

6.4.2 Classifier Training

The CNN architectures trained on the datasets (6.6) are provided in **Table 6.6**. The main architecture form of convolutional, pooling and perceptron layers stacked after another has been chosen from past works that tried also supervised damage identification with 1D convolutional networks [24,95,108,48]. Parameter tuning was performed with trial and error to achieve good training results and keep the minimum number of trainable parameters for best generalization [38]. That means the architecture of **Table 6.6** includes networks with enough and not excessive fitting power for the specific problems.

The training dynamics curves are shown in **Figure 6.15** and **Figure 6.16** for the two separate damage identification problems for 10 random start BPs. The Adaptive Moment Estimation (adam) algorithm was used with default keras [82] parameters and learning rate (0.001).

Table 6.6: CNN architecture used

Layer type	Filter length (time steps)	Neurons	Magnitude/Activation	Other
Convolutional	30	3 (D ₁ -D ₂) 2 (D ₃ -D ₄)	tanh	Trainable parameters 817 (D ₁ -D ₂) 485 (D ₃ -D ₄) Batch size 50 (D ₁ -D ₂) 200 (D ₃ -D ₄)
Pooling	-		3	
Convolutional	30		tanh	
Pooling	-		3	
Convolutional	30	1	tanh	
Pooling	-		3	
Perceptron	-	6 (D ₁ -D ₂)	tanh	
Perceptron	-	5 (D ₃ -D ₄)	tanh	
Classification	-	-	Sigmoid/Softmax	
Loss Function	Categorical Cross-entropy			

Already, some important observations can be made that may give a notion on the reliability of subsequent experimental states identification or in other words experimental generalization. First, both damage identification CNNs doing D₁-D₂ and D₃-D₄ achieved high accuracy and low loss values. That means the damage separation task was successfully performed for the FE solutions space contained in the dataset (6.6) and the networks provided effective classification. However, the D₁-D₂ damage scenario required more training epochs and almost double training parameters. This can indicate already a less convenient loss surface topology for generalization [38] in the D₁-D₂ problem. In addition, the training curves show a not as smooth learning behavior for the D₁-D₂ compared to the D₃-D₄. This has already been linked with bad experimental generalization [108] possibly leading to rough loss surfaces not so robust in model-experiment feature map shift. It is left now to see how these observations reflect to the experimental states prediction for the present test case.

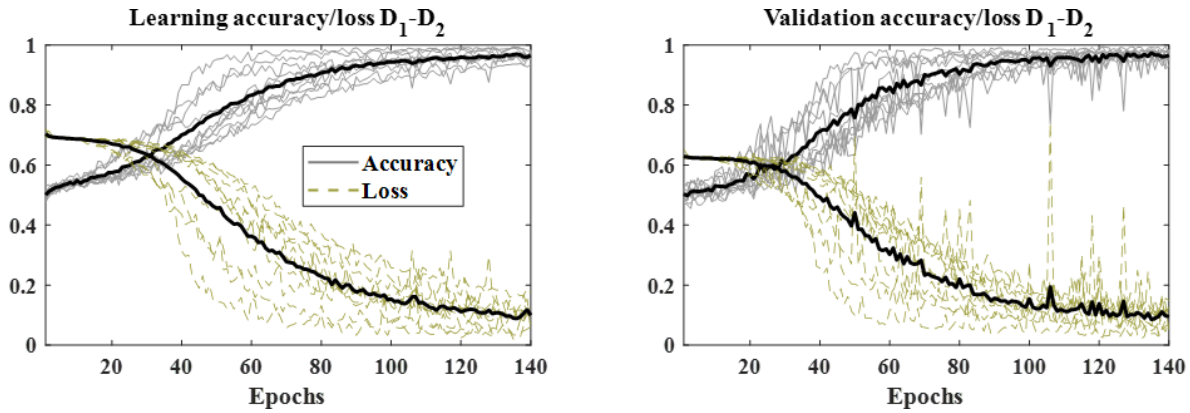


Figure 6.15: Training curves of accuracy and loss for 10 random start BPs for the networks associated with the D1-D2 damage identification. Mean performance with black line

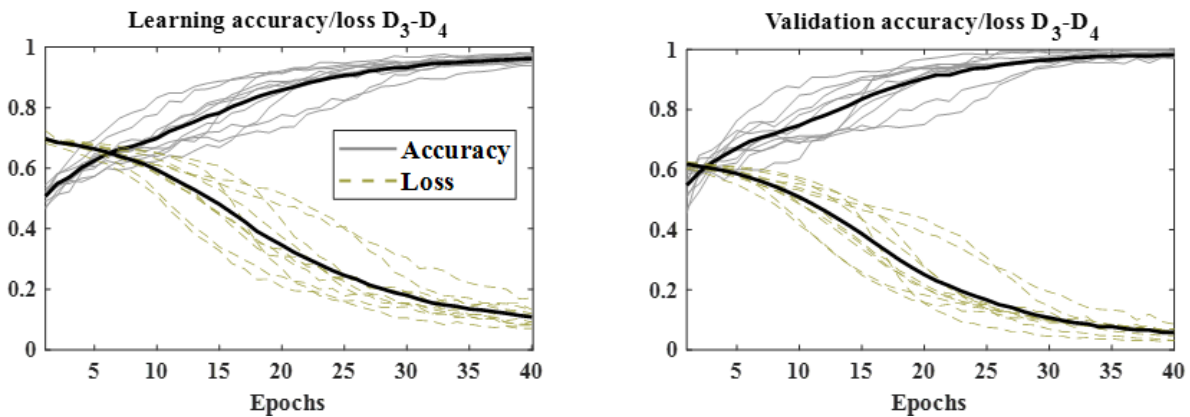


Figure 6.16: Training curves of accuracy and loss for 10 random start BPs for the networks associated with the D3-D4 damage identification. Mean performance with black line

6.4.3 Experimental Validation and Feature Maps

The trained CNNs of paragraph 6.4.2 are validated on experimental generalization in this paragraph. Measured accelerations from corresponding physical states D_1 , D_2 and D_3 , D_4 are used as inputs and the class predictions are given in histograms in **Figure 6.17** and **Figure 6.18**. In total 10 measurements of each physical state are indicatively showed. The nature of impact excitation has a small variance effect on the structural response and 10 inputs are adequate to describe network response.

The class prediction scores are the output from the sigmoid/softmax layer of the CNN. All scores shown were calculated with ensembling of 10 random start BP networks. The predictions come in values between 0 and 1 with the class threshold being 0.5. Blue is used for the Class 1 score that the network predicts on the input and red for Class 2. The sum of blue and red column is always equal to 1. From the prediction results it is obvious that the D_1 - D_2 identification problem case is governed by strong bias towards the D_1 class. The prediction scores show a stiff outcome towards the first class meaning that the learned features from the numerical data are influencing the

prediction less than model error. On the other hand, the D₃-D₄ problem manages to generalize on the corresponding experimental states responding in the correct direction for both D₃ and D₄ inputs. That means the model error has less influence on the learned features for the specific problem.

At this stage the model error effect for each damage identification problem or the “effective” error (as discussed in section 6.2) is checked by the zero input convolutional feature maps. The final convolutional and pooling layer arranged in **Table 6.6** outputs the feature maps h calculated by the convolutional part of the network as in equations (6.4) for the damaged cases and (6.5) for the intact. The resulting feature maps for the specific CNN architecture is a vector h of 4 components [4×1] for both damage identification problems. The feature maps are weighted in the first layer of perceptrons according to $Wh + b = 0$ as in 2.5, with W being a [6×4] or [5×4] trainable matrix and b the trainable [6×1] or [5×1] bias vector. Focus is given only on the feature map clusters however to observe the feature shifts. The plots of clusters for the feature map components, for the total of 6 combinations of components in the vector h are provided in **Figure 6.19** and **Figure 6.20** from representative networks in the ensemble. The zero input feature maps, meaning when Healthy states are used according to equation (6.5) are plotted for comparison. The reader should notice that for the numerical feature maps 500 cases from each Health state have been used randomly selected from the full training set that contains the Damaged states and the common Healthy state. The same methodology of presentation is followed throughout this work.

The feature map plots validate the experimental generalization behavior of the histogram plots. For the D₁-D₂ case the feature maps of **Figure 6.19** are clustered towards the D₁ side, while it is interesting to see that this is already evident from the zero input maps of the Healthy states. That means model error from the Healthy states is already perceived by the network as large enough for the specific classification problem. In other words, the numerical and experimental Healthy states are not similar enough, which is easily observed in the distance between the corresponding scattered points. In contrast, the D₃-D₄ problem feature maps in **Figure 6.20** show that model error is not as significant with the zero input feature maps of the Healthy states being closer. As a result, the experimental damage states scatter closer to the correct numerical ones. These interesting observations in feature map shift can provide towards reliability indexing for numerical data training on damage identification. In next section, the behavior is additionally validated in a numerical example.

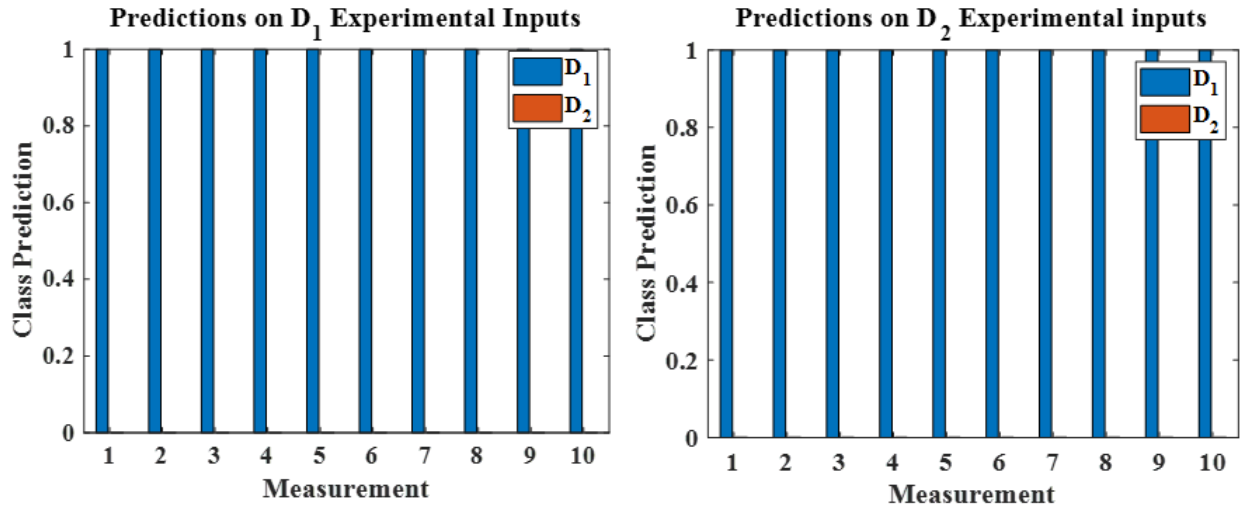


Figure 6.17: Class prediction histograms for the experimental D1-D2 identification/classification

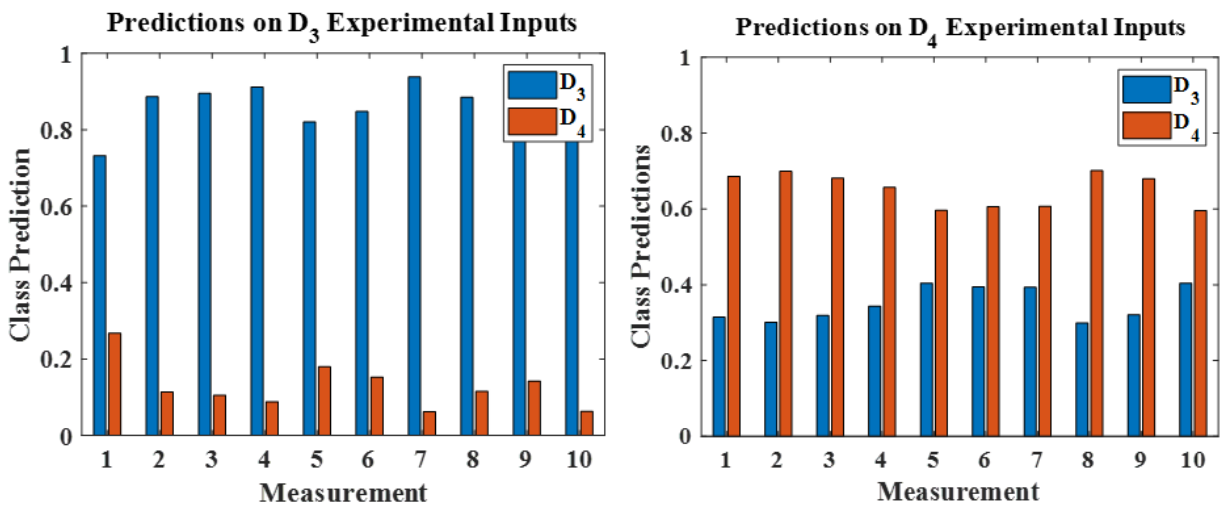


Figure 6.18: Class prediction histograms for the experimental D3-D4 identification/classification

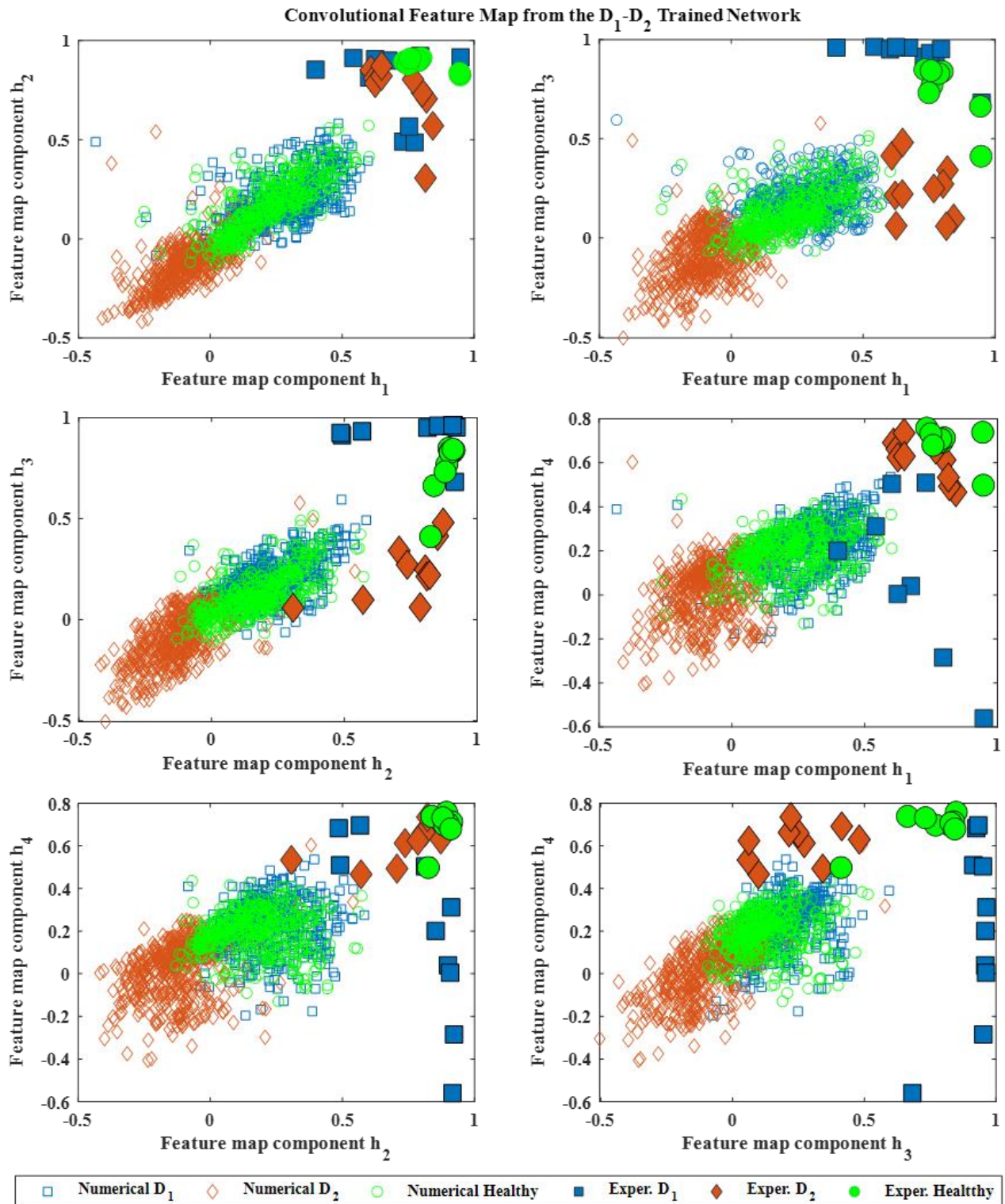


Figure 6.19: Convolutional feature map components for the D_1 - D_2 damage identification network. Feature maps are plotted for numerical inputs used in training and experimental used for validation

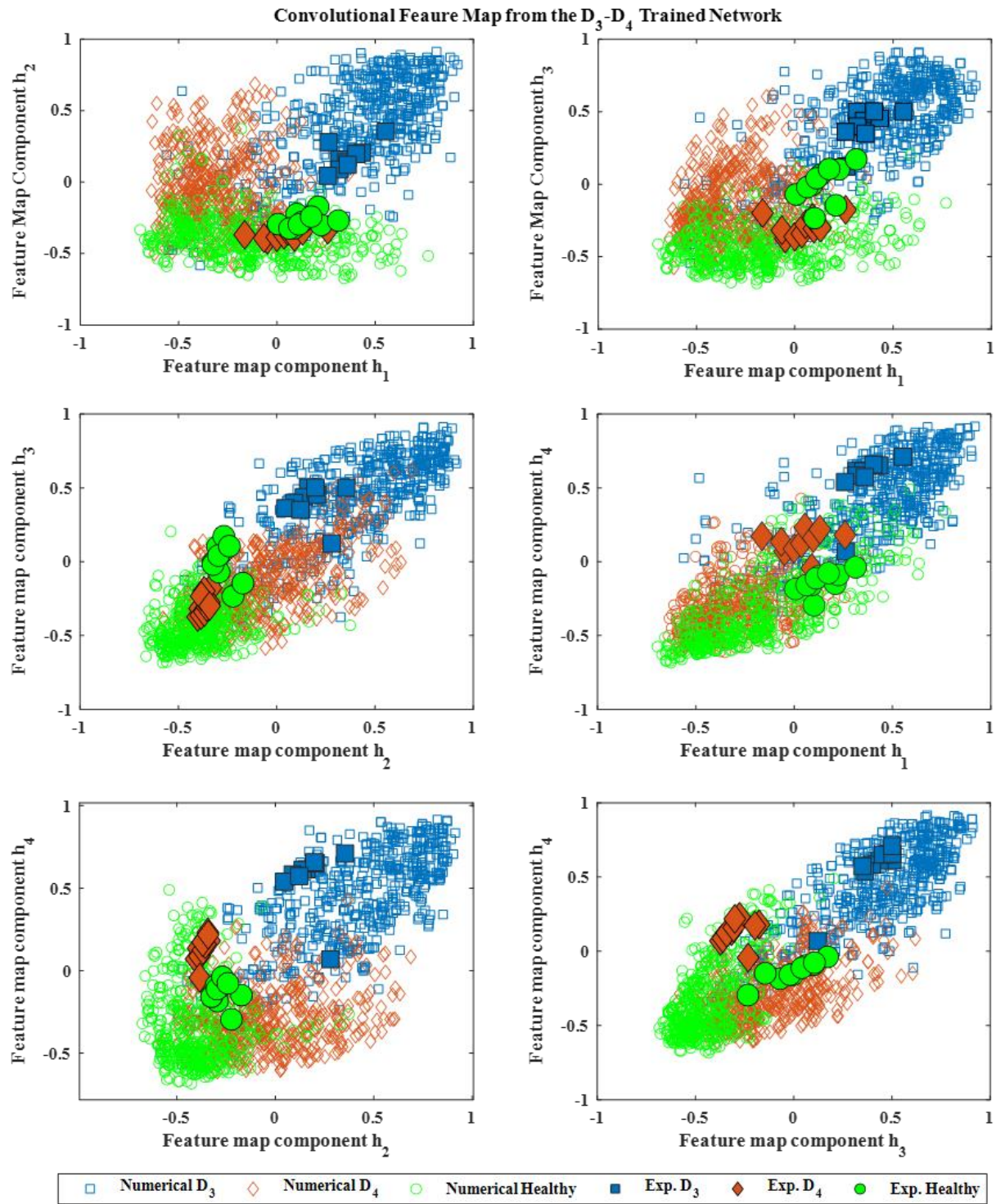


Figure 6.20: Convolutional feature map components for the D3-D4 damage identification network. Feature maps are plotted for numerical inputs used in training and experimental used for validation

6.5 Bias as a Function of Model Error

In the present section an investigation on bias effects is given to validate further the behavior presented in paragraph 6.4.3. It is tested how consistently the expected generalization with respect to damage magnitude and error evolves in the space of FE parameters solutions. A simplified numerical model is developed for convenience in solver times and data generation. A FE parameters set is defined as a reference and CNNs are trained on FE models with progressively diverging parameters from the reference. The purpose is to simulate generalization from one data set to another.

6.5.1 Training Data with Progressive Distancing from the Reference

The simplified numerical model for testing is made of 432 beam elements and is shown in **Figure 6.21**. The nominal beam section sizing and steel material parameters $E = 210GPa$ and $\rho = 7.8kg / m^3$ were assigned for all members. A typical damping ratio of 0.05 was finally assigned.

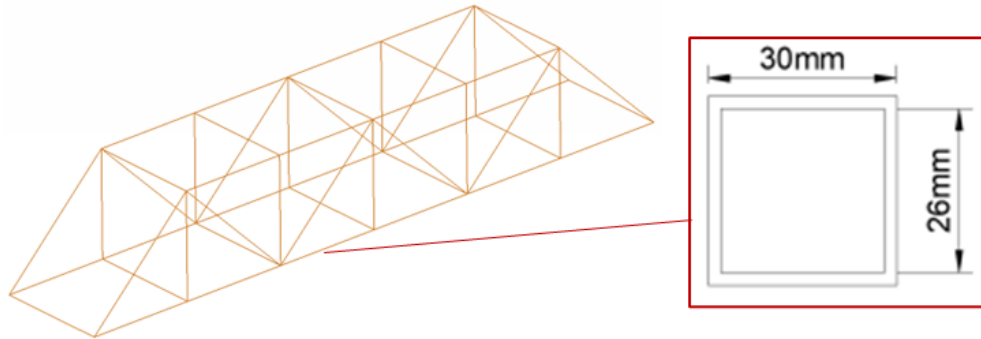


Figure 6.21: Simplified Truss model made of beam elements (left). Section sizing (right)

The same impacts as in **Figure 6.13** are used as excitation for the following data generation. Sample time response and mode shapes are given in **Figure 6.22** and **Figure 6.23**. Both present qualitative similarities with the detailed FE model and the experiment of **Figure 6.7** and **Figure 6.8**, even though a generally stiffer system with higher natural frequencies is calculated. This information is provided for indicative purposes and the reader should not be confused with trying to compare to the highly detailed model. The exact goal of the current section is to replicate the bias behavior in a system that is not strictly identical to the detailed FE or experimental system, in order to avoid attaching to specific structural dynamics.

Concluding this paragraph, the same damage identification problems are tested as in paragraph 6.3.3. Therefore, the same scenarios are simulated with the simplified FE model. For the D₁-D₂ classification, the rigidity is reduced by 75% for the beam element to roughly approximate the $\frac{3}{4}$ cut of the beam section. For the D₃-D₄ the complete truss member is removed. The training data sets are build using Algorithm 6.1 in a modal solution with a $\pm 5\%$ uniform random deviation from nominal values given in the beginning of the section. To include deviation from a reference set, diverging material stiffness is distributed in 5 sets as in **Table 6.7**. The Set 1 is defined as the

reference set that may simulate for example the unknown experimental system properties, while Set 2 to 4 simulate a progressive deviation of 5 to 15%. The excitations used are the same described in paragraph 6.4.3.

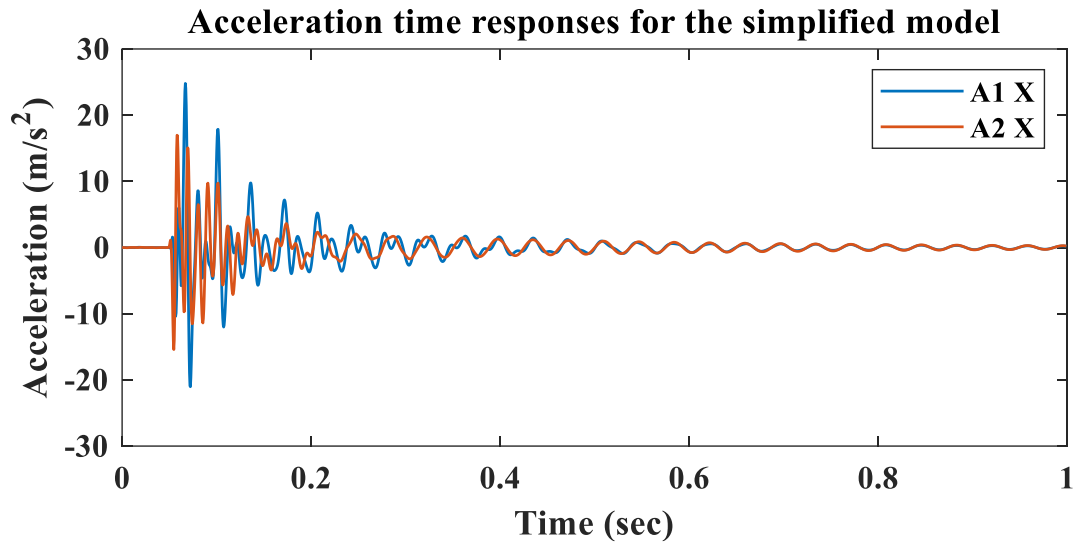


Figure 6.22: Sample acceleration time response of the simplified Truss for some impact excitation

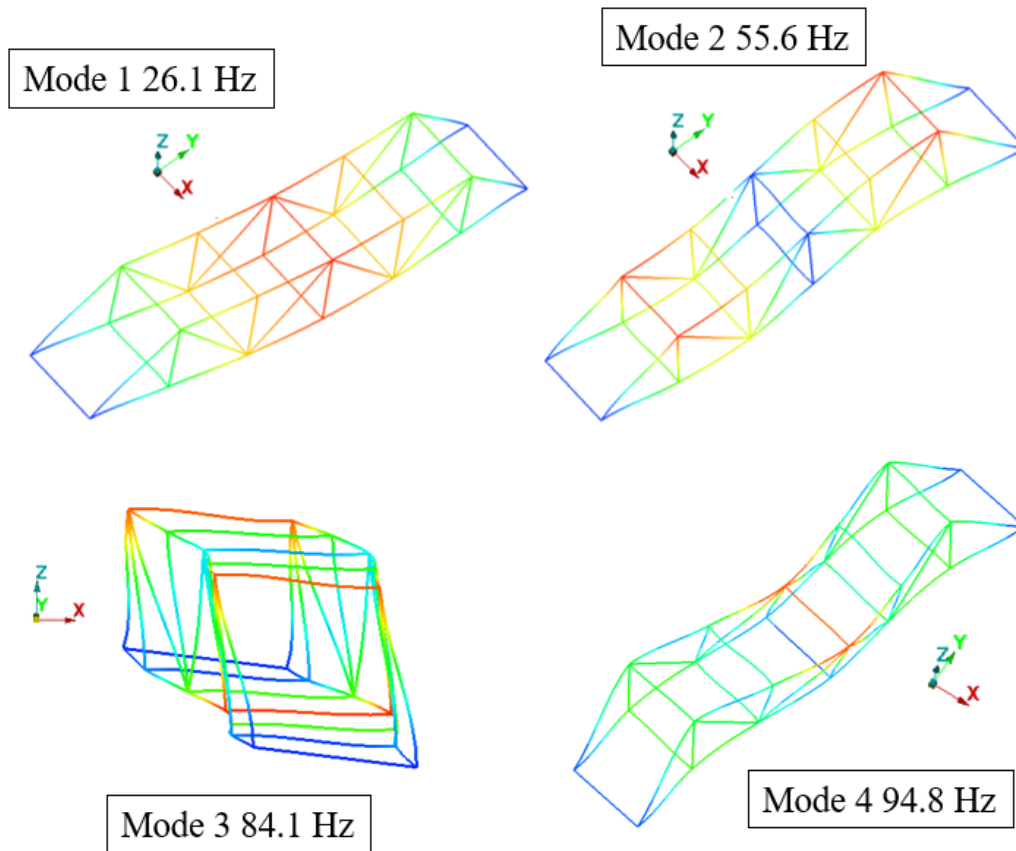


Figure 6.23: Indicative mode shapes of the simplified Truss

Table 6.7: FE material stiffness in training data sets

	Set1 (reference)	Set 2	Set 3	Set 4
Young's Modulus E [GPa]	$210 \pm 5\%$	$(210 \cdot 1.05) \pm 5\%$	$(210 \cdot 1.10) \pm 5\%$	$(210 \cdot 1.15) \pm 5\%$

The amounts of data generated for every Set 1 to 4 are finally as in **Table 6.5** and each Set 1 to 4 is organized in acceleration inputs and labels accordingly. The simulation time was approximately 11 seconds for each load case, meaning around 50 times less than the detailed FE model, justifying the convenience of using the simplified model for the data testing of this section.

6.5.2 Classifier Training

For training now with CNN classifiers, the architecture of **Table 6.6** is repeated with some small differences that were required for optimal training of **Table 6.7**. More specifically for D₁-D₂ data 8 perceptron neurons were used instead of 6 and for D₂-D₆ data 4-6 perceptron neurons instead of 5 were applied in different Set 2-4 training. Batch size was adjusted as well to 100-110 training examples. The main CNN is kept therefore unchanged, but the network minimum fitting power has to slightly increase in order to classify damage cases with low loss and high accuracy for the whole FE solutions space. That could be attributed to the different modal parameters of the simple truss, however it is not investigated further and it should be noted that training was performed effectively again as shown in the learning curves. In **Figure 6.24-Figure 6.26** the curves for corresponding training on Sets 2-4 are provided. The general picture is repeated as in paragraph **6.4.2** with the D₁-D₂ problem having a rougher training behavior with less smooth training. It is left to see now how this is reflected on generalization to Set 1.

6.5.3 Results on Dataset Generalization and Feature Maps

In the present paragraph the results of generalization to Set 1 from networks trained on Set 2 to Set 4 in paragraph **6.5.2** are provided. Since the FE parameter Sets 1-4 were covered by a number of 1000 cases, the average class bias is given to indicate how the candidate solution spaces Set 2-4 generalize on Set 1. **Figure 6.27** contains a depiction of the average Class 1 and Class 2 biases. The trend for Class 1 shows that there is higher chance to have biased predictions for Set 1 values for the D₁-D₂ problem and as training data further moves away from Set 1, it becomes more evident. It can be assumed therefore that the experimental generalization problem is governed by a similar bias behavior which was observed in paragraph **6.4.3** and also showed better generalization for the D₃-D₄ identification problem.

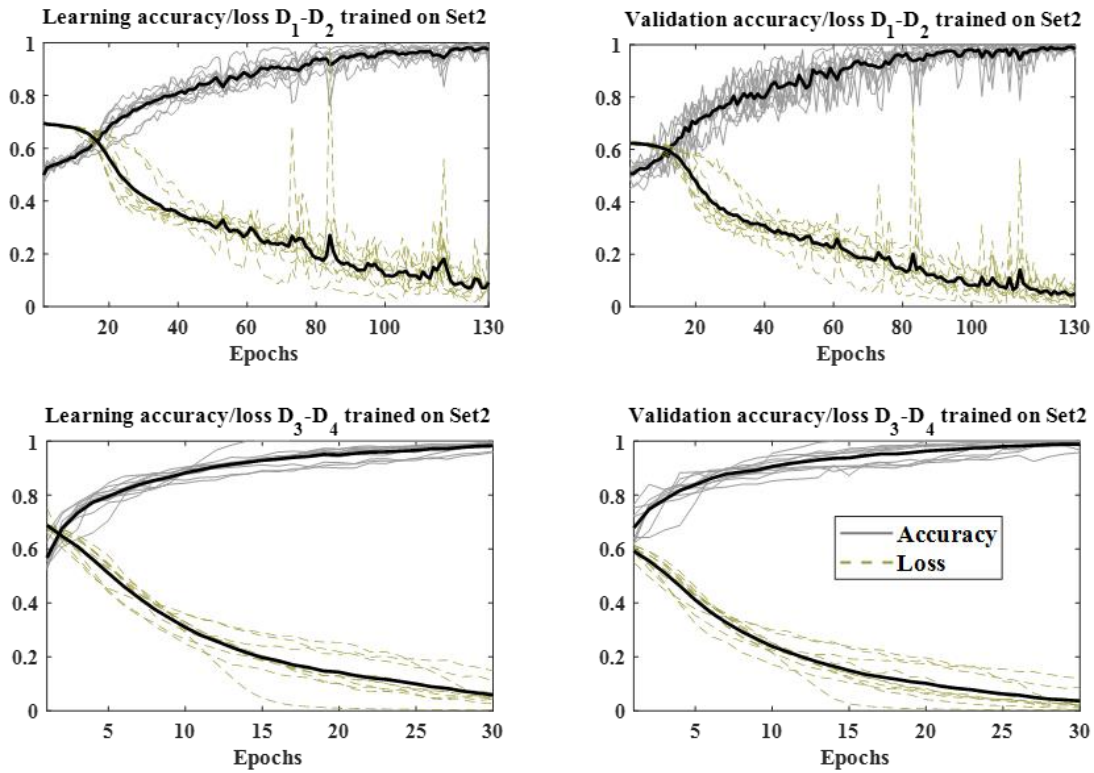


Figure 6.24: Training curves for 10 random start BP networks trained on Set2 numerical data

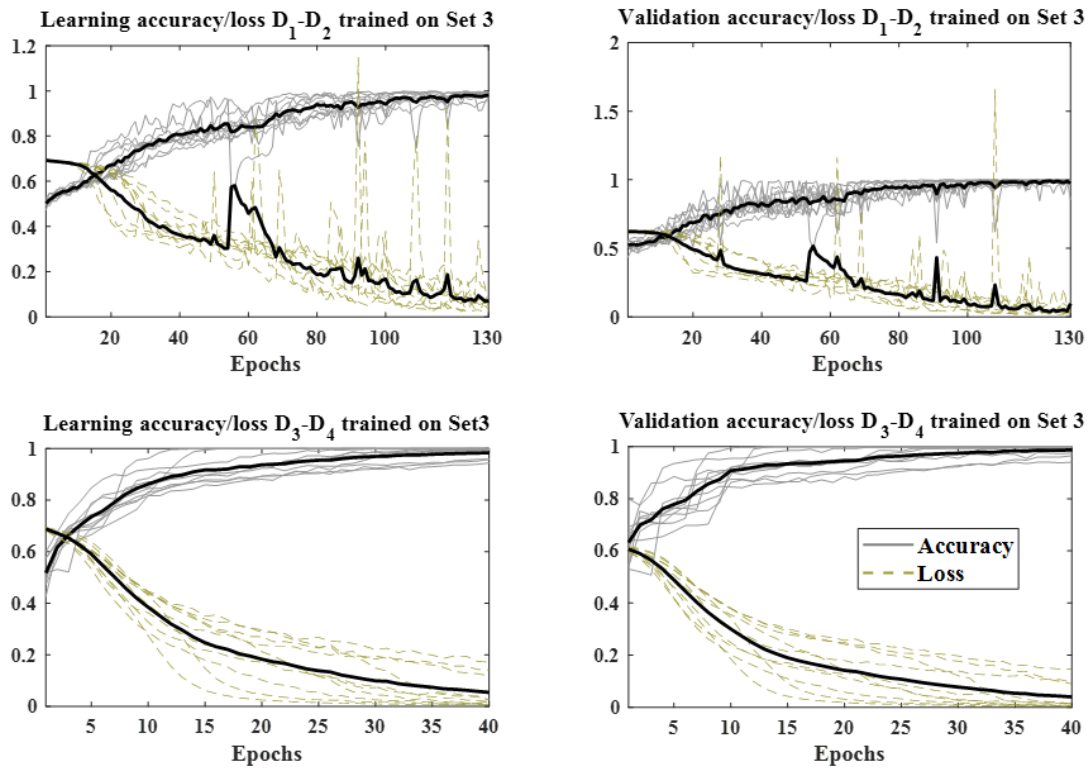


Figure 6.25: Training curves for 10 random start BP networks trained on Set3 numerical data

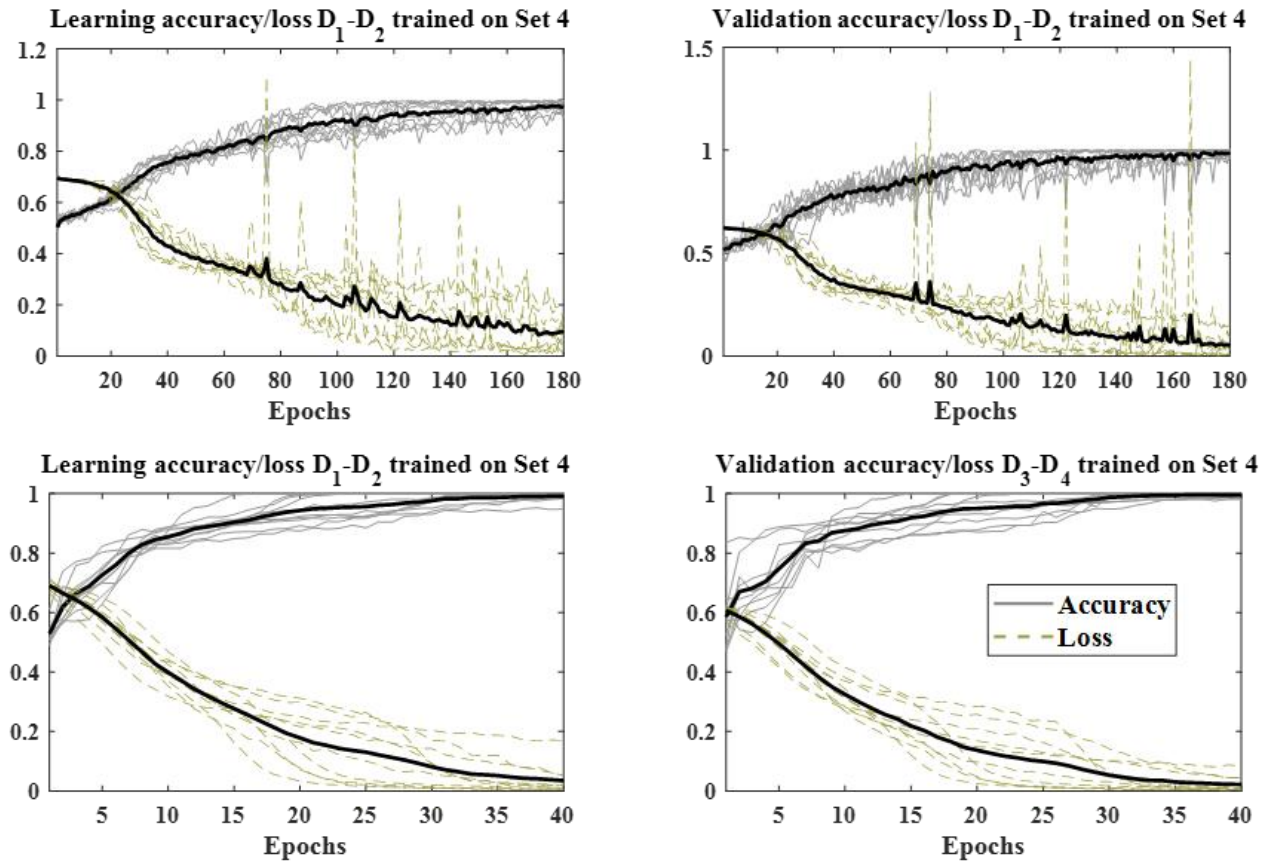


Figure 6.26: Training curves for 10 random start BPs networks trained on Set4 numerical data

Interesting also is the fact that the standard deviation of class bias on Set 1 increases as training data moves further from Set 1. For example, the average Set 1 Class 1 bias when networks are trained on Set 2, which is the lowest for both D_1 - D_2 and D_3 - D_4 problems, comes with a standard deviation of 0.0563 and 0.0593 respectively. On the other hand, when networks are trained on Set 4, standard deviation is calculated as 0.1462 and 0.1505. Prediction histograms by Set 4 trained networks are shown in **Figure 6.28** for D_2 and D_4 inputs.

Even though data was generated with a $\pm 5\%$ deviation in material properties for both D_2 and D_4 inputs, a more unstable classification behavior with more cases switching through the class boundary is recorded for the former. This qualitative observation shows additionally that a damage identification system trained by numerical data can be uncertain in generalization to the experimental solution space. Uncertainty shows to depend on how good the reference properties are known and how difficult the identification problem may be. The combination of how good the properties of the set to generalize on have been covered and how difficult the identification problem is, was indicated as well in paragraph 6.4.3 by the similarity on the zero input feature maps.

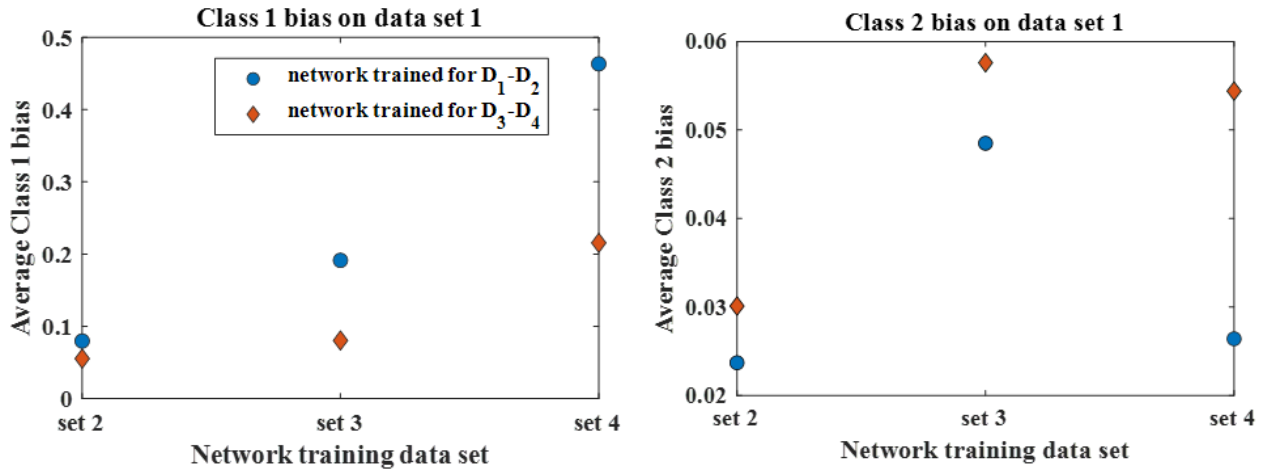


Figure 6.27: Results on average class bias reflected on Set 1 data from networks trained on Set 2 to Set 4 numerical data

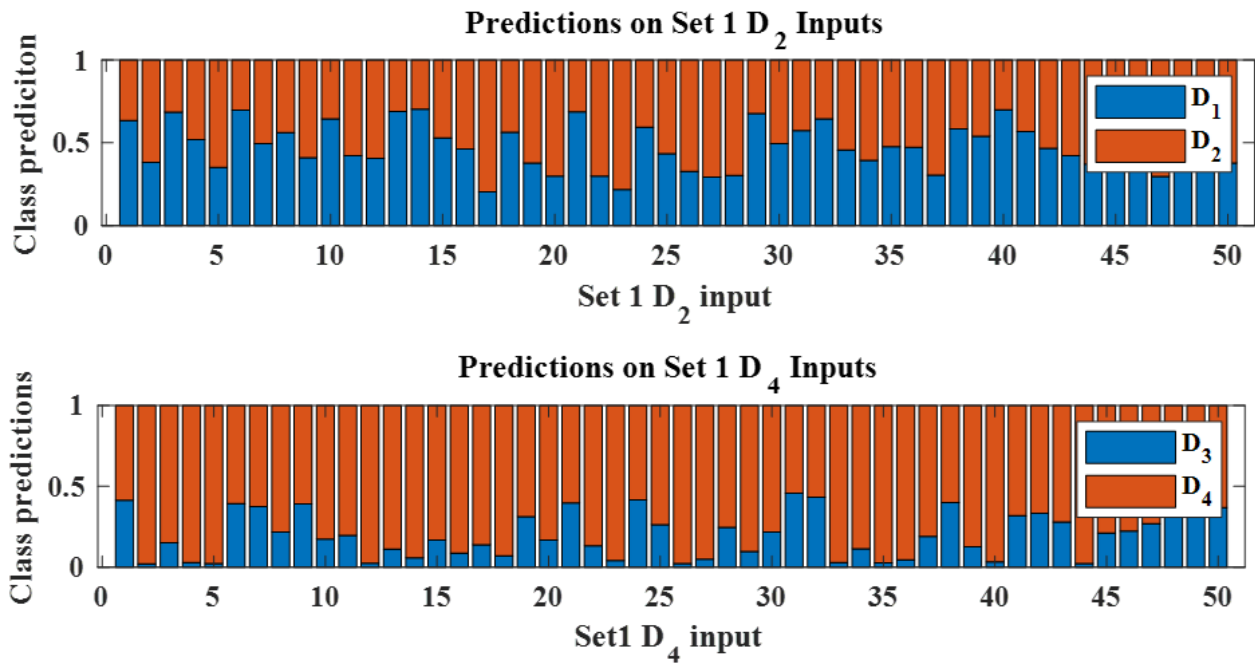


Figure 6.28: Indicative predictions for D2 (up) and D4 (down) inputs from corresponding networks trained on Set 4 data

Additionally, in this paragraph the feature maps are indexed again for the simplified truss model. In **Figure 6.29** and **Figure 6.30** representative ensemble network feature maps are plotted for the characteristic cases of data training on Set 2 and 4 which present the lowest and highest biases. Notice that 2 component combination clusters from the feature vector h are shown for ease of comparison in the same page. For the Set 2 trained classifiers, the feature maps show almost identical patterns for both D₁-D₂ and D₃-D₄ problems corresponding to the relatively small +5% mean difference in material properties of Set 2 to Set 1. The zero input feature maps as well reflect

this fact meaning that the difference in Set 1 and Set 2 responses is not significant. On the other hand, for the networks trained on Set 4, as expected from the mean bias in **Figure 6.27** the D_1 - D_2 problem networks start presenting a shift towards the D_1 class. This is visible already in the zero input feature maps that can indicate this trend. The D_3 - D_4 problem behaves again as in paragraph **6.4.3** with less comparable shift to the D_1 - D_2 problem which directly influences generalization on Set 1.

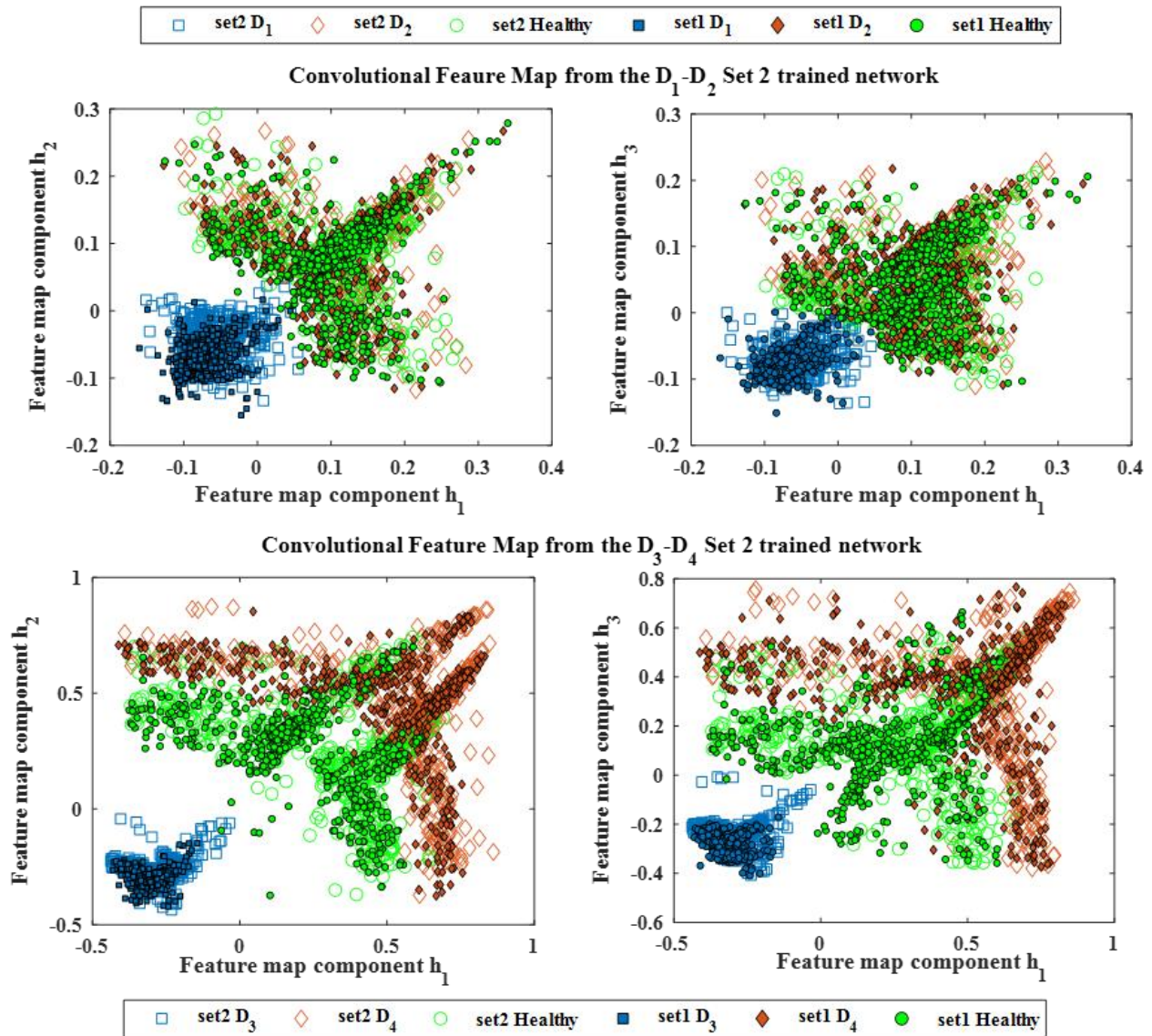


Figure 6.29: Convolutional feature map components for a representative D_1 - D_2 (up) and D_3 - D_4 (down) damage identification network. Feature maps are plotted for numerical inputs used in training from Set 2 and numerical inputs from Set 1 where they are assessed in general

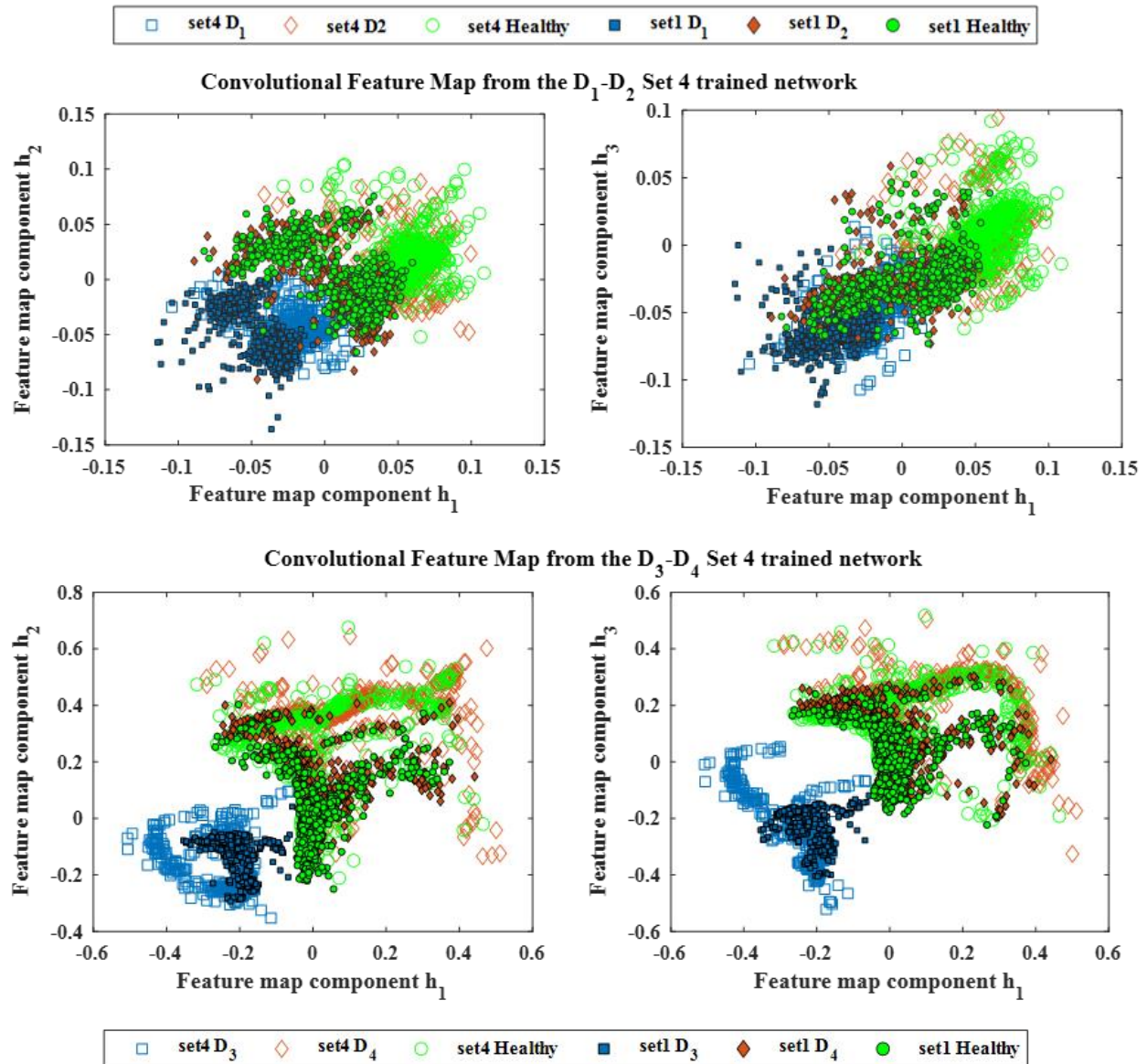


Figure 6.30: Convolutional feature map components for a representative D1-D2 (up) and D3-D4 (down) damage identification network. Feature maps are plotted for numerical inputs used in training from Set 4 and numerical inputs from Set 1 where they are assed in genera

Concluding this section, in the binary classification character of the problems studied in the present work, the zero input feature maps seem to be clustering with Class 2 inputs. That means similarity between training and generalization zero input maps could be measured by comparing the class prediction difference of zero input feature maps. To provide a more consistent relation of zero inputs feature similarity, in **Figure 6.31** the scatter plot of the absolute deviation $\delta = |\sigma^{set1} - E(\sigma^{set4})|$ of a Set 1 healthy class prediction σ^{set1} with the expected Set 4 healthy prediction label $E(\sigma^{set4})$ is given. The plot is provided for the most pronounced case of bias, meaning D1-D2 separation trained on Set 4. The scatter plot verifies that for the specific problem

case studied, similarity on zero input feature maps is indeed an index of how the network perceives error on the Healthy state. Higher mismatch on the zero inputs follows in a linear like trend with the calculated bias. Such testing with simulated data can be encouraged for further investigation with FE models in a wider modal properties range, to probe a possible common behavior. This method to measure similarity however does not need to be used in Section 4 D_1 - D_2 identification case where the zero input experimental feature maps already cluster far away from the numerical as in **Figure 6.19**.

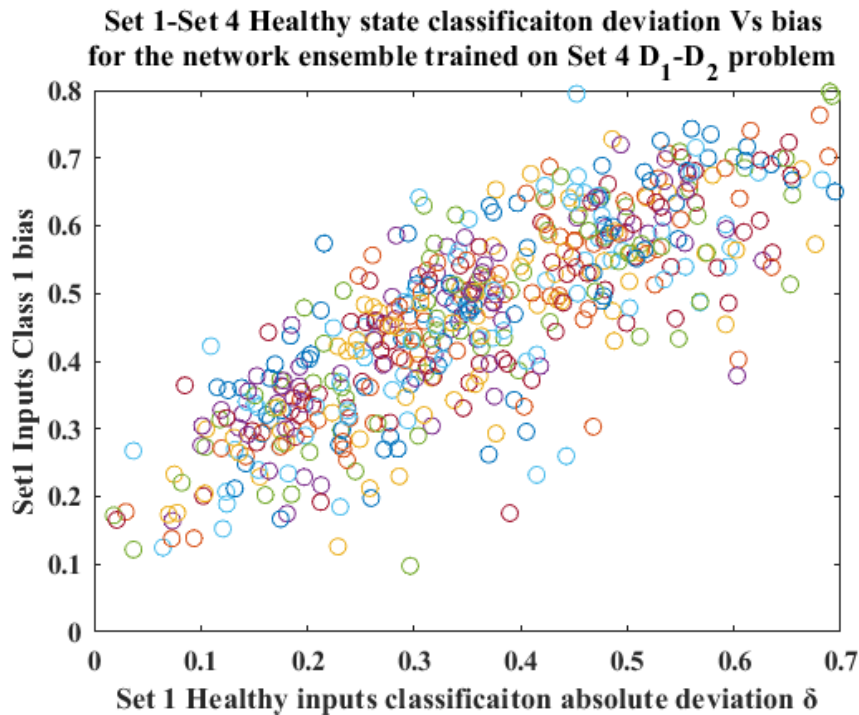


Figure 6.31: Relationship of zero or healthy inputs feature maps difference to the classification bias for the network trained on D_1 - D_2 damage identification on Set 4 data

6.6 Discussion

In the present chapter a binary damage identification problem was studied for an experimental lab scale bridge truss structure for two different damage detection scenarios. The first damage detection scenario includes a cut on beam truss member placed on two different locations and the second scenario a complete removal of the corresponding beams. As numerical data from a FE model was used to generate training sets for a CNN classifier, model error plays the most important role in correct generalization to experimental states, especially for the first case scenario of small damage separation.

It was assumed that larger magnitudes of damage (or more distinct damages) would be less influenced by model error in a numerically trained damage detection problem. This was showcased

in **6.4** were the small damage separation problem D_1 - D_2 presented a complete bias towards one class compared to the larger damage D_3 - D_4 which behaved in the correct direction as seen in **Figure 6.19** and **Figure 6.20**. To additionally validate that phenomenon, a simple truss model was constructed and used for data generation to emulate how generalization may be reflected on a reference set when progressively distancing the training data from it. In **Figure 6.27** and **Figure 6.28** it was seen that the safest way to go with numerical training data would of course be a perfectly fit FE model on the reference states. Statistically speaking, it was shown that lower classification bias and classification shifting can be expected in the reference solution space for better fit models or more distinct damages. As a qualitative interpretation that means the more difficult the damage identification problem, the better fit FE model will be necessary and uncertainties in model properties can result in classification shifting. However, since in practice a perfectly fit FE model to measurement precision is not realistic, the tradeoff between model error or model updating effort and damage magnitude needs to be investigated.

The main novelty of the current work was presented as indexing how the model error was perceived by the trained ANN, depending on the damage identification scenario. As seen in **Figure 6.19** and **Figure 6.20** for the detailed FE model data and the experiment, as well as the simplified truss in **Figure 6.29** and **Figure 6.30**, this perceived or effective model error can show up in the zero input of healthy states feature maps comparison. Training data further away from the reference, combined with more demanding damage identification shows more disagreement in healthy inputs feature maps giving shift in subsequent generalizations. For the moment, it was not tested how and if from this disagreement in healthy input feature maps it is possible to predict subsequent classification bias. That would require in some essence information from the actual unknown system in an experimental case for example. The almost linear relationship of classification bias and the healthy input predicted labels by the network presented in **Figure 6.31**, cannot be assumed to hold arbitrarily for other systems than the one tested. However, comparing healthy input feature maps can already serve as a guide of what kind of damage identification scenarios should be avoided or preferred with the available FE model in hand. For example, since the main idea is in some way avoiding less distinct damage identification cases, the engineer can choose to apply a better sensor network for that purpose.

Revisiting the detailed FE model data generation for instance, in the experimental D_3 - D_4 scenario using 2 sensor locations this instead of 5, a useful comparison can be made in such a manner. In **Figure 6.32** the training curves are presented for 2 sensor location training. The network architecture is the same as in **Table 6.6**, however 55 epochs were necessary highlighting a more demanding problem now using information from less locations. Classification of experimental inputs and plots of feature maps are given in **Figure 6.33** and **Figure 6.34**.

The worse generalization with high Class 1 bias this time compared to **Figure 6.20** that used 5 sensor locations can be already indicated from the zero bias healthy inputs in **Figure 6.34**. The engineer in this case may opt for alternative solutions when observing the zero bias feature map shift, such as increasing the number of sensor locations on the structure, improve the FE model or

avoid completely numerical training data at all. Additionally, that means that damage classification information, which does not only depend on damage magnitude but sensor locations as well, is what makes online classification more distinct or robust to model error in numerically trained classifiers.

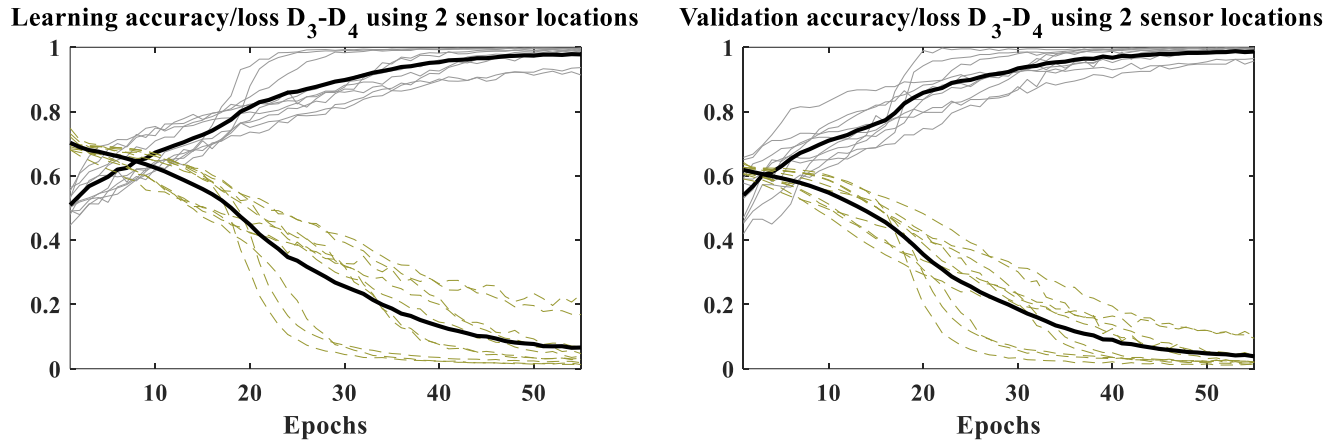


Figure 6.32: Training curves of accuracy and loss for 10 random start BPs for the networks associated with the D3-D4 damage identification trained on 2 sensor locations

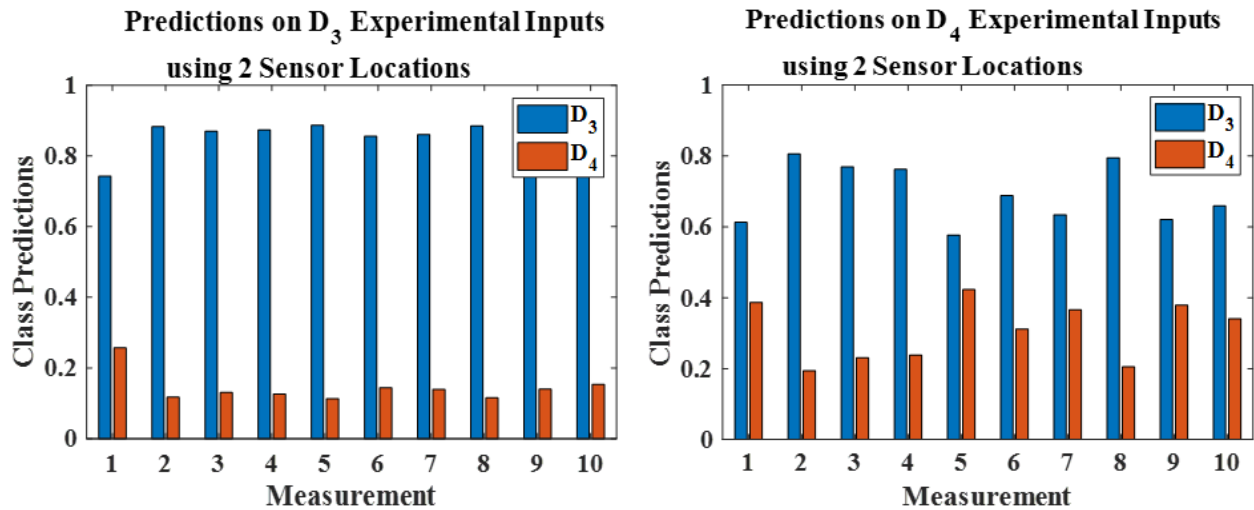


Figure 6.33: Class prediction histograms for the experimental D3-D4 identification/classification by networks trained on 2 sensor locations

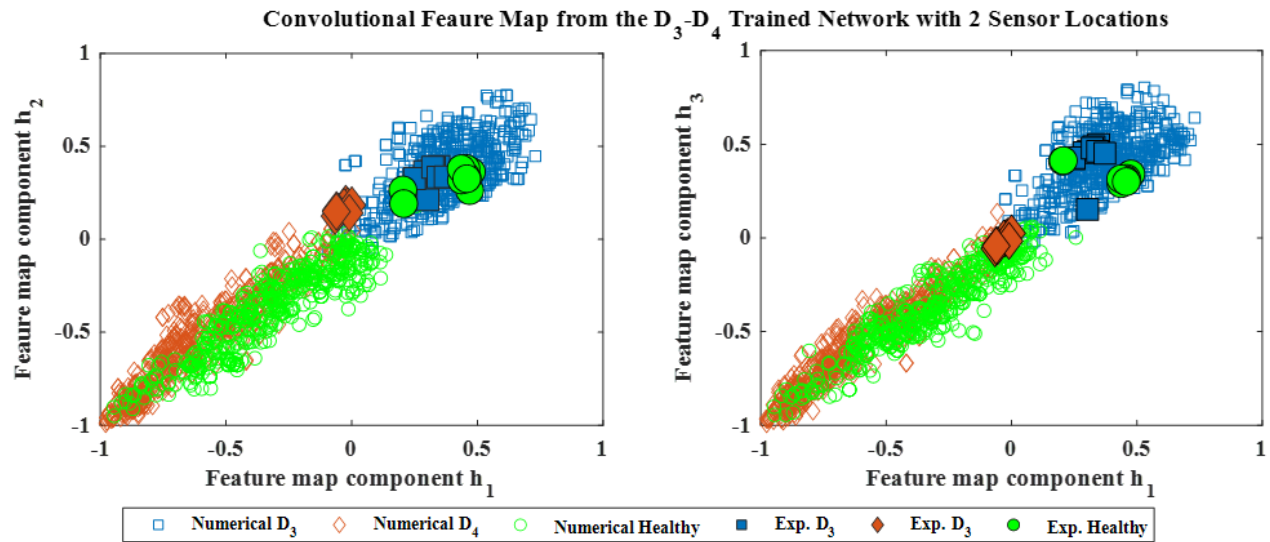


Figure 6.34: Convolutional feature map components for the D_3 - D_4 damage identification network trained on 2 sensor locations. Feature maps are plotted for numerical inputs used in training and experimental used for validation

A notion of the useful damage identification information that was present is additionally provided to complete the picture. The experimental FFTs are given for the D_1 - D_2 and D_3 - D_4 cases in **Figure 6.35** and **Figure 6.36**, compared with the healthy response for 5 impacts. The D_1 - D_2 responses seem to be difficult to distinguish with naked eye and one would expect it would require a very well fit model. The D_3 - D_4 scenarios on the other hand, even though more pronounced differences exist from the Healthy response, a not such a great deviation is between them. It can be also seen that damage case identification seems to benefit from information in all sensors, justifying the increased bias of the numerically trained models when channels are removed. The behavior therefore observed in the feature maps comparison throughout this work follows the difficulty of the damage distinction problem to the final classification. It has to be noted again that damage magnitude and easy classification separation do not go strictly together.

Finally, focus on specific neural network architecture has not been provided in the present work, since the scope is confined in giving a novel description of the effect of model error on unseen experimental damage separation. The reader may follow more relevant works that employ more sophisticated architectures in damage detection such as Fully Convolutional Neural Networks (FCN) [11, 26] which can handle sensor readings in different network branches, or multiple convolutional filter combinations architectures [95]. It can be expected that such network architectures compared to the current may lead to less biased predictions on the online stage and could be subject of future work. The numerical to experimental online monitoring should also not be thought to be confined within the supervised DL framework but other classification ML models could be tested. Vibration based data SHM ML models [24,25,133,134] such as SVM, Auto Regressive (AR) or decision trees (DT) are possible candidates to improve online performance on demanding damage separation cases such as D_1 - D_2 .

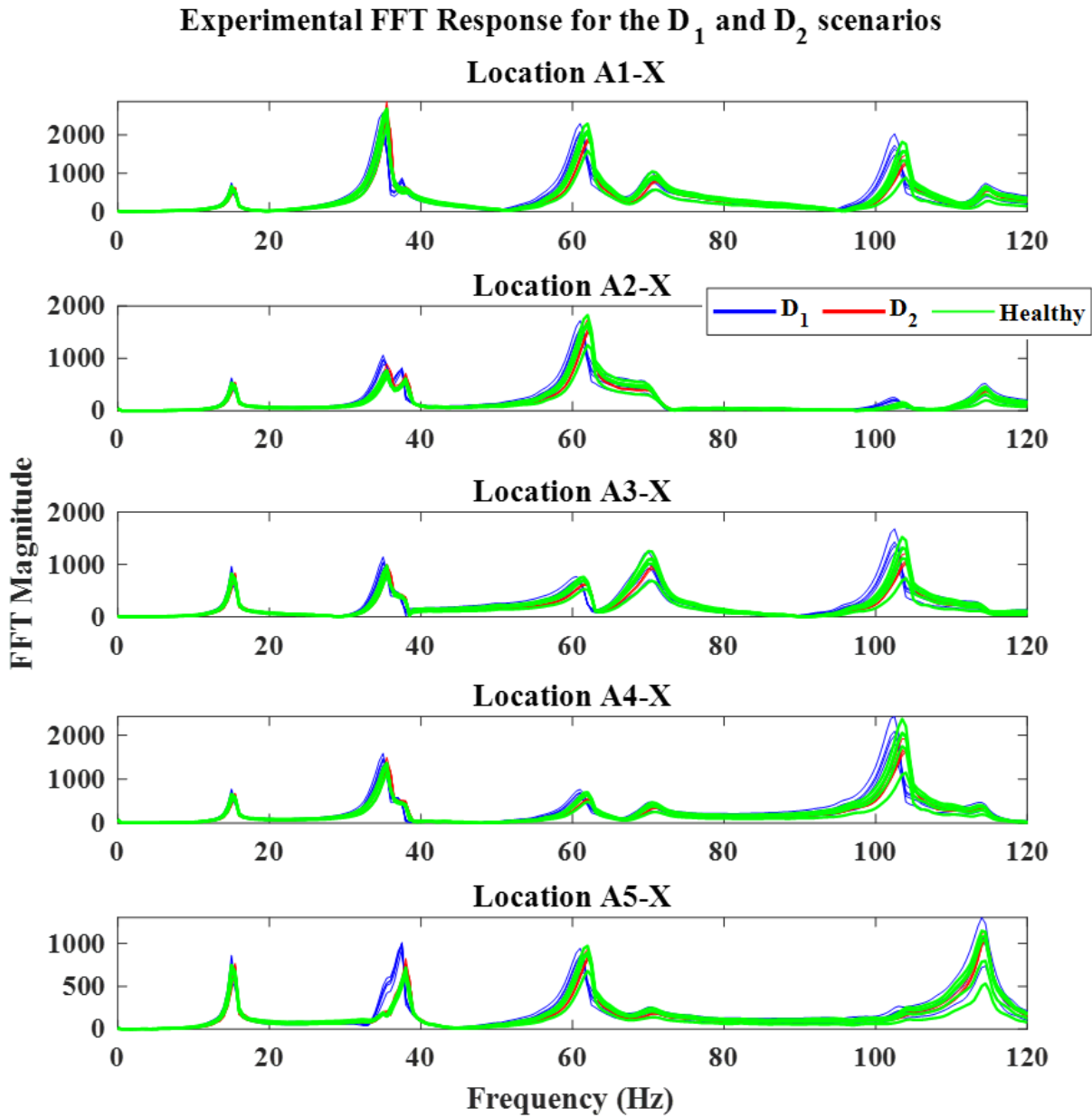


Figure 6.35: Comparison in Frequency with measured experimental responses in all sensor locations for different health states of the structure in the D1-D2 problem

6.7 Conclusions

The present chapter studies model error effects for an experimental lab-scale bridge truss damage identification with supervised classifiers trained on numerical data. More and less distinct damage identification scenarios are tested and numerical data reliability is evaluated as a function of model error and damage identification difficulty.

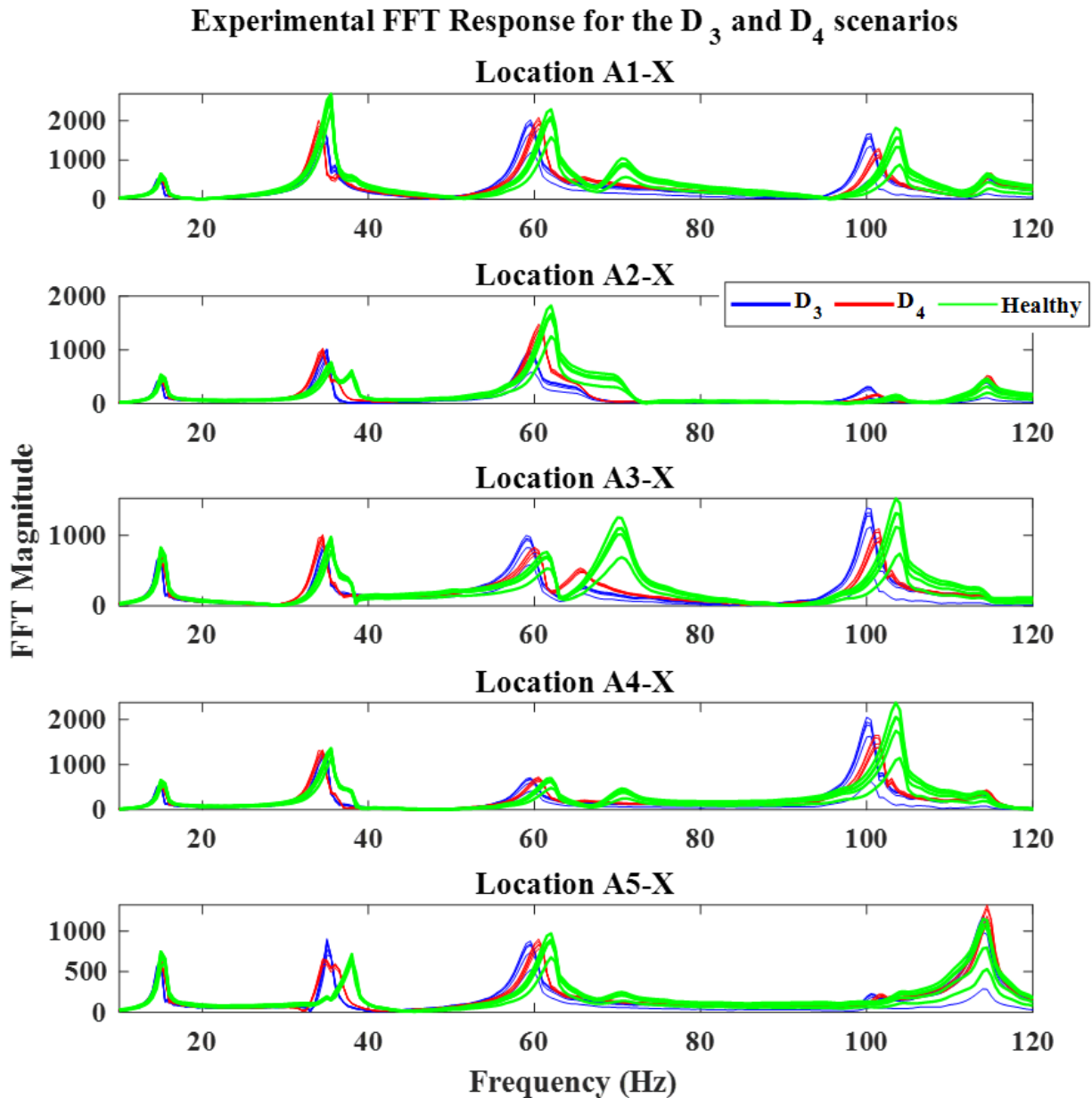


Figure 6.36: Comparison in Frequency with measured experimental responses in all sensor locations for different health states of the structure in the D3-D4 problem

It is found that for the tested structure the experimental damage cases can be more reliably identified when larger magnitude damage or in other words more distinct damage cases are requested for identification. This is additionally validated numerically for a simpler FE model of similar dynamics with corresponding damage cases. It was shown that the chance of biased prediction is higher in less distinct damages and training data further away from the reference.

The effective model error per damage identification scenario was found to be indicated on the convolutional feature maps of the healthy states. The ANNs perceived less error when more

Chapter 6-Conclusions

distinct damage cases scenarios were requested to be classified and better generalization was acquired.

The present work novelties and contribution in testing the reliability of numerical data may aid designers of damage detection and SHM systems with FE models. Further study is encouraged by the findings of the current work in order to explore the limits of numerically generated data.

Conclusions

7.1 Conclusions of thesis

In this final chapter, the conclusions are given based on the analysis and results of the previous chapters. The present thesis deals with Structural Health Monitoring (SHM) and damage identification of structures, using supervised Artificial Neural Network (ANN) classifiers trained by numerical Finite Element (FE) responses. As explained in **Chapter 1** the main motivation behind the presented research was the problem of data availability for damaged states that governs much of practical SHM applications. A set of questions were posed after the proposed methodology of simulated training data was presented. The concluding remarks can be given as answers to these questions:

How to generate labeled training datasets by optimal FE models?

The first concluding remark concerns the numerical data generation which is the main novelty of the present work. Throughout **Chapters 3, 4, 5** and **6** a repetitive load case scheme algorithm was employed for labelled training dataset generation with optimal FE models. It was shown that ANN classifiers with such FE training data can generalize on the real experimental structures. FE models were initially optimized on the intact or Healthy state only and were after used to produce data simulating the operational conditions. All numerically trained classifiers were tested experimentally and the present thesis contributes in the literature in the full spectrum of theory to practice.

How to consider modeling errors that simulated responses carry?

In the second concluding remark, it was shown that classifiers trained by FE data can be guided to learn more robust patterns for experimental generalization when uncertainty simulation on parameters is followed. Except the parameters that would first come in mind like density, elasticity constants or damping, damage parameters were also simulated in such a way. For example, when the connection stiffness value was approximated in paragraph **4.4.1** or stiffness reduction was

simulated for a range of values in difficult to model polymer reinforced damage in paragraph **5.4.1**. The test case in **Chapters 5** specifically studied the generalization improvement of classifiers when various uncertainties were simulated with the proposed data generation algorithm.

What kind of classification strategy and CNN model structuring should be followed for best experimental generalization?

Third conclusion is that Convolutional Neural Network (CNN) supervised classifiers can be applied for monitoring and damage identification tasks and be tuned with different techniques, such as *multifilter* averaging or hierarchical classification to improve the performance on the corresponding experimental states identification. Results were provided in **Chapters 3** and **4** about how such techniques in formulating the detection problem can improve the accuracy of the monitoring system.

How much can such a simulated training data methodology be finally trusted or can it be applied arbitrarily?

Fourth and most important, it was shown that model accuracy plays the prominent role in such a model-based data approach. In **Chapter 3** it was shown that model updating can influence the results in positive way as expected, since simulated and corresponding experimental responses have less disagreement. However, an analytical approach was not given on how much and for what kind of expected damages the FE trained classifiers can be trusted. This would be the main limitation of the proposed methodology. **Chapter 6** on the other hand proposed an interesting approach on how reliability of the proposed methodology could be indexed in advance, meaning before the actual damage occurs. It was found that reliability depends on the model accuracy and damage identification problem effort for the ANN classifier. That novel reliability indexing could contribute to future simulation-based data SHM and damage detection.

The accurate damage states simulation remains however, meaning that the proposed methodology should be considered in cases where the expected damage scenarios can accurately be derived from the intact state model. In the test set-up of **Chapter 6** where the reliability estimation was tested, the investigated scenarios were given as cuts or missing members which can be easily derived from the intact state. Therefore, the trustworthiness of the methodology will be unknown in not well defined or simulated damage scenarios. This is also the main limitation of the proposed FE based training data methodology.

7.2 Future Work

Future work potential for the presented methodology would be in essence unlimited, since as a data-based approach, validation on different structures of various damages and excitations is always towards building more confidence in the method. More specific points of focus could be suggested however.

Chapter 7-Future Work

First, in the present thesis only linear FE models were considered. In practical monitoring cases and early detection, for example in breathing cracks [135] or loose bolts [136], simulating non-linear effects might be important to be included. It could therefore be proposed that the present methodology is tested for cases with non-linear behaviour.

Second, the proposed simulation-based training data approach could find potential applications in set-ups that fall within the condition monitoring or multibody field. Few literature sources that exist [137] indicate a promising space for new research.

Third, the methodology that was tested in **Chapter 6** with comparison on feature maps for reliability indexing, could be explored further. Approximating in advance for what kind of scenarios the numerically trained classifiers can be trusted, would be the point of most importance for the literature.

Fourth, since the main topic that concerns the present thesis is the simulated data generation for supervised damage identification and not the specific Deep Learning models, other data processing Machine Learning (ML) models could be tested additionally on the simulated datasets. ML models such as SVM or Auto Regressive (AR) models [5-7,24,25,31,32,133,134] have also been successfully tested in vibration based SHM applications and could be investigated for possibly better performance in experimental generalization with FE generated datasets. The choice of CNN in the present work was purely for self-learning capabilities directly on raw data and minimal preprocessing as was explained in **Chapter 1**.

Finally, it could be investigated whether the initial experimental cost for updating the FE model could be invested towards using the numerical responses in complementing unsupervised monitoring systems. As explained in **Chapter 1** various operational and environmental conditions that such an experimental data-based system will need to cover could be simulated as well. Results in **Chapters 3** and **4** showed that, in the so called first stage detection (healthy or damaged) high reliability could be expected.

8

Bibliography

- [1] Maes, K., van Meerbeeck, L., Reynders, E. P. B., & Lombaert, G. (2022). Validation of vibration-based structural health monitoring on retrofitted railway bridge KW51. *Mechanical Systems and Signal Processing*, 165. <https://doi.org/10.1016/j.ymsp.2021.108380>
- [2] Sony, S., Gamage, S., Sadhu, A., & Samarabandu, J. (2022). Vibration-based multiclass damage detection and localization using long short-term memory networks. *Structures*, 35. <https://doi.org/10.1016/j.istruc.2021.10.088>
- [3] HaHassan Daneshvar, M., & Sarmadi, H. (2022). Unsupervised learning-based damage assessment of full-scale civil structures under long-term and short-term monitoring. *Engineering Structures*, 256. <https://doi.org/10.1016/j.engstruct.2022.114059>
- [4] Sakaris, C. S., Sakellariou, J. S., & Fassois, S. D. (2021). Multi-site damage precise localization via the random vibration functional model based method: Formulation & concept validation. *Mechanical Systems and Signal Processing*, 160. <https://doi.org/10.1016/j.ymsp.2021.107880>
- [5] Mosavi, A. A., Dickey, D., Seracino, R., & Rizkalla, S. (2012). Identifying damage locations under ambient vibrations utilizing vector autoregressive models and Mahalanobis distances. *Mechanical Systems and Signal Processing*, 26(1). <https://doi.org/10.1016/j.ymsp.2011.06.009>
- [6] Gui, G., Pan, H., Lin, Z., Li, Y., & Yuan, Z. (2017). Data-driven support vector machine with optimization techniques for structural health monitoring and damage detection. *KSCE Journal of Civil Engineering*, 21(2). <https://doi.org/10.1007/s12205-017-1518-5>
- [7] Vamvoudakis-Stefanou, K. J., Sakellariou, J. S., & Fassois, S. D. (2018). Vibration-based damage detection for a population of nominally identical structures: Unsupervised Multiple Model (MM) statistical time series type methods. *Mechanical Systems and Signal Processing*, 111. <https://doi.org/10.1016/j.ymsp.2018.03.054>
- [8] Soleimani-Babakamali, M. H., Sepasdar, R., Nasrollahzadeh, K., & Sarlo, R. (2022). A system reliability approach to real-time unsupervised structural health monitoring without prior information. *Mechanical Systems and Signal Processing*, 171. <https://doi.org/10.1016/j.ymsp.2022.108913>
- [9] Meixedo, A., Santos, J., Ribeiro, D., Caçada, R., & Todd, M. D. (2022). Online unsupervised detection of structural changes using train-induced dynamic responses. *Mechanical Systems and Signal Processing*, 165. <https://doi.org/10.1016/j.ymsp.2021.108268>
- [10] Figueiredo, E., & Brownjohn, J. (2022). Three decades of statistical pattern recognition paradigm for SHM of bridges. In *Structural Health Monitoring*. <https://doi.org/10.1177/14759217221075241>

Chapter 8-Bibliography

- [11] Rosafalco, L., Torzoni, M., Manzoni, A., Mariani, S., & Corigliano, A. (2021). Online structural health monitoring by model order reduction and deep learning algorithms. *Computers and Structures*, 255. <https://doi.org/10.1016/j.compstruc.2021.106604>
- [12] Döhler, M., Hille, F., Mevel, L., & Rucker, W. (2014). Structural health monitoring with statistical methods during progressive damage test of S101 Bridge. *Engineering Structures*, 69. <https://doi.org/10.1016/j.engstruct.2014.03.010>
- [13] García, D., & Tcherniak, D. (2019). An experimental study on the data-driven structural health monitoring of large wind turbine blades using a single accelerometer and actuator. *Mechanical Systems and Signal Processing*, 127. <https://doi.org/10.1016/j.ymsp.2019.02.062>
- [14] Soo Lon Wah, W., Chen, Y. T., & Owen, J. S. (2021). A regression-based damage detection method for structures subjected to changing environmental and operational conditions. *Engineering Structures*, 228. <https://doi.org/10.1016/j.engstruct.2020.111462>
- [15] Padil, K. H., Bakhary, N., Abdulkareem, M., Li, J., & Hao, H. (2020). Non-probabilistic method to consider uncertainties in frequency response function for vibration-based damage detection using Artificial Neural Network. *Journal of Sound and Vibration*, 467. <https://doi.org/10.1016/j.jsv.2019.115069>
- [16] Mousavi, Z., Varahram, S., Etefagh, M. M., Sadeghi, M. H., & Razavi, S. N. (2021). Deep neural networks–based damage detection using vibration signals of finite element model and real intact state: An evaluation via a lab-scale offshore jacket structure. *Structural Health Monitoring*, 20(1). <https://doi.org/10.1177/1475921720932614>
- [17] Peng, Z., Li, J., & Hao, H. (2022). Structural damage detection via phase space based manifold learning under changing environmental and operational conditions. *Engineering Structures*, 263, 114420. <https://doi.org/10.1016/j.engstruct.2022.114420>
- [18] Augustyn, D., Cosack, N., & Ulriksen, M. D. (2022). On the influence of environmental and operational variability on modal parameters of offshore wind support structures. *Marine Structures*, 84. <https://doi.org/10.1016/j.marstruc.2022.103185>
- [19] Torzoni, M., Rosafalco, L., Manzoni, A., Mariani, S., & Corigliano, A. (2022). SHM under varying environmental conditions: an approach based on model order reduction and deep learning. *Computers and Structures*, 266. <https://doi.org/10.1016/j.compstruc.2022.106790>
- [20] Papadimitriou, C., Ntotsios, E., Giagopoulos, D., & Natsiavas, S. (2012). Variability of updated finite element models and their predictions consistent with vibration measurements. *Structural Control and Health Monitoring*, 19(5). <https://doi.org/10.1002/stc.453>
- [21] Giagopoulos, D., & Arailopoulos, A. (2017). Computational framework for model updating of large scale linear and nonlinear finite element models using state of the art evolution strategy. *Computers and Structures*, 192. <https://doi.org/10.1016/j.compstruc.2017.07.004>
- [22] Christodoulou, K., Ntotsios, E., Papadimitriou, C., & Panetsos, P. (2008). Structural model updating and prediction variability using Pareto optimal models. *Computer Methods in Applied Mechanics and Engineering*, 198(1). <https://doi.org/10.1016/j.cma.2008.04.010>
- [23] Entezami, A., Shariatmadar, H., & Mariani, S. (2020). Early damage assessment in large-scale structures by innovative statistical pattern recognition methods based on time series modeling and novelty detection. *Advances in Engineering Software*, 150. <https://doi.org/10.1016/j.advengsoft.2020.102923>
- [24] Avci, O., Abdeljaber, O., Kiranyaz, S., Hussein, M., Gabbouj, M., & Inman, D. J. (2021). A review of vibration-based damage detection in civil structures: From traditional methods to Machine Learning and Deep Learning applications. In *Mechanical Systems and Signal Processing* (Vol. 147). <https://doi.org/10.1016/j.ymsp.2020.107077>
- [25] Bigoni, C., & Hesthaven, J. S. (2020). Simulation-based Anomaly Detection and Damage Localization: an application to Structural Health Monitoring. *Computer Methods in Applied Mechanics and Engineering*, 363. <https://doi.org/10.1016/j.cma.2020.112896>

Chapter 8-Bibliography

- [26] Rosafalco, L., Manzoni, A., Mariani, S., & Corigliano, A. (2020). Fully convolutional networks for structural health monitoring through multivariate time series classification. *Advanced Modeling and Simulation in Engineering Sciences*, 7(1). <https://doi.org/10.1186/s40323-020-00174-1>
- [27] Zhao, R., Yan, R., Chen, Z., Mao, K., Wang, P., & Gao, R. X. (2019). Deep learning and its applications to machine health monitoring. In *Mechanical Systems and Signal Processing* (Vol. 115). <https://doi.org/10.1016/j.ymssp.2018.05.050>
- [28] Yu, Y., Wang, C., Gu, X., & Li, J. (2019). A novel deep learning-based method for damage identification of smart building structures. *Structural Health Monitoring*, 18(1). <https://doi.org/10.1177/1475921718804132>
- [29] Bao, Y., Chen, Z., Wei, S., Xu, Y., Tang, Z., & Li, H. (2019). The State of the Art of Data Science and Engineering in Structural Health Monitoring. *Engineering*, 5(2). <https://doi.org/10.1016/j.eng.2018.11.027>
- [30] Barraza, J. F., Droguett, E. L., Naranjo, V. M., & Martins, M. R. (2020). Capsule Neural Networks for structural damage localization and quantification using transmissibility data. *Applied Soft Computing Journal*, 97. <https://doi.org/10.1016/j.asoc.2020.106732>
- [31] Spanos, N. A., Sakellariou, J. S., & Fassois, S. D. (2020). Vibration-response-only statistical time series structural health monitoring methods: A comprehensive assessment via a scale jacket structure. *Structural Health Monitoring*, 19(3). <https://doi.org/10.1177/1475921719862487>
- [32] Poulimenos, A. G., & Sakellariou, J. S. (2019). A transmittance-based methodology for damage detection under uncertainty: An application to a set of composite beams with manufacturing variability subject to impact damage and varying operating conditions. *Structural Health Monitoring*, 18(1). <https://doi.org/10.1177/1475921718779190>
- [33] Abdeljaber, O., Avci, O., Kiranyaz, S., Gabbouj, M., & Inman, D. J. (2017). Real-time vibration-based structural damage detection using one-dimensional convolutional neural networks. *Journal of Sound and Vibration*, 388. <https://doi.org/10.1016/j.jsv.2016.10.043>
- [34] Dang, V. H., Vu, T. C., Nguyen, B. D., Nguyen, Q. H., & Nguyen, T. D. (2022). Structural damage detection framework based on graph convolutional network directly using vibration data. *Structures*, 38. <https://doi.org/10.1016/j.istruc.2022.01.066>
- [35] Zhang, Y., Miyamori, Y., Mikami, S., & Saito, T. (2019). Vibration-based structural state identification by a 1-dimensional convolutional neural network. *Computer-Aided Civil and Infrastructure Engineering*, 34(9). <https://doi.org/10.1111/mice.12447>
- [36] Dang, H. v., Raza, M., Nguyen, T. v., Bui-Tien, T., & Nguyen, H. X. (2021). Deep learning-based detection of structural damage using time-series data. *Structure and Infrastructure Engineering*, 17(11). <https://doi.org/10.1080/15732479.2020.1815225>
- [37] Tang, Z., Chen, Z., Bao, Y., & Li, H. (2019). Convolutional neural network-based data anomaly detection method using multiple information for structural health monitoring. *Structural Control and Health Monitoring*, 26(1). <https://doi.org/10.1002/stc.2296>
- [38] Borovykh, A., Oosterlee, C. W., & Bohté, S. M. (2019). Generalization in fully-connected neural networks for time series forecasting. *Journal of Computational Science*, 36. <https://doi.org/10.1016/j.jocs.2019.07.007>
- [39] Tong, Z., & Tanaka, G. (2019). Hybrid pooling for enhancement of generalization ability in deep convolutional neural networks. *Neurocomputing*, 333. <https://doi.org/10.1016/j.neucom.2018.12.036>
- [40] Huang, J., Wang, S., Zhou, G., Hu, W., & Yu, G. (2022). Evaluation on the generalization of a learned convolutional neural network for MRI reconstruction. *Magnetic Resonance Imaging*, 87. <https://doi.org/10.1016/j.mri.2021.12.003>
- [41] Fernandez-Navamuel, A., Zamora-Sánchez, D., Omella, Á. J., Pardo, D., Garcia-Sanchez, D., & Magalhães, F. (2022). Supervised Deep Learning with Finite Element simulations for damage identification in bridges. *Engineering Structures*, 257. <https://doi.org/10.1016/j.engstruct.2022.114016>

Chapter 8-Bibliography

- [42] Lee, J. J., Lee, J. W., Yi, J. H., Yun, C. B., & Jung, H. Y. (2005). Neural networks-based damage detection for bridges considering errors in baseline finite element models. *Journal of Sound and Vibration*, 280(3–5). <https://doi.org/10.1016/j.jsv.2004.01.003>
- [43] Ghiasi, A., Moghaddam, M. K., Ng, C.-T., Sheikh, A. H., & Shi, J. Q. (2022). Damage classification of in-service steel railway bridges using a novel vibration-based convolutional neural network. *Engineering Structures*, 264, 114474. <https://doi.org/10.1016/j.engstruct.2022.114474>
- [44] Taddei, T., Penn, J. D., Yano, M., & Patera, A. T. (2018). Simulation-Based Classification; a Model-Order-Reduction Approach for Structural Health Monitoring. *Archives of Computational Methods in Engineering*, 25(1). <https://doi.org/10.1007/s11831-016-9185-0>
- [45] Avci, O., Alkhamis, K., Abdeljaber, O., Alsharo, A., & Hussein, M. (2022). Operational modal analysis and finite element model updating of a 230 m tall tower. *Structures*, 37. <https://doi.org/10.1016/j.istruc.2021.12.078>
- [46] Arailopoulos, A., Giagopoulos, D., Zacharakis, I., & Pipili, E. (2018). Integrated reverse engineering strategy for large-scale mechanical systems: Application to a steam turbine rotor. *Frontiers in Built Environment*, 4. <https://doi.org/10.3389/fbuil.2018.00055>
- [47] Zhao, W., Gupta, A., Regan, C. D., Miglani, J., Kapania, R. K., & Seiler, P. J. (2019). Component data assisted finite element model updating of composite flying-wing aircraft using multi-level optimization. *Aerospace Science and Technology*, 95. <https://doi.org/10.1016/j.ast.2019.105486>
- [48] Hansen, N., Müller, S. D., & Koumoutsakos, P. (2003). Reducing the time complexity of the derandomized evolution strategy with covariance matrix adaptation (CMA-ES). *Evolutionary Computation*, 11(1). <https://doi.org/10.1162/106365603321828970>
- [49] Hansen, N. (2006). The CMA evolution strategy: A comparing review. *Studies in Fuzziness and Soft Computing*, 192. https://doi.org/10.1007/11007937_4
- [50] Giagopoulos, D., Arailopoulos, A., Dertimanis, V., Papadimitriou, C., Chatzi, E., & Grompanopoulos, K. (2019). Structural health monitoring and fatigue damage estimation using vibration measurements and finite element model updating. *Structural Health Monitoring*, 18(4). <https://doi.org/10.1177/1475921718790188>
- [51] Zhang, J., Maes, K., Roeck, G. de, & Lombaert, G. (2021). Model updating for a large multi-span quasi-periodic viaduct based on free wave characteristics. *Journal of Sound and Vibration*, 506. <https://doi.org/10.1016/j.jsv.2021.116161>
- [52] Zhang, Z., Sun, C., & Guo, B. (2022). Transfer-learning guided Bayesian model updating for damage identification considering modeling uncertainty. *Mechanical Systems and Signal Processing*, 166. <https://doi.org/10.1016/j.ymssp.2021.108426>
- [53] Mandler, A., Döhler, M., & Ventura, C. E. (2021). A reliability-based approach to determine the minimum detectable damage for statistical damage detection. *Mechanical Systems and Signal Processing*, 154. <https://doi.org/10.1016/j.ymssp.2020.107561>
- [54] Bao, X., Fan, T., Shi, C., & Yang, G. (2021). Deep learning methods for damage detection of jacket-type offshore platforms. *Process Safety and Environmental Protection*, 154. <https://doi.org/10.1016/j.psep.2021.08.031>
- [55] Yang, R., Singh, S. K., Tavakkoli, M., Amiri, N., Yang, Y., Karami, M. A., & Rai, R. (2020). CNN-LSTM deep learning architecture for computer vision-based modal frequency detection. *Mechanical Systems and Signal Processing*, 144. <https://doi.org/10.1016/j.ymssp.2020.106885>
- [56] Liao, S., Liu, H., Yang, J., & Ge, Y. (2022). A channel-spatial-temporal attention-based network for vibration-based damage detection. *Information Sciences*, 606, 213–229. <https://doi.org/10.1016/j.ins.2022.05.042>
- [57] Yang, J., Zhang, L., Chen, C., Li, Y., Li, R., Wang, G., Jiang, S., & Zeng, Z. (2020). A hierarchical deep convolutional neural network and gated recurrent unit framework for structural damage detection. *Information Sciences*, 540. <https://doi.org/10.1016/j.ins.2020.05.090>

Chapter 8-Bibliography

- [58] Landauskas, M., Cao, M., & Ragulskis, M. (2020). Permutation entropy-based 2D feature extraction for bearing fault diagnosis. *Nonlinear Dynamics*, 102(3), 1717–1731. <https://doi.org/10.1007/s11071-020-06014-6>
- [59] Flah, M., Ragab, M., Lazhari, M., & Nehdi, M. L. (2022). Localization and classification of structural damage using deep learning single-channel signal-based measurement. *Automation in Construction*, 139. <https://doi.org/10.1016/j.autcon.2022.104271>
- [60] Zhu, S., Zhang, Q., Zhai, W., Yuan, Z., & Cai, C. (2021). Sensor deploying for damage identification of vibration isolator in floating-slab track using deep residual network. *Measurement: Journal of the International Measurement Confederation*, 183. <https://doi.org/10.1016/j.measurement.2021.109801>
- [61] Bigoni, C., Zhang, Z., & Hesthaven, J. S. (2020). Systematic sensor placement for structural anomaly detection in the absence of damaged states. *Computer Methods in Applied Mechanics and Engineering*, 371. <https://doi.org/10.1016/j.cma.2020.113315>
- [62] Giagopoulos, D., Chatziparasidis, I., & Sapidis, N. S. (2018). Dynamic and structural integrity analysis of a complete elevator system through a Mixed Computational-Experimental Finite Element Methodology. *Engineering Structures*, 160. <https://doi.org/10.1016/j.engstruct.2018.01.018>
- [63] Markogiannaki, O., Arailopoulos, A., Giagopoulos, D., & Papadimitriou, C. (2022). Vibration-based Damage Localization and Quantification Framework of Large-Scale Truss Structures. *Structural Health Monitoring*, 147592172211004. <https://doi.org/10.1177/14759217221100443>
- [64] Zacharakis, I., Giagopoulos, D., Arailopoulos, A., & Markogiannaki, O. (2022). Optimal finite element modeling of filament wound CFRP tubes. *Engineering Structures*, 253. <https://doi.org/10.1016/j.engstruct.2021.113808>
- [65] Grafe H. (1995). Review of frequency response function updating methods. BRITEURANUS BRE2-CT94-0946
- [66] Pereira, S., Reynders, E., Magalhães, F., Cunha, Á., & Gomes, J. P. (2020). The role of modal parameters uncertainty estimation in automated modal identification, modal tracking and data normalization. *Engineering Structures*, 224. <https://doi.org/10.1016/j.engstruct.2020.111208>
- [67] Reynders, E., Pintelon, R., & de Roeck, G. (2008). Uncertainty bounds on modal parameters obtained from stochastic subspace identification. *Mechanical Systems and Signal Processing*, 22(4). <https://doi.org/10.1016/j.ymsp.2007.10.009>
- [68] Ping, M., Jia, X., Papadimitriou, C., Han, X., & Jiang, C. (2022). Statistics-based Bayesian modeling framework for uncertainty quantification and propagation. *Mechanical Systems and Signal Processing*, 174. <https://doi.org/10.1016/j.ymsp.2022.109102>
- [69] Sedehi, O., Papadimitriou, C., & Katafygiotis, L. S. (2022). Hierarchical Bayesian uncertainty quantification of Finite Element models using modal statistical information. *Mechanical Systems and Signal Processing*, 179, 109296. <https://doi.org/10.1016/j.ymsp.2022.109296>
- [70] Shorten, C., & Khoshgoftaar, T. M. (2019). A survey on Image Data Augmentation for Deep Learning. *Journal of Big Data*, 6(1). <https://doi.org/10.1186/s40537-019-0197-0>
- [71] Rashid, K. M., & Louis, J. (2019). Times-series data augmentation and deep learning for construction equipment activity recognition. *Advanced Engineering Informatics*, 42. <https://doi.org/10.1016/j.aei.2019.100944>
- [72] Lu, H., Zhao, X., Tao, B., & Ding, H. (2022). A state-classification approach for light-weight robotic drilling using model-based data augmentation and multi-level deep learning. *Mechanical Systems and Signal Processing*, 167. <https://doi.org/10.1016/j.ymsp.2021.108480>
- [73] Jiang, Y., Malliaras, P., Chen, B., & Kulić, D. (2021). Model-based data augmentation for user-independent fatigue estimation. *Computers in Biology and Medicine*, 137. <https://doi.org/10.1016/j.combiomed.2021.104839>
- [74] Lu, Y., Tian, Z., Zhang, Q., Zhou, R., & Chu, C. (2021). Data augmentation strategy for short-term heating load prediction model of residential building. *Energy*, 235. <https://doi.org/10.1016/j.energy.2021.121328>

Chapter 8-Bibliography

- [75] Yoo, Y., Jung, U. J., Han, Y. H., & Lee, J. (2021). Data Augmentation-Based Prediction of System Level Performance under Model and Parameter Uncertainties: Role of Designable Generative Adversarial Networks (DGAN). *Reliability Engineering and System Safety*, 206. <https://doi.org/10.1016/j.ress.2020.107316>
- [76] Daouk, S., Louf, F., Dorival, O., Champaney, L., & Audebert, S. (2015). Uncertainties in structural dynamics: Overview and comparative analysis of methods. *Mechanics and Industry*, 16(4). <https://doi.org/10.1051/meca/2015010>
- [77] Bathe, K. J. (1996). Finite Element Procedures. In *Englewood Cliffs New Jersey*.
- [78] Aggarwal, C. C. (2018). Neural Networks and Deep Learning: A Textbook. In *Artificial Intelligence*.
- [79] Kiranyaz, S., Gastli, A., Ben-Brahim, L., Al-Emadi, N., & Gabbouj, M. (2019). Real-Time Fault Detection and Identification for MMC Using 1-D Convolutional Neural Networks. *IEEE Transactions on Industrial Electronics*, 66(11). <https://doi.org/10.1109/TIE.2018.2833045>
- [80] Sindi, H., Nour, M., Rawa, M., Öztürk, Ş., & Polat, K. (2021). Random fully connected layered 1D CNN for solving the Z-bus loss allocation problem. *Measurement: Journal of the International Measurement Confederation*, 171. <https://doi.org/10.1016/j.measurement.2020.108794>
- [81] Nagi, J., Ducatelle, F., di Caro, G. A., Cireşan, D., Meier, U., Giusti, A., Nagi, F., Schmidhuber, J., & Gambardella, L. M. (2011). Max-pooling convolutional neural networks for vision-based hand gesture recognition. *2011 IEEE International Conference on Signal and Image Processing Applications, ICSIPA 2011*. <https://doi.org/10.1109/ICSIPA.2011.6144164>
- [82] F. Chollet, (2015) keras, GitHub. <https://github.com/fchollet/keras>
- [83] Srivastava, N., Hinton, G., Krizhevsky, A., Sutskever, I., & Salakhutdinov, R. (2014). Dropout: A simple way to prevent neural networks from overfitting. *Journal of Machine Learning Research*, 15.
- [84] Kovács, G., Tóth, L., van Compernelle, D., & Ganapathy, S. (2017). Increasing the robustness of CNN acoustic models using autoregressive moving average spectrogram features and channel dropout. *Pattern Recognition Letters*, 100. <https://doi.org/10.1016/j.patrec.2017.09.023>
- [85] Khan, S. H., Hayat, M., & Porikli, F. (2019). Regularization of deep neural networks with spectral dropout. *Neural Networks*, 110. <https://doi.org/10.1016/j.neunet.2018.09.009>
- [86] Zeng, Y., Dai, T., Chen, B., Xia, S. T., & Lu, J. (2021). Correlation-based structural dropout for convolutional neural networks. *Pattern Recognition*, 120. <https://doi.org/10.1016/j.patcog.2021.108117>
- [87] Hagan, M. T., Demuth, H. B., & Beale, M. H. (1995). Neural Network Design. *Boston Massachusetts PWS*, 2. <https://doi.org/10.1007/1-84628-303-5>
- [88] Rumelhart, D. E., Hinton, G. E., & Williams, R. J. (1986). Learning representations by back-propagating errors. *Nature*, 323(6088). <https://doi.org/10.1038/323533a0>
- [89] Kosko, B., Audhkhasi, K., & Osoba, O. (2020). Noise can speed backpropagation learning and deep bidirectional pretraining. *Neural Networks*, 129. <https://doi.org/10.1016/j.neunet.2020.04.004>
- [90] Zhang, J. R., Zhang, J., Lok, T. M., & Lyu, M. R. (2007). A hybrid particle swarm optimization-back-propagation algorithm for feedforward neural network training. *Applied Mathematics and Computation*, 185(2). <https://doi.org/10.1016/j.amc.2006.07.025>
- [91] Wang, X. G., Tang, Z., Tamura, H., Ishii, M., & Sun, W. D. (2004). An improved backpropagation algorithm to avoid the local minima problem. *Neurocomputing*, 56(1–4). <https://doi.org/10.1016/j.neucom.2003.08.006>
- [92] Wang, X. G., Tang, Z., Tamura, H., & Ishii, M. (2004). A modified error function for the backpropagation algorithm. *Neurocomputing*, 57(1–4). <https://doi.org/10.1016/j.neucom.2003.12.006>
- [93] PERRONE, M. P., & COOPER, L. N. (1995). *When networks disagree: Ensemble methods for hybrid neural networks*. https://doi.org/10.1142/9789812795885_0025

Chapter 8-Bibliography

- [94] Cruz, Y. J., Rivas, M., Quiza, R., Villalonga, A., Haber, R. E., & Beruvides, G. (2021). Ensemble of convolutional neural networks based on an evolutionary algorithm applied to an industrial welding process. *Computers in Industry*, 133. <https://doi.org/10.1016/j.compind.2021.103530>
- [95] Seventekidis, P., Giagopoulos, D., Arailopoulos, A., & Markogiannaki, O. (2020). Structural Health Monitoring using deep learning with optimal finite element model generated data. *Mechanical Systems and Signal Processing*, 145. <https://doi.org/10.1016/j.ymsp.2020.106972>
- [96] Wickramasinghe, W. R., Thambiratnam, D. P., Chan, T. H. T., & Nguyen, T. (2016). Vibration characteristics and damage detection in a suspension bridge. *Journal of Sound and Vibration*, 375. <https://doi.org/10.1016/j.jsv.2016.04.025>
- [97] Yapar, O., Basu, P. K., Volgyesi, P., & Ledeczki, A. (2015). Structural health monitoring of bridges with piezoelectric AE sensors. *Engineering Failure Analysis*, 56. <https://doi.org/10.1016/j.engfailanal.2015.03.009>
- [98] Sousa Tomé, E., Pimentel, M., & Figueiras, J. (2020). Damage detection under environmental and operational effects using cointegration analysis – Application to experimental data from a cable-stayed bridge. *Mechanical Systems and Signal Processing*, 135. <https://doi.org/10.1016/j.ymsp.2019.106386>
- [99] Tcherniak, D., & Mølgaard, L. L. (2017). Active vibration-based structural health monitoring system for wind turbine blade: Demonstration on an operating Vestas V27 wind turbine. *Structural Health Monitoring*, 16(5). <https://doi.org/10.1177/1475921717722725>
- [100] Hu, W., Chang, H., & Gu, X. (2019). A novel fault diagnosis technique for wind turbine gearbox. *Applied Soft Computing Journal*, 82. <https://doi.org/10.1016/j.asoc.2019.105556>
- [101] Elasha, F., Greaves, M., & Mba, D. (2018). Planetary bearing defect detection in a commercial helicopter main gearbox with vibration and acoustic emission. *Structural Health Monitoring*, 17(5). <https://doi.org/10.1177/1475921717738713>
- [102] Ksica, F., Hadas, Z., & Hlinka, J. (2019). Integration and test of piezocomposite sensors for structure health monitoring in aerospace. *Measurement: Journal of the International Measurement Confederation*, 147. <https://doi.org/10.1016/j.measurement.2019.106861>
- [103] Fuentes, R., Dwyer-Joyce, R. S., Marshall, M. B., Wheals, J., & Cross, E. J. (2020). Detection of sub-surface damage in wind turbine bearings using acoustic emissions and probabilistic modelling. *Renewable Energy*, 147. <https://doi.org/10.1016/j.renene.2019.08.019>
- [104] Zenisek, J., Holzinger, F., & Affenzeller, M. (2019). Machine learning based concept drift detection for predictive maintenance. *Computers and Industrial Engineering*, 137. <https://doi.org/10.1016/j.cie.2019.106031>
- [105] Bayane, I., Mankar, A., Brühwiler, E., & Sørensen, J. D. (2019). Quantification of traffic and temperature effects on the fatigue safety of a reinforced-concrete bridge deck based on monitoring data. *Engineering Structures*, 196. <https://doi.org/10.1016/j.engstruct.2019.109357>
- [106] Kwasniewski, L., Li, H., Wekezer, J., & Malachowski, J. (2006). Finite element analysis of vehicle-bridge interaction. In *Finite Elements in Analysis and Design* (Vol. 42, Issue 11). <https://doi.org/10.1016/j.finel.2006.01.014>
- [107] Khodabandehlou, H., Pekcan, G., & Fadali, M. S. (2019). Vibration-based structural condition assessment using convolution neural networks. *Structural Control and Health Monitoring*, 26(2). <https://doi.org/10.1002/stc.2308>
- [108] Seventekidis, P., & Giagopoulos, D. (2021). A combined finite element and hierarchical Deep learning approach for structural health monitoring: Test on a pin-joint composite truss structure. *Mechanical Systems and Signal Processing*, 157. <https://doi.org/10.1016/j.ymsp.2021.107735>
- [109] Mousavi, Z., Etefagh, M. M., Sadeghi, M. H., & Razavi, S. N. (2020). Developing deep neural network for damage detection of beam-like structures using dynamic response based on FE model and real healthy state. *Applied Acoustics*, 168. <https://doi.org/10.1016/j.apacoust.2020.107402>

Chapter 8-Bibliography

- [110] Wang, F., Chen, Z., & Song, G. (2020). Monitoring of multi-bolt connection looseness using entropy-based active sensing and genetic algorithm-based least square support vector machine. *Mechanical Systems and Signal Processing*, 136. <https://doi.org/10.1016/j.ymssp.2019.106507>
- [111] He, K., & Zhu, W. D. (2014). Detecting loosening of bolted connections in a pipeline using changes in natural frequencies. *Journal of Vibration and Acoustics, Transactions of the ASME*, 136(3). <https://doi.org/10.1115/1.4026973>
- [112] Kim, J., Yoon, J. C., & Kang, B. S. (2007). Finite element analysis and modeling of structure with bolted joints. *Applied Mathematical Modelling*, 31(5). <https://doi.org/10.1016/j.apm.2006.03.020>
- [113] Huda, F., Kajiwara, I., Hosoya, N., & Kawamura, S. (2013). Bolt loosening analysis and diagnosis by non-contact laser excitation vibration tests. *Mechanical Systems and Signal Processing*, 40(2). <https://doi.org/10.1016/j.ymssp.2013.05.023>
- [114] Cleva, C., Cachet, C., Cabrol-Bass, D., & Forrest, T. P. (1997). Advantages of a hierarchical system of neural-networks for the interpretation of infrared spectra in structure determination. *Analytica Chimica Acta*, 348(1-3). [https://doi.org/10.1016/S0003-2670\(97\)00151-7](https://doi.org/10.1016/S0003-2670(97)00151-7)
- [115] Seo, Y., & Shin, K. shik. (2019). Hierarchical convolutional neural networks for fashion image classification. *Expert Systems with Applications*, 116. <https://doi.org/10.1016/j.eswa.2018.09.022>
- [116] Adams, S., Meekins, R., Beling, P. A., Farinholt, K., Brown, N., Polter, S., & Dong, Q. (2019). Hierarchical fault classification for resource constrained systems. *Mechanical Systems and Signal Processing*, 134. <https://doi.org/10.1016/j.ymssp.2019.106266>
- [117] Worden, K., Manson, G., & Fieller, N. R. J. (2000). Damage detection using outlier analysis. *Journal of Sound and Vibration*, 229(3). <https://doi.org/10.1006/jsvi.1999.2514>
- [118] Kopsaftopoulos, F. P., & Fassois, S. D. (2010). Vibration based health monitoring for a lightweight truss structure: Experimental assessment of several statistical time series methods. *Mechanical Systems and Signal Processing*, 24(7). <https://doi.org/10.1016/j.ymssp.2010.05.013>
- [119] Zhao, G., Xiong, Z., Jin, X., Hou, L., & Gao, W. (2018). Prediction of contact stiffness in bolted interface with natural frequency experiment and FE analysis. *Tribology International*, 127. <https://doi.org/10.1016/j.triboint.2018.05.044>
- [120] Ay, A. M., Khoo, S., & Wang, Y. (2019). Probability distribution of decay rate: a statistical time-domain damping parameter for structural health damage identification. *Structural Health Monitoring*, 18(1). <https://doi.org/10.1177/1475921718817336>
- [121] MSC Nastran 2020 Dynamic Analysis User's Guide, Modal Transient response, 2020. p. 204-206
- [122] Seventekidis, P., & Giagopoulos, D. (2022). Model-based damage identification with simulated transmittance deviations and deep learning classification. *Structural Health Monitoring*. <https://doi.org/10.1177/14759217211054348>
- [123] Zhang, H., Schulz, M. J., Naser, A., Ferguson, F., & Pai, P. F. (1999). Structural health monitoring using transmittance functions. *Mechanical Systems and Signal Processing*, 13(5). <https://doi.org/10.1006/mssp.1999.1228>
- [124] Caccese, V., Mewer, R., & Vel, S. S. (2004). Detection of bolt load loss in hybrid composite/metal bolted connections. *Engineering Structures*, 26(7). <https://doi.org/10.1016/j.engstruct.2004.02.008>
- [125] Yang, Q., Tan, L., Wu, B. Q., Tian, G. L., Xu, L., Yang, J. T., Jiang, J. H., & Yu, R. Q. (2020). Beyond one-against-all (OAA) and one-against-one (OAO): An exhaustive and parallel half-against-half (HAH) strategy for multi-class classification and applications to metabolomics. *Chemometrics and Intelligent Laboratory Systems*, 204. <https://doi.org/10.1016/j.chemolab.2020.104107>
- [126] Sietsma, J., & Dow, R. J. F. (1991). Creating artificial neural networks that generalize. *Neural Networks*, 4(1). [https://doi.org/10.1016/0893-6080\(91\)90033-2](https://doi.org/10.1016/0893-6080(91)90033-2)

Chapter 8-Bibliography

- [127] Zhu, Z., Peng, G., Chen, Y., & Gao, H. (2019). A convolutional neural network based on a capsule network with strong generalization for bearing fault diagnosis. *Neurocomputing*, 323. <https://doi.org/10.1016/j.neucom.2018.09.050>
- [128] Wang, H., Yang, W., Zhao, Z., Luo, T., Wang, J., & Tang, Y. (2019). Rademacher dropout: An adaptive dropout for deep neural network via optimizing generalization gap. *Neurocomputing*, 357. <https://doi.org/10.1016/j.neucom.2019.05.008>
- [129] Worden, K., & Burrows, A. P. (2001). Optimal sensor placement for fault detection. *Engineering Structures*, 23(8). [https://doi.org/10.1016/S0141-0296\(00\)00118-8](https://doi.org/10.1016/S0141-0296(00)00118-8)
- [130] Colombo, L., Todd, M. D., Sbarufatti, C., & Giglio, M. (2022). On statistical Multi-Objective optimization of sensor networks and optimal detector derivation for structural health monitoring. *Mechanical Systems and Signal Processing*, 167. <https://doi.org/10.1016/j.ymssp.2021.108528>
- [131] Koutsovasilis, P., & Beitel Schmidt, M. (2010). Model order reduction of finite element models: Improved component mode synthesis. *Mathematical and Computer Modelling of Dynamical Systems*, 16(1). <https://doi.org/10.1080/13873951003590214>
- [132] Kim, J. H., Boo, S. H., & Lee, P. S. (2019). A dynamic condensation method with free interface substructuring. *Mechanical Systems and Signal Processing*, 129. <https://doi.org/10.1016/j.ymssp.2019.04.021>
- [133] Thai, H. T. (2022). Machine learning for structural engineering: A state-of-the-art review. In *Structures* (Vol. 38). <https://doi.org/10.1016/j.istruc.2022.02.003>
- [134] Gordan, M., Sabbagh-Yazdi, S. R., Ismail, Z., Ghaedi, K., Carroll, P., McCrum, D., & Samali, B. (2022). State-of-the-art review on advancements of data mining in structural health monitoring. In *Measurement: Journal of the International Measurement Confederation* (Vol. 193). <https://doi.org/10.1016/j.measurement.2022.110939>
- [135] Prawin, J., & Rama Mohan Rao, A. (2020). Vibration-based breathing crack identification using non-linear intermodulation components under noisy environment. *Structural Health Monitoring*, 19(1). <https://doi.org/10.1177/1475921719836953>
- [136] Pirdayr, A., Mohammadi, M., Javad Kazemzadeh-Parsi, M., & Rajabi, M. (2021). Self-loosening effects on vibration characteristics of plates with bolted joints: An experimental and finite element analysis. *Measurement: Journal of the International Measurement Confederation*, 185. <https://doi.org/10.1016/j.measurement.2021.109922>
- [137] Sobie, C., Freitas, C., & Nicolai, M. (2018). Simulation-driven machine learning: Bearing fault classification. *Mechanical Systems and Signal Processing*, 99. <https://doi.org/10.1016/j.ymssp.2017.06.025>
- [138] Santos, A., Figueiredo, E., Silva, M. F. M., Sales, C. S., & Costa, J. C. W. A. (2016). Machine learning algorithms for damage detection: Kernel-based approaches. *Journal of Sound and Vibration*, 363. <https://doi.org/10.1016/j.jsv.2015.11.008>
- [139] Liu, A., Wang, L., Bornn, L., & Farrar, C. (2019). Robust structural health monitoring under environmental and operational uncertainty with switching state-space autoregressive models. *Structural Health Monitoring*, 18(2). <https://doi.org/10.1177/1475921718757721>
- [140] Sony, S., Gamage, S., Sadhu, A., & Samarabandu, J. (2022). Multiclass Damage Identification in a Full-Scale Bridge Using Optimally Tuned One-Dimensional Convolutional Neural Network. *Journal of Computing in Civil Engineering*, 36(2). [https://doi.org/10.1061/\(asce\)cp.1943-5487.0001003](https://doi.org/10.1061/(asce)cp.1943-5487.0001003)
- [141] Parand Akbari, Francis Ogoke, Ning-Yu Kao, Kazem Meidani, Chun-Yu Yeh, William Lee, Amir Barati Farimani. (2022). MeltpoolNet: Melt pool characteristic prediction in Metal Additive Manufacturing using machine learning. *Additive Manufacturing* 55, <https://doi.org/10.1016/j.addma.2022.102817>